ROTATIONAL FLOW ANALYSIS OF SOME FLUIDS USING RADIAL BASIS FUNCTION PSEUDOSPECTRAL METHOD

Thesis Submitted for the Award of the Degree of

DOCTOR OF PHILOSOPHY

in

Mathematics

By

Himanshu

Registration Number: 42100137

Supervised By

Dr. Gurpreet Singh Bhatia (11518)

Associate Professor

Department of Mathematics

Lovely Professional University, Punjab

Co-Supervised by

Dr. Rajesh Kumar Chandrawat

Assistant Professor

School of Engineering & I.T.

Manipal Academy of Higher Education, Dubai

LOVELY PROFESSIONAL UNIVERSITY, PUNJAB

2025

DECLARATION

I, hereby declared that the presented work in the thesis entitled "**Rotational Flow Analysis of Some Fluids using Radial Basis Function Pseudospectral Method**" in fulfilment of degree of **Doctor of Philosophy (Ph. D.)** is outcome of research work carried out by me under the supervision of **Dr. Gurpreet Singh Bhatia**, working as **Associate Professor**, in the **Department of Mathematics**, Lovely Professional University, Punjab, India and under the co-supervision of **Dr. Rajesh Kumar Chandrawat** working as **Assistant Professor**, in the School of Engineering & I.T., Manipal Academy of Higher Education, Dubai. In keeping with general practice of reporting scientific observations, due acknowledgements have been made whenever work described here has been based on findings of other investigator. This work has not been submitted in part or full to any other University or Institute for the award of any degree.

(Signature)

Name of the scholar: Himanshu

Registration No.: 42100137

Department of Mathematics

School of Chemical Engineering and Physical Sciences

Lovely Professional University,

Punjab, India

CERTIFICATE

This is to certify that the work reported in the Ph. D. thesis entitled "**Rotational Flow Analysis of Some Fluids using Radial Basis Function Pseudospectral Method**" submitted in fulfillment of the requirement for the award of degree of **Doctor of Philosophy (Ph.D.)** in the **Department of Mathematics** is a research work carried out by **Himanshu (42100137)**, is bonafide record of his/her original work carried out under my supervision and that no part of thesis has been submitted for any other degree, diploma or equivalent course.

Name of supervisor: Dr. Gurpreet Singh Bhatia

Designation: Associate Professor

Department of Mathematics

School of Chemical Engineering and Physical Sciences

Lovely Professional University, Punjab

Name of Co-Supervisor: Dr Rajesh Kumar Chandrawat

Designation: Assistant Professor

School of Engineering & IT

Manipal Academy of Higher Education, Dubai

Abstract

This thesis presents a comprehensive numerical investigation into the behavior of various complex fluids namely dusty fluid, micropolar dusty fluid, and Jeffrey fluid within confined channel flows under the influence of rotation and magnetic fields. Motivated by the growing relevance of non-Newtonian and particle-laden fluid systems in industrial and geophysical applications, the work aims to offer accurate and insightful computational models by leveraging the Radial Basis Function Pseudospectral Method (RBF-PSM). Both horizontal and inclined channel configurations are considered to examine the interplay between geometric orientation, body forces, and fluid properties on flow behavior and energy requirements.

Despite extensive advancements in fluid dynamics, limited studies address the combined influence of rotation, magnetic fields, and channel inclination on complex fluids such as dusty, micropolar, and Jeffrey fluids. Existing models often neglect multiphase interactions and microstructural effects, while classical numerical schemes may not offer the precision needed for such complex environments. Additionally, there is a lack of comprehensive studies incorporating detailed energy considerations across varying flow configurations.

The thesis is organized into five chapters, each contributing to the overarching goal of understanding and quantifying complex flow phenomena through meshless numerical methods. The results demonstrate that rotation, magnetic field strength, fluid microstructure, inclination angle, and non-Newtonian properties significantly influence velocity distributions, microrotation characteristics, thermal transport, stability behavior, and pumping power requirements. The findings also validate the suitability and

robustness of the RBF-PSM for solving complex, nonlinear fluid flow problems in rotating frames with high accuracy.

Acknowledgments

I express my sincere gratitude to all who contributed to the successful completion of this thesis.

This thesis would not have been possible without the unwavering support and encouragement of one individual, to whom I am deeply grateful, my **supervisor, Dr. Gurpreet Singh Bhatia**. He was always there whenever I asked for help, offering insightful advice and constructive feedback. During times when I felt like giving up, he motivated and supported me tirelessly, instilling in me the confidence to persevere. I consider myself truly fortunate to have had him by my side throughout this endeavor.

I would also like to extend my heartfelt thanks to my **co-supervisor, Dr. Rajesh Kumar Chandrawat** for his invaluable support and guidance. At critical moments when we needed it the most, his timely help, thoughtful suggestions, and academic insight made a significant difference. His willingness to step in and assist during key stages of this research was truly appreciated and instrumental in shaping the final outcome of this work.

I would also like to express my sincere gratitude to **Lovely Professional University, Punjab** for awarding me the **"Collaboration Based And Related" scholarship**, which provided essential financial support to complete this thesis. This scholarship significantly eased my financial burden by covering my academic fees, allowing me to focus wholeheartedly on my research.

I am equally thankful to my college, **Dr. Bhim Rao Ambedkar Govt. College, Kaithal**, where I am currently working. Their understanding and support throughout this period have been invaluable. I am especially grateful to the staff for providing me with the flexibility and time needed to focus on my thesis by easing my administrative responsibilities during crucial stages of this research. Their cooperation and encouragement played a vital role in helping me balance professional responsibilities with academic work.

Finally, I owe my deepest gratitude to **my family** for their unconditional love and unwavering support through every high and low. Their belief in me remained constant, even during the most challenging phases of this journey. It is their strength, patience, and sacrifices that made this achievement possible.

Thank you for being a part of this achievement.

Himanshu

Contents

List of Symbols

ρ_f: Density of the fluid

P: Pressure

μ: Dynamic viscosity

$\mathbf{u}$: Fluid velocity

$\mathbf{u} = (u_1, u_2, u_3)$: Components of fluid velocity in x, y, and z direction

t: Time

Ω: Angular velocity

Q: Volume flow rate

ΔP: Pressure drop

P_{pow}: Pumping power

L: Characteristic length

U_0: Characteristic velocity

c_p: Specific heat at constant pressure

T: Temperature

ΔT: Temperature difference

v: Kinematic viscosity

B_0: External magnetic field

σ: Electrical conductivity

η: Micropolar parameter

κ: Micro rotation viscosity

$\mathbf{M}$: Microrotation vector

γ: Spin viscosity

ρ_p: Density of fluid particle

K: Drag coefficient

ϕ: Radial basis function

λ_i: Unknown interpolate coefficients

A: Matrix of Euclidean distance at RBF

D_1: First order differentiation matrix at RBF

D_2: Second order differentiation matrix at RBF

k: Thermal conductivity

$\mathbf{q}$: Heat flux vector

Φ: Viscous dissipation function

T_p: Temperature of particle phase

c_{pp}: Specific heat of fluid particle

$\mathbf{F}_L$: Lorentz force per unit volume

List of Abbreviations

Abbreviation	**Full Form**
CFD	Computational Fluid Dynamics
MHD	Magnetohydrodynamics
RBF	Radial Basis Function
PDE	Partial Differential Equation
RBF-PSM	Radial Basis Function Pseudospectral Method
ODE	Ordinary Differential Equation
SSP RK43	Strong Stability Preserving Runge-Kutta Method of order 3 with 4 Stages
MCBS DQM	Modified Cubic B-Spline Differential Quadrature Method

List of Tables

List of Figures

Chapter 1

Introduction

1.1 Fluids and Computational Fluid Dynamics

A fluid is a substance that flows under an applied force, distinguishing it from a solid, and encompasses materials such as water (a liquid) and air (a gas). Its loosely arranged molecules allow it to deform under any shear stress, preventing it from retaining a fixed shape. In engineering, fluids are examined through their physical properties such as density, viscosity, and pressure, which determine their behavior under different temperatures and forces, shedding light on their roles in systems like pipes or machinery.

Fluids are fundamental to engineering and industrial operations, driving processes that range from power generation to material transport. In mechanical systems, fluids like water or oil facilitate energy transfer in hydraulic machinery, while gases like air shape aerodynamic designs in aerospace. Specialized fluids such as micropolar, dusty, and Jeffrey fluids play a critical role in applications like chemical processing or polymer manufacturing, where their unique flow behaviours, influenced by channel orientation, demand precise analysis. To harness these fluids effectively, computational fluid dynamics (CFD) emerges as an essential tool, enabling engineers to predict and optimize flow characteristics under varying conditions. Studying CFD is vital because it reveals how fluid properties affect system efficiency, such as pumping power in confined channels.

CFD transforms the study of fluid behavior by employing numerical simulations to solve complex equations governing flow, such as those describing momentum and energy conservation. This approach shines where experimental or analytical methods fall short, offering a window into intricate dynamics—like the velocity profiles of micropolar, dusty, and Jeffrey fluids in flat or slanted channels. In engineering, CFD finds application in designing efficient systems, from predicting pressure drops in pipelines to optimizing pump performance by calculating power requirements. In industries, it fosters innovation by modelling real-world conditions, like the behaviour of particle-filled dusty fluids under shear or the response of Jeffrey fluids to non-Newtonian forces. By providing detailed, predictive data, CFD not only enhances theoretical models but also guides practical decisions, making it a cornerstone for advancing fluid-related technologies and improving industrial outcomes.

1.2 Classification of Fluid Flows

Fluid flow can be classified into various categories based on factors such as velocity, viscosity, compressibility, and external forces, essential for engineering analysis. These classifications explain fluid behavior in systems like channels, pipelines, and turbines. Figure 1.1 illustrates the classification of fluid flows.

(a) **Based on Velocity Variation**

   (i) **Steady Flow**: Occurs when fluid properties, such as velocity and pressure, remain constant over time at a specific point, simplifying flow predictions, for example, water flowing steadily through a uniform pipe.

   (ii) **Unsteady Flow**: Features fluid properties that vary with time at a given point, complicating analysis due to temporal changes, for example, waves or surges in a river during a storm.

(b) **Based on Viscosity Effects**

   (i) **Viscous Flow**: Characterized by significant viscosity effects, where internal friction influences flow, particularly near solid boundaries, for example,

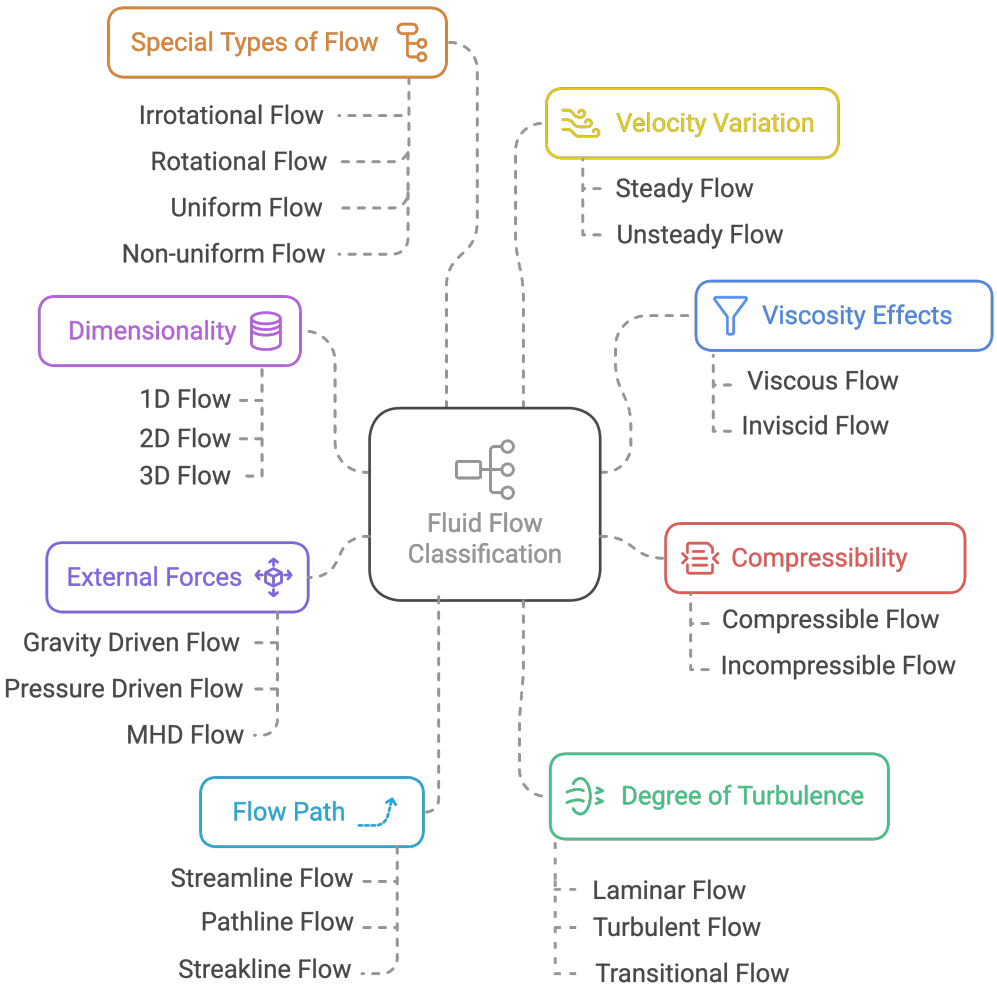

Fig. 1.1 Classification of Fluid Flows

slow oil movement in a pipe displaying shear stress.

(ii) **Inviscid Flow**: Assumes negligible viscosity, an idealized case ignoring friction, simplifying theoretical studies, for example, air flowing frictionlessly over an aircraft wing.

(c) **Based on Compressibility**

(i) **Compressible Flow**: Involves significant density variations under pressure, prevalent in high-speed gases, for example, air in a supersonic jet where density changes impact aerodynamics.

(ii) **Incompressible Flow**: Maintains nearly constant density, typical for low-speed liquids, easing flow calculations, for example, water in a domestic pipeline under steady conditions.

(d) **Based on Degree of Turbulence**

(i) **Laminar Flow**: Describes smooth, orderly flow with layered, non-turbulent motion, governed by low Reynolds numbers, for example, slow water flow in a narrow tube.

(ii) **Turbulent Flow**: Exhibits chaotic, irregular flow with eddies and mixing, characteristic of high Reynolds numbers, for example, fast river currents over rocks.

(iii) **Transitional Flow**: Represents an intermediate state between laminar and turbulent, with partial order and irregularity, for example, water transitioning in a pipe as speed increases.

(e) **Based on Flow Path**

(i) **Streamline Flow**: Features fluid particles following well-defined, continuous paths, typical in steady, orderly flows, for example, air moving smoothly around a streamlined object.

(ii) **Pathline Flow**: Traces the actual path of a single fluid particle over time, useful for unsteady flows, for example, smoke particle trajectories in wind.

(iii) **Streakline Flow**: Marks the locus of particles passing through a fixed point, visualizing flow patterns, for example, dye lines in water revealing current paths.

(f) **Based on External Forces**

(i) **Gravity-Driven Flow**: Occurs when gravity propels fluid motion, common in open systems, for example, river water flowing downhill due to gravity.

(ii) **Pressure-Driven Flow**: Results from pressure gradients forcing fluid movement, prevalent in closed systems, for example, oil pumped through pipelines under pressure.

(iii) **Magnetohydrodynamic (MHD) Flow**: Involves fluid motion influenced by magnetic fields, significant in plasma or conductive fluids, for example, liquid metal flow in magnetic confinement.

(g) **Based on Dimensionality**

(i) **One-Dimensional (1D) Flow**: Assumes flow properties vary only along one direction, simplifying analysis, for example, water flow in a straight, uniform pipe.

(ii) **Two-Dimensional (2D) Flow**: Involves variations in two spatial directions, useful for planar systems, for example, airflow over a flat plate.

(iii) **Three-Dimensional (3D) Flow**: Features variations in all three dimensions, reflecting complex real-world flows, for example, turbulent air around a sphere.

(h) **Special Types of Flow**

(i) **Rotational Flow**: Occurs when fluid elements rotate, exhibiting nonzero vorticity, complicating flow analysis, for example, water in a whirlpool.

(ii) **Irrotational Flow**: Features fluid elements without rotation, with zero vorticity, simplifying theoretical models, for example, water flowing smoothly past a streamlined object.

(iii) **Uniform Flow**: Maintains constant properties, such as velocity, across the flow field, aiding design, for example, steady air over a flat surface.

(iv) **Non-Uniform Flow**: Exhibits spatial variations in properties, challenging engineering predictions, for example, water accelerating in a narrowing channel.

1.3 Fluid Properties

Having explored the nature of fluids and their flow classifications, we now examine the key properties that define their behavior in engineering contexts. Figure 1.2 showcases

the key properties of the fluid.

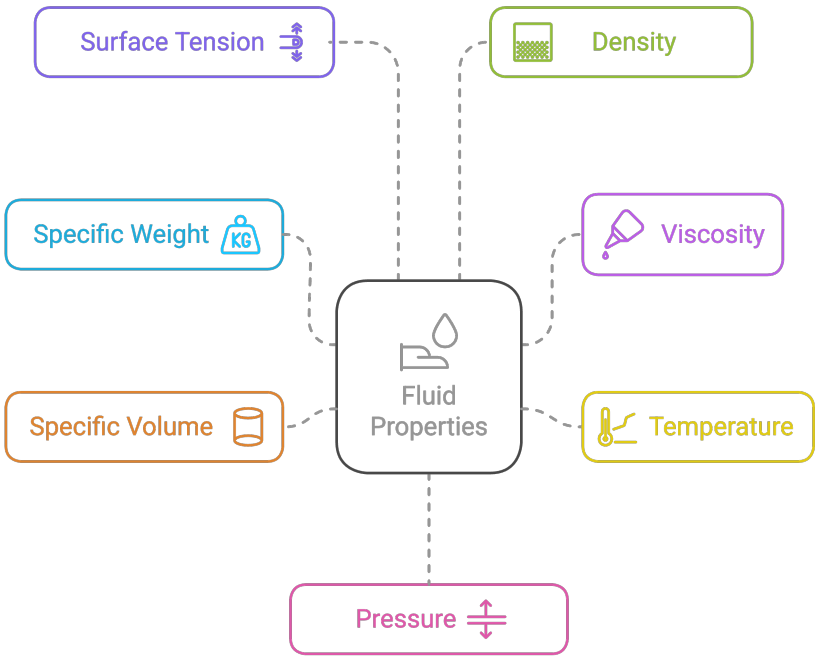

Fig. 1.2 Classification of Fluid Properties

(a) **Density**: Quantifies the mass per unit volume of a fluid, critical for analyzing flow dynamics and stability in engineering systems such as channels or reservoirs. It varies with temperature and pressure.

(b) **Viscosity**: Measures a fluid's resistance to shear deformation, influencing frictional losses and flow characteristics in conduits or lubrication applications. It depends on fluid composition and temperature.

(c) **Temperature**: Assesses the thermal energy of a fluid, altering its viscosity and density, pivotal in processes involving heat transfer or phase changes.

(d) **Pressure**: Defines the force per unit area exerted by a fluid, governing its motion

and distribution in confined or open systems. It varies with depth and external conditions.

(e) **Specific Volume**: Represents the volume per unit mass of a fluid, inversely proportional to density, essential for evaluating compressibility in engineering designs.

(f) **Specific Weight**: Evaluates the gravitational force per unit volume, crucial for determining fluid-induced loads on structures like dams or storage tanks. It varies with gravitational field.

(g) **Surface Tension**: Quantifies the cohesive force per unit length at a fluid's surface, governing interfacial phenomena in microscale systems or droplet dynamics.

1.4 Classification of Fluids

Fluids can be categorized based on properties such as viscosity, compressibility, and composition, which are fundamental for accurate analysis, modeling, and design in engineering and scientific applications. These classifications explain fluid behavior in diverse systems, from pipelines to reactors, as detailed below. Figure 1.3 presents an overview of the different types of fluid classifications.

(a) **Based on Density Variation**

(i) **Ideal Fluids**: Hypothetical fluids with zero viscosity and constant density, incompressible for theoretical simplicity. Example: Frictionless water assumed in idealized pipe flow studies.

(ii) **Real Fluids**: Actual fluids exhibiting viscosity and variable density, subject to compressibility and friction. Example: Air flowing through a turbine or water in a river, requiring detailed analysis.

(b) **Based on Electrical Conductivity**

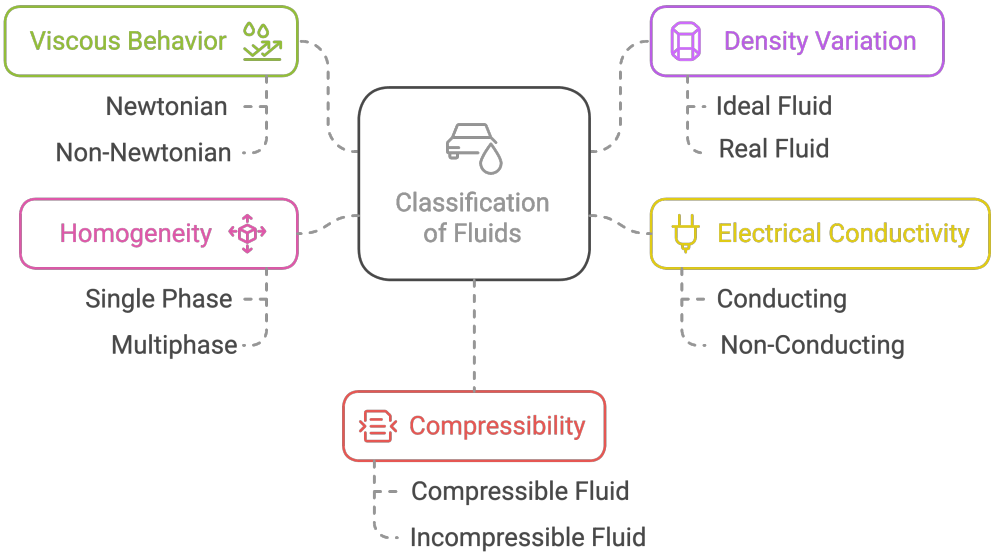

Fig. 1.3 Classification of Fluids

(i) **Conducting Fluids (MHD Fluids)**: Fluids capable of conducting electricity, influenced by magnetic fields in magnetohydrodynamics. Example: Liquid sodium in nuclear reactors or plasma in fusion devices.

(ii) **Non-Conducting Fluids**: Fluids with negligible electrical conductivity, unaffected by magnetic fields. Example: Distilled water or most oils in hydraulic systems.

(c) **Based on Compressibility**

(i) **Incompressible Fluids**: Fluids with minimal density changes under pressure, simplifying flow analysis for low-speed applications. Example: Water in a domestic pipeline or oil in slow-moving machinery.

(ii) **Compressible Fluids**: Fluids whose density varies significantly with pressure, critical at high speeds or temperatures. Example: Steam in a boiler or air in a supersonic jet, affecting performance.

(d) **Based on Homogeneity**

(i) **Single-phase Fluids**: Fluids with a uniform phase, free of phase boundaries, facilitating straightforward modeling. Example: Pure water in a tank or dry air in ventilation systems.

(ii) **Multiphase Fluids**: Fluids comprising multiple phases, requiring complex analysis due to phase interactions. Example: An oil-water emulsion in extraction processes or blood with cells and plasma.

(e) **Based on Viscosity Behavior**

(i) **Newtonian Fluid:** A Newtonian fluid exhibits a linear relationship between shear stress and the rate of strain, characterized by constant viscosity under varying shear rates, making it ideal for predictable flow analysis in engineering. Such fluids, like water, air, gasoline, and alcohol, follow Newton's law of viscosity, enabling straightforward modeling in systems such as pipelines, aerodynamics, and hydraulic machinery. Their behavior simplifies the study of flow dynamics, contrasting with non-Newtonian fluids, and is crucial for applications involving steady or laminar flows, aligning with the analysis of fluid velocities in channels.

Newton's Law of Viscosity: Newton's law of viscosity states that the shear stress in a Newtonian fluid is directly proportional to the velocity gradient. It governs the fluid's resistance to flow, with viscosity remaining constant [1].

$$\tau = \mu \frac{d\mathbf{u}}{dy} \tag{1.1}$$

- τ (Pa) = Shear stress, the force per unit area.
- μ (Pa·s) = Dynamic viscosity.
- $\mathbf{u}$ (m/s) = Velocity, the speed of fluid flow perpendicular to the shear direction.
- y (m) = Distance perpendicular to the flow direction, defining the gradient across fluid layers.

(ii) **Non-Newtonian Fluid:** In non-Newtonian fluids, the relationship between shear stress and strain rate is nonlinear, deviating from Newton's law of viscosity and making flow analysis more challenging. Unlike Newtonian fluids with constant viscosity, these fluids viscosity varies—decreasing, increasing, or requiring a yield stress—depending on shear. Examples include blood, tar, sperm, heavy oils and lubricants crucial for engineering applications like biomechanics or industrial processing, and advanced fluid systems, including micropolar, dusty, and Jeffrey fluids, which we will explore in upcoming sections.

1.5 Governing Equations

This section examines three fundamental equations, which together govern fluid flow and heat transfer in engineering systems.

(a) Continuity Equation

(b) Equation of Motion (Navier Stokes Equation)

(c) Energy Equation (Heat Transfer Equation)

1.5.1 Continuity Equation

The continuity equation in fluid dynamics embodies the principle of mass conservation, asserting that the mass of a fluid entering a system must equal the mass leaving it, barring any accumulation or depletion within the system. This fundamental concept ensures that mass is neither created nor destroyed, forming the backbone of flow analysis in engineering applications like pipelines or channels, where fluid behavior must be precisely predicted.

Derivation Using an Infinitesimal Control Volume

Let us derive the continuity equation by considering a fixed control volume in the shape of a rectangular parallelepiped with dimensions dx, dy, and dz, positioned in a Cartesian

coordinate system, as illustrated in Figure 1.4. This infinitesimal volume element has a volume $dV = dx\,dy\,dz$, and we analyze the mass flow through its faces to establish the mass balance.

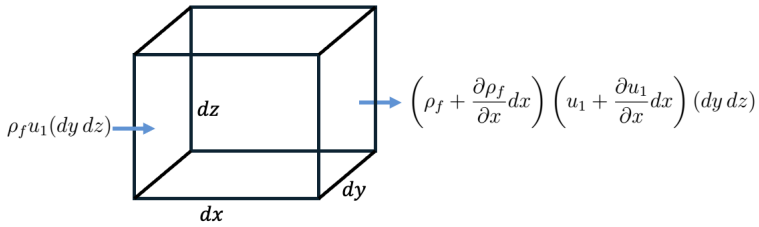

Fig. 1.4 Differential control volume with dimensions dx, dy, and dz, aligned with Cartesian axes.

Let:

- ρ_f = Fluid density.
- $\mathbf{u}$ = Velocity vector.
- u_1, u_2, u_3 = Velocity components.
- t = Time.

(a) **Mass Flow Rate Through Faces:** Consider the mass flow rate through the faces perpendicular to the x-axis. At the face $x = x$ (left face), the velocity component is u_1, and the density is ρ_f. The area of this face is $dy\,dz$, so the mass flow rate entering is:

$$\text{mass flow rate in} = \rho_f u_1 (dy\,dz) \tag{1.2}$$

At the opposite face, $x = x + dx$ (right face), the density is approximately $\rho_f + \frac{\partial \rho_f}{\partial x}dx$, and the velocity is $u_1 + \frac{\partial u_1}{\partial x}dx$ due to Taylor series expansion. The mass flow rate leaving this face (outflow) is:

$$\text{mass flow rate out} = \left(\rho_f + \frac{\partial \rho_f}{\partial x}dx\right)\left(u_1 + \frac{\partial u_1}{\partial x}dx\right)(dy\,dz) \tag{1.3}$$

Neglecting higher-order terms (since dx is small), the net mass flow rate in the x-direction is:

$$\text{(mass flow rate in) - (mass flow rate out)} = -\frac{\partial(\rho_f u_1)}{\partial x}(dx\,dy\,dz) \tag{1.4}$$

Similarly, for the y-direction (faces at y and $y + dy$) and z-direction (faces at z and $z + dz$), the net mass flow rates are:

$$\text{net mass flow rate in } y = -\frac{\partial(\rho_f u_2)}{\partial y}(dx\,dy\,dz) \tag{1.5}$$

$$\text{net mass flow rate in } z = -\frac{\partial(\rho_f u_3)}{\partial z}(dx\,dy\,dz) \tag{1.6}$$

The total net mass flow rate into the volume element is the sum of these contributions:

$$\text{total net mass flow rate} = -\left[\frac{\partial(\rho_f u_1)}{\partial x} + \frac{\partial(\rho_f u_2)}{\partial y} + \frac{\partial(\rho_f u_3)}{\partial z}\right](dx\,dy\,dz) \tag{1.7}$$

In vector form, this is the divergence of the mass flux:

$$\text{total net mass flow rate} = -\nabla \cdot (\rho_f \mathbf{u})(dx\,dy\,dz) \tag{1.8}$$

where $\nabla \cdot (\rho_f \mathbf{u}) = \dfrac{\partial(\rho_f u_x)}{\partial x} + \dfrac{\partial(\rho_f u_y)}{\partial y} + \dfrac{\partial(\rho_f u_z)}{\partial z}$

(b) **Rate of Change of Mass Inside the Volume:** The mass inside the volume element is $\rho_f(dx\,dy\,dz)$. Since density may change with time, the rate of change of mass within the element is:

$$\frac{d}{dt}[\rho_f(dx\,dy\,dz)] = \frac{\partial \rho_f}{\partial t}(dx\,dy\,dz) \tag{1.9}$$

assuming the volume $dx\,dy\,dz$ is fixed.

(c) **Mass Conservation Principle:** Mass conservation requires that the rate of increase of mass inside the volume element equals the net mass flow rate entering it:

$$\frac{\partial \rho_f}{\partial t}(dx\,dy\,dz) = -\nabla \cdot (\rho_f \mathbf{u})(dx\,dy\,dz) \tag{1.10}$$

Dividing through by the volume $dx\,dy\,dz$, we obtain the continuity equation as described by [2]:

$$\frac{\partial \rho_f}{\partial t} + \nabla \cdot (\rho_f \mathbf{u}) = 0 \tag{1.11}$$

This represents the general expression of the continuity equation, applicable to both compressible and incompressible fluids. For incompressible fluids, where ρ_f is constant, the equation simplifies to:

$$\nabla \cdot \mathbf{u} = 0 \tag{1.12}$$

This derived equation ensures mass conservation, a critical tool for analyzing fluid flow in this thesis, such as velocity profiles in channels.

1.5.2 Equation of Motion (Navier-Stokes Equation)

The equation of motion, commonly known as the Navier-Stokes equation, governs the dynamics of fluid flow by balancing forces acting on a fluid, including inertia, pressure, viscosity, and external effects like gravity. This fundamental equation is essential for predicting fluid behavior in engineering systems such as channels, turbines, and pipelines, where understanding velocity and pressure distributions is critical. Let us derive it step by step using a small volume element to see how these forces come together.

Derivation Using an Infinitesimal Control Volume

To derive the Navier-Stokes equation, imagine a tiny fixed control volume shaped element as defined above and illustrated in Figure 1.4.

- ρ_f = Density.
- $\mathbf{u}$ = Velocity vector with components u_1, u_1, u_3.
- P = Pressure.
- μ = Dynamic viscosity.
- g = Body force like gravity.

(a) **Mass and Acceleration:** The mass of the fluid inside the volume element is $\rho_f \, dV = \rho_f \, dx \, dy \, dz$. The acceleration of the fluid includes local changes over time and convective effects due to flow. The material derivative of velocity, which captures the total acceleration, is:

$$\frac{D\mathbf{u}}{Dt} = \frac{\partial \mathbf{u}}{\partial t} + (\mathbf{u} \cdot \nabla)\mathbf{u} \tag{1.13}$$

For the x-component, this becomes:

$$\frac{Du_1}{Dt} = \frac{\partial u_1}{\partial t} + u_1 \frac{\partial u_1}{\partial x} + u_2 \frac{\partial u_1}{\partial y} + u_3 \frac{\partial u_1}{\partial z} \tag{1.14}$$

The force (mass times acceleration) in the x-direction is then:

$$\rho_f \, \frac{Du_1}{Dt} \, dV \tag{1.15}$$

(b) **Forces Acting on the Volume Element:** We need to balance this with all forces: pressure, viscous forces, and body forces.

(i) **Pressure Force**: Pressure P acts normal to each face. At the left face ($x = x$), the pressure force is $-P \, dy \, dz$ (negative because it acts inward). At the right face ($x = x + dx$), pressure is $P + \frac{\partial P}{\partial x} dx$, so the force is $-(P + \frac{\partial P}{\partial x} dx) dy \, dz$. The net pressure force in x-direction is:

$$\text{Net pressure force} = -(P + \frac{\partial P}{\partial x} dx) dy \, dz + P \, dy \, dz = -\frac{\partial P}{\partial x} dx \, dy \, dz \tag{1.16}$$

Similar calculations for y and z directions yield net forces:

$$-\frac{\partial P}{\partial y} dx\, dy\, dz \tag{1.17}$$

$$-\frac{\partial P}{\partial z} dx\, dy\, dz \tag{1.18}$$

(ii) **Viscous Forces**: Viscosity resists shear. The shear stress:

$$\tau_{ij} = \mu(\frac{\partial u_i}{\partial x_j} + \frac{\partial u_j}{\partial x_i}) \tag{1.19}$$

For the x-direction, consider the stress τ_{xx} (normal) and shear stresses τ_{xy}, τ_{xz} (on side faces). The net viscous force in x involves differences across dx, dy, dz. The viscous term, approximated using the Laplacian, contributes:

$$\mu \nabla^2 u_1\, dV$$

(iii) **Body Force**: Gravity $\rho_f \mathbf{g}\, dV$ acts throughout the volume, with x-component $\rho_f g_1\, dV$.

(c) **Force Balance:** As per Newton's second law, the combined forces acting on a body equals the rate of change of momentum:

$$\sum F = \rho_f \frac{D\mathbf{u}}{Dt}\, dV \tag{1.20}$$

Summing pressure, viscous, and body forces in x-direction:

$$-\frac{\partial P}{\partial x} dx\, dy\, dz + \mu \frac{\partial^2 u_1}{\partial x^2} dx\, dy\, dz + \rho_f g_1\, dx\, dy\, dz =$$

$$\rho_f \left(\frac{\partial u_1}{\partial t} + u_1 \frac{\partial u_1}{\partial x} + u_2 \frac{\partial u_1}{\partial y} + u_3 \frac{\partial u_1}{\partial z} \right) dx\, dy\, dz \tag{1.21}$$

Dividing by $dV = dx\,dy\,dz$:

$$\rho_f \frac{Du_1}{Dt} = -\frac{\partial P}{\partial x} + \mu \nabla^2 u_1 + \rho_f g_1 \tag{1.22}$$

In vector form, for all directions, this becomes the Navier-Stokes equation as shown by [2]:

$$\rho_f \frac{D\mathbf{u}}{Dt} = -\nabla P + \mu \nabla^2 \mathbf{u} + \rho_f \mathbf{g} \tag{1.23}$$

This equation, derived from force balance, captures fluid motion, essential for analyzing velocity profiles.

1.5.3 Energy Equation (Heat Transfer)

In fluid dynamics, the energy equation represents the conservation of energy, indicating that changes in a fluid system's total energy occur only through heat transfer, work performed on or by the system, and internal energy transformations such as viscous dissipation. This equation, rooted in the first law of thermodynamics, is essential for predicting temperature distributions and heat transfer in engineering applications, including channels, heat exchangers, and thermal management systems.

Derivation Using an Infinitesimal Control Volume

Consider a rectangular parallelepiped as described in Figure 1.4, with dimensions dx, dy, and dz, aligned with the Cartesian axes. The volume of this infinitesimal element is $dV = dx\,dy\,dz$. We analyze the balance of energy within this element, focusing on internal energy and heat transfer.
Let:

- ρ_f = Density of the fluid.
- T = Temperature.
- u_i = Velocity components in x, y, z directions (u_1, u_2, u_3).

- k = Thermal conductivity.
- c_p = Specific heat at constant volume.
- $\mathbf{q}$ = Heat flux vector.
- Φ = Viscous dissipation function.

(a) **Rate of Change of Internal Energy Inside the Volume:** The total internal energy inside the volume element is $\rho_f \, u \, dV$, where u is the specific internal energy. The rate of change of internal energy within the element is:

$$\frac{\partial}{\partial t}(\rho_f u) \, dx \, dy \, dz \tag{1.24}$$

(b) **Net Energy Inflow by Convection:** Energy is transported into and out of the volume by fluid motion (convection). The net rate of internal energy inflow in the x-direction is:

$$\begin{aligned} \text{Inflow at } x: \quad & (\rho_f u u_1) \, dy \, dz \\ \text{Outflow at } x + dx: \quad & \left[\rho_f u u_1 + \frac{\partial (\rho_f u u_1)}{\partial x} dx \right] dy \, dz \\ \text{Net inflow in } x = & - \frac{\partial (\rho_f u u_1)}{\partial x} \, dx \, dy \, dz \end{aligned}$$

Similarly, for y and z directions, the total net convective inflow is:

$$- \left[\frac{\partial (\rho_f u u_1)}{\partial x} + \frac{\partial (\rho_f u u_2)}{\partial y} + \frac{\partial (\rho_f u u_3)}{\partial z} \right] dx \, dy \, dz = -\nabla \cdot (\rho_f u \mathbf{u}) \, dV \tag{1.25}$$

(c) **Net Heat Inflow by Conduction:** Heat enters and leaves the control volume by conduction, described by Fourier's law:

$$\mathbf{q} = -k \nabla T \tag{1.26}$$

The net heat inflow by conduction in the x-direction is:

$$\begin{aligned} \text{Inflow at } x: \quad & q_1\, dy\, dz \\ \text{Outflow at } x+dx: \quad & \left[q_1 + \frac{\partial q_1}{\partial x} dx\right] dy\, dz \\ \text{Net inflow in } x = & -\frac{\partial q_1}{\partial x}\, dx\, dy\, dz \end{aligned}$$

Summing over all directions, the total net conductive inflow is:

$$-\nabla \cdot \mathbf{q}\, dV = \nabla \cdot (k \nabla T)\, dV \tag{1.27}$$

(d) **Internal Heat Generation by Viscous Dissipation:** Viscous effects convert mechanical energy into thermal energy within the fluid. The rate of internal heat generation per unit volume is denoted by Φ, so the total generation within the element is:

$$\Phi\, dx\, dy\, dz \tag{1.28}$$

(e) **Energy Conservation Principle:** The total rate of increase of internal energy inside the volume must equal the sum of the net inflow by convection, net inflow by conduction, and internal heat generation:

$$\frac{\partial}{\partial t}(\rho_f u)\, dV = -\nabla \cdot (\rho_f u \mathbf{u})\, dV + \nabla \cdot (k \nabla T)\, dV + \Phi\, dV \tag{1.29}$$

Dividing through by dV, we have:

$$\frac{\partial (\rho_f u)}{\partial t} + \nabla \cdot (\rho_f u \mathbf{u}) = \nabla \cdot (k \nabla T) + \Phi \tag{1.30}$$

(f) **Expressing in Terms of the Material Derivative:** Recall that the material derivative (substantial derivative) is defined as:

$$\frac{D}{Dt} = \frac{\partial}{\partial t} + \mathbf{u} \cdot \nabla \tag{1.31}$$

For any scalar quantity f:

$$\frac{Df}{Dt} = \frac{\partial f}{\partial t} + \mathbf{u} \cdot \nabla f \tag{1.32}$$

Applying this to internal energy per unit mass (u), and using the continuity equation, the left side simplifies to:

$$\rho_f \frac{Du}{Dt} \tag{1.33}$$

Thus, the energy equation becomes:

$$\rho_f \frac{Du}{Dt} = \nabla \cdot (k \nabla T) + \Phi \tag{1.34}$$

(g) **Relating Internal Energy to Temperature:** For most fluids,

$$u = c_p T \tag{1.35}$$

where c_p stands for the specific heat under constant volume conditions. Therefore,

$$\frac{Du}{Dt} = c_p \frac{DT}{Dt} \tag{1.36}$$

and the energy equation may be expressed as described by [3]:

$$\rho_f c_p \frac{DT}{Dt} = \nabla \cdot (k \nabla T) + \Phi \tag{1.37}$$

(h) **Physical Meaning of Each Term:**

- $\rho_f c_p \frac{DT}{Dt}$ = Rate of increase of internal energy due to both local and convective temperature changes.
- $\nabla \cdot (k \nabla T)$ = Net heat added to the control volume by conduction (diffusion of heat).
- Φ = Rate of heat generation by viscous dissipation (conversion of mechanical energy into thermal energy).

(i) **Special Case: Pure Heat Conduction (No Fluid Motion):** If the fluid is stationary ($\mathbf{u} = 0$), the convection term vanishes, and the equation reduces to the classical heat conduction equation:

$$\rho_f c_p \frac{\partial T}{\partial t} = \nabla \cdot (k \nabla T) + \Phi \tag{1.38}$$

If viscous dissipation is negligible ($\Phi = 0$) and properties are constant, this further simplifies to:

$$\frac{\partial T}{\partial t} = \alpha \nabla^2 T \tag{1.39}$$

where $\alpha = \frac{k}{\rho_f c_p}$ is the thermal diffusivity.

The energy equation derived above mathematically expresses the conservation of energy in a fluid, accounting for convective and conductive heat transfer, as well as internal heat generation by viscous effects. This equation is fundamental for analyzing temperature fields and heat transfer in fluid flows, complementing the continuity and momentum equations to provide a complete description of fluid behavior in engineering systems.

1.6 Fluid Models

In this section, we will examine the following fluid models, each of which presents unique characteristics and behavior in fluid dynamics.

(a) Micropolar Fluids

(b) Dusty Fluids

(c) Jeffrey Fluids

(d) Magnetohydrodynamic (MHD) Flow

1.6.1 Micropolar Fluids

Micropolar fluids are a class of non-Newtonian fluids that extend classical continuum mechanics to account for the behavior of fluids containing suspended microstructures,

such as particles or fibers, which exhibit rotational motion in addition to translational velocity.

(a) **Development of the Micropolar Fluid Model:** The micropolar fluid model was introduced by Eringen [4] in 1967 as an extension of the classical fluid dynamics theory to account for the rotational motion of particles suspended in the fluid medium. This theory incorporates both the translational velocity of the fluid and the angular velocity (or micro-rotation) of the microelements, leading to a set of coupled differential equations for fluid motion. The key difference between micropolar fluids and traditional Newtonian fluids is that the stress tensor in micropolar fluids includes additional terms for couple stresses, which arise from the micro-rotation of the suspended particles. These equations consider both the rate of strain and the rotational motion of microelements, providing a deeper insight into the dynamics of complex fluids. Mathematically, the equations governing micropolar fluids are obtained from the fundamental laws of mass conservation, linear and angular momentum, and energy transfer. The inclusion of micro-rotation terms in the equations enables the model to capture a range of physical phenomena such as shear thickening, shear thinning, and the effects of microstructural interactions within the fluid [5].

(b) **Examples of Micropolar Fluids:** Several real-world fluids exhibit micropolar characteristics due to the presence of suspended microelements that rotate independently of the fluid's bulk motion. Human blood, a suspension of red blood cells and plasma, is a typical example; the rotation of red blood cells affects blood's rheological properties, particularly in microcirculatory systems. Similarly, anisotropic fluids, such as suspensions of fibers or nanoparticles, exhibit directional dependence in flow characteristics, making them suitable for micropolar fluid modeling, as noted by Eringen [6]. Polymer solutions also display micropolar behavior due to interactions between polymer chains and the surrounding solvent. Guedri et al. [7] highlight that the model effectively describes their shear thinning or thickening properties, which are critical in polymer processing.

(c) **Applications of Micropolar Fluids in Engineering and Industry:** Micropolar fluid theory has proven valuable across a range of scientific and engineering fields, particularly in modeling complex flow behaviors. Sui et al. [8] applied this framework to polymer extrusion, predicting shear-thinning behavior through microrotation-velocity coupling to optimize flow rates and product quality. Vasu et al. [9] extended these principles to biomedical engineering, modeling blood flow in stenotic arteries by capturing asymmetric stresses and microrotation effects from red blood cell interactions, using Eringen's micropolar theory and nanoparticle dynamics. Tanuja et al. [10] leveraged micropolar-Newtonian hybrid nanofluids in cooling systems, boosting thermal efficiency in electronics and energy devices through microstructure-mediated heat transfer. Sowmya et al. [11] demonstrated that micropolar fluid theory enhances load capacity and reduces friction in high-pressure lubrication systems, outperforming Newtonian fluids by up to 30

(d) **Recent Research and Developments (Micropolar Fluid):** The study of micropolar fluids has advanced significantly in recent years, offering deeper insights into complex flow behaviors across various engineering and biomedical applications. Devakar and Raje [12] conducted a study on the unsteady MHD flow involving immiscible micropolar and Newtonian fluids between parallel plates. Their investigation emphasized how various physical parameters influence both velocity and temperature fields, providing insights into transient behaviors in mixed fluid systems. Similarly, Abbas et al. [13] analyzed two-dimensional stagnation-point flow in micropolar fluids, introducing modifications relevant to orthogonal impingement scenarios. Bhattacharyya et al. [14] provided an analytical treatment of micropolar fluid flow and heat transfer over a porous shrinking sheet using the homotopy analysis method (HAM), demonstrating dual solutions for velocity and microrotation profiles under thermal radiation effects. Furthermore, Chen et al. [15] focused on thermal radiation effects in micropolar fluid flow across a flexible surface. They applied an optically thick approximation to reformulate the radiative heat transfer equation. Mekheimer and Kot [16] developed a model using

micropolar fluid theory to study blood flow in a narrowing artery with stenosis. Their results demonstrated that, in contrast to traditional Newtonian models, incorporating micropolar effects leads to significant changes in pressure distribution and velocity fields, thereby improving the precision of blood flow representation. Similarly, Aurangzaib et al. [17] studied the boundary layer and heat transfer behavior over a stretching porous surface, showing how micropolarity influences thermal boundary layer formation. Moreover, Aski et al. [18] investigated the role of suction and injection in controlling micropolar fluid flow through a permeable duct. Their work contributes to fluid control mechanisms in confined geometries. Jangili et al. [19] utilized a homotopy approach to estimate entropy generation in magneto-micropolar buoyancy-driven flow inside solar heating ducts. Their findings include combined effects of natural convection and micro-rotation on temperature and velocity profiles. Mehryan et al. [20] investigated natural convection within porous media filled with micropolar nanofluids, broadening the applicability of micropolar models to energy storage and environmental engineering. In a related study, Bég et al. [21] assessed inclined channel flows of micropolar fluids with MHD effects, examining linear and angular momentum interactions under electromagnetic influences. P. Aparna et al. [22] presented a detailed analysis of rotational flow around a transparent sphere in an incompressible micropolar fluid, including energy, angular momentum, and concentration profiles.

(e) **Governing Equations of Micropolar Fluid:** Micropolar fluid theory expands upon classical fluid mechanics by accounting for the microstructure of fluids, allowing for the independent rotation of fluid particles. The set of governing equations has been derived in accordance with the theoretical framework of [4].

(i) **Continuity Equation:** For a compressible micropolar fluid, the equation is given by:

$$\frac{\partial \rho_f}{\partial t} + \nabla \cdot (\rho_f \mathbf{u}) = 0 \tag{1.40}$$

For an incompressible fluid, where the density remains constant, the conti-

nuity equation simplifies to:

$$\nabla \cdot \mathbf{u} = 0 \tag{1.41}$$

(ii) **Linear Momentum Equation:** The linear momentum equation for a micropolar fluid generalizes the classical Navier-Stokes equation by incorporating the effects of microrotation. In compact form, using the material derivative, it is written as:

$$\rho_f \frac{D\mathbf{u}}{Dt} = -\nabla P + (\mu + \kappa)\nabla^2 \mathbf{u} + \kappa \nabla \times \mathbf{M} + \mathbf{f} \tag{1.42}$$

Expanding the material derivative, $\frac{D\mathbf{u}}{Dt} = \frac{\partial \mathbf{u}}{\partial t} + (\mathbf{u} \cdot \nabla)\mathbf{u}$, the equation becomes:

$$\rho_f \left(\frac{\partial \mathbf{u}}{\partial t} + (\mathbf{u} \cdot \nabla)\mathbf{u} \right) = -\nabla P + (\mu + \kappa)\nabla^2 \mathbf{u} + \kappa \nabla \times \mathbf{M} + \mathbf{f} \tag{1.43}$$

where:

- μ = Dynamic viscosity.
- κ = Vortex (microrotation) viscosity.
- $\mathbf{M}$ = Microrotation vector (angular velocity of microelements).
- $\mathbf{f}$ = External body forces (such as gravity).

(iii) **Angular Momentum Equation:**

$$\rho_f j \frac{D\mathbf{M}}{Dt} = \gamma \nabla^2 \mathbf{M} - \kappa \left(2\mathbf{M} - \nabla \times \mathbf{u}\right) + \mathbf{c} \tag{1.44}$$

where:

- j = Microinertia per unit mass (a measure of the rotational inertia of the microelements).
- $\frac{D\mathbf{M}}{Dt}$ = Material derivative of the microrotation vector.
- γ = Spin viscosity (associated with the diffusion of microrotation).
- $\mathbf{c}$ = External body couples (torques per unit volume) acting on the fluid.

(iv) **Energy Equation (Temperature):** The energy equation for a micropolar fluid, incorporating the effects of microrotation is as follows:

$$\rho_f c_p \left(\frac{\partial T}{\partial t} + \mathbf{u} \cdot \nabla T \right) = \nabla \cdot (k \nabla T) + \Phi \tag{1.45}$$

Expanding the dissipation function Φ for a micropolar fluid, we have:

$$\Phi = \mu \sum_{i,j} \left(\frac{\partial u_i}{\partial x_j} \right)^2 + \kappa \left| 2\mathbf{M} + \nabla \times \mathbf{u} \right|^2 + \gamma \sum_{i,j} \left(\frac{\partial M_i}{\partial x_j} \right)^2 \tag{1.46}$$

where:

- c_p = Specific heat at constant pressure.
- T = Temperature.
- k = Thermal conductivity.
- Φ = Dissipation function.
- u_i = i-th component of the velocity vector.
- M_i = i-th component of the microrotation vector.
- x_j : j-th spatial coordinate.

Thus, the explicit form of the energy equation for a micropolar fluid is:

$$\begin{aligned} \rho_f c_p \left(\frac{\partial T}{\partial t} + \mathbf{u} \cdot \nabla T \right) = \nabla \cdot (k \nabla T) &+ \mu \sum_{i,j} \left(\frac{\partial u_i}{\partial x_j} \right)^2 \\ &+ \kappa \left| 2\mathbf{M} + \nabla \times \mathbf{u} \right|^2 \\ &+ \gamma \sum_{i,j} \left(\frac{\partial M_i}{\partial x_j} \right)^2 \end{aligned} \tag{1.47}$$

The terms on the right-hand side represent, respectively, heat conduction, classical viscous dissipation, microrotational (vortex viscosity) dissipation, and dissipation due to spatial gradients of microrotation (spin viscosity).

Thus the development of the micropolar fluid model by Eringen has provided a valuable framework for understanding complex fluid behaviors in systems with suspended microelements.

1.6.2 Dusty Fluids

Dusty fluid theory provides a comprehensive framework for understanding the behavior of fluids containing suspended particles. This model is particularly useful for describing systems where both the fluid medium and solid particles interact in a way that influences the overall flow and transport properties.

(a) **Development of Dusty Fluid Model:** The development of the dusty fluid model began with Saffman [23, 24], who introduced a model to examine the influence of suspended particles on the stability of laminar flow in Newtonian fluids. This foundational work laid the groundwork for understanding dusty fluid behavior in simple flow configurations. Marble [25] established foundational principles for dusty gas dynamics, emphasizing the interplay between gas-phase turbulence and particle inertia through dimensionless parameters such as the Stokes number, which governs particle response to flow fluctuations. Similarly, Drew [26] analyzed transient two-phase gas-particle flows, employing asymptotic and numerical methods to study momentum coupling under pressure gradients and gravitational effects, advancing the mathematical modeling of industrial and environmental suspensions. Furthermore, Bég et al. [27] advanced the analysis of swirling flows using spectral collocation methods, investigating the impact of anisotropic slip, blowing effects, and porous media on heat/mass transfer in bioconvective von Karman flows with nanoparticles and microorganisms. Mathematically, the formulation describing dusty fluid flow is developed by applying the fundamental laws of conservation, accounting for mass, momentum, and energy exchanges between the fluid and suspended particles. These equations account for the interactions between the fluid and suspended particles, including drag forces, particle-particle collisions, and particle-wall effects, which are crucial for accurately modeling particulate flows in various engineering systems.

(b) **Examples of Dusty Fluids:** Dusty fluids are commonly encountered in various natural and industrial processes. Liu et al. [28] advanced aerosol dynamics modeling by simulating interactions between sulfate, carbonaceous particles, dust, and sea salt, demonstrating how condensation and coagulation processes govern

pollutant transport and deposition in atmospheric systems. Wang et al. [29] employed CFD and discrete phase modeling (DPM) to analyze dust particle trajectories in industrial environments, enabling the design of optimized ventilation and filtration systems for mitigating airborne pollutants. Kumar et al. [30] demonstrated the utility of CFD in analyzing pressure drop and shear stress in horizontal crude oil pipelines, highlighting how particle size and fluid velocity influence transport efficiency under turbulent flow conditions. Similarly, Lavanya and Bhattacharyya [31] highlighted that CFD and dusty fluid models are instrumental in optimizing the mixing and transport of fine powders during pharmaceutical manufacturing, ensuring uniformity and efficiency in tablet production processes.

(c) **Applications of Dusty Fluid in Engineering and Industry:** Dusty fluid models play a crucial role in engineering and industry, particularly in designing systems that involve particulate flows. Gireesha et al. [32] demonstrated that dusty fluid models optimize heat transfer in MHD flows over stretching sheets, where viscous dissipation and particle-fluid interactions enhance thermal efficiency in industrial systems like polymer fabrication and mineral oil purification. Similarly, Armstrong [33] showed their importance in the chemical and pharmaceutical industries for analyzing the mixing and transport of fine powders in gases, optimizing the design of reactors, dryers, and blenders to ensure efficient particle-fluid mixing and consistent product quality.

(d) **Recent Research and Developments (Dusty Fluid):** Debnath and Ghosh [34] explored the oscillatory hydromagnetic flow of dusty fluids in a channel, evaluating the mass exchange occurring between the fluid and particulate phases. This study contributed to the understanding of the transient behavior of particle-laden flows under magnetic fields. Datta et al. [35] examined pulsatile time-dependent dusty flow in a channel using Laplace transform techniques. Their study contributed to the modeling of transient dusty flows, which are common in many practical applications involving fluctuating flow conditions. Dey [36] analyzed the convective flow of non-Newtonian dusty fluids with viscous heating effects. His work was important for understanding the role of temperature

gradients in dusty fluid dynamics, particularly in high-temperature industrial applications. Jalil et al. [37] derived a precise solution to describe the magnetohydrodynamic behavior of dusty fluid motion past a stretching surface. Their study showed that increasing magnetic field strength reduces both flow velocity and boundary layer thickness, offering valuable insights for particle-laden flow applications. Reddimalla et al. [38] performed an analytical investigation of the transient magnetohydrodynamic behavior of dusty fluid flow inside a circular cylinder under a constant pressure gradient. Their findings revealed that an increase in magnetic field intensity results in decreased velocities for both the fluid and the suspended particles, providing valuable insights for managing particulate transport in cylindrical flow systems such as pipelines and reactors. Similarly, Attia [39] presented an analytical solution for unsteady magnetohydrodynamic flow of a dusty fluid through a circular pipe under a constant pressure gradient. He demonstrated that increasing magnetic field strength significantly dampens both fluid and particle velocities, offering valuable insights for controlling particulate transport in pipeline systems. Makinde and Chinyoka [40] analyzed transient magnetohydrodynamic flow of a dusty fluid in a channel with variable viscosity and Navier slip boundary conditions. Their findings showed that increased magnetic field strength and slip at the walls significantly reduce both fluid and particle velocities, offering key insights into the design of slip-enhanced flow control and magnetic damping systems. Bilal et al. [41] analyzed Couette flow of a viscoelastic dusty fluid in a rotating frame under magnetic fields, demonstrating how Coriolis forces and viscoelasticity jointly modulate particle-fluid interactions, with applications in polymer processing and biomedical fluid dynamics. Lou et al. [42] investigated entropy generation in rotating MHD flows of micropolar dusty fluids, highlighting the synergistic role of Coriolis and Lorentz forces in minimizing thermodynamic irreversibility. Their analysis revealed that particle-fluid interactions suppress entropy production, thereby optimizing thermal efficiency in high-temperature industrial systems such as nuclear reactors and furnaces, contributing to more sustainable energy-intensive operations.

(e) **Governing Equations of Dusty Fluid:** Dusty fluids are multiphase systems consisting of a carrier fluid and suspended solid particles (dust). To accurately describe their dynamics, it is necessary to account for the conservation of mass and momentum for both the fluid phase and the particle phase, as well as the interaction forces between them. This section outlines the continuity, momentum, and energy formulations for both fluid and particle phases, incorporating interaction terms that describe the exchange processes involving mass, momentum, and energy, as described by Saffman [23].

(i) **Continuity Equations:**

1. *Fluid Phase:*

$$\frac{\partial \rho_f}{\partial t} + \nabla \cdot (\rho_f \mathbf{u}) = 0 \tag{1.48}$$

2. *Particle Phase:*

$$\frac{\partial \rho_p}{\partial t} + \nabla \cdot (\rho_p \mathbf{u}_p) = 0 \tag{1.49}$$

where:

- ρ_f = Fluid density.
- $\mathbf{u}$ = Fluid velocity.
- ρ_p = Particle (dust) density.
- $\mathbf{u}_p$ = Particle velocity.

For incompressible phases, the continuity equations reduce to $\nabla \cdot \mathbf{u} = 0$ and $\nabla \cdot \mathbf{u}_p = 0$.

(ii) **Linear Momentum Equations:**

1. *Fluid Phase:*

$$\rho_f \left(\frac{\partial \mathbf{u}}{\partial t} + (\mathbf{u} \cdot \nabla)\mathbf{u} \right) = -\nabla P + \mu \nabla^2 \mathbf{u} + K(\mathbf{u}_p - \mathbf{u}) + \rho_f \mathbf{g} \tag{1.50}$$

2. *Particle Phase:*

$$\rho_p \left(\frac{\partial \mathbf{u}_p}{\partial t} + (\mathbf{u}_p \cdot \nabla)\mathbf{u}_p \right) = -K(\mathbf{u}_p - \mathbf{u}) + \rho_p \mathbf{g} \tag{1.51}$$

where:

- P = Pressure.
- μ = Dynamic viscosity associated with the fluid.
- $\nabla^2 \mathbf{u}$ = Viscous diffusion.
- K = Drag coefficient, which depends on particle size, shape, concentration, and fluid viscosity.
- $(\mathbf{u}_p - \mathbf{u})$ = Relative velocity
- $\mathbf{g}$ = Acceleration arising from gravitational or other body forces.

Explanation of the Drag Force: The term $K(\mathbf{u}_p - \mathbf{u})$ denotes the drag interaction per unit volume, arising from the influence of dust particles on the fluid. This interaction scales with the velocity gap between the two phases. The same term, with opposite sign, appears in the particle phase equation, ensuring that the action-reaction principle (Newton's third law) is satisfied. The proportionality constant K ensures the correct physical units and encodes the effect of particle and fluid properties on the drag force.

(iii) **Energy Equation (Temperature) for Dusty Fluid:** The energy equations for a dusty fluid system, accounting for both the fluid and particle phases, are given as follows:

1. *Fluid Phase:*

$$\rho_f c_p \left(\frac{\partial T}{\partial t} + \mathbf{u} \cdot \nabla T \right) = k\nabla^2 T - \frac{\rho_p c_{pp}}{\tau_T}(T - T_p) + Q \tag{1.52}$$

2. *Particle Phase:*

$$\rho_p c_{pp} \left(\frac{\partial T_p}{\partial t} + \mathbf{u}_p \cdot \nabla T_p \right) = \frac{\rho_p c_{pp}}{\tau_T}(T - T_p) \tag{1.53}$$

where:

- T and T_p = Fluid and particle phase temperatures.
- c_p and c_{pp} = Specific heats of the fluid and particles.
- k = Thermal conductivity.
- τ_T = Thermal relaxation time.
- Q = Source term.

These equations model the thermal energy balance for each phase, including convective transport, thermal diffusion (for the fluid), interphase heat exchange, and possible internal heat generation.

(f) **Governing Equations of Dusty Fluid with Volume Fraction Effects:** The previously presented governing equations are based on the dilute suspension assumption, wherein the volume fraction of the particulate phase is considered negligible. Under such conditions, the influence of particles on the available flow volume and the dynamics of the fluid is minimal, and the fluid is assumed to occupy the entire domain.

However, in practical scenarios involving moderate to dense suspensions, the volume occupied by the particles becomes non-negligible. To model such systems accurately, the finite volume of particles must be incorporated explicitly into the governing equations. Let ϕ_p denote the volume fraction of the particle (dust) phase. Consequently, the volume fraction of the fluid phase is given by $1 - \phi_p$. These definitions ensure that the sum of the phase fractions at any point in space and time remains equal to unity, preserving mass conservation. The subsequent equations are derived as presented in [36].

(i) **Continuity Equations:**

1. *Fluid Phase:*

$$\frac{\partial}{\partial t}\left[(1-\phi_p)\rho_f\right] + \nabla \cdot \left[(1-\phi_p)\rho_f \mathbf{u}\right] = 0 \tag{1.54}$$

2. *Particle Phase:*

$$\frac{\partial}{\partial t}\left(\phi_p \rho_p\right) + \nabla \cdot \left(\phi_p \rho_p \mathbf{u}_p\right) = 0 \tag{1.55}$$

(ii) **Momentum Equations:**

1. *Fluid Phase:*

$$(1-\phi_p)\rho_f \left(\frac{\partial \mathbf{u}}{\partial t} + (\mathbf{u}\cdot\nabla)\mathbf{u}\right) = -(1-\phi_p)\nabla P + \mu\nabla^2\mathbf{u} + \frac{\phi_p\rho_p}{\tau_p}(\mathbf{u}_p - \mathbf{u}) + (1-\phi_p)\rho_f\mathbf{g} \tag{1.56}$$

2. *Particle Phase:*

$$\phi_p\rho_p \left(\frac{\partial \mathbf{u}_p}{\partial t} + (\mathbf{u}_p\cdot\nabla)\mathbf{u}_p\right) = -\phi_p\nabla P - \frac{\phi_p\rho_p}{\tau_p}(\mathbf{u}_p - \mathbf{u}) + \phi_p\rho_p\mathbf{g} \tag{1.57}$$

where τ_p is the relaxation time associated with the momentum exchange between the two phases, and $\mathbf{g}$ denotes the body force vector (e.g., gravity).

(iii) **Energy Equations**:

1. *Fluid Phase:*

$$(1-\phi_p)\rho_f c_p \left(\frac{\partial T}{\partial t} + \mathbf{u}\cdot\nabla T\right) = k\nabla^2 T - \frac{\phi_p\rho_p c_{pp}}{\tau_T}(T - T_p) + (1-\phi_p)Q \tag{1.58}$$

2. *Particle Phase:*

$$\phi_p\rho_p c_{pp} \left(\frac{\partial T_p}{\partial t} + \mathbf{u}_p\cdot\nabla T_p\right) = \frac{\phi_p\rho_p c_{pp}}{\tau_T}(T - T_p) + \phi_p Q_p \tag{1.59}$$

The dusty fluid model provides a fundamental framework for studying the behavior of fluids containing suspended particles. Originating with Saffman's work, it has been essential in understanding the dynamics of particulate-laden flows, where interactions between the fluid and particles influence key flow properties, particularly in areas such as aerosol dynamics, combustion, and particle transport in pipelines.

1.6.3 Jeffrey Fluids

The Jeffery fluid model provides a key framework for understanding the behavior of viscoelastic fluids that exhibit both viscosity and elasticity without a yield stress. It is particularly useful for describing systems where the fluid's flow properties are influenced by interactions between the fluid medium and suspended particles. The model finds extensive applications across disciplines such as biomedical engineering, polymer processing, and environmental science, providing important understanding of the rheological behavior of complex fluids.

(a) **Development of Jeffrey Fluid Model:** The Jeffery fluid model, named after G. B. Jeffery, was introduced in 1922 as a constitutive framework for characterizing the flow behavior of suspensions and viscoelastic fluids [43]. It was originally developed to analyze the motion of ellipsoidal particles suspended in a Newtonian fluid, especially in the context of dilute suspensions. Jeffery's pioneering work laid the foundation for understanding complex fluid behaviors, where the material exhibits both viscous and elastic characteristics depending on the time scale of observation. Furthermore, Truesdell and Noll [44] highlighted that, in contrast to Newtonian fluids, Jeffery fluids are capable of capturing the effects of stress relaxation and retardation by employing linear differential equations. This feature makes them particularly useful for modeling specific types of non-Newtonian fluid behavior.

(b) **Examples of Jeffery Fluids:** The Jeffrey fluid formulation is extensively utilized in physical and engineering applications because of its capability to capture both relaxation and retardation phenomena characteristic of viscoelastic materials. For instance, Kahshan et al. [45] employed the Jeffrey fluid framework to model filtration processes in flat plate hemodialyzers. Their results demonstrated that the model effectively captures key transport characteristics such as ultrafiltration rates and pressure drops, making it valuable for biomedical fluid dynamics. Similarly, Ahmad et al. [46] investigated the magnetohydrodynamic oscillatory flow of Jeffrey fluid through a porous channel. This study further highlighted the model's relevance in simulating unsteady transport phenomena that occur in

physiological systems and industrial filtration processes, particularly where both magnetic fields and porous structures are involved.

(c) **Applications of Jeffery Fluid:** The Jeffery fluid model, owing to its mathematical simplicity and capacity to represent viscoelastic properties, has been widely applied across various fields of engineering and science. In particular, in biomedical engineering, Nallapu and Radhakrishnamacharya [47] utilized the Jeffrey fluid model to analyze two-phase blood flow in small-diameter tubes under the influence of a magnetic field, offering valuable insights into microcirculation dynamics. Furthermore, Rao [48] demonstrated its relevance in polymer processing, where it aids in predicting flow behavior during extrusion and molding procedures. Moreover, in computational fluid dynamics, Siddiqa and Ellahi [49] established the importance of the Jeffery fluid model in analyzing complex flow mechanisms, including peristaltic motion, boundary layer formation over stretching surfaces, and magnetohydrodynamic effects in electrically conducting fluids.

(d) **Recent Research and Developments (Jeffrey Fluid):** Over the years, the Jeffery fluid model has undergone significant extensions and refinements, accommodating new physical phenomena and applications. Initially developed in the early 20th century, the model has seen remarkable advancements, particularly in the last few decades. Specifically, researchers have incorporated various factors such as magnetic fields (magnetohydrodynamics), thermal radiation, porous media flow, and nanoparticle suspensions, expanding its applicability across multiple disciplines.

For instance, Raje et al. [50] applied the Jeffrey fluid model to study entropy generation in inclined porous pipes under convective boundaries, revealing how magnetic effects and thermodynamic irreversibilities influence heat transfer and fluid dynamics. Similarly, Dey [51] employed a dusty Jeffrey fluid model to examine electrically conducting particulate flow within a rotating channel under the influence of Hall currents. Through perturbation analysis, the study provided analytical solutions for fluid and particulate velocity fields, demonstrat-

ing key interactions between magnetic field strength, rotation rate, and particle dispersion. As computational techniques advanced, researchers began to use sophisticated methods to solve the increasingly complex equations governing Jeffery fluids. For example, Motsa et al. [52] employed the Homotopy Analysis Method (HAM) to solve nonlinear Jeffery-Hamel flow equations, demonstrating accelerated convergence compared to traditional perturbation techniques. Likewise, Ashraf et al. [53] applied the Generalized Differential Quadrature Method (GDQM) to simulate magnetohydrodynamic peristaltic nanofluid flow, enhancing predictive accuracy for physiological transport phenomena. Furthermore, Asgir et al. [54] integrated Caputo and Caputo-Fabrizio fractional derivatives into the Jeffrey fluid model to analyze MHD flow in vertical channels, revealing enhanced memory effects in viscoelastic biofluids. In the context of biomedical engineering, Nallapu and Radhakrishnamacharya [47] demonstrated the applicability of the Jeffrey model in simulating two-phase blood flow through narrow capillaries, capturing the Fahraeus-Lindqvist effect. Moreover, Siddiqa et al. [49] have extended the Jeffery fluid model to include nanoparticle suspensions, with significant implications for drug delivery systems, such as targeted cancer therapies. In industrial settings, Rao [48] demonstrated the model's utility in predicting the behavior of viscoelastic materials during polymer processing, particularly in extrusion and molding.

(e) **Governing Equations of Jeffrey Fluid:** The following constitutive equations, along with the corresponding momentum and energy equations, are presented in [55].

(i) **Constitutive Equations:** The constitutive equations describe the relationship between the stress and the rate of deformation in a Jeffrey fluid. They can be expressed in terms of the Cauchy stress tensor and the extra stress tensor.

1. *Cauchy Stress Tensor Form:* The total Cauchy stress tensor $\mathbf{T}$ for a

Jeffrey fluid is given by:

$$\mathbf{T} = -P\mathbf{I} + \mathbf{S} \tag{1.60}$$

where:

- P = Pressure.
- $\mathbf{I}$ = Identity tensor.
- $\mathbf{S}$ = Extra (deviatoric) stress tensor.

2. *Extra Stress Tensor* ($\mathbf{S}$): The extra stress tensor $\mathbf{S}$ for a Jeffrey fluid is defined by:

$$\mathbf{S} + \lambda_1 \frac{D\mathbf{S}}{Dt} = \mu \left(\mathbf{R}_1 + \lambda_2 \frac{D\mathbf{R}_1}{Dt} \right) \tag{1.61}$$

where:

- μ = Dynamic viscosity.
- λ_1 = Relaxation time parameter.
- λ_2 = Retardation time parameter.
- $\mathbf{R}_1 = \nabla\mathbf{u} + (\nabla\mathbf{u})^T$ = First Rivlin–Ericksen tensor (rate-of-strain tensor).
- $\frac{D}{Dt}$ = Material (substantial) derivative.

Alternatively, this can be rearranged as [56]

$$\mathbf{S} = \frac{\mu}{1 + \lambda_1} \left[\mathbf{R}_1 + \lambda_2 \frac{D\mathbf{R}_1}{Dt} \right] \tag{1.62}$$

for certain steady or simplified cases.

(ii) **Continuity and Momentum Equations:** The dynamics of an incompressible Jeffrey fluid are described by the following equations:

1. *Continuity Equation (Incompressibility Condition):*

$$\nabla \cdot \mathbf{u} = 0 \tag{1.63}$$

where $\mathbf{u}$ is the velocity vector.

2. *Momentum Equation:*

$$\rho_f \left(\frac{\partial \mathbf{u}}{\partial t} + \mathbf{u} \cdot \nabla \mathbf{u} \right) = -\nabla P + \nabla \cdot \mathbf{S} \tag{1.64}$$

(iii) **Energy Equation (Temperature) for Jeffrey Fluid**: The energy equation for a Jeffrey fluid, which expresses the conservation of thermal energy within the system, is given by:

$$\rho_f c_p \left(\frac{\partial T}{\partial t} + \mathbf{u} \cdot \nabla T \right) = \nabla \cdot (k \nabla T) + \Phi \tag{1.65}$$

where

- ρ_f = Fluid density.
- c_p = Specific heat at constant pressure.
- T = Temperature.
- $\mathbf{u}$ = Velocity vector.
- k = Thermal conductivity.
- Φ = Viscous dissipation function.

This equation accounts for the rate of change of internal energy due to both local and convective temperature changes (left side), balanced by heat conduction and internal heat generation through viscous dissipation (right side). The energy equation above provides a complete description of the temperature field in Jeffrey fluid flows, complementing the constitutive and momentum equations for a comprehensive analysis of heat transfer phenomena.

In summary, the Jeffery fluid model has proven to be a versatile tool in both theoretical and applied research. Its applications have expanded from basic fluid dynamics to complex systems involving biofluids, nanofluids, and materials under varying external conditions.

1.6.4 Magnetohydrodynamic (MHD) Flow

Magnetohydrodynamics examines the dynamics of electrically conductive fluids when subjected to magnetic fields. The coupling of the magnetic field with fluid motion gives rise to various phenomena, such as the induction of electric currents, the development of complex flow structures, and notable alterations in both the thermal and dynamic characteristics of the fluid.

(a) **Development of MHD:** The theoretical foundation of MHD can be traced back to the 1940s, with significant contributions by Alfvén [57], who first demonstrated the interaction between magnetic fields and electrically conducting fluids. Initially, MHD focused on idealized models, such as conducting fluids in steady magnetic fields. Batchelor [58] made early contributions by providing the fundamental framework for understanding MHD in isotropic fluids. As research progressed, the integration of more complex fluid models gained momentum. Chen [59] played a pivotal in extending MHD theory to incorporate micropolar and dusty fluids, providing more accurate representations of systems encountered in astrophysical and plasma dynamics. With the advent of CFD and the increased availability of high-performance computing, MHD evolved to encompass more sophisticated models, including non-Newtonian, micropolar, and dusty fluid systems.

(b) **Applications of MHD in Engineering and Industry:** Molokov et al. [60] discussed MHD effects in liquid metal blankets for fusion reactors, highlighting their role in heat removal and magnetic damping of turbulent flows. Similarly, Foliforov [61] demonstrated the efficacy of MHD-based magnetic pumps in industrial mercury production and handling, emphasizing their reliability due to the absence of mechanical components and fully sealed flow systems. In addition, Kitanov and Podol'skii [62] demonstrated the application of MHD principles in eddy-current braking systems for high-speed trains, where non-contact magnetic interactions enable rapid deceleration while minimizing wear and weather-dependent adhesion limitations. Furthermore, Haghparast and Pahlavani [63] demonstrated that the geometry of MHD channels, specifically helical versus lin-

ear configurations, significantly influences thrust generation and electrical efficiency.

(c) **Recent Research and Developments (MHD):** Magnetohydrodynamics has witnessed significant development over the decades, particularly in its application to different fluid models. MHD has evolved significantly over the years, particularly in understanding fluid behavior under the influence of magnetic fields. Initially, the focus was on simple fluids such as Newtonian fluids, where MHD effects like the interaction between magnetic fields and fluid flow were explored for their influence on velocity profiles and flow characteristics. The early work by Alfvén [57] in MHD, which examined electrically conducting fluids, laid the foundation for further exploration of MHD effects in more complex fluids. Subsequently, the study of micropolar fluids, which introduced micro-rotations and couple stresses, advanced MHD research. Eringen [4] developed the concept of micropolar fluids, and later studies such as those by Devakar and Raje [12] examined the unsteady flow of micropolar fluids, showing how these effects influence velocity and temperature profiles in MHD conditions.

As MHD research progressed, *dusty fluids*—which involve the interaction of suspended particles with a fluid—became a subject of interest in the context of MHD. Sproull [64] examined the dynamics of dusty fluid flow under the influence of magnetic fields, investigating how suspended solid particles affect the viscosity and flow characteristics of gases. Building on such insights, Saffman [23] conducted foundational analyses on MHD-particle interactions in dusty gases, establishing early theoretical frameworks for understanding how magnetic fields influence particle-laden flows in both industrial and astrophysical contexts. Later, Manjunatha et al. [65] conducted a detailed investigation into MHD dusty fluid flow, incorporating the effects of variable viscosity and thermal conductivity. Their findings highlighted the significant impact of these factors on velocity and temperature distributions, offering valuable insights for enhancing heat transfer efficiency in industrial fluid flow systems.

In a related development, *Jeffrey fluids*, a class of non-Newtonian fluids that exhibit anisotropic properties, added another layer of complexity to MHD. Jeffrey's fluid dynamics are influenced by both the rotational effects and the interaction with magnetic fields. Research by Hayat et al. [66] explored how magnetic fields and rotational forces modify velocity and temperature profiles in MHD systems involving Jeffrey fluids. Similarly, Abd-Alla et al. [67], Akram, and Nadeem [68] explored the impact of magnetic fields on peristaltic flow, highlighting how these fields hinder the movement of the fluid. In addition, they examine the influence of gravity on the fluid's behavior within the channel.

More recently, *micropolar dusty fluids* have become increasingly significant in MHD research, particularly in complex systems where rotation, magnetic fields, and thermal effects interact. The work by Ahmad et al. [69] examined how rotation and magnetic fields influence micropolar dusty fluid dynamics in inclined channels, showing how these interactions impact the velocity, temperature, and heat transfer properties of the fluids. Similarly, Yadav and Roshan [70] examined how electric and magnetic fields impact blood flow behavior, evaluating the effects of different parameters on key flow variables, including average flow rate over time, total volumetric discharge, gradient and elevation of pressure, surface friction within the tube, and overall mechanical performance. Additionally, Nadeem et al. [71] investigated the flow of a micropolar nanofluid between two rotating plates under the influence of a magnetic field. Their study explores how rotation, magnetic field intensity, and the micropolar characteristics of the fluid affect both flow behavior and heat transfer, employing both analytical and numerical methods.

In recent years, the study of Magnetohydrodynamic flow with both *magnetic field* and *thermal effects* has garnered considerable attention, particularly due to its significance in various engineering and industrial applications. The coupling of magnetic fields with thermal gradients in electrically conductive fluids has led to complex flow behavior, with profound implications for heat transfer processes.

The interaction between magnetic fields and thermal effects in MHD systems influences several flow characteristics, including velocity profiles, temperature distribution, and heat transfer efficiency. Ghadikolaei et al. [72] demonstrated that magnetic fields play a crucial role in affecting the flow of micropolar dusty fluids through porous channels, thereby influencing both temperature distribution and particle dynamics. Furthermore, Nadeem et al. [71] studied the behavior and thermal transport of a micropolar nanofluid between rotating plates under a magnetic field, demonstrating that rotation, magnetic field strength, and the fluid's micropolar characteristics significantly influence both velocity and temperature profiles. Similarly, Javed and Siddiqi [73] studied viscosity-dependent micropolar fluid motion under MHD effects, while Yadav et al. [74] explored the impact of oriented magnetic fields and thermal radiation on entropy production in porous channels with micropolar and Newtonian fluids, deriving expressions for thermal transport, flow velocity, and entropy generation, and validating their findings against existing studies. Moreover, Gerdroodbary et al. [75] studied how thermal radiation affects traditional Jeffrey-Hamel flow, observing that higher values of the thermal radiation parameter increase the temperature profile. In addition, Fiza et al. [76] studied MHD Jeffrey fluid behavior in horizontal channels with Hall currents, examining how rotation and magnetic field strength affect the temperature and velocity fields. In a separate study, Rani [77] investigated oscillatory Couette flow of Jeffrey fluid between two parallel plates, showing that both magnetic fields and radiative heat transfer significantly influence flow behavior and heat transfer rates. Furthermore, Bhatti et al. [78] analyzed the effects of thermal radiation on peristaltic propulsion in an electromagnetic hydrodynamic system with a non-Newtonian fluid and suspended particles, highlighting radiation's influence on flow behavior and heat transfer. Recently, Abbas et al. [79] studied the effects of chemical reactions, ion slip, and thermal radiation on unsteady MHD dusty fluid flow through porous media, finding that thermal radiation improves temperature distribution and higher Hall and slip parameters enhance velocity uniformity. Additionally, Dey et al. [80] studied the magnetohydrodynamic be-

havior of a stratified dusty fluid and found that higher magnetic parameter values slow down the flow.

In conclusion, Magnetohydrodynamic flow, which involves the interaction of magnetic fields with electrically conductive fluids, has undergone substantial development, particularly in its application to complex fluids such as dusty, Jeffrey, and micropolar fluids, in conjunction with thermal effects. Recent advancements in research have deepened our understanding of MHD's impact on optimizing heat transfer, fluid dynamics, and energy systems, with widespread applications across diverse industrial and engineering domains.

1.7 Rotating Frame of Reference in Fluid Dynamics

The concept of a rotating frame of reference arises from the need to describe motion as observed in a non-inertial coordinate system that is itself rotating with respect to an inertial frame. This framework becomes essential when analyzing geophysical, astrophysical, and engineering problems where rotation plays a dominant role.

In fluid dynamics, analyzing flow behavior often requires the adoption of an appropriate reference frame. A *rotating frame of reference* refers to a non-inertial coordinate system that rotates at a fixed angular velocity Ω compared to a stationary inertial frame. The dynamics of fluid motion observed in such a rotating frame differ significantly from those in a stationary frame due to the appearance of additional apparent forces.

(a) **Development and Recent Research on Rotating Frame of Reference:** The concept of a rotating frame of reference has its roots in classical mechanics and celestial dynamics. The concept was first formalized by Isaac Newton in his discussion of non-inertial frames; however, it was Leonhard Euler, as documented by Truesdell [81], who in the 18^{th} century explicitly introduced the mathematical treatment of motion in rotating systems. The modern understanding of fictitious forces—namely, the Coriolis and centrifugal forces—was significantly advanced by Gaspard-Gustave Coriolis in 1835, whose work on rotating machinery laid the foundation for their application in rotating fluid systems [82].

In fluid dynamics, the rotating frame was historically employed to model atmospheric and oceanic flows, where the Earth's rotation introduces significant deviations from inertial behavior [83]. With the rise of CFD in the latter half of the 20^{th} century, rotating frames became an integral part of simulations involving turbomachinery, cyclone modeling, and convective heat transfer in rotating systems [84, 85].

Recent research continues to explore the complex dynamics arising in rotating systems. Notable developments include the study of flow instabilities induced by Coriolis forces in rotating channels [86], enhanced mixing performance in curved microchannels through rotationally induced secondary flows [87], and investigations into the role of angular momentum in rotating multiphase flows and magnetohydrodynamics [88]. Modern numerical techniques, including spectral and pseudospectral methods, now enable precise simulation of such flows under various boundary and force conditions.

(b) **Applicatoins of Rotating frame of reference:** The rotating frame of reference is vital in modeling geophysical flows, where it aids in accurately predicting large-scale atmospheric and oceanic circulations influenced by Earth's rotation [83]. In turbomachinery, it enables precise analysis of flow behavior in rotating ducts and channels [84]. Microfluidic systems exploit rotational effects to enhance mixing efficiency in compact devices [87]. Additionally, in rotating channel studies, Coriolis-induced instabilities lead to vortex formations that improve convective transport, making the rotating frame essential across both fundamental research and industrial applications [86].

(c) **Governing Equations in Rotating Frame:** The systematic formulation of the equations of motion in a rotating reference frame was completed in the context of fluid dynamics by applying Newton's second law to a control volume in a non-inertial frame. Before delving into the governing equations and physical implications, it is useful to define two fundamental quantities:

(i) **Vorticity:** is a vector field that represents the local rotation at a point in the

fluid, where the magnitude of the vorticity indicates the strength of rotation and the direction represents the axis of rotation. In the context of rotating systems, vorticity provides a measure of angular velocity, which is crucial for understanding the effects of rotation on fluid dynamics. It is mathematically defined as [1]:

$$\vec{\omega} = \nabla \times \mathbf{u} \tag{1.66}$$

Where:

- $\vec{\omega}$ = Vorticity vector.
- $\mathbf{u}$ = Velocity vector.
- $\nabla\times$ = Curl operator.

(ii) **Angular velocity:** is an intrinsic property that describes the local spin of the fluid particles. This relationship is fundamental to understanding how rotational flow influences momentum and heat transfer within a system. Mathematically it is define as half of the vorticity [1].

$$\Omega = \frac{1}{2}(\nabla \times \mathbf{u}) \tag{1.67}$$

Starting from the Navier–Stokes equation in an inertial frame as discussed in Section 1.5.2:

$$\rho_f \frac{D\mathbf{u}}{Dt} = -\nabla P + \mu\nabla^2\mathbf{u} + \rho_f\mathbf{g} \tag{1.68}$$

To transform this into a rotating frame of reference with angular velocity Ω, the acceleration must be adjusted to include apparent forces. The total acceleration observed in an inertial frame can be expressed in terms of the rotating frame as per [89]:

$$\left(\frac{D\mathbf{u}}{Dt}\right)_{\text{inertial}} = \left(\frac{D\mathbf{u}}{Dt}\right)_{\text{rot}} + 2(\Omega \times \mathbf{u}) + \Omega \times (\Omega \times \mathbf{r}) \tag{1.69}$$

Substituting into the inertial Navier–Stokes equation gives the governing equation in the rotating frame:

$$\rho_f \frac{D\mathbf{u}}{Dt} = -\nabla P + \mu \nabla^2 \mathbf{u} + \rho_f \mathbf{g} - 2\rho_f (\Omega \times \mathbf{u}) - \rho_f \Omega \times (\Omega \times \mathbf{r}) \tag{1.70}$$

Here, the terms involving Ω represent fictitious forces arising due to rotation: the Coriolis and centrifugal forces.

The centrifugal force term $\rho_f \Omega \times (\Omega \times \mathbf{r})$ is conservative in nature and can be expressed as the gradient of a scalar potential. Therefore, it can be absorbed into the pressure term by defining a modified pressure P^* such that [89]:

$$P^* = P - \frac{1}{2}\rho_f |\Omega \times \mathbf{r}|^2 \tag{1.71}$$

With this substitution, the governing equation [89] in the rotating frame simplifies to:

$$\rho_f \frac{D\mathbf{u}}{Dt} = -\nabla P^* + \mu \nabla^2 \mathbf{u} + \rho_f \mathbf{g} - 2\rho_f (\Omega \times \mathbf{u}) \tag{1.72}$$

This form is frequently employed in geophysical and engineering fluid dynamics applications, where the centrifugal effects are incorporated within the pressure field, allowing the Coriolis force to remain as the dominant rotational effect.
where:

- $\mathbf{u}$ = Fluid velocity vector
- ρ_f = Fluid density
- P^* = Modified pressure
- μ = Dynamic viscosity
- $\mathbf{g}$ = Gravitational acceleration vector item Ω = Angular velocity

(d) **Coriolis and Centrifugal Forces:** In a rotating frame of reference, two additional body forces appear in the momentum equation: the Coriolis force and the

centrifugal force [89].

(i) **Coriolis Force:**

$$\mathbf{F}_{\text{Coriolis}} = -2\rho_f(\Omega \times \mathbf{u}) \tag{1.73}$$

This velocity-dependent force acts perpendicular to both the angular velocity and the motion of the fluid element. It influences the flow structure significantly, especially in large-scale geophysical or confined rotating systems.

(ii) **Centrifugal Force:**

$$\mathbf{F}_{\text{Centrifugal}} = -\rho_f\Omega \times (\Omega \times \mathbf{r}) \tag{1.74}$$

These two fictitious forces must be explicitly retained in the momentum balance to ensure physically accurate solutions in the rotating frame.

Including rotational influences in fluid dynamic models is vital to realistically describe the dynamics of complex fluids. The synergy between rotation and non-Newtonian characteristics enhances our understanding of flow phenomena across diverse applications such as engineering systems, geophysical flows, and physiological processes.

1.8 Hydrodynamic Parameters

In this section, we examine the following hydrodynamic parameters and highlight their significance in analyzing and optimizing fluid transport systems.

(a) Volume Flow Rate

(b) Pressure Drop

(c) Pumping Power

1.8.1 Volume Flow Rate

The volume flow rate (Q) quantifies the volume of fluid that flows through a given cross-sectional area per unit time. It is a key parameter for assessing the capacity and efficiency of fluid transport systems, typically measured in m^3/s or L/min. The general relationship for volume flow rate is given by [90]:

$$Q = A \cdot U_{\mathrm{av}} \tag{1.75}$$

where:

- Q = Volume flow rate $(\mathrm{m}^3/\mathrm{s})$.
- A = Cross-sectional area of the pipe or channel (m^2).
- U_{av} = Average velocity within fluid (m/s).

Average velocity across a cross-section is given by:

$$U_{\mathrm{av}} = \frac{1}{A} \int_A u^* \, dA \tag{1.76}$$

Here, u^* denotes the local velocity at each point on the cross-sectional area, and the integral accounts for the velocity distribution across the entire area.

1.8.2 Pressure Drop

Pressure drop (ΔP) is the reduction in fluid pressure as it flows through a pipe or channel, primarily caused by resistance to flow due to friction and other factors within the system. It is a crucial parameter in fluid dynamics, as it directly influences the energy required for fluid transport and the efficiency of piping systems.
For steady, incompressible flow conditions, the pressure loss is commonly determined through the Darcy–Weisbach relation [91].:

$$\Delta P = f_d \cdot \frac{L_p}{D} \cdot \frac{\rho_f U_{av}^2}{2} \tag{1.77}$$

where:

- ΔP = Pressure drop (Pa).
- f_d = Darcy friction factor (dimensionless).
- L_p = Length of the pipe (m).
- D = Diameter of the pipe (m).
- ρ_f = Fluid density (kg/m^3).
- U_{av} = Average fluid velocity (m/s).

The *Darcy friction factor* (f_d) is influenced by whether the flow is laminar or turbulent, as well as by pipe surface roughness. For laminar flow, the friction factor is given by:

$$f_d = \frac{64}{\mathrm{Re}} \quad \text{for} \quad \mathrm{Re} < 2000 \tag{1.78}$$

where Re denotes the Reynolds number:

$$\mathrm{Re} = \frac{\rho_f U_0 D}{\mu}$$

1.8.3 Pumping Power

Pumping power (P_{pow}) quantifies the mechanical energy needed per unit time to sustain the desired rate of flow against the system's pressure drop. It is a critical parameter in evaluating the operational efficiency of pumps and fluid transport systems. The relationship for pumping power is given by [91]:

$$P_{pow} = Q \cdot \Delta P \tag{1.79}$$

where:

- P_{pow} = Pumping power (W).
- Q = Volume flow rate $(\mathrm{m}^3/\mathrm{s})$.
- ΔP = Total pressure drop (Pa).

This equation emphasizes that energy consumption is directly influenced by both the rate of flow and the corresponding pressure drop, emphasizing the importance of optimizing fluid transport systems for energy efficiency.

A comprehensive understanding of volume flow rate, pressure drop, and pumping power is essential for the analysis and optimization of hydrodynamic systems. These parameters are integral to hydraulic engineering and play a pivotal role in ensuring the efficient and reliable design of fluid transport infrastructure [92, 93].

1.9 Non-Dimensional Parameters

Non-dimensional parameters are fundamental in fluid dynamics, enabling the comparison of different flow systems, simplifying governing equations, and revealing dominant physical effects. This section details several key non-dimensional parameters relevant to flow analysis [1].

(a) **Reynolds Number (Re)**

The Reynolds number quantifies the ratio of inertial forces to viscous forces in a fluid flow. It is a primary indicator of whether the flow is laminar or turbulent. Mathematically, it is described as:

$$Re = \frac{\rho_f U_0 L}{\mu} \tag{1.80}$$

where:

- ρ_f = Fluid density ($\mathrm{kg/m^3}$).
- U_0 = Characteristic velocity ($\mathrm{m/s}$).
- L = Characteristic length (m).
- μ = Dynamic viscosity ($\mathrm{Pa \cdot s}$).

A low Re indicates laminar flow (dominated by viscosity), while a high Re indicates turbulent flow (dominated by inertia). It is crucial in predicting flow regimes and scaling experimental results to real systems.

(b) **Eckert Number (Ec)**

The Eckert number expresses the ratio of a flow's kinetic energy to the enthalpy difference due to temperature, characterizing heat dissipation in high-speed flows. It is defined as:

$$Ec = \frac{{U_0}^2}{c_p \Delta T} \tag{1.81}$$

where:

- c_p = Specific heat at constant pressure ($\mathrm{J}/(\mathrm{kg} \cdot \mathrm{K})$).
- ΔT = Temperature difference (K).

The Eckert number is important in compressible flows and high-speed heat transfer, indicating the extent to which kinetic energy is converted to internal energy.

(c) **Prandtl Number (Pr)**

The Prandtl number can also be expressed as the ratio of the product of specific heat at constant pressure and dynamic viscosity to thermal conductivity. It is described as:

$$Pr = \frac{c_p \cdot \mu}{k} \tag{1.82}$$

where:

- k = Thermal conductivity ($\mathrm{W}/(\mathrm{m} \cdot \mathrm{K})$).

A low Pr (e.g., for liquid metals) implies heat diffuses much faster than momentum, while a high Pr (e.g., for oils) means momentum diffuses faster than heat.

(d) **Hartmann Number (Ha)**

The Hartmann number measures the ratio of electromagnetic (Lorentz) force to

viscous force in magnetohydrodynamic flows. Mathematical relationship as follows:

$$Ha = B_0 L \sqrt{\frac{\sigma}{\mu}}$$
$$(Ha)^2 = B_0^2 L^2 \frac{\sigma}{\mu} \tag{1.83}$$

where:

- B_0 = Magnetic flux density (T).
- σ = Electrical conductivity $(\mathrm{S/m})$.

A high Ha indicates strong magnetic field effects, leading to suppression of turbulence and modification of velocity profiles in conducting fluids.

(e) **Micropolar Parameter (η)**

The micropolar parameter characterizes the influence of microstructure (microrotation) in micropolar fluids, which possess microelements capable of rotation. It is defined as:

$$\eta = \frac{\kappa}{\mu} \tag{1.84}$$

where:

- κ = Vortex viscosity (microrotation viscosity).
- μ = Dynamic viscosity.

This parameter is significant in analyzing non-Newtonian fluids with microstructure, affecting stress distribution and rotational flow characteristics.

(f) **Particle Concentration Parameter (R)**

Definition: The particle concentration parameter quantifies the volume fraction or concentration of suspended particles in a fluid. It is given by:

$$R = \frac{V_p}{V_t} \tag{1.85}$$

where:

- V_p = Volume of particles.
- V_t = Total volume of suspension.

It is essential in multiphase and nanofluid flows, influencing viscosity, thermal conductivity, and overall flow behavior.

(g) **Ion Slip Parameter (Bi)**

Definition: The ion slip parameter represents the effect of ion slip (relative motion between ions and electrons) in electrically conducting fluids, especially in MHD flows.It is expressed as:

$$Bi = \frac{\beta}{\sigma} \tag{1.86}$$

where:

- β = Ion slip coefficient.
- σ = Electrical conductivity.

Ion slip modifies the current density and Lorentz force, affecting velocity and temperature profiles in MHD flows.

(h) **Hall Parameter (Be)**

Definition: The Hall parameter quantifies the influence of the Hall effect (interaction between magnetic field and electric current) in MHD flows. It is given by:

$$Be = \omega_e \tau_e \tag{1.87}$$

where:

- ω_e = Electron cyclotron frequency.
- τ_e = Electron collision time.

A high Hall parameter alters the direction of current flow and modifies the MHD force balance, impacting flow and stability.

(i) **Ekman Number (Ek)**

Definition: The Ekman number expresses the ratio of viscous forces to Coriolis forces in rotating flows. It is described as:

$$Ek = \frac{\nu}{2\Omega L^2} \tag{1.88}$$

where:

- ν = Kinematic viscosity.
- Ω = Angular velocity.

Low Ek indicates dominant rotational (Coriolis) effects, relevant in geophysical and astrophysical flows.

(j) **Coriolis Frequency Parameter (C)**

Definition: The Coriolis frequency parameter characterizes the influence of planetary rotation on fluid motion. Mathematically, it is described as:

$$C = 2\Omega \sin\theta \tag{1.89}$$

where:

- Ω = Angular velocity of rotation.
- θ = Latitude.

It is crucial in atmospheric and oceanic dynamics, governing the behavior of large-scale rotating flows.

(k) **Jeffrey Fluid Parameter (λ_1, λ_2)**

Jeffrey fluid parameters describe the ratio of relaxation and retardation times in the constitutive model for viscoelastic (Jeffrey) fluids.

$$\text{Jeffrey parameter} = \frac{\lambda_1}{\lambda_2} \tag{1.90}$$

where:

- λ_1 = Relaxation time.
- λ_2 = Retardation time.

These parameters are vital for modeling and analyzing non-Newtonian, viscoelastic fluid behaviors in rotational and oscillatory flows.

1.10 Radial Basis Function

1.10.1 Introduction

Radial Basis Functions (RBFs) have become a cornerstone in numerical analysis, computational science, and engineering due to their flexibility, mesh-free nature, and ability to handle complex, multidimensional, and scattered data. Over the past decades, significant advancements have been made in both the theoretical underpinnings and practical applications of RBFs, particularly in solving partial differential equations (PDEs). Buhmann [94] and Kansa [95] have noted, RBFs have become indispensable in fields such as fluid mechanics, geophysics, and image processing, particularly when domain geometries are complex and classical meshing strategies become infeasible.

1.10.2 Development of Radial Basis Functions

The concept of RBF interpolation emerged in the early 1970s when Hardy [96] introduced the method as a means to approximate scattered data points. Since then, the technique has undergone significant advancements. Duchon [97] further advanced the field by introducing thin-plate splines, which minimized bending energy and provided a robust mathematical framework for interpolation. Micchelli's work [98] on conditionally positive definite functions laid the mathematical foundation for the solvability of RBF interpolation problems, ensuring the existence and uniqueness of solutions. Buhmann's [94] comprehensive treatise synthesized much of the progress in RBF theory, offering

insights into algorithms and practical applications. Kansa [95] later pioneered the use of RBFs for solving PDEs via a collocation method, marking a significant advance in mesh-free numerical analysis.

1.10.3 Mathematical Definition

Let $\mathbf{x}, \mathbf{x}_i \in \mathbb{R}^d$ be two points in a d-dimensional domain, and define the Euclidean distance $r = \|\mathbf{x} - \mathbf{x}_i\|$. A radial basis function $\phi : \mathbb{R}_0^+ \to \mathbb{R}$ is defined as [99]:

$$\phi(\mathbf{x}, \mathbf{x}_i) = \phi(r) = \phi(\|\mathbf{x} - \mathbf{x}_i\|) \tag{1.91}$$

To approximate a scalar field $z(\mathbf{x})$, we express it as a linear combination of RBFs:

$$z(\mathbf{x}) \approx \sum_{i=1}^{N} \lambda_i \, \phi(\|\mathbf{x} - \mathbf{x}_i\|) \tag{1.92}$$

where:

- N = Number of collocation points.
- λ_i = Unknown coefficients.
- ϕ = Chosen radial basis function (RBF) kernel.

This definition of RBFs is discussed in detail in the works of Fasshauer [99].

1.10.4 Types of Radial Basis Functions

The choice of RBF significantly affects the approximation accuracy, numerical conditioning, and computational cost. Table 1.1 summarizes commonly used RBFs [100].

Table 1.1: Radial Basis Functions and their Mathematical Definitions

Name of the RBF	**Equation**
Gaussian Function	$\phi(r) = e^{-(\epsilon r^2)}$
Linear Radial Basis Function	$\phi(r) = r$
Multi quadratic Function	$\phi(r) = \sqrt{1 + (\epsilon r)^2}$
Inverse Quadratic Function	$\phi(r) = \frac{1}{1 + (\epsilon r)^2}$
Inverse Multi quadratic Function	$\phi(r) = \frac{1}{\sqrt{1 + (\epsilon r)^2}}$
Polyharmonic Spline	$\phi(r) = \begin{cases} r^{2k-1}, & k \in \mathbb{N} \\ r^{2k}\ln(r), & k \in \mathbb{N} \end{cases}$
Cubic Matern	$\phi(r) = e^{-\epsilon r}\left(15 + 15\epsilon r + 6(\epsilon r)^2 + (\epsilon r)^3\right)$
Thin Plate Spline	$\phi(r) = r^2\ln(r)$
Compactly Supported Wendland Function	$\phi(r) = (1 - \varepsilon r)_+^6\left(35(\varepsilon r)^2 + 18(\varepsilon r) + 3\right)$

1.10.5 The Shape Parameter: Role and Significance

In infinitely smooth RBFs such as Gaussian, Multi quadratic (MQ), and Inverse Quadratic (IMQ), the shape parameter ϵ governs the spread of the basis function. It plays a critical role in controlling the trade-off between approximation accuracy and numerical stability:

- Small ϵ results in flatter RBFs, improving stability but potentially degrading approximation quality.

- Large ϵ leads to sharper RBFs, enhancing accuracy but causing ill-conditioning in the interpolation matrix.

The optimal choice of ϵ is problem-specific and may be obtained through techniques such as cross-validation or residual minimization [101].

1.10.6 Recent Research Trends

Recent studies have emphasized improving the efficiency, stability, and accuracy of RBF-based computational techniques. Notably, Wendland [102] developed compactly supported RBFs to address the challenge of computational cost in large-scale problems by limiting the influence of each basis function to a local neighborhood, thus improving sparsity and efficiency. Fornberg and Flyer [103] have contributed stable algorithms for constructing differentiation matrices using RBFs, which are crucial for high-dimensional PDEs and geoscientific applications. The RBF Pseudospectral Method (RBF-PSM) merges the strengths of RBFs and spectral methods, achieving exponential convergence for smooth problems and superior accuracy over traditional finite difference or finite element approaches. Wright et al. [104] and Fornberg et al. [105] further improved the reliability and efficiency of pseudospectral discretization by stabilizing the computation of multiquadric interpolants and introducing compact finite difference schemes on scattered nodes based on Radial Basis Functions, thereby enhancing both the precision and robustness of Radial Basis Function methods across diverse applications.

PDEs are fundamental to modeling a wide range of physical phenomena across engineering and scientific disciplines. However, obtaining analytical solutions to nonlinear or complex PDEs is often infeasible, necessitating the development of robust numerical methods. Among these, RBF methods have emerged as powerful and flexible computational tools for approximating solutions to PDEs, particularly due to their mesh-free nature and ability to handle scattered data in multidimensional and irregular domains. Ling and Kansa [106] developed adaptive RBF algorithms that enhance computational efficiency and accuracy by effectively addressing irregular domain geometries and scattered data distributions. In addition, Bayona [107], Flyer and Fornberg [108] proposed stability improvements in Gaussian RBF interpolation methods, which ensure reliable and accurate PDE solutions across diverse problem settings.

The versatility of RBFs extends beyond interpolation to complex fluid dynamics and MHD problems, where the mesh-free property of RBFs has been particularly advan-

tageous for modeling fluid flows in irregular or dynamic domains, where traditional grid-based methods struggle. Recent studies confirm the efficiency of radial basis functions in simulating complex MHD flows as well as thermal transport in rotating and inclined channels, highlighting their growing significance in scientific and engineering applications.

1.10.7 Radial Basis Function Pseudospectral Method (RBF-PSM)

Radial Basis Function methods have emerged as powerful meshfree techniques for the numerical solution of partial differential equations. Among the various approaches leveraging RBFs are the RBF Differential Quadrature (RBF-DQ) method, Kansa's method, and RBF Finite Difference (RBF-FD) methods. Each of these exhibits particular strengths in approximating PDE solutions on scattered nodes without requiring mesh generation. However, the *RBF Pseudospectral Method* is especially notable for combining the global approximation properties of RBFs with the spectral accuracy typically associated with classical pseudospectral methods.

The RBF-PSM combines global approximation via Radial Basis Functions with the high-order accuracy of spectral methods. This approach constructs differentiation matrices using RBF interpolants, providing flexibility in node placement and enabling the handling of complex geometries and boundary conditions [109, 110]. For smooth PDE solutions such as those arising in incompressible fluid flow, RBF-PSM achieves exponential convergence, provided the underlying RBF is sufficiently smooth. As demonstrated by Fornberg and Flyer [103], the method excels in high-precision problems, including fluid flow simulations, and offers an effective tool for solving complex, multi-dimensional domains.

Following this, an example is presented to illustrate the application of RBF-PSM in solving a representative PDE.

(a) **Problem Statement:**

Consider the general one-dimensional second-order partial differential equation

[111]:

$$\frac{\partial z}{\partial t} + a(x,t)\frac{\partial^2 z}{\partial x^2} + b(x,t)\frac{\partial z}{\partial x} + c(x,t)z = s(x,t), \quad x \in [0,1], \quad t > 0 \tag{1.93}$$

with initial and boundary conditions:

$$z(x,0) = f(x), \quad x \in [0,1] \tag{1.94}$$

$$z(0,t) = g_1(t), \quad z(1,t) = g_2(t), \quad t > 0 \tag{1.95}$$

(b) **RBF Approximation:**

We discretize the domain $[0,1]$ into N nodes denoted by $\{x_i\}_{i=1}^{N}$, where $x_1 = 0$ and $x_N = 1$, and the nodes can be uniformly or non-uniformly spaced. The solution is approximated using radial basis functions as

$$z(x,t) \approx \sum_{j=1}^{N} \lambda_j(t)\, \phi(\|x - x_j\|) \tag{1.96}$$

Evaluating (1.96) at the nodes x_i, we get:

$$\begin{bmatrix} z(x_1,t) \\ z(x_2,t) \\ \vdots \\ z(x_N,t) \end{bmatrix} = \begin{bmatrix} \phi(\|x_1 - x_1\|) & \cdots & \phi(\|x_1 - x_N\|) \\ \phi(\|x_2 - x_1\|) & \cdots & \phi(\|x_2 - x_N\|) \\ \vdots & \ddots & \vdots \\ \phi(\|x_N - x_1\|) & \cdots & \phi(\|x_N - x_N\|) \end{bmatrix} \begin{bmatrix} \lambda_1(t) \\ \lambda_2(t) \\ \vdots \\ \lambda_N(t) \end{bmatrix} \tag{1.97}$$

Compactly, this becomes:

$$\mathbf{z} = A\boldsymbol{\lambda} \tag{1.98}$$

where

$$A_{ij} = \phi(\|x_i - x_j\|), \quad \boldsymbol{\lambda} = \begin{bmatrix} \lambda_1(t) \\ \lambda_2(t) \\ \vdots \\ \lambda_N(t) \end{bmatrix}, \quad \mathbf{z} = \begin{bmatrix} z_1(t) \\ z_2(t) \\ \vdots \\ z_N(t) \end{bmatrix} \tag{1.99}$$

Assuming A is invertible, we solve for the RBF coefficients:

$$\boldsymbol{\lambda} = A^{-1}\mathbf{z} \tag{1.100}$$

(c) **Differentiation Matrix:**

To compute the spatial derivative, differentiate (1.96):

$$\frac{\partial z}{\partial x}(x,t) \approx \sum_{j=1}^{N} \lambda_j(t) \frac{\partial}{\partial x}\phi(\|x - x_j\|) \tag{1.101}$$

$$\frac{\partial^2 z}{\partial x^2}(x,t) \approx \sum_{j=1}^{N} \lambda_j(t) \frac{\partial^2}{\partial x^2}\phi(\|x - x_j\|) \tag{1.102}$$

Evaluating (1.101) and (1.102) at the nodes x_i, we obtain:

$$\mathbf{z}'(t) = \begin{bmatrix} \frac{\partial z}{\partial x}(x_1,t) \\ \frac{\partial z}{\partial x}(x_2,t) \\ \vdots \\ \frac{\partial z}{\partial x}(x_N,t) \end{bmatrix} = \begin{bmatrix} \frac{\partial}{\partial x}\phi(\|x_1 - x_1\|) & \cdots & \frac{\partial}{\partial x}\phi(\|x_1 - x_N\|) \\ \frac{\partial}{\partial x}\phi(\|x_2 - x_1\|) & \cdots & \frac{\partial}{\partial x}\phi(\|x_2 - x_N\|) \\ \vdots & \ddots & \vdots \\ \frac{\partial}{\partial x}\phi(\|x_N - x_1\|) & \cdots & \frac{\partial}{\partial x}\phi(\|x_N - x_N\|) \end{bmatrix} \begin{bmatrix} \lambda_1(t) \\ \lambda_2(t) \\ \vdots \\ \lambda_N(t) \end{bmatrix} \tag{1.103}$$

$$\mathbf{z}''(t) = \begin{bmatrix} \frac{\partial^2 z}{\partial x^2}(x_1,t) \\ \frac{\partial^2 z}{\partial x^2}(x_2,t) \\ \vdots \\ \frac{\partial^2 z}{\partial x^2}(x_N,t) \end{bmatrix} = \begin{bmatrix} \frac{\partial^2}{\partial x^2}\phi(\|x_1 - x_1\|) & \cdots & \frac{\partial^2}{\partial x^2}\phi(\|x_1 - x_N\|) \\ \frac{\partial^2}{\partial x^2}\phi(\|x_2 - x_1\|) & \cdots & \frac{\partial^2}{\partial x^2}\phi(\|x_2 - x_N\|) \\ \vdots & \ddots & \vdots \\ \frac{\partial^2}{\partial x^2}\phi(\|x_N - x_1\|) & \cdots & \frac{\partial^2}{\partial x^2}\phi(\|x_N - x_N\|) \end{bmatrix} \begin{bmatrix} \lambda_1(t) \\ \lambda_2(t) \\ \vdots \\ \lambda_N(t) \end{bmatrix} \tag{1.104}$$

and Define:

$$D_x = \left[\frac{\partial}{\partial x}\phi(\|x_i - x_j\|)\right]_{i,j=1}^{N}, \quad D_{xx} = \left[\frac{\partial^2}{\partial x^2}\phi(\|x_i - x_j\|)\right]_{i,j=1}^{N} \tag{1.105}$$

Then,

$$\mathbf{z}' = D_x\,\boldsymbol{\lambda} \tag{1.106}$$

$$\mathbf{z}'' = D_{xx}\,\boldsymbol{\lambda} \tag{1.107}$$

Substitute (1.100) into (1.106) and (1.107):

$$\mathbf{z}' = D_x A^{-1}\mathbf{z} = D_1\mathbf{z} \tag{1.108}$$

$$\mathbf{z}'' = D_{xx}A^{-1}\mathbf{z} = D_2\mathbf{z} \tag{1.109}$$

where $D_1 = D_x A^{-1}$ and $D_2 = D_{xx}A^{-1}$ are the differentiation matrices.

(d) **Discretization of the PDE:**

Substitute into the PDE (1.93) evaluated at the nodes:

$$\frac{d}{dt}\mathbf{z}(t) + a(x,t)(D_2\mathbf{z}(t)) + b(x,t)(D_1\mathbf{z}(t)) + c(x,t)\mathbf{z}(t) = \mathbf{s}(x,t) \tag{1.110}$$

This yields a system of Ordinary Differential Equations (ODEs):

$$\frac{d}{dt}\mathbf{z}(t) = -a(x,t)(D_2\mathbf{z}(t)) - b(x,t)(D_1\mathbf{z}(t)) - c(x,t)\mathbf{z}(t) + \mathbf{s}(x,t) \tag{1.111}$$

(e) **Boundary Condition Enforcement:**

Initial Condition:

$$\mathbf{z}(0) = \begin{bmatrix} f(x_1) \\ f(x_2) \\ \vdots \\ f(x_N) \end{bmatrix}$$

Boundary Conditions:

Enforce the boundary conditions at $x_1 = 0$ and $x_N = 1$ by:

- Replacing the first and last equations in the ODE system with the boundary conditions.
- Modifying the system matrix to ensure the boundary values are satisfied at each time step.

For Dirichlet boundaries:

$$z_1(t) = g_1(t), \quad z_N(t) = g_2(t)$$

(f) **Numerical Integration:**
Integrate the resulting ODE system in time using an appropriate method (e.g., Runge-Kutta), starting from the initial condition and enforcing the boundary conditions at each time step.

(g) **Shape Parameter Selection for Radial Basis Functions:**
RBF can be identified based on smoothness i.e., some RBFs are infinitely smooth and some are piecewise smooth. For all infinitely smooth RBF, a parameter $\epsilon > 0$ is present which decides the shape of the RBF, known as the shape parameter. The shape parameter plays an important role in accuracy, so choosing a good value of shape parameter is important.
Optimal ϵ selection is achieved via the Leave-One-Out Cross-Validation (LOOCV) algorithm, which minimizes approximation errors by iteratively excluding data points [112]. This technique involves isolating each data point x_j from the dataset, computing an RBF approximation $\phi_N^j(x)$ using the remaining points, and evaluating the error $E_k = |z(x_k) - \phi_N^k(x)|$ at the excluded point. This process, repeated for all n points, yields an error vector, as expressed in equation form.

$$E = [E_1, E_2, \ldots, E_n] \tag{1.112}$$

To enhance computational efficiency, Rippa introduces a streamlined method, defining the error as:

$$E_j = \frac{\lambda_j}{\phi_{jj}^{-1}} \tag{1.113}$$

where λ_j represents the interpolation coefficient, and ϕ_{jj}^{-1} is the j-th diagonal element of the inverse interpolation matrix ϕ^{-1}. This formulation reduces the need for repeated full matrix inversions, a significant advantage in large datasets. Rippa further applies Brent's method to minimize the error function, transforming the task into an optimization problem. The objective is to minimize $\|E\|$ leveraging the relationship from equation (1.108)

$$\phi^T (D_1)^T = (D_x)^T \tag{1.114}$$

Using equation (1.113), the error simplifies to

$$E_j = \frac{(D_1)^T}{\phi_{jj}^{-1}} \tag{1.115}$$

This approach ensures robustness in selecting ϵ, which governs the radial spread of RBFs such as Gaussian or multiquadric functions, as seen in standard RBF formulations. A smaller ϵ results in flatter, more global functions, while a larger ϵ produces sharper, localized responses, directly impacting the conditioning and accuracy of the interpolation matrix. Ferreira and Fasshauer [113] extend Rippa's method, proposing an enhanced cost function minimization strategy, such as Fasshauer's criterion, to refine ϵ selection further. This criterion, employed here, accounts for additional regularization, improving performance in noisy or ill-conditioned datasets. Together, these techniques provide a rigorous framework for optimizing RBF-based approximations in multidimensional interpolation problems.

Chapter 2

Numerical Analysis of Dusty Fluid Flow under Rotating Frame of Reference

2.1 Introduction

Dusty fluid refers to a two-phase mixture in which a fluid, either a liquid or a gas, carries dispersed solid particles, commonly known as dust. These particles may occur naturally or be added intentionally, and their presence fundamentally alters the flow characteristics of the carrier fluid. The foundational mathematical model for studying dusty fluid flows was introduced by Saffman [23] as discussed in *item (a) of Section 1.6.2*, who examined the behavior of dusty gases and established the basis for subsequent research in this area. In recent years, investigations on dusty fluid dynamics have received growing attention because of their importance in diverse engineering and environmental applications, covering sectors such as automotive, chemical, coating, and energy industries. The unique two-phase nature of dusty fluids leads to complex interactions between the fluid and the suspended particles, impacting viscosity, flow stability, and transport properties.

Channel geometries play a pivotal role in the efficient transport of dusty fluids in both industrial and geophysical contexts, with horizontal and inclined channels rep-

resenting two fundamental configurations. A horizontal channel comprises two parallel plates aligned horizontally, while an inclined channel is constructed with a slope relative to the horizontal, leveraging gravity to assist fluid movement. The orientation of the channel significantly influences flow dynamics: in horizontal channels, gravity acts uniformly and primarily perpendicular to the direction of flow, whereas in inclined channels, gravity introduces a component along the flow direction, thereby affecting flow rate, pressure distribution, and overall system efficiency. Chandrawat et al. [114] developed a theoretical formulation combined with numerical analysis employing the MCBS-DQM to investigate unsteady two-phase flow involving a fluid-fluid interface, dusty fluid, and Eringen's micropolar fluid within horizontal channels. Inclined channels are widely utilized in hydraulic engineering, wastewater treatment, and irrigation systems due to their capacity to facilitate natural fluid transport and reduce pumping energy requirements. Chakraborty and Medhi [115] investigated magnetohydrodynamic flow and thermal transport characteristics of a dusty viscoelastic fluid inside a sloped channel filled with a porous structure, focusing on how variations in viscosity and pressure influence the flow behavior. Their research highlighted how the interplay between the magnetic field, temperature, and medium porosity affects fluid flow and heat transfer behavior. Roja et al. [116] examined the effects of channel inclination and porous medium properties on entropy generation and flow irreversibility, revealing the substantial impact of Darcy-Forchheimer drag and the channel's inclined angle on fluid flow and emphasizing its importance in optimizing fluid transport for engineering applications. Collectively, these studies underscore that channel orientation and geometry are critical determinants of dusty fluid flow behavior and system performance.

Rotational and electrically conductive dusty fluid flows are characterized by the combined effects of system rotation and electrical conductivity, which introduce significant complexities into the flow dynamics. When the system is subjected to rotation, both the fluid and the suspended particles experience centrifugal and Coriolis forces, which can significantly alter the velocity profiles and flow structure. Bég et al. [117] developed a mathematical model for magnetohydrodynamic oscillatory Couette flow in a rotating, highly permeable medium subjected to an oblique magnetic field. Their analysis

considers a fluid-filled channel bounded by two parallel plates, with one plate rotating about its axis and the fluid exposed to a magnetic field oriented at an angle to the plates. The study examines how plate rotation, magnetic field strength and orientation, medium permeability, and oscillation frequency affect the flow behavior. Kalpana et al. [118] offer important insights into stratified dusty fluid flow in inclined channels, showing that incorporating rotational effects can markedly affect fluid momentum and heat transfer characteristics in similar physical systems.

Electrical conductivity introduces additional complexity through magnetohydrodynamic (MHD) effects, as previously discussed in *Section 1.6.4*. When an electrically conducting dusty fluid flows in the presence of a magnetic field, the fluid experiences a Lorentz force, which acts perpendicular to both the magnetic field and the velocity of the fluid. This force creates resistance to flow, modifies pressure distributions, and can lead to intricate flow structures. The interplay between magnetic fields and fluid motion is central to the field of MHD, which has important applications in energy systems, materials processing, and astrophysical phenomena. Chandrasekhar [119] established that magnetic fields stabilize rotating conductive fluids by suppressing hydrodynamic instabilities via Lorentz forces in systems like Taylor-Couette flow and Rayleigh-Bénard convection. His foundational work revealed how magnetic fields modify velocity profiles and streamline patterns, establishing critical thresholds for stability in astrophysical and industrial applications. Vidyanidhi et al. [120] examined MHD Couette flow and heat transfer in a rotating system, demonstrating that magnetic field-rotation interactions alter velocity and temperature profiles, thereby affecting heat transfer rates. Overall, these studies emphasize the significant role of magnetic fields in governing the dynamics and regulation of dusty fluids with electrical conductivity.

Despite extensive research on dusty fluid dynamics, significant gaps remain in the comprehensive understanding of such flows under the simultaneous influence of rotation and magnetic fields, particularly within both horizontal and inclined channel geometries. Much of the prior work has focused on simplified scenarios or has treated these effects in isolation, often overlooking the combined impact of rotation and magneto-

hydrodynamic forces on the velocity profiles and overall flow structure. Furthermore, the practical implications of these phenomena in industrial and engineering applications have not been fully explored. In addition to examining the velocity characteristics of the fluid and particle phases, there is a notable lack of studies addressing the associated pumping power requirements, an essential factor for system design and optimization. This work aims to address these gaps by providing a detailed analysis of dusty fluid flow in both horizontal and inclined channels, incorporating the effects of rotation and electrical conductivity, and by evaluating the pumping power using the calculated volume flow rate and pressure drop.

To achieve these objectives, this chapter is organized into two main parts. The first part focuses on the mathematical modeling of dusty fluid flow in a horizontal channel, followed by the development of a numerical solution and a discussion of the resulting velocity profiles for various dimensionless parameters, as well as the calculation of pumping power based on the computed volume flow rate and pressure drop. The second part applies a similar approach to the inclined channel configuration, presenting the corresponding mathematical formulation, numerical analysis, interpretation of velocity profiles, and evaluation of pumping power. The chapter concludes by highlighting the main outcomes and their practical relevance.

2.2 Mathematical Modeling of Dusty Fluid Flow under Horizontal Channel

This study investigates the unsteady flow of an incompressible, electrically conductive dusty fluid containing suspended dust particles within a horizontal channel bounded by two parallel plates (see Figure 2.1). The flow is driven by the combined effects of the upper plate's motion and a constant pressure gradient along the channel. The system operates under the influence of both a uniform external magnetic field applied perpendicular to the flow and a uniform angular velocity (rotation) about an axis perpendicular to the plates. The model accounts for the interactions between the fluid and dust particles, as well as the effects of rotation and magnetohydrodynamics.

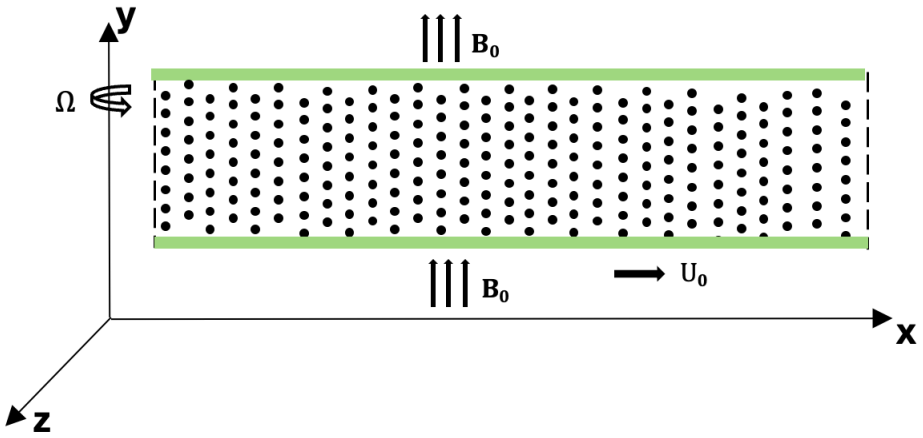

Fig. 2.1 Schematic of a Horizontal Channel with Dusty Fluid Flow

2.2.1 Key Features of the Model

(a) **Horizontal Channel Geometry:**

(i) The flow occurs between two infinite, parallel plates separated by a finite distance, forming a horizontal channel.

(ii) The upper plate moves at a uniform velocity, while a steady pressure gradient is applied in the x-direction to drive the fluid motion.

(b) **Electrically Conductive Dusty Fluid:**

(i) The fluid is incompressible and electrically conductive, enabling interaction with an externally applied magnetic field.

(ii) The dust particles are considered spherical and uniformly dispersed, with uniform temperature maintained within each particle.

(c) **External Magnetic Field:**

(i) A uniform magnetic field B_0 is imposed in the y-direction, perpendicular to the main flow direction.

(d) **Rotating Reference Frame:**

(i) The entire system rotates with a constant angular velocity Ω about the y-axis, introducing Coriolis and centrifugal forces into the flow dynamics.

(ii) The Coriolis force is explicitly included in the momentum equations, while the centrifugal force is absorbed into the modified pressure term due to the incompressibility assumption and the geometry of the channel as discussed in *Section 1.7*.

(e) **Flow Dynamics and Interacting Forces:**

(i) The flow exhibits primary and secondary velocity components in the x- and z-axes, respectively, with the secondary motion induced by the applied rotation.

(ii) The primary motion is controlled by the applied pressure gradient and the movement of the plate, whereas the secondary flow and total momentum transfer are affected by the Coriolis and Lorentz forces.

(iii) The velocity field is described as $\mathbf{u} = u_1\mathbf{i} + u_2\mathbf{j} + u_3\mathbf{k}$, representing three-dimensional flow characteristics.

2.2.2 Governing Equations for Dusty Fluid and Dust Particles

The dusty fluid is modeled as a two-phase system comprising a continuous fluid phase and a dispersed particle (dust) phase. The following continuity and momentum equations [23], adopted from *item (e) of Section 1.6.2*.

(a) **Continuity Equations:** (Same as Equations (1.48) and (1.49) from *Section 1.6.2*)

(i) Fluid phase:

$$\frac{\partial \rho_f}{\partial t} + \nabla \cdot (\rho_f \mathbf{u}) = 0 \tag{2.1}$$

(ii) Particle phase:

$$\frac{\partial \rho_p}{\partial t} + \nabla \cdot (\rho_p \mathbf{u}_p) = 0 \tag{2.2}$$

For incompressible flow, these reduce to:

$$\nabla \cdot \mathbf{u} = 0, \qquad \nabla \cdot \mathbf{u}_p = 0$$

where:

- ρ_f = Fluid density.
- $\mathbf{u}$ = Fluid velocity.
- ρ_p = Particle (dust) density.
- $\mathbf{u}_p$ = Particle velocity.

(b) **Momentum Equations:** (Same as Equations (1.50) and (1.51) from *Subsection 1.6.2*)

(i) Fluid phase:

$$\rho_f \left(\frac{\partial \mathbf{u}}{\partial t} + (\mathbf{u} \cdot \nabla)\mathbf{u} \right) = -\nabla P + \mu \nabla^2 \mathbf{u} + K(\mathbf{u}_p - \mathbf{u}) + \rho_f \mathbf{g} \tag{2.3}$$

(ii) Particle phase:

$$\rho_p \left(\frac{\partial \mathbf{u}_p}{\partial t} + (\mathbf{u}_p \cdot \nabla)\mathbf{u}_p \right) = -K(\mathbf{u}_p - \mathbf{u}) + \rho_p \mathbf{g} \tag{2.4}$$

where K is the drag coefficient, and $(\mathbf{u}_p - \mathbf{u})$ is the relative velocity between particles and fluid.

(c) **Incorporation of Rotation:** To account for rotation, the governing equations are modified by introducing Coriolis and centrifugal effects. In a rotating frame with angular velocity Ω, the fluid momentum equation gains an additional term $2\rho_f(\Omega \times \mathbf{u})$, representing the Coriolis force (as shown in Equation (1.73)).

(d) **Incorporation of Magnetic Field:** The presence of an external magnetic field introduces the Lorentz force, which acts as a body force on the electrically conductive fluid. For a magnetic field B_0 in the y-direction, the Lorentz force per unit volume is given by:

$$\mathbf{F}_L = \frac{\sigma B_0^2 (1 + Bi \cdot Be)\mathbf{u}}{(1 + Bi \cdot Be)^2 + Be^2} \tag{2.5}$$

where σ is the electrical conductivity, Bi is the ion slip parameter, and Be is the Hall parameter.

(e) **Modified Governing Equations:** By combining the standard equations (2.3) and (2.4) with the rotation and magnetic field (Equation (2.5)) effects, the modified equations for both the phases become:

(i) Fluid Phase:

$$\rho_f \left(\frac{\partial \mathbf{u}}{\partial t} + 2(\Omega \times \mathbf{u}) + (\mathbf{u} \cdot \nabla)\mathbf{u} \right) = -\nabla P + \mu \nabla^2 \mathbf{u} - K(\mathbf{u} - \mathbf{u}_p) + \mathbf{F}_L + \rho_f \mathbf{g} \tag{2.6}$$

(ii) Particle Phase:

$$\rho_p \left(\frac{\partial \mathbf{u}_p}{\partial t} + (\mathbf{u}_p \cdot \nabla)\mathbf{u}_p \right) = K(\mathbf{u} - \mathbf{u}_p) + \rho_p \mathbf{g} \tag{2.7}$$

where:

- $\mathbf{u} = (u_1, 0, u_3)$ is the fluid velocity vector in the x, y, and z directions respectively,
- $\mathbf{u}_p = (u_{1p}, 0, u_{3p})$ is the dust particle velocity vector,
- ρ_f, ρ_p = Densities of fluid and particles respectively.
- μ = Dynamic viscosity.
- K = Drag coefficient representing the interaction between the fluid and the suspended particles.
- g = Gravitational acceleration vector.

Due to the geometry of the problem, all variables depend only on the transverse coordinate y and time t, and the flow is assumed unidirectional in the x and z directions.

(f) **Dimensionless Variables and Scales:** To facilitate the mathematical analysis, the following characteristic scales are introduced:

- Characteristic length scale (half-distance between plates) = L
- Characteristic velocity scale = U_0
- Characteristic time scale = $\dfrac{L}{U_0}$
- Pressure scale = $\rho_f U_0^2$

Using these scales, dimensionless variables are defined as

$$y^* = \frac{y}{L}, \quad t^* = \frac{tU_0}{L}, \quad u^* = \frac{u}{U_0}, \quad u_p^* = \frac{u_p}{U_0}, \quad p^* = \frac{P}{\rho_f U_0^2}. \tag{2.8}$$

For simplicity, the asterisks will be omitted in the following sections.

(g) **Initial and Boundary Conditions:** The system is solved subject to the following initial and boundary conditions in dimensionless form:

(i) Initial conditions: At $t = 0$

$$u_1(y,0) = u_3(y,0) = u_{1p}(y,0) = u_{3p}(y,0) = 0$$

(ii) Boundary conditions: At the plates $y = -1$ and $y = 1$ (for all $t > 0$)

$$u_1(-1,t) = u_{1p}(-1,t) = 0, \quad u_3(-1,t) = u_{3p}(-1,t) = 0$$

$$u_1(1,t) = u_{1p}(1,t) = 1, \quad u_3(1,t) = u_{3p}(1,t) = 1$$

(h) **Dimensionless Parameters:** Several dimensionless parameters arise naturally in the non-dimensionalization process, capturing the relative effects of fluid-particle interaction, magnetic field, rotation, and inertial forces (for details refer to *Section 1.9*):

Reynolds number:	$Re = \dfrac{\rho_f U_0 L}{\mu}$
Particle concentration parameter:	$R = \dfrac{KL^2\rho_p}{\mu}$
Hartmann number:	$Ha^2 = \dfrac{\sigma B_0^2 L^2}{\mu}$
Coriolis frequency parameter:	$C = 4\pi\Omega$
Ekman number:	$Ek = \dfrac{Re}{4\pi}$
Particle mass parameter:	$G = \dfrac{\rho_p}{\rho_f}$

(i) **Dimensionless Form of Governing Equations:** Given the assumptions of unidirectional flow, the velocity components are $u_1(y,t)$ in the x-direction and $u_3(y,t)$ in the z-direction, with no motion in the y-direction. Using the modified governing equations (2.6) and (2.7), along with appropriate dimensionless variables, initial and boundary conditions, and non-dimensional parameters (such as Re, $(Ha)^2$, R, G, C, and Ek), the resulting non-dimensional system of partial differential equations governing dusty fluid flow in a rotating frame under an applied magnetic field is given by:

$$\frac{\partial u_1}{\partial t} = G_e(t) + \frac{1}{Re}\frac{\partial^2 u_1}{\partial y^2} - \frac{Ha^2}{Re}\frac{(1+B_iB_e)u_1 + B_e u_3}{(1+B_iB_e)^2 + B_e^2} - \frac{R}{Re}(u_1 - u_{1p}) - \frac{2CEk}{Re}u_3 \tag{2.9}$$

$$\frac{\partial u_3}{\partial t} = \frac{1}{Re}\frac{\partial^2 u_3}{\partial y^2} - \frac{Ha^2}{Re}\frac{(1+B_iB_e)u_3 + B_e u_1}{(1+B_iB_e)^2 + B_e^2} - \frac{R}{Re}(u_3 - u_{3p}) + \frac{2CEk}{Re}u_1 \tag{2.10}$$

$$\frac{\partial u_{1p}}{\partial t} = \frac{1}{G}(u_1 - u_{1p}) - \frac{C}{2\pi}u_{3p} \tag{2.11}$$

$$\frac{\partial u_{3p}}{\partial t} = \frac{1}{G}(u_3 - u_{3p}) + \frac{C}{2\pi}u_{1p} \tag{2.12}$$

2.2.3 Numerical Solution using Radial Basis Function Pseudospectral Method

The numerical solution of the fundamental PDE's describing the dusty fluid flow and particle dynamics requires efficient and accurate computational techniques. RBF methods have emerged as robust meshfree numerical schemes for solving PDEs, particularly due to their flexibility in handling complex geometries and boundary conditions without the need for traditional grid generation. A detailed discussion of Radial Basis Functions, including their development, mathematical definition, and key properties, has been presented in *Chapter 1* (*Section 1.10*). In particular, the RBF-PSM, outlined in *Section 1.10.7*, serves as the foundational methodology for solving the governing equations (2.9) to (2.12) of the dusty fluid flow. Among various RBF-based approaches, the RBF-PSM is distinguished by its combination of global approximation properties and spectral accuracy, making it highly suitable for solving fluid flow problems involving coupled phases such as dusty fluids.

The following step-by-step algorithm outlines the implementation procedure of the RBF-PSM, highlighting its key computational stages for solving the governing equations efficiently and accurately.

(a) **Domain Discretization:** The domain is discretized into N scattered node points $\{y_i\}_{i=1}^{N}$ over the spatial coordinate $y \in [-1, 1]$.

(b) **Selection of Radial Basis Function:** A range of radial basis functions can be utilized depending on the specific conditions, as outlined by Buhmann in his study [121]. Table 1.1 presents various RBFs, such as Gaussian, linear, and multiquadric functions, each featuring a shape parameter, $\epsilon > 0$. This parameter shapes the function's geometry; with lower ϵ values producing flatter forms, influencing the function's application and behavior.

A suitable radial basis function ϕ is selected to approximate the solution. In this study, we use the *Wendland RBF* [122], which is compactly supported and defined

as:

$$\phi(r) = (1 - \varepsilon r)_+^6 \left(35(\varepsilon r)^2 + 18(\varepsilon r) + 3\right) \tag{2.13}$$

where:

- $r = \|z\|$ is the distance from the center point,
- ϵ is a shape parameter controlling the flatness of the RBF and will be selected as described in item (g) of Section 1.10

The Wendland radial basis function combines compact support and strict positive definiteness, which inherently ensures sparse differentiation matrices, computational efficiency, and numerical stability. These characteristics make it uniquely suited for solving partial differential equations in rotating magnetohydrodynamic systems with complex geometries.

(c) **Function Approximation:** The solution functions, including fluid and particle velocity components $u_1(y,t), u_3(y,t), u_{1p}(y,t), u_{3p}(y,t)$ are approximated as linear combinations of radial basis functions centered at these nodes.

The approximate solution for $z(y,t)$ is expressed as:

$$z(y,t) \approx \sum_{j=1}^{N} \lambda_j(t)\, \phi(\|y - y_j\|) \tag{2.14}$$

where

- $\phi =$ Wendland RBF
- $\lambda_j(t)$ = Interpolate coefficients

(d) **Matrix formulation and differentiation matrices:** Following the methodology outlined in *Section 1.10.7*, the differentiation matrices corresponding to first and second spatial derivatives are constructed as:

$$D_1 = D_x A^{-1}, \quad D_2 = D_{xx} A^{-1}, \tag{2.15}$$

where A is the interpolation matrix with entries $A_{ij} = \phi(\|y_i - y_j\|)$, and D_x, D_{xx} are matrices formed by evaluating the first and second derivatives of ϕ at the node points y_i.

(e) **Transformation to ODEs:** Hence, the system of partial differential equations (2.9) to (2.12), governing the dimensionless velocities of the fluid and particle phases, are transformed into a system of ODEs with respect to time:

$$\frac{du_1}{dt} = G_e(t) + \frac{1}{Re}D_2 u_1 - \frac{Ha^2}{Re}\frac{(1 + Bi\,Be)}{(1 + Bi\,Be)^2 + Be^2}u_1 - \frac{Ha^2}{Re}\frac{Be}{(1 + Bi\,Be)^2 + Be^2}u_3 - \frac{R}{Re}(u_1 - u_{1p}) - \frac{2CEk}{Re}u_3 \tag{2.16}$$

$$\frac{du_3}{dt} = \frac{1}{Re}D_2 u_3 - \frac{Ha^2}{Re}\frac{(1 + Bi\,Be)}{(1 + Bi\,Be)^2 + Be^2}u_3 - \frac{Ha^2}{Re}\frac{Be}{(1 + Bi\,Be)^2 + Be^2}u_1 - \frac{R}{Re}(u_3 - u_{3p}) + \frac{2CEk}{Re}u_1 \tag{2.17}$$

$$\frac{du_{1p}}{dt} = \frac{1}{G}(u_1 - u_{1p}) - \frac{C}{2\pi}u_{3p} \tag{2.18}$$

$$\frac{du_{3p}}{dt} = \frac{1}{G}(u_3 - u_{3p}) + \frac{C}{2\pi}u_{1p} \tag{2.19}$$

Here, u_1, u_3, u_{1p}, u_{3p} are velocity components at the node points. The terms D_1 and D_2 represent the first and second derivative differentiation matrices, respectively. The parameters Re (Reynolds number), Ha (Hartmann number), Bi (ion slip parameter), Be (Hall parameter), R (particle concentration parameter), C (Coriolis parameter), Ek (Ekman number), and G (particle mass parameter) are dimensionless quantities.

Now, these ordinary differential equations can be solved using numerical methods such as the Runge-Kutta scheme or other suitable time-integration techniques, enabling the analysis of the transient behavior of dusty fluid flow influenced by rotation and magnetic fields.

SSP RK43 Time Integration Scheme:

Given the above system of ODEs, the time integration is performed using the Strong Stability Preserving Runge-Kutta Method of order 3 with 4 Stages (SSP RK43) [123].

Let the current time be t^n with solution vectors

$$\mathbf{U}^n = \begin{bmatrix} u_1^n \\ u_3^n \\ u_{1p}^n \\ u_{3p}^n \end{bmatrix}$$

and time-step size Δt. The SSP RK43 scheme advances the solution as follows.

Given the initial conditions at time $t = 0$, the velocity components of the fluid and particle phases satisfy:

$$u_1^0 = u_3^0 = u_{1p}^0 = u_{3p}^0 = 0,$$

where the superscript 0 denotes the initial time level.

Therefore, the initial solution vector $\mathbf{U}^0$ is defined as

$$\mathbf{U}^0 = \begin{bmatrix} u_1^0 \\ u_3^0 \\ u_{1p}^0 \\ u_{3p}^0 \end{bmatrix} = \begin{bmatrix} 0 \\ 0 \\ 0 \\ 0 \end{bmatrix}.$$

This vector forms the starting point for the SSP RK43 time integration scheme.

Step 1:

$$u_1^{(1)} = u_1^0 + \frac{\Delta t}{2} F_1\big(t^0, \mathbf{U}^0\big)$$

$$u_3^{(1)} = u_3^0 + \frac{\Delta t}{2} F_2\big(t^0, \mathbf{U}^0\big)$$

$$u_{1p}^{(1)} = u_{1p}^0 + \frac{\Delta t}{2} F_3\big(t^0, \mathbf{U}^0\big)$$

$$u_{3p}^{(1)} = u_{3p}^0 + \frac{\Delta t}{2} F_4\big(t^0, \mathbf{U}^0\big)$$

Apply boundary conditions to $u_1^{(1)}, u_3^{(1)}, u_{1p}^{(1)}, u_{3p}^{(1)}$.

Step 2:

$$u_1^{(2)} = u_1^{(1)} + \frac{\Delta t}{2} F_1\big(t^n + \frac{\Delta t}{2}, \mathbf{U}^{(1)}\big)$$
$$u_3^{(2)} = u_3^{(1)} + \frac{\Delta t}{2} F_2\big(t^n + \frac{\Delta t}{2}, \mathbf{U}^{(1)}\big)$$
$$u_{1p}^{(2)} = u_{1p}^{(1)} + \frac{\Delta t}{2} F_3\big(t^n + \frac{\Delta t}{2}, \mathbf{U}^{(1)}\big)$$
$$u_{3p}^{(2)} = u_{3p}^{(1)} + \frac{\Delta t}{2} F_4\big(t^n + \frac{\Delta t}{2}, \mathbf{U}^{(1)}\big)$$

Apply boundary conditions to $u_1^{(2)}, u_3^{(2)}, u_{1p}^{(2)}, u_{3p}^{(2)}$.

Step 3:

$$u_1^{(3)} = \frac{2}{3}u_1^n + \frac{1}{3}u_1^{(2)} + \frac{\Delta t}{6}F_1\big(t^n + \Delta t, \mathbf{U}^{(2)}\big)$$
$$u_3^{(3)} = \frac{2}{3}u_3^n + \frac{1}{3}u_3^{(2)} + \frac{\Delta t}{6}F_2\big(t^n + \Delta t, \mathbf{U}^{(2)}\big)$$
$$u_{1p}^{(3)} = \frac{2}{3}u_{1p}^n + \frac{1}{3}u_{1p}^{(2)} + \frac{\Delta t}{6}F_3\big(t^n + \Delta t, \mathbf{U}^{(2)}\big)$$
$$u_{3p}^{(3)} = \frac{2}{3}u_{3p}^n + \frac{1}{3}u_{3p}^{(2)} + \frac{\Delta t}{6}F_4\big(t^n + \Delta t, \mathbf{U}^{(2)}\big)$$

Apply boundary conditions to $u_1^{(3)}, u_3^{(3)}, u_{1p}^{(3)}, u_{3p}^{(3)}$.

Step 4 (Final):

$$u_1 = u_1^{(3)} + \frac{\Delta t}{2}F_1\big(t^n + \frac{\Delta t}{2}, \mathbf{U}^{(3)}\big)$$
$$u_3 = u_3^{(3)} + \frac{\Delta t}{2}F_2\big(t^n + \frac{\Delta t}{2}, \mathbf{U}^{(3)}\big)$$
$$u_{1p} = u_{1p}^{(3)} + \frac{\Delta t}{2}F_3\big(t^n + \frac{\Delta t}{2}, \mathbf{U}^{(3)}\big)$$
$$u_{3p} = u_{3p}^{(3)} + \frac{\Delta t}{2}F_4\big(t^n + \frac{\Delta t}{2}, \mathbf{U}^{(3)}\big)$$

Apply boundary conditions to u_1, u_3, u_{1p}, u_{3p}.

Where the right-hand side functions F_i are defined by the ODE system (2.16) **to** (2.19)**:**

$$F_1(t,\mathbf{U}) = G_e(t) + \frac{1}{Re}D_2u_1 - \frac{Ha^2}{Re}\frac{(1+Bi\,Be)}{(1+Bi\,Be)^2+Be^2}u_1 - \frac{Ha^2}{Re}\frac{Be}{(1+Bi\,Be)^2+Be^2}u_3 - \frac{R}{Re}(u_1-u_{1p}) - \frac{2CEk}{Re}u_3$$

$$F_2(t,\mathbf{U}) = G_e(t) + \frac{1}{Re}D_2u_3 - \frac{Ha^2}{Re}\frac{(1+Bi\,Be)}{(1+Bi\,Be)^2+Be^2}u_3 - \frac{Ha^2}{Re}\frac{Be}{(1+Bi\,Be)^2+Be^2}u_1 - \frac{R}{Re}(u_3-u_{3p}) + \frac{2CEk}{Re}u_1$$

$$F_3(t,\mathbf{U}) = \frac{1}{G}(u_1-u_{1p}) - \frac{C}{2\pi}u_{3p}$$

$$F_4(t,\mathbf{U}) = \frac{1}{G}(u_3-u_{3p}) + \frac{C}{2\pi}u_{1p}$$

2.2.4 Pumping Power Analysis

Pumping power represents the mechanical energy required to maintain fluid flow against pressure losses within a system, reflecting the operational efficiency of fluid transport devices.

Volume flow rate (Q) denotes the amount of fluid transported per unit time through a defined cross-sectional area and is given by [90]:

$$Q = A \cdot U_{av} \quad \text{(Equation (1.75), } \textit{Section 1.8.1)} \tag{2.20}$$

where A denotes the cross-sectional area and U_{av} is the average fluid velocity.

Pressure drop (ΔP) is the reduction in fluid pressure due to frictional and other resistive forces encountered during flow. It is given by the Darcy–Weisbach equation [91]:

$$\Delta P = f_d \cdot \frac{L_p}{D} \cdot \frac{\rho_f U_{av}^2}{2} \quad \text{(Equation (1.77), } \textit{Section 1.8.2)} \tag{2.21}$$

where f_d is the Darcy friction factor, L_p is the length of channel, D is the channel diameter, and ρ_f is the fluid density.

Pumping power (P_{pow}) represents the rate of mechanical energy supplied to overcome

the pressure drop at the given flow rate and is calculated as [91]:

$$P_{pow} = Q \cdot \Delta P \quad \text{(Equation (1.79), } \textit{Section 1.8.3)} \tag{2.22}$$

These parameters have been discussed comprehensively in *Chapter 1* (*Section 1.8.1* to *1.8.3*).

The fluid density $\rho_f = 997.1\,\text{kg/m}^3$ was used for water has been used consistently for these calculations, in line with established literature [124].

Table 2.1 reports the computed values of volume flow rate, pressure drop, and pumping power under different parameter settings. The results indicate that that pumping power initially increases with time, reaching a maximum at $t = 0.5$, before subsequently decreasing, which aligns with the temporal trends in volume flow rate and pressure drop.

Variations in particle mass concentration G, particle concentration R, Hartmann number Ha^2, Ion Slip parameter Bi, and other dimensionless parameters influence pumping power. Notably, as the particle concentration R decreases, dusty fluids require more pumping power compared to non-dusty fluids flowing through horizontal channels. This behavior is due to the inclusion of solid particles, resulting in enhanced effective viscosity and additional resistance to flow, thereby increasing the energy required for pumping. Parameters such as G, Bi, and Be exhibit a direct correlation with increasing pumping power, reflecting enhanced fluid resistance due to ion slip and electromagnetic effects. Conversely, increasing Ha^2 tends to reduce pumping power, indicating the complex interplay of electromagnetic forces modulating flow resistance. Additionally, in rotating systems, the Coriolis force induces secondary flow structures that impact fluid dynamics and consequently influence the required pumping power.

Table 2.1: Volume Flow Rate, Pressure Drop, and Pumping Power for Various Parameter Values

Parameter	**Volume Flow Rate**	**Pressure Drop**	**Pumping Power**
$t = 0.1$	0.2573	95.0771	24.4609
$t = 0.3$	0.3720	198.7327	73.9201

continued on next page

Table 2.1: Volume Flow Rate, Pressure Drop, and Pumping Power for various parameters

Parameter	**Volume Flow Rate**	**Pressure Drop**	**Pumping Power**
$t = 0.5$	0.3955	224.6822	88.8612
$t = 0.7$	0.3736	200.4973	74.9069
$t = 0.9$	0.3292	155.6985	51.2608
$G = 0.005$	0.3955	224.6822	88.8612
$G = 0.0025$	0.3962	225.4703	89.3291
$G = 0.0016$	0.3964	225.7579	89.5001
$G = 0.00125$	0.3965	225.8702	89.5669
$G = 0.001$	0.3966	225.9506	89.6147
$R = 1$	0.3941	223.1011	87.9248
$R = 2$	0.3913	219.9691	86.0799
$R = 3$	0.3886	216.8771	84.2713
$R = 4$	0.3858	213.8246	82.4984
$R = 5$	0.3831	210.8114	80.7607
$\mathrm{Ha}^2 = 2$	0.3955	224.6822	88.8612
$\mathrm{Ha}^2 = 3$	0.3896	218.0318	84.9452
$\mathrm{Ha}^2 = 4$	0.3839	211.7160	81.2811
$\mathrm{Ha}^2 = 5$	0.3784	205.7141	77.8493
$\mathrm{Ha}^2 = 6$	0.3731	200.0068	74.6322
$\mathrm{Bi} = 2$	0.3955	224.6822	88.8612
$\mathrm{Bi} = 3$	0.3996	229.3790	91.6620
$\mathrm{Bi} = 4$	0.4018	231.9116	93.1843
$\mathrm{Bi} = 5$	0.4031	233.4506	94.1134
$\mathrm{Bi} = 6$	0.4040	234.4696	94.7303
$\mathrm{Be} = 2$	0.3955	224.6822	88.8612
$\mathrm{Be} = 3$	0.3988	228.5072	91.1399

continued on next page

Table 2.1: Volume Flow Rate, Pressure Drop, and Pumping Power for various parameters

Parameter	**Volume Flow Rate**	**Pressure Drop**	**Pumping Power**
$\mathrm{Be} = 4$	0.4008	230.7348	92.4759
$\mathrm{Be} = 5$	0.4021	232.1895	93.3518
$\mathrm{Be} = 6$	0.4029	233.2131	93.9698
$E_k = 0.15$	0.4662	312.1457	145.5107
$E_k = 0.25$	0.3955	224.6822	88.8612
$E_k = 0.35$	0.3217	148.6628	47.8258
$E_k = 0.45$	0.2479	88.3074	21.8955
$\mathrm{Re} = 2$	0.3955	224.6822	88.8612
$\mathrm{Re} = 4$	0.3550	90.5344	32.1436
$\mathrm{Re} = 6$	0.3119	46.5919	14.5340
$\mathrm{Re} = 8$	0.2807	28.2906	7.9406
$\Omega = 0.4$	0.4317	267.6911	115.5606
$\Omega = 0.5$	0.3955	224.6822	88.8612
$\Omega = 0.6$	0.3585	184.6217	66.1886
$\Omega = 0.7$	0.3211	148.1363	47.5720

end of table

2.2.5 RBF-PSM Validation and Stability Analysis

To check the validity of the applied RBF-PSM, the obtained results are compared with a well-established differential quadrature method (DQM) which is a numerical method that approximates derivatives of a function using weighted sums of function values at discrete points. The primary and secondary velocity profiles are obtained with both the numerical schemes for $t = 0.5$ and are represented graphically with Figure 2.2. It is observed from the graph that both methods are in good agreement for the result of the velocity profiles. The stability of a numerical method using the matrix method is essential for producing accurate results over time without diverging or becoming unstable.

The matrix method involves analyzing the matrix linked with the system of equations that the numerical method is solving and determining its eigenvalues. The eigenvalues reveal information about the method's stability because they are associated with the growth or decay of errors over time. A numerical method is regarded as stable when the real parts of its eigenvalues are non-positive, indicating that any errors introduced at a given time step either diminish or remain constant in subsequent time steps. Figure 2.3 represents the eigenvalues of the associated matrix for $N = 50$ which demonstrates that the eigenvalues have zero real parts.

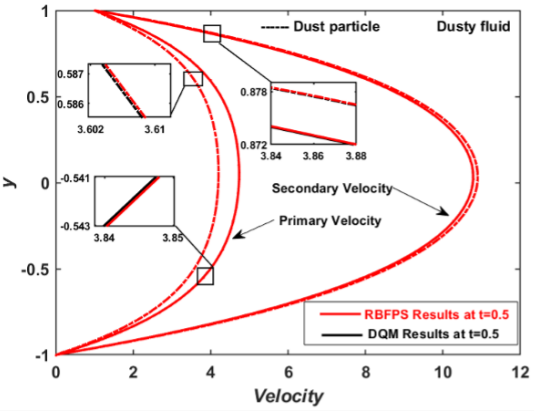

Fig. 2.2 Comparison of Primary and Secondary Velocity Profiles at time ($t = 0.5$) for Dusty Fluid Using MCBS-DQM and RBF-PSM

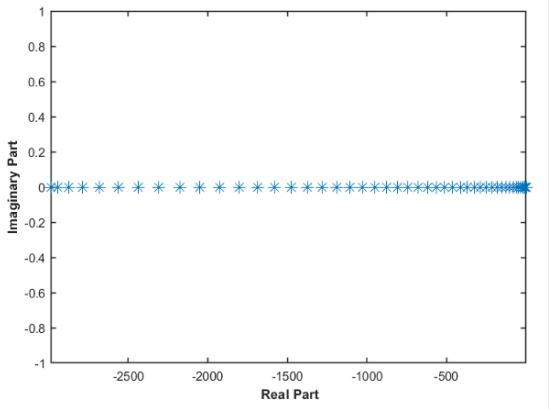

Fig. 2.3 Stability Diagram Obtained Through Eigenvalue Analysis of the Corresponding Matrix for $N = 50$

2.2.6 Skin Friction Coefficient

Skin friction is the tangential resistive force per unit area exerted when a fluid moves close to a boundary surface. It quantifies the fluid's resistance against the solid boundary and is a critical factor in fluid flow analysis. For dusty fluid flowing between horizontal plates, the skin friction coefficient at the lower and upper plates is defined as [1]:

$$C_{f_1} = \frac{2(\tau_m)_{y=-1}}{\rho_f U_0} = \frac{2}{Re}\left(\frac{\partial u_1}{\partial y}\right)_{y=-1}, \quad C_{f_2} = \frac{2(\tau_m)_{y=1}}{\rho_f U_0} = \frac{2}{Re}\left(\frac{\partial u_1}{\partial y}\right)_{y=1} \tag{2.23}$$

$$C_{f_1}^{(secondary)} = \frac{2}{Re}\left(\frac{\partial u_3}{\partial y}\right)_{y=-1}, \quad C_{f_2}^{(secondary)} = \frac{2}{Re}\left(\frac{\partial u_3}{\partial y}\right)_{y=1} \tag{2.24}$$

where

- τ_m = Shear stress at the wall.
- ρ_f = Fluid density.
- Re = Reynolds number.
- u_1 and u_3 are the velocity components of the fluid in the primary (x) and secondary (z) directions respectively.
- U_0 = Characteristic velocity
- $y = \pm 1$ = Locations of the lower and upper plates, respectively.

The computed skin friction coefficients under varying physical parameters are presented in Table 2.2. The results indicate that at the lower plate, the skin friction coefficients for both primary and secondary velocities increase with time (t), pressure gradient (Ge), Reynolds number (Re), and ion slip parameter (Bi). A slight increasing trend is also observed with particle mass parameter (G) and Hall parameter (Be). Conversely, increases in particle concentration (R), Hartmann number (Ha^2), and angular velocity (Ω) result in a decrease in skin friction coefficients.

At the upper plate, the skin friction coefficients generally decrease with increases in time, pressure gradient, Reynolds number, ion slip parameter, Hall parameter, and particle mass parameter, while increasing with the Hartmann number. Notably, the primary velocity skin friction coefficient at the upper plate increases with particle concentration, Ekman number (Ek), and angular velocity, whereas the secondary velocity skin friction coefficient decreases with these parameters.

These variations can be attributed to the rotational effects present in the fluid system, where the primary velocity aligns with the rotation direction and the secondary velocity is perpendicular to it. The Ekman number characterizes the ratio of viscous to Coriolis forces; an increase in Ek reduces viscous forces, thereby lowering resistance and skin friction. Overall, the interplay of these parameters illustrates the complex behavior of resistance forces in dusty fluid flow within a rotating horizontal channel.

Table 2.2: Skin Friction Coefficients for Various Parameter Values

Parameter	**Primary Velocity**		**Secondary Velocity**	
	C_{f_1}	C_{f_2}	C_{f_1}	C_{f_2}
$t = 0.1000$	9.3650	-6.3708	10.4273	-8.2091
$t = 0.2000$	12.3565	-9.9043	15.2984	-13.9448
$t = 0.4000$	14.7469	-12.5149	22.6999	-21.9808
$G = 0.0100$	14.8648	-12.6334	25.6980	-25.1217
$G = 0.0030$	14.9412	-12.7210	25.7052	-25.1248
$G = 0.0020$	14.9525	-12.7339	25.7054	-25.1243
$Ge = 10.0000$	7.4628	-5.2395	12.8781	-12.2990
$Ge = 20.0000$	14.9189	-12.6956	25.7042	-25.1251
$Ge = 30.0000$	22.3750	-20.1516	38.5303	-37.9512
$Re = 2.0000$	7.4594	-6.3478	12.8521	-12.5625
$Re = 3.0000$	10.7317	-9.6017	15.3470	-14.9169
$Re = 4.0000$	13.2926	-12.1190	17.3658	-16.8046
$R = 0.4000$	25.7044	-25.1246	14.9302	-12.7084
$R = 0.6000$	25.7040	-25.1256	14.9076	-12.6827
$R = 0.8000$	25.7035	-25.1266	14.8852	-12.6571
$Ha^2 = 2.0000$	14.9189	-12.6956	25.7042	-25.1251
$Ha^2 = 3.0000$	14.6812	-12.4088	25.2005	-24.5508
$Ha^2 = 4.0000$	14.4521	-12.1314	24.7137	-23.9948
$Bi = 2.0000$	14.9189	-12.6956	25.7042	-25.1251
$Bi = 3.0000$	15.0847	-12.8924	25.9971	-25.4593
$Bi = 4.0000$	15.1733	-12.9982	26.1695	-25.6556
$Be = 2.0000$	16.3781	-14.3510	25.1441	-24.4413
$Be = 3.0000$	16.5374	-14.5401	25.4372	-24.7749
$Be = 4.0000$	16.6289	-14.6485	25.6019	-24.9623

continued on next page

Table 2.2: Skin Friction Coefficients for Various Parameter Values

Parameter	**Primary Velocity**		**Secondary Velocity**	
	C_{f_1}	C_{f_2}	C_{f_1}	C_{f_2}
$\Omega = 0.4000$	16.3781	-14.3510	25.1441	-24.4413
$\Omega = 0.5000$	14.9189	-12.6956	25.7042	-25.1251
$\Omega = 0.6000$	13.4279	-11.0046	26.1217	-25.6554
$Ek = 0.1500$	17.7677	-15.9290	24.4554	-23.6201
$Ek = 0.2500$	14.9189	-12.6956	25.7042	-25.1251
$Ek = 0.3500$	11.9444	-9.3218	26.3939	-26.0282

end of table

2.2.7 Analysis of Velocity Profiles

In this subsection, the velocity characteristics of the considered flow are analyzed with respect to a range of governing parameters. The discussion is organized to highlight how variations in time, pressure gradient, Reynolds number, Hartmann number, particle concentration parameter, ion slip parameter, Hall parameter, Ekman number, Coriolis frequency parameter, and particle mass parameter influence both the primary and secondary velocity profiles. Special attention is given to the comparative impact of these parameters, since some exert dominant effects on the flow field while others contribute more subtle modifications. The graphical representation of results is therefore interpreted not only in terms of trends but also in relation to the relative strength of these controlling factors. For each case, the underlying physical mechanisms and forces—such as inertial, viscous, electromagnetic, and rotational effects—are examined to explain the observed trends in the graphical results. This systematic analysis not only clarifies the role of individual parameters but also provides deeper insights into the interplay of fluid inertia, particle dynamics, magnetic field interactions, and rotational influences that collectively govern the behavior of the velocity field.

Figures 2.4 and 2.5 illustrate the variation of primary and secondary velocities in the dusty fluid flow influenced by rotation and a transverse magnetic field. As time progresses from $t = 0.2$ to $t = 0.4$, both velocities increase due to the acceleration provided by the upper plate in motion and the steady pressure gradient along the channel. The velocity profiles exhibit a parabolic shape because fluid particles near the moving plate gain the highest momentum, while those adjacent to the stationary plate remain nearly at rest due to viscous resistance. This causes a smooth gradient in velocity across the channel, characteristic of viscous flow in confined geometries. The increasing gap between the dusty fluid (solid lines) and dust particle (dashed lines) velocities reflects the inertia and drag experienced by particles, causing them to respond more slowly and lag behind the fluid motion. Rotation introduces Coriolis forces that generate the secondary velocity component shown in Figure 2.5, which grows with time as the flow develops further.

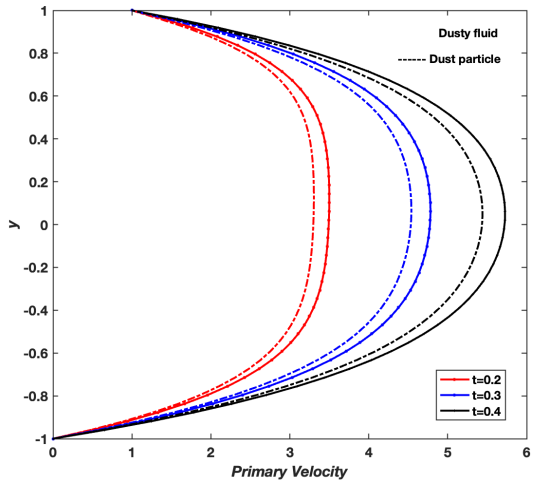

Fig. 2.4 Primary velocity profiles of fluid flow with varying t and with $Ge = 20$, $Re = 2$, $R = 0.5$, $Ek = 0.25$, $Bi = 2$, $Be = 2$, $C = 4\pi(0.4)$, $G = 0.005$, and $Ha^2 = 2$.

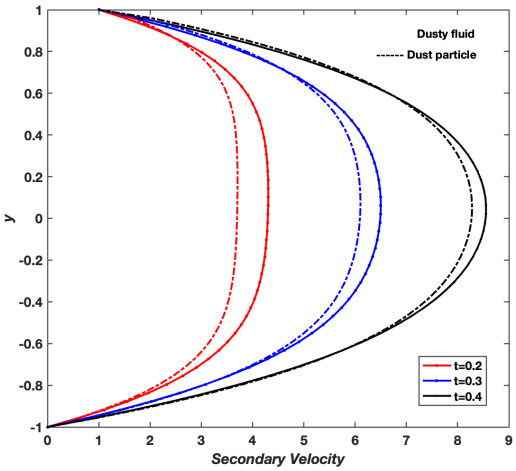

Fig. 2.5 Secondary velocity profiles of fluid flow with varying t and with $Ge = 20$, $Re = 2$, $R = 0.5$, $Ek = 0.25$, $Bi = 2$, $Be = 2$, $C = 4\pi(0.4)$, $G = 0.05$, and $Ha^2 = 2$.

The velocity profiles of the dusty fluid and dust particles, as shown in Figures 2.6 and 2.7, demonstrate a clear dependence on the pressure gradient parameter (Ge). Increasing (Ge) from 10 to 30 intensifies both primary and secondary velocities, reflecting the stronger driving force in the channel. The primary velocity profile becomes more distinctly parabolic due to increased shear near the boundaries, influenced by the upper plate motion and Lorentz force. Concurrently, the secondary velocity, driven by rotational Coriolis effects, also strengthens with (Ge), indicating enhanced cross-flow momentum. A consistent velocity slip between fluid and particles is observed, but this slip reduces as (Ge) increases, suggesting stronger phase coupling under higher pressure gradients. Symmetry of the profiles about the channel centerline remains intact across all Ge values.

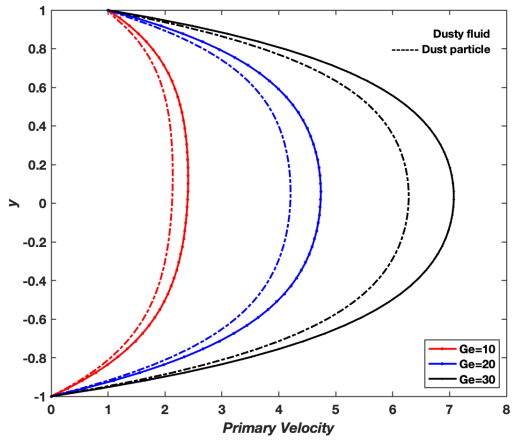

Fig. 2.6 Primary velocity profiles of fluid flow with varying constant pressure Ge and with $t = 0.5$, $Re = 2$, $R = 0.5$, $Ek = 0.25$, $Bi = 2$, $Be = 2$, $C = 4\pi(0.4)$, $G = 0.005$, and $Ha^2 = 2$.

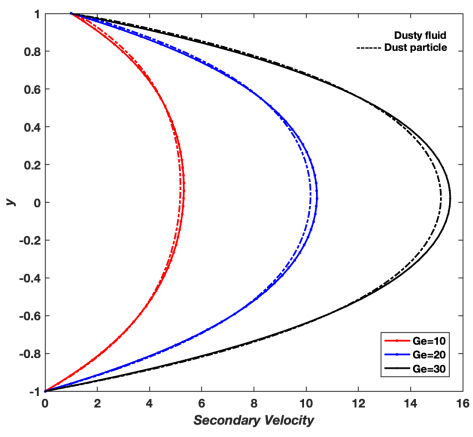

Fig. 2.7 Secondary velocity profiles of fluid flow with varying constant pressure Ge with $t = 0.5$, $Re = 2$, $R = 0.5$, $Ek = 0.25$, $Bi = 2$, $Be = 2$, $C = 4\pi(0.4)$, $G = 0.05$, and $Ha^2 = 2$.

Figures 2.8 and 2.9 show how the Reynolds number (Re) affects the primary and secondary velocity profiles of dusty fluid flow in a rotating horizontal channel. With increasing (Re), the primary velocity profile (Figure 2.8) becomes fuller and reaches a higher peak, as stronger inertial forces overcome viscous resistance, reducing velocity gradients near the walls. Meanwhile, the secondary velocity profile (Figure 2.9), driven by Coriolis forces due to rotation about the y-axis, grows in magnitude with Re, reflecting enhanced transverse circulation and mixing across the channel. The magnetic field induced Lorentz force acts to suppress velocity fluctuations, introducing a mild damping effect on the flow, while the drag interaction between dust particles and fluid moderates momentum transfer, smoothing the velocity distributions.

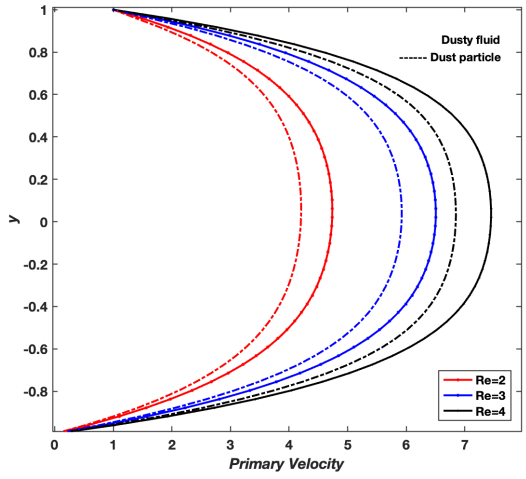

Fig. 2.8 Primary velocity profiles of fluid flow with varying Reynolds number Re and with $t = 0.5$, $R = 0.5$, $Ek = 0.25$, $Bi = 2$, $Be = 2$, $C = 4\pi(0.4)$, $G = 0.005$, and $Ha^2 = 2$.

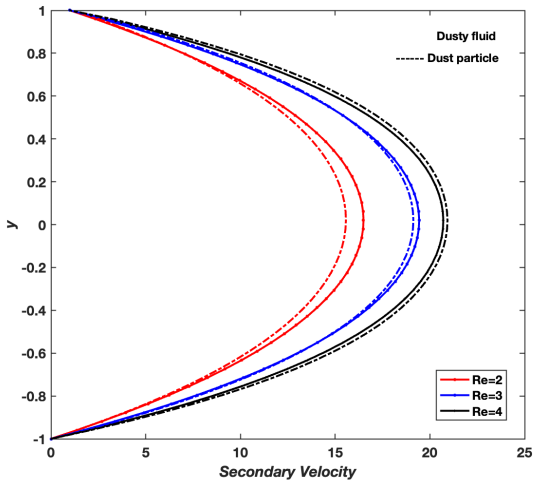

Fig. 2.9 Secondary velocity profiles of fluid flow with varying Reynolds number Re with $Ge = 20$, $t = 0.5$, $R = 0.5$, $Ek = 0.25$, $Bi = 2$, $Be = 2$, $C = 4\pi(0.4)$, $G = 0.05$, and $Ha^2 = 2$.

The velocity profiles in Figures 2.10 and 2.11 show that as the Hartmann number (Ha^2) increases, both primary and secondary velocities of the dusty fluid and dust particles decrease. This is because (Ha^2) measures the strength of the magnetic force compared to viscous forces, and higher values mean a stronger magnetic force that resists the fluid motion. As a result, the flow slows down, with lower peak speeds and weaker secondary flows caused by rotation. The magnetic force smooths out velocity differences in both fluid and particles, reducing mixing and momentum transfer. Therefore, increasing (Ha^2) stabilizes the flow and lowers velocity, demonstrating the strong effect of magnetic fields on this dusty fluid system.

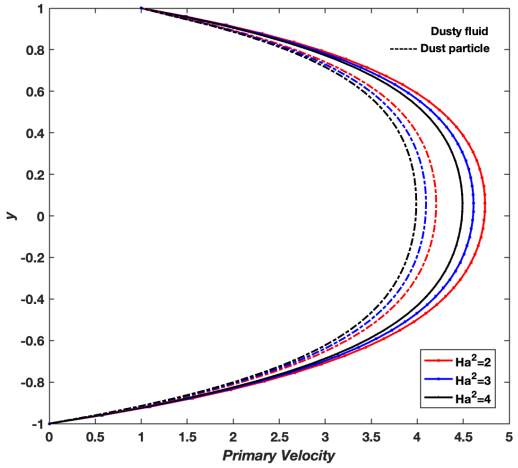

Fig. 2.10 Primary velocity profiles of fluid flow with varying Hartmann number Ha^2 and with $R = 0.5$, $Re = 2$, $t = 0.5$, $Ek = 0.25$, $Bi = 2$, $Be = 2$, $C = 4\pi(0.4)$, and $G = 0.005$.

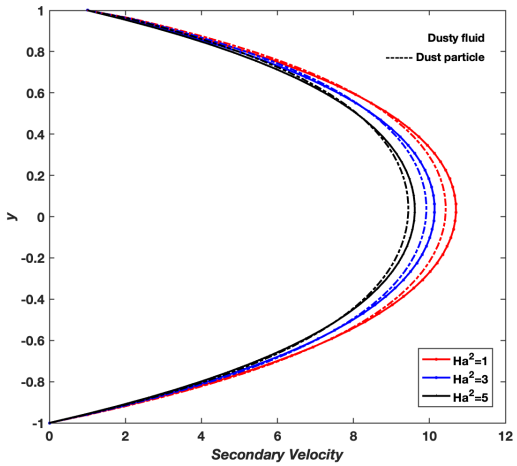

Fig. 2.11 Secondary velocity profiles of fluid flow with varying Hartmann number Ha^2 with $Ge = 20$, $t = 0.5$, $Re = 2$, $R = 0.5$, $Ek = 0.25$, $Bi = 2$, $Be = 2$, $C = 4\pi(0.4)$, and $G = 0.05$.

Figures 2.12 and 2.13 demonstrate that increasing the particle concentration parameter (R) leads to a noticeable decrease in both primary and secondary velocity magnitudes. The zoomed-in sections emphasize this decline, which results from the increased particle concentration raising the effective density and inertia of the mixture. This intensifies the drag force between fluid and particles, resisting fluid motion and reducing momentum transfer. Consequently, both peak velocities and secondary flows driven by rotation weaken. Viscous forces further smooth velocity gradients, while Coriolis forces maintain the secondary flow pattern.

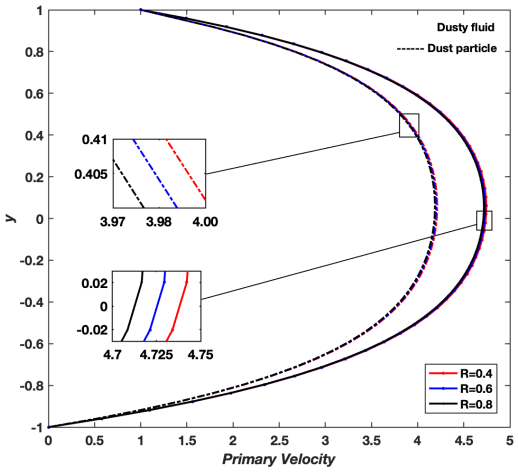

Fig. 2.12 Primary velocity profiles of fluid flow with varying Particle concentration parameter R and with $Re = 2$, $t = 0.5$, $Ek = 0.25$, $Bi = 2$, $Be = 2$, $C = 4\pi(0.4)$, $G = 0.005$, and $Ha^2 = 2$.

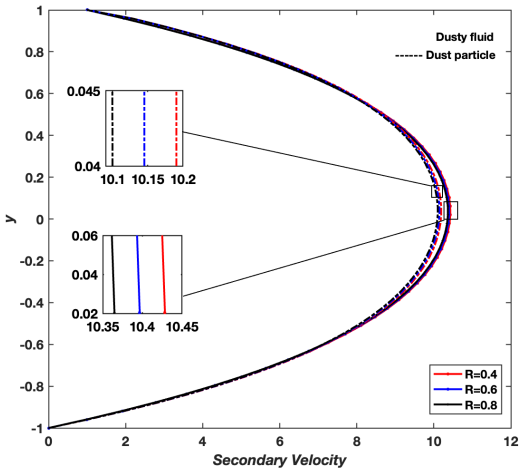

Fig. 2.13 Secondary velocity profiles of fluid flow with varying Particle concentration parameter R with $Be = 2$, $Bi = 2$, $Ek = 0.25$, $C = 4\pi(0.4)$, $Ha^2 = 2$, $Ge = 20$, $t = 0.5$, $Re = 2$, and $G = 0.05$.

Figures 2.14 and 2.15 show that increasing the ion slip parameter (Bi) from 2 to 4 leads to higher primary and secondary velocities for both phases. The ion slip parameter characterizes the relative motion between ions and the neutral fluid under the magnetic field. As (Bi) increases, it effectively reduces the electromagnetic drag exerted by the Lorentz force on the fluid. This reduction in electromagnetic resistance allows the fluid and particles to accelerate more freely, resulting in increased momentum throughout the flow. The enhancement in primary velocity reflects improved fluid transport capacity, while the rise in secondary velocity indicates stronger transverse motions influenced by the altered electromagnetic interaction.

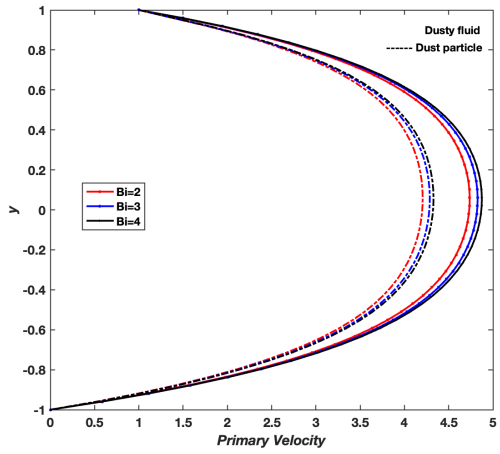

Fig. 2.14 Primary velocity profiles of fluid flow with varying Ion Slip parameter Bi and with $R = 0.5$, $Re = 2$, $t = 0.5$, $Ek = 0.25$, $Be = 2$, $C = 4\pi(0.4)$, $G = 0.005$, and $Ha^2 = 2$.

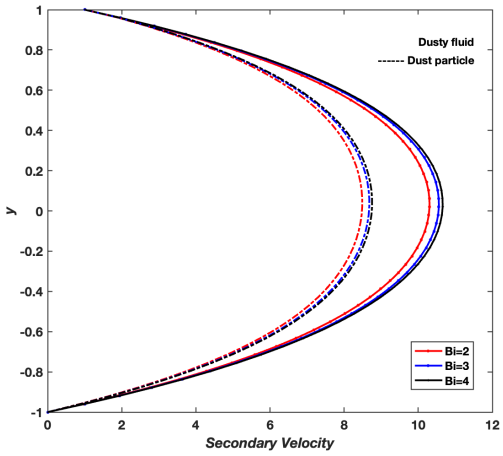

Fig. 2.15 Secondary velocity profiles of fluid flow with varying Ion Slip parameter Bi with $Ek = 0.25$, $C = 4\pi(0.4)$, $Ha^2 = 2$, $Ge = 20$, $t = 0.5$, $Re = 2$, $R = 0.5$, $Be = 2$, and $G = 0.1$.

Figures 2.16 and 2.17 illustrate the effect of varying the Hall parameter (Be) on the primary and secondary velocity profiles. The primary velocity increases notably as (Be) rises from 2 to 3, indicating that moderate enhancement of Hall effects reduces electromagnetic resistance, allowing greater fluid momentum. Although the velocity continues to increase when (Be) changes from 3 to 4, the rate of increase diminishes, suggesting a saturation effect where further strengthening of Hall currents yields diminishing returns in velocity augmentation. Meanwhile, the secondary velocity consistently grows with increasing (Be), reflecting stronger transverse flows driven by the combined electromagnetic and rotational forces.

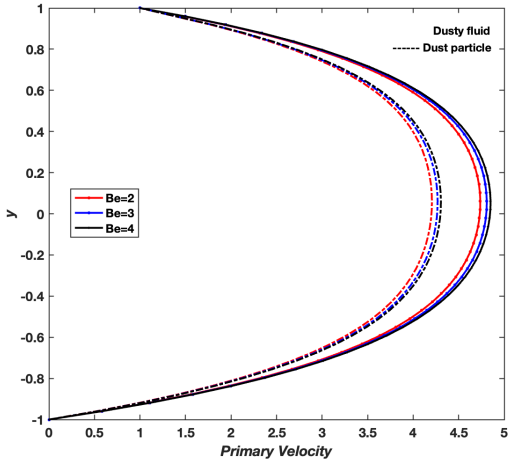

Fig. 2.16 Primary velocity profiles of fluid flow with varying Hall parameter Be and with $R = 0.5$, $Re = 2$, $t = 0.5$, $Ek = 0.25$, $Bi = 2$, $C = 4\pi(0.4)$, $G = 0.005$, and $Ha^2 = 2$.

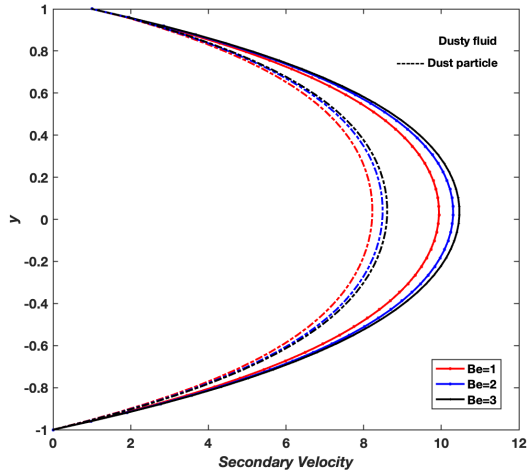

Fig. 2.17 Secondary velocity profiles of fluid flow with varying Hall parameter Be with $Bi = 2$, $Ek = 0.25$, $C = 4\pi(0.4)$, $Ha^2 = 2$, $Ge = 20$, $t = 0.5$, $Re = 2$, $R = 0.5$, and $G = 0.1$.

Figures 2.18 and 2.19 illustrate how variations in the Ekman number (Ek) affect the primary and secondary flow characteristics of both the dusty fluid and particle phases. With increasing Ek, a reduction in the primary velocity is observed, whereas the secondary velocity shows a corresponding rise. The decrease in primary velocity occurs because a higher Ek signifies stronger rotational effects relative to viscous forces, which tend to suppress the flow component aligned with the pressure gradient. Conversely, the increase in secondary velocity reflects the enhanced transverse circulation induced by the intensified Coriolis forces associated with higher rotation rates. This rotational influence redistributes momentum from the primary flow direction into the secondary flow, resulting in the observed trade-off between velocity components.

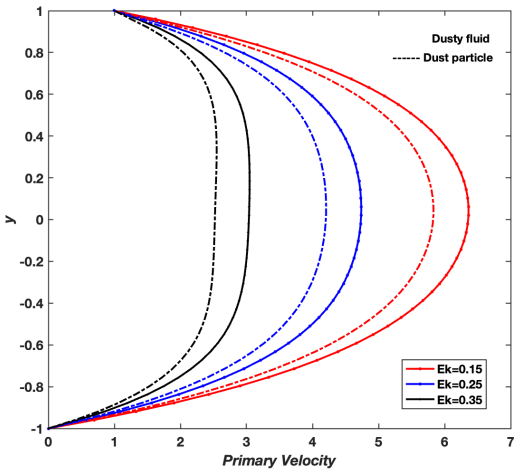

Fig. 2.18 Primary velocity profiles of fluid flow with varying Ekman number Ek and with $R = 0.5$, $Re = 2$, $t = 0.5$, $Bi = 2$, $Be = 2$, $C = 4\pi(0.4)$, $G = 0.005$, and $Ha^2 = 2$.

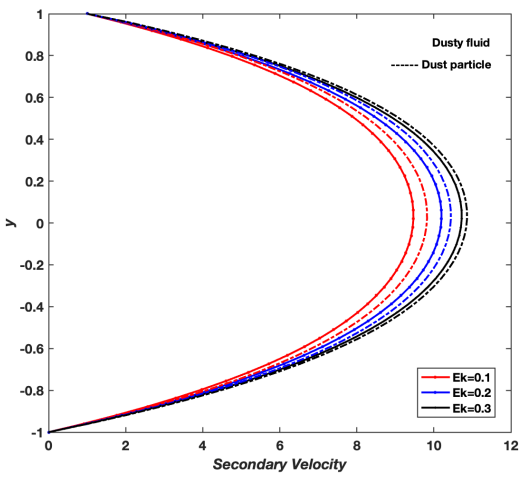

Fig. 2.19 Secondary velocity profiles of fluid flow with varying Ekman number Ek with $C = 4\pi(0.4)$, $Ha^2 = 2$, $Ge = 20$, $t = 0.5$, $Re = 2$, $R = 0.5$, $Bi = 2$, $Be = 2$, and $G = 0.01$.

Figures 2.20 and 2.21 illustrate the effect of increasing the Coriolis frequency parameter (C) on the primary and secondary velocity profiles of dusty fluid and dust particle phases. As (C) increases, the primary velocity decreases while the secondary velocity correspondingly increases. This inverse relationship arises because higher Coriolis frequency intensifies the rotational forces acting perpendicular to the flow direction, which redistributes momentum from the primary flow into the secondary transverse flow. The resulting enhanced secondary circulation causes the characteristic velocity profiles, where the primary flow slows due to this momentum diversion, and the secondary flow strengthens. The lag observed between the dusty fluid and dust particle velocities is attributed to the drag and inertia differences between the phases, with particles responding more slowly to changes in flow conditions.

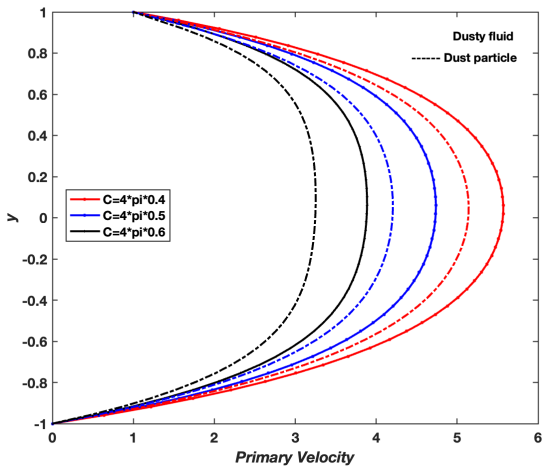

Fig. 2.20 Primary velocity profiles of fluid flow with varying Coriolis frequency parameter C and with $Ek = 0.25$, $R = 0.5$, $Re = 2$, Time $t = 0.5$, $Bi = 2$, $Be = 2$, $G = 0.005$, and $Ha^2 = 2$.

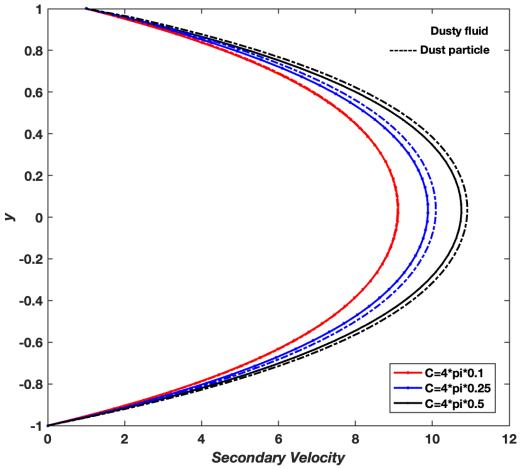

Fig. 2.21 Secondary velocity profiles of fluid flow with varying Coriolis frequency parameter C with $Ha^2 = 2$, $Ge = 20$, Time $t = 0.5$, $Re = 2$, $R = 0.5$, $Ek = 0.25$, $Bi = 2$, $Be = 2$, and $G = 0.02$.

Changes in the particle mass parameter (G) have a notable effect on both the velocity profiles, as shown in Figures 2.22 and 2.23. Increasing (G) leads to higher velocities in both phases for the primary and secondary flow components. This rise is due to the greater inertia from heavier particles, which enhances the overall momentum within the flow. The stronger coupling between fluid and particles facilitates more effective momentum transfer, resulting in increased fluid velocities. Additionally, the increase in secondary velocity indicates intensified transverse circulation driven by enhanced momentum exchange and rotational forces.

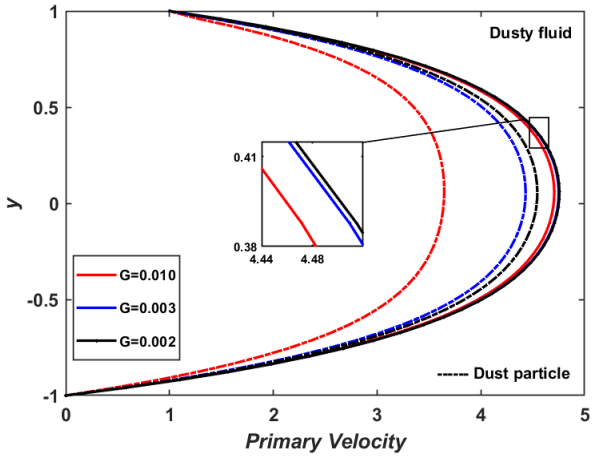

Fig. 2.22 Primary velocity profiles of fluid flow with varying Particle mass parameter G, $Ge = 20$, $t = 0.5$, $Re = 2$, $R = 0.5$, $Ek = 0.25$, $Bi = 2$, $Be = 2$, $C = 4\pi(0.4)$, and $Ha^2 = 2$.

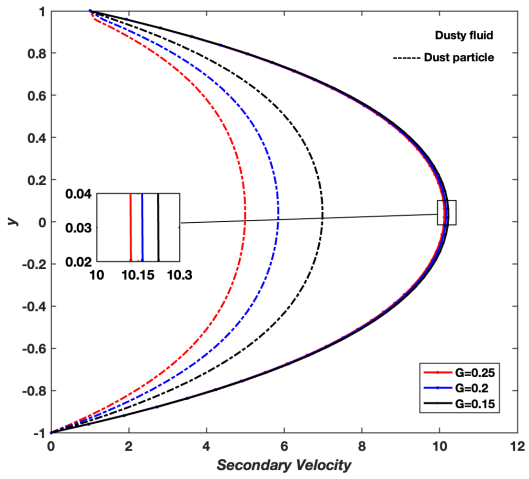

Fig. 2.23 Secondary velocity profiles of fluid flow with varying Particle mass parameter G with $Be = 2$, $Bi = 2$, $Ek = 0.25$, $C = 4\pi(0.4)$, $Ha^2 = 2$, $Ge = 20$, $t = 0.5$, $Re = 2$, and $R = 0.5$.

2.3 Mathematical Modeling of Dusty Fluid Flow in an Inclined Channel

This section develops the mathematical framework for an electrically conducting dusty flow in an *inclined channel* configuration, considering the simultaneous effects of a rotating frame of reference, magnetic fields, and gravitational force acting along the slope (see Figure 2.24). The flow is considered between two infinite, parallel walls, spaced $2L$ apart, and inclined at an angle θ relative to the horizontal. The channel inclination introduces a component of gravitational acceleration acting along the flow direction, significantly impacting the momentum balance and flow behavior.

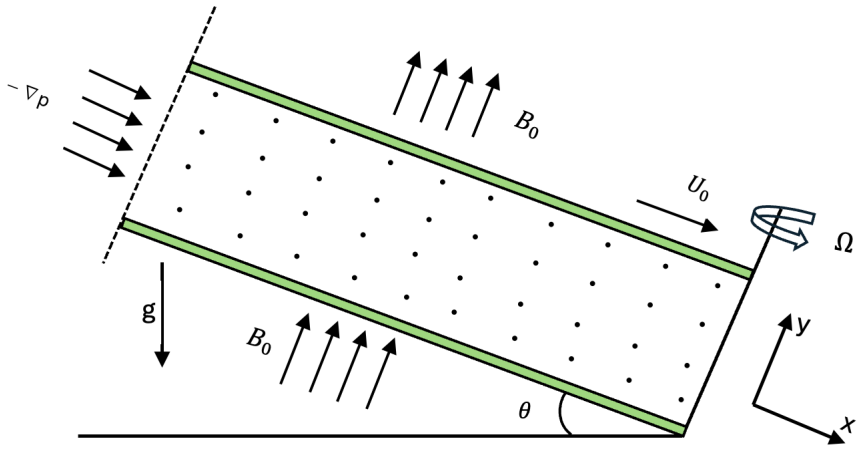

Fig. 2.24 Schematic of an Inclined Channel with Dusty Fluid Flow

2.3.1 Key Features of the Model

(a) **Inclined Channel Geometry:**

(i) The flow domain consists of two infinite parallel plates inclined at an angle θ to the horizontal.

(ii) The flow is unidirectional along the x-axis aligned with the channel incline, driven by the motion of the upper plate and a constant pressure gradient.

(iii) The transverse coordinate y measures the distance perpendicular to the plates, scaled by the half-distance L.

(b) **Dusty Fluid and Particle Phase:**

(i) The fluid is incompressible and electrically conductive, containing uniformly dispersed spherical dust particles.

(ii) Particle temperature uniformity and two-phase interaction effects are incorporated through drag coupling.

(c) **Rotation and Magnetic Field:**

(i) The system undergoes rotation at a fixed angular velocity Ω around the y-axis, explicitly introducing Coriolis effects while embedding centrifugal contributions within the modified pressure term.

(ii) A steady magnetic field B_0 is imposed along the y-direction, generating Lorentz forces that influence the charged fluid.

(d) **Inclination and Gravity Effects:**

(i) Gravitational acceleration $\mathbf{g}$ projects a component $g \sin\theta$ along the inclined channel, acting as a body force influencing both fluid and particle phases.

(ii) This component modifies the momentum equations, necessitating careful inclusion in the model.

(e) **Velocity Field Components:**

(i) The velocity vector of the fluid is $\mathbf{u} = (u_1, 0, u_3)$, representing primary flow along x and secondary flow along z due to rotation-induced Coriolis effects.

(ii) The particle velocity vector is $\mathbf{u}_p = (u_{1p}, 0, u_{3p})$.

2.3.2 Modified Governing Equations

Building on the modified governing equations for dusty fluid flow in a rotating frame under magnetic field effects, as derived earlier in *item (e) of Section 2.2.2* (Equation

(2.6) and (2.7)), the present analysis incorporates the gravitational force component arising from the channel's inclination. This additional body force influences the fluid and particle phases simultaneously, thereby extending the model to incorporate the impact of channel inclination on flow behavior.

The dimensional momentum equations for fluid and particle phases become

$$\rho_f \left(\frac{\partial \mathbf{u}}{\partial t} + 2(\Omega \times \mathbf{u}) + (\mathbf{u} \cdot \nabla)\mathbf{u} \right) = -\nabla P + \mu \nabla^2 \mathbf{u} - K(\mathbf{u} - \mathbf{u}_p) + \mathbf{F}_L + \rho_f \mathbf{g}_\theta \quad (2.25)$$

$$\rho_p \left(\frac{\partial \mathbf{u}_p}{\partial t} + (\mathbf{u}_p \cdot \nabla)\mathbf{u}_p \right) = K(\mathbf{u} - \mathbf{u}_p) + \rho_p \mathbf{g}_\theta \quad (2.26)$$

where $\mathbf{g}_\theta = g \sin\theta \, \mathbf{i}$ is the gravitational acceleration component along the channel incline, and $\mathbf{F}_L$ is the Lorentz force.

Assuming unidirectional flow and neglecting nonlinear convection terms due to laminar conditions, the component-wise momentum equations reduce to:

$$\rho_f \frac{\partial u_1}{\partial t} = -\frac{\partial P}{\partial x} + \mu \frac{\partial^2 u_1}{\partial y^2} - K(u_1 - u_{1p}) + F_{Lx} - 2\rho_f \Omega u_3 + \rho_f g \sin\theta \quad (2.27)$$

$$\rho_f \frac{\partial u_3}{\partial t} = \mu \frac{\partial^2 u_3}{\partial y^2} - K(u_3 - u_{3p}) + F_{Lz} + 2\rho_f \Omega u_1 \quad (2.28)$$

$$\rho_p \frac{\partial u_{1p}}{\partial t} = K(u_1 - u_{1p}) + \rho_p g \sin\theta - C_1 u_{3p} \quad (2.29)$$

$$\rho_p \frac{\partial u_{3p}}{\partial t} = K(u_3 - u_{3p}) + C_1 u_{1p} \quad (2.30)$$

where $C_1 = \rho_p 2\Omega$ is the Coriolis frequency parameter for particles. The Lorentz force components F_{Lx} and F_{Lz} depend on the ion slip and Hall parameters.

(a) **Dimensionless Variables:** Using the characteristic length L (half-distance between plates), velocity scale U_0, and time scale $\frac{L}{U_0}$, define the dimensionless variables as:

$$y^* = \frac{y}{L}, \quad t^* = \frac{tU_0}{L}, \quad u_1^* = \frac{u_1}{U_0}, \quad u_3^* = \frac{u_3}{U_0}, \quad u_{1p}^* = \frac{u_{1p}}{U_0}, \quad u_{3p}^* = \frac{u_{3p}}{U_0} \quad (2.31)$$

The gravitational acceleration component acting along the inclined channel is

scaled relative to the characteristic inertial forces in the flow, introducing the dimensionless parameter

$$F = \frac{U_0^2}{gL}, \tag{2.32}$$

For brevity, the asterisks denoting dimensionless variables are omitted in subsequent expressions.

(b) **Initial and Boundary Conditions:**

The initial and boundary conditions applied are:

- Initial conditions at $t = 0$:

$$u_1(y,0) = u_3(y,0) = u_{1p}(y,0) = u_{3p}(y,0) = 0$$

- Boundary conditions at the plates $y = \pm 1$ (for all $t > 0$) :

$$u_1(-1,t) = u_{1p}(-1,t) = 0, \quad u_3(-1,t) = u_{3p}(-1,t) = 0,$$

$$u_1(1,t) = u_{1p}(1,t) = 1, \quad u_3(1,t) = u_{3p}(1,t) = 1$$

(c) **Dimensionless Governing Equations:**

After non-dimensionalization and simplification, the system of partial differential equations governing dusty fluid flow in a rotating frame under an applied magnetic field takes the form:

$$\frac{\partial u_1}{\partial t} = Ge(t) + \frac{1}{Re}\frac{\partial^2 u_1}{\partial y^2} - \frac{Ha^2}{Re}\left(\frac{(1 + Bi\,Be)u_1 + Be\,u_3}{(1 + Bi\,Be)^2 + Be^2}\right) - \frac{R}{Re}(u_1 - u_{1p}) - \frac{2CEk}{Re}u_3 + \frac{\sin\theta}{F} \tag{2.33}$$

$$\frac{\partial u_3}{\partial t} = \frac{1}{Re}\frac{\partial^2 u_3}{\partial y^2} - \frac{Ha^2}{Re}\left(\frac{(1 + Bi\,Be)u_3 + Be\,u_1}{(1 + Bi\,Be)^2 + Be^2}\right) - \frac{R}{Re}(u_3 - u_{3p}) + \frac{2CEk}{Re}u_1 \tag{2.34}$$

$$\frac{\partial u_{1p}}{\partial t} = \frac{1}{G}(u_1 - u_{1p}) - \frac{C}{2\pi}u_{3p} + \frac{\sin\theta}{F} \tag{2.35}$$

$$\frac{\partial u_{3p}}{\partial t} = \frac{1}{G}(u_3 - u_{3p}) + \frac{C}{2\pi}u_{1p} \tag{2.36}$$

The dimensionless parameters Re, Ha^2, R, Bi, and Be are as defined in the previous chapter (refer *Section 1.9*).

2.3.3 Numerical Solution using Radial Basis Function Pseudospectral Method

The dimensionless system of PDEs describing the motion of a dusty fluid in a rotating frame under an applied magnetic field, as given by equations (2.33) to (2.36), can be efficiently solved using the RBF-PSM. The approach follows the numerical framework established in *Section 2.2.3* for the earlier set of governing equations (2.9) to (2.12), which is based on the methodology outlined in *Chapter 1*, *Section 1.10*, and particularly the RBF-PSM detailed in *Section 1.10.7*, thereby leveraging the advantages of meshfree global approximations and spectral accuracy inherent to RBF-PSM.

Initially, the spatial domain $y \in [-1, 1]$ is discretized into N scattered node points $\{y_i\}_{i=1}^{N}$, consistent with the discretization strategy described in *Section 2.2.3*. The solution variables $u_1(y,t), u_3(y,t), u_{1p}(y,t), u_{3p}(y,t)$ are approximated as linear combinations of selected radial basis functions ϕ, centered at these nodes, such that

$$z(y,t) \approx \sum_{j=1}^{N} \lambda_j(t)\, \phi(\|y - y_j\|), \tag{2.37}$$

where $\lambda_j(t)$ are the time-dependent interpolation coefficients and ϕ is chosen as the Wendland radial basis function for its desirable smoothness and compact support properties (see Equation (2.13)).

Differentiation matrices corresponding to first and second spatial derivatives are con-

structed by evaluating the derivatives of ϕ at the nodes, resulting in

$$D_1 = D_x A^{-1}, \quad D_2 = D_{xx} A^{-1}, \tag{2.38}$$

where A is the interpolation matrix with entries $A_{ij} = \phi(\|y_i - y_j\|)$, and D_x, D_{xx} contain the first and second derivatives of ϕ with respect to the spatial variable y evaluated at the nodes (refer to Equation (1.105) in *Section 1.10.7*).

By substituting these differentiation matrices into the dimensionless governing equations (2.33) to (2.36), the system is transformed into a set of coupled ordinary differential equations in time:

$$\begin{aligned}\frac{du_1}{dt} &= Ge(t) + \frac{1}{Re} D_2 u_1 - \frac{Ha^2}{Re} \frac{(1 + Bi\, Be)u_1 + Be\, u_3}{(1 + Bi\, Be)^2 + Be^2} \\ &\quad - \frac{R}{Re}(u_1 - u_{1p}) - \frac{2CEk}{Re} u_3 + \frac{\sin\theta}{F}\end{aligned} \tag{2.39}$$

$$\begin{aligned}\frac{du_3}{dt} &= \frac{1}{Re} D_2 u_3 - \frac{Ha^2}{Re} \frac{(1 + Bi\, Be)u_3 + Be\, u_1}{(1 + Bi\, Be)^2 + Be^2} - \frac{R}{Re}(u_3 - u_{3p}) \\ &\quad + \frac{2CEk}{Re} u_1\end{aligned} \tag{2.40}$$

$$\frac{du_{1p}}{dt} = \frac{1}{G}(u_1 - u_{1p}) - \frac{C}{2\pi} u_{3p} + \frac{\sin\theta}{F} \tag{2.41}$$

$$\frac{du_{3p}}{dt} = \frac{1}{G}(u_3 - u_{3p}) + \frac{C}{2\pi} u_{1p} \tag{2.42}$$

Here, the velocity vectors u_1, u_3, u_{1p}, u_{3p} represent the values at the discrete node points, and the differentiation matrices D_1, D_2 operate on these vectors to approximate spatial derivatives. The dimensionless parameters $Re, Ha, R, Bi, Be, C, Ek, G, F$ and the forcing term $Ge(t)$ retain the definitions provided in *Section 1.9*.

The resulting system of ordinary differential equations is advanced in time using the SSP RK43. This integration technique, outlined in *Section 2.2.3*, provides robust stability and precision for capturing transient behaviors, while ensuring that boundary conditions are rigorously applied at each temporal iteration.

2.3.4 Pumping Power Analysis

Pumping power quantifies the mechanical energy required to maintain fluid flow against pressure losses, indicating the efficiency of fluid transport systems. This concept has been introduced and discussed in detail in *Chapter 1 (Section 1.8)*.

For the present study, a crude oil density of $\rho_f = 847\, kg/m^3$ is adopted, consistent with values reported in existing literature [124].

Table 2.3 presents the variation of pumping power with changes in key parameters, including time (t), Reynolds number (Re), rotation parameter (R), Ekman number (Ek), Hartmann number (Ha^2), inclination angle (θ), etc. It is noted that time (t) and inclination angle θ have the most substantial impact on pumping power, with both leading to higher energy requirements due to increased flow resistance over time and greater gravitational opposition, respectively. The Reynolds number (Re) also plays a key role in reducing pumping power as fluid inertia increases, whereas parameters like Bi, Be, R, Ek, and Ha^2 exhibit relatively minor effects, contributing to more stable flow conditions in MHD flows. The Reynolds number shows a strong inverse relationship with pumping power. Higher Reynolds numbers indicate more inertia-dominated flow, reducing the relative impact of viscous forces. As a result, the fluid flows more easily, requiring less energy to be maintained. In essence, higher Re values correspond to more efficient flow, which is reflected in the reduced pumping power. The table clearly shows that the pumping power is strongly influenced by the inclination angle θ. When the channel is more steeply inclined, the gravitational force acting against the flow intensifies, significantly increasing the resistance and thereby requiring much more energy to maintain the fluid flow when no external pressure is applied to the flow.

Table 2.3: Pumping Power for Various Parameter Values

Parameter	**Pumping Power**	**Parameter**	**Pumping Power**
$t = 0.001$	1.395993364	$Bi = 1$	48.26186901
$t = 0.003$	13.95436541	$Bi = 2$	48.28303389
$t = 0.005$	48.28303389	$Bi = 3$	48.29670748

continued on next page

Table 2.3: Pumping power with different parameters

Parameter	**Pumping Power**	**Parameter**	**Pumping Power**
$t = 0.007$	113.4424066	$Bi = 4$	48.30537511
$t = 0.009$	217.6900698	$Bi = 5$	48.31121725
$Re = 1$	113.0388464	$Be = 1$	48.24219902
$Re = 2$	48.28303389	$Be = 2$	48.28303389
$Re = 3$	29.96813288	$Be = 3$	48.29976454
$Re = 4$	21.54448406	$Be = 4$	48.30883576
$Re = 5$	16.75328849	$Be = 5$	48.31452163
$R = 0.1$	48.2890299	$Ek = 0.15$	48.30600489
$R = 0.5$	48.28303389	$Ek = 0.25$	48.28303389
$R = 1.0$	48.27554489	$Ek = 0.35$	48.25966414
$R = 1.5$	48.26806257	$Ek = 0.45$	48.23589616
$R = 2.0$	48.26058693	$Ek = 0.55$	48.21173044
$Ha = 1$	48.31112483	$\theta = \left(\frac{\pi}{180}\right) \times 0.001$	5.582753047
$Ha = 2$	48.28303389	$\theta = \left(\frac{\pi}{180}\right) \times 0.002$	19.85136742
$Ha = 3$	48.25496336	$\theta = \left(\frac{\pi}{180}\right) \times 0.003$	48.28303389
$Ha = 4$	48.22691323	$\theta = \left(\frac{\pi}{180}\right) \times 0.004$	95.76162629
$Ha = 5$	48.19888348	$\theta = \left(\frac{\pi}{180}\right) \times 0.005$	167.1710184

end of table

2.3.5 Stability Analysis

The evaluation of numerical method stability is a crucial aspect of computational analysis, as it ensures the reliability of results and prevents divergence in solutions. This study adopts a matrix-based stability analysis, a widely recognized approach in numerical linear algebra, to assess the robustness of the proposed numerical method for solving differential equations. The methodology involves representing the numerical solution in terms of its linear difference equation, constructing the associated matrix, and ana-

lyzing its eigenvalues. According to the stability criterion, stability is ensured when all eigenvalues possess negative real parts, signifying that numerical disturbances diminish with time.

Stability tests were performed for discretization levels of $N = 30$ and $N = 50$. For $N = 30$, the eigenvalues lie on the left side of the complex plane, indicating negative real parts with very small imaginary components, as can be observed from Figure 2.25. This indicates strong stability. Similarly, for $N = 50$, the eigenvalues continue to exhibit strictly negative real parts with no imaginary contributions, as depicted in Figure 2.26. The consistent negativity of the real parts across both cases confirms that the numerical method remains stable even as the number of node points increases. This uniform behavior across different levels of discretization demonstrates the robustness and reliability of the proposed numerical approach.

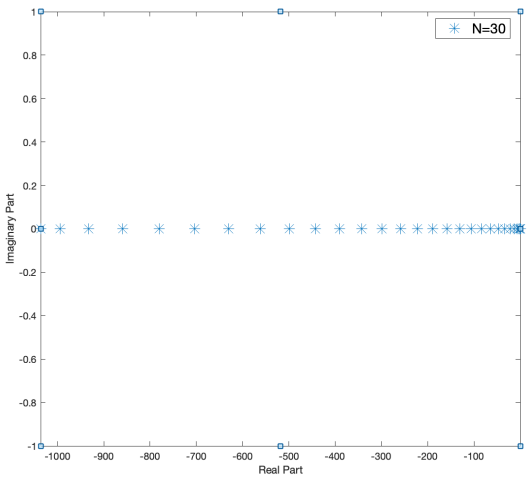

Fig. 2.25 Stability diagram derived through eigenvalue analysis of the associated matrix for $N = 30$

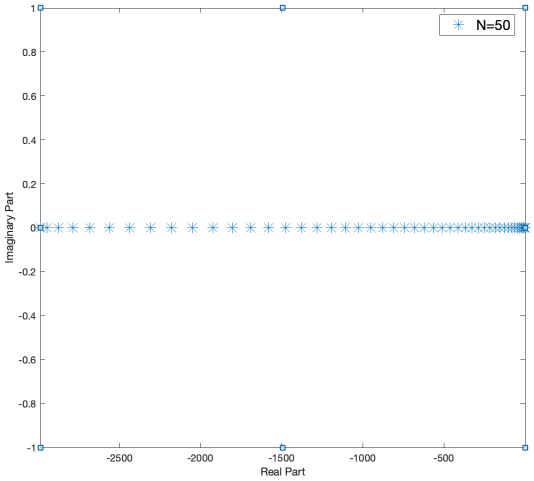

Fig. 2.26 Stability diagram derived through eigenvalue analysis of the associated matrix for $N = 50$

2.3.6 Analysis of Velocity Profiles

The velocity profiles are analyzed with respect to key governing parameters, including time, pressure gradient, Reynolds number, Hartmann number, particle concentration parameter, ion slip parameter, Hall parameter, Ekman number, Coriolis frequency parameter, particle mass parameter, and inclination angle. The discussion highlights how variations in these parameters influence the flow characteristics and the physical mechanisms responsible for the resulting velocity distributions.

The velocity profiles of a dusty fluid and dust particles suspended in it are shown in Figures 2.27 and 2.28 for primary and secondary velocity at various time points ($t = 0.3, 0.5,$ and 0.7). Both profiles exhibit a parabolic shape. Laminar flow between parallel plates is characterized by this, the velocity is highest at the center ($y = 0$) and decreases towards the walls. The fluid and particle velocity profiles alter as time increases (from $t = 0.3$ to $t = 0.7$). The velocity lag gradually decreases as the overall velocity magnitude increases. This implies that the particles are catching up to the fluid flow by gradually accelerating.

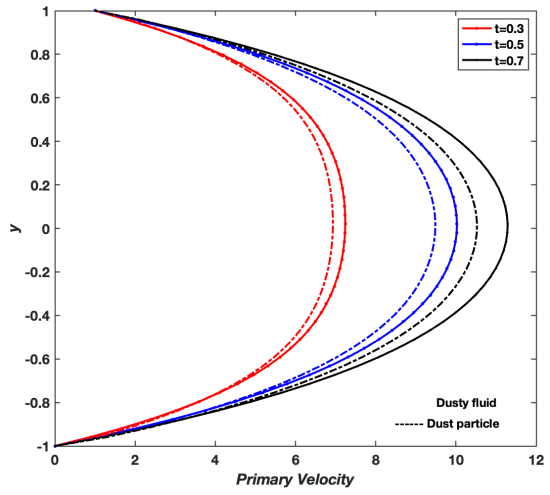

Fig. 2.27 Primary velocity profiles of fluid flow with varying time t, Ge= 5, G= 0.01, Re= 2, R= 1, $Ha^2 = 2$, Bi= 2, Be= 2, C= $4 * \pi * 0.5$, Ek= 0.25, $\theta = (\pi/180) * 0.0025$

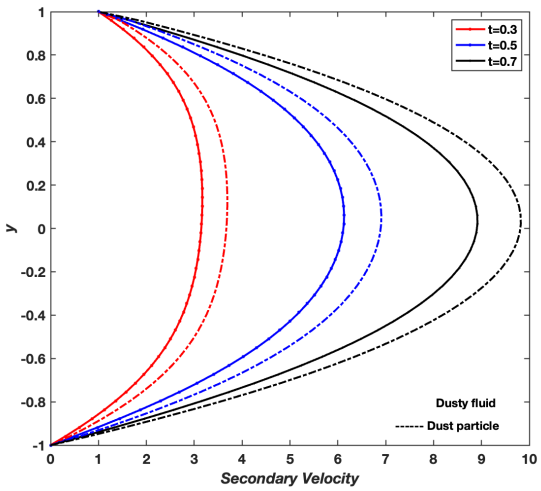

Fig. 2.28 Secondary velocity profiles of fluid flow with varying time t, Ge= 5, G= 0.01, Re= 2, R= 1, $Ha^2 = 2$, Bi= 2, Be= 2, C= $4 * \pi * 0.5$, Ek= 0.25, $\theta = (\pi/180) * 0.0025$

Reynolds number (Re) provides a dimensionless comparison of inertial and viscous forces, enabling prediction of flow patterns in fluids experiencing motion. A flow's likelihood of being laminar—smooth and orderly—or turbulent—chaotic and fluctuating—is determined in part by the Reynolds number. The primary and secondary velocity profiles for dusty fluid (solid lines) and dust particles (dashed lines) under various Reynolds numbers ($Re = 1, 1.5,$ and 2) while holding other parameters constant are shown in Figures 2.29 and 2.30. when it comes to primary velocity the principal velocity profiles steepen as the Reynolds number rises from $Re = 1$ to $Re = 2$. These observations imply increased shear forces and momentum transfer at the walls, sharper velocity gradients, elevated flow energy, and the possibility of turbulence. In the case of secondary velocity, the gap between the fluid and dust phase tends to widen slightly as the Reynolds number grows. Both the dusty fluid and the suspended particles exhibit a parabolic profile in their primary and secondary velocities.

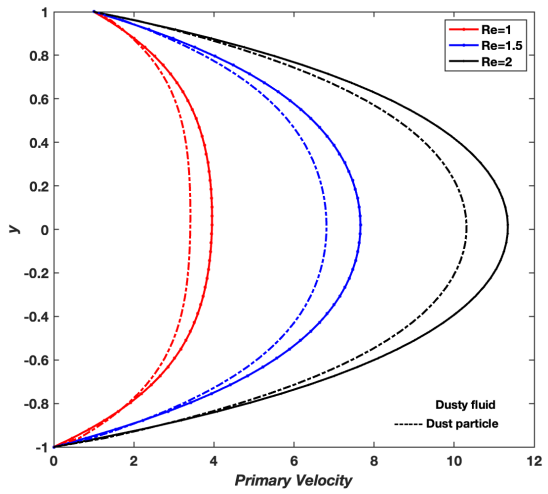

Fig. 2.29 Primary velocity profiles of fluid flow with varying Reynolds number Re, t= 1, Ge= 5, G= 0.01, Re= 2, R= 1, $Ha^2 = 2$, Bi= 2, Be= 2, C= $4{*}\pi{*}0.5$, Ek= 0.25, $\theta = (\pi/180) * 0.0025$

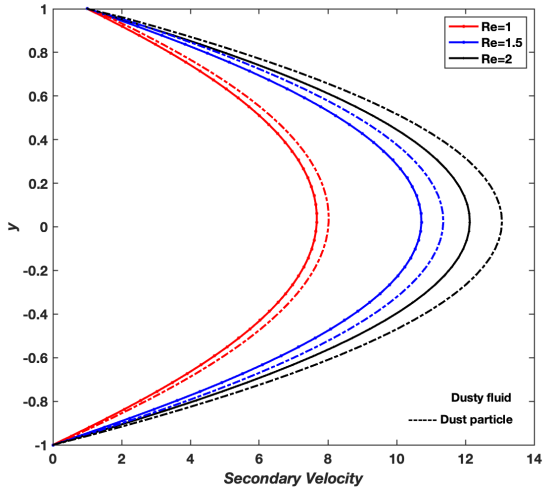

Fig. 2.30 Secondary velocity profiles of fluid flow with varying Reynolds number Re, t= 1, Ge= 5, G= 0.01, R= 1, $Ha^2 = 2$, Bi= 2, Be= 2, C= $4 * \pi * 0.5$, Ek= 0.25, $\theta = (\pi/180) * 0.0025$

The particle concentration parameter (R) is used in the analysis of dusty fluid flows to quantify the proportion of solid particles within the fluid. It is defined as the mass concentration of particles divided by the mass concentration of the fluid. The particle concentration parameter quantifies the amount of particles "loaded" into the fluid. Higher (R) values signify an increased proportion of particles in the fluid, whereas lower values reflect a reduced concentration. Figures 2.31 and 2.32 illustrate the primary and secondary velocity profiles for dusty fluid (solid lines) and dust particles (dashed lines) under different values of (R). As (R) increases, the inertia of the dust-fluid mixture increases. In the primary flow direction (x-axis), more dust particles mean the fluid has to carry more mass, which resists motion due to inertia. This reduces the net primary velocity of both the fluid and dust particles.

However, in the secondary direction (z-axis), which is induced by rotational effects, the dust particles add extra rotational inertia, leading to enhanced Coriolis-driven flow. Hence, secondary velocity increases.

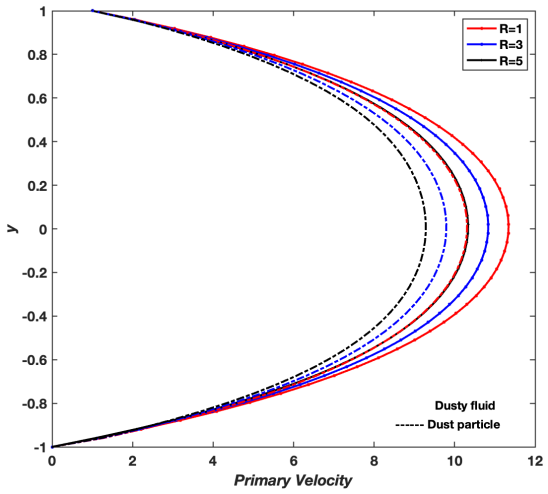

Fig. 2.31 Primary velocity profiles of fluid flow with varying particle concentration parameter R, t= 1, Ge= 5, G= 0.01, $Ha^2 = 2$, Bi= 2, Be= 2, C= $4 * \pi * 0.5$, Ek= 0.25, $\theta = (\pi/180) * 0.0025$

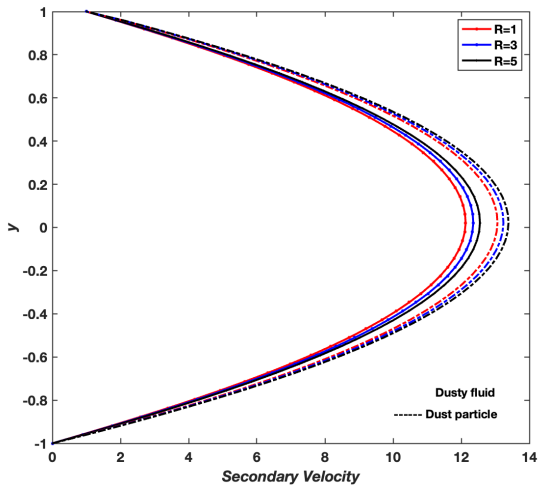

Fig. 2.32 Secondary velocity profiles of fluid flow with varying particle concentration parameter R, t= 1, Ge= 5, G= 0.01, $Ha^2 = 2$, Bi= 2, Be= 2, C= $4 * \pi * 0.5$, Ek= 0.25, $\theta = (\pi/180) * 0.0025$

Figure 2.33 shows the primary velocity profiles of the dusty fluid and particles when subjected to a magnetic field. Due to the flow characteristics, the resulting profiles exhibit a parabolic pattern. As shown in Figure 2.33, the primary velocity profiles decrease with increasing Hartmann number (Ha^2) due to the enhanced Lorentz force, which strongly resists the pressure-driven flow, thereby reducing the motion of both the fluid and dust particles. Similarly, Figure 2.34 illustrates that the secondary velocity also decreases as (Ha^2) increases, though to a lesser extent. This is because the magnetic field suppresses the rotationally induced secondary flow by damping the transverse velocity components. Overall, the increasing (Ha^2) highlights the dominance of electromagnetic damping over viscous and inertial forces in the flow field.

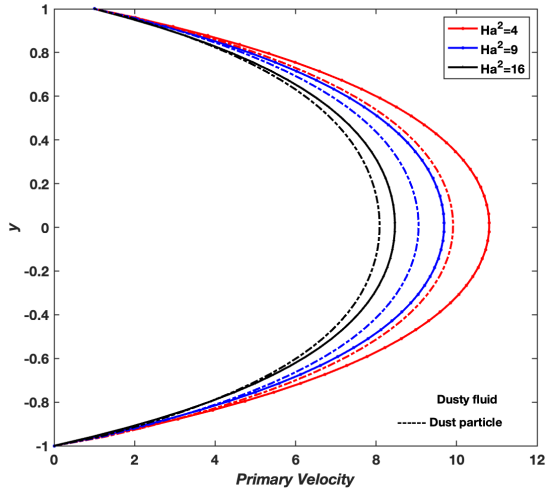

Fig. 2.33 Primary velocity profiles of fluid flow with varying Hartmann Number Ha^2, t= 1, Re= 2, Ge= 5, G= 0.01, R= 1, Bi= 2, Be= 2, C= $4 * \pi * 0.5$, Ek= 0.25, $\theta = (\pi/180) * 0.0025$

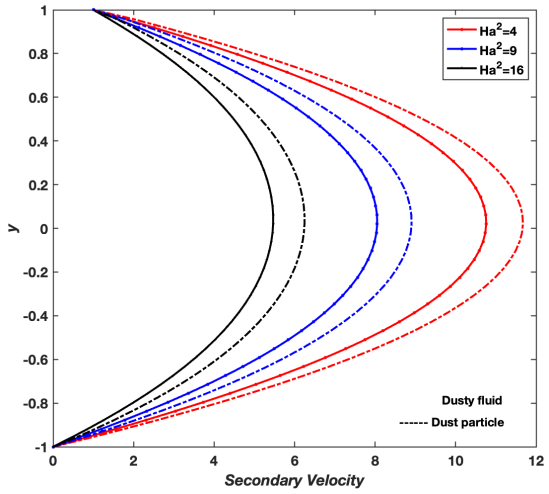

Fig. 2.34 Secondary velocity profiles of fluid flow with varying hall parameter Ha^2, t= 1, Re= 2, Ge= 5, G= 0.01, R= 1, Bi= 2, Be= 2, C= $4 * \pi * 0.5$, Ek= 0.25, $\theta = (\pi/180) * 0.0025$

The ion slip parameter (Bi) quantifies the relative significance of ion-neutral collisions compared to ion-electron collisions in a partially ionized plasma. As depicted in Figure 2.35 and Figure 2.36, both primary and secondary velocity profiles increase with rising ion slip parameter (Bi). This trend is primarily due to the weakening of the Lorentz force caused by enhanced ion slip, which reduces the electromagnetic resistance opposing fluid motion. With reduced magnetic damping, the fluid flows more freely, resulting in higher velocities in both directions. Additionally, the decreased opposition allows for more efficient momentum transfer from the fluid to the dust particles, leading to a noticeable rise in particle velocities. In the secondary flow, the Coriolis force becomes more effective as the electromagnetic suppression weakens, further contributing to the increase in velocity. Hence, higher ion slip facilitates enhanced motion by mitigating magnetic field effects.

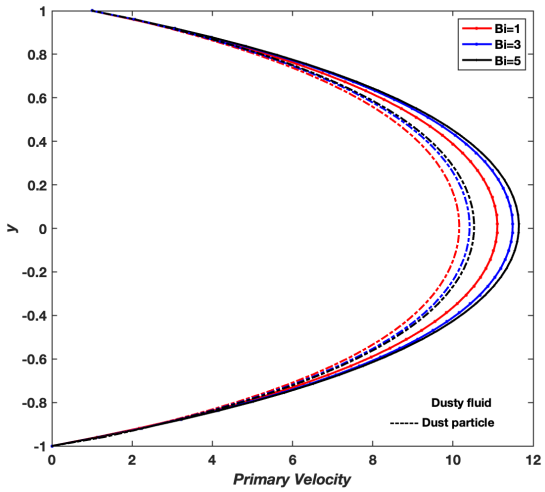

Fig. 2.35 Primary velocity profiles of fluid flow with Ion Slip parameter Bi, t= 1, Re= 2, Ge= 5, G= 0.01, R= 1, $Ha^2 = 2$, Be= 2, C= $4 * \pi * 0.5$, Ek= 0.25, $\theta = (\pi/180) * 0.0025$

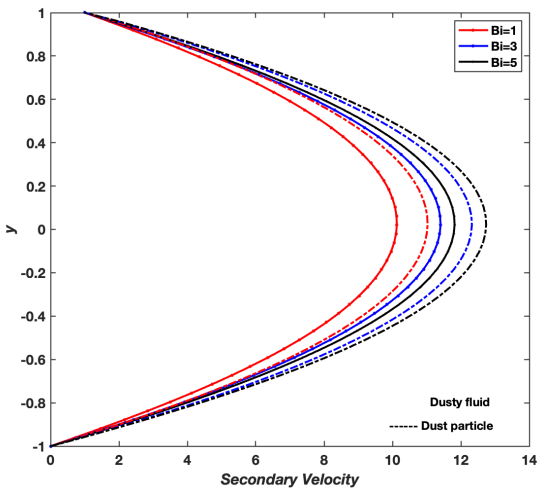

Fig. 2.36 Secondary velocity profiles of fluid flow with Ion Slip parameter Bi, t= 1, Re= 2, Ge= 5, G= 0.01, R= 1, $Ha^2 = 2$, Be= 2, C= $4 * \pi * 0.5$, Ek= 0.25, $\theta = (\pi/180) * 0.0025$

The dimensionless hall parameter, commonly represented as (Be), describes the intensity of the Hall effect in a conducting fluid or plasma. A crucial quantity in MHD, the study of the interaction of magnetic fields with electrically conducting fluids, is the Hall parameter. As illustrated in Figure 2.37 and Figure 2.38, both primary and secondary velocity profiles increase with the Hall parameter (Be), with a more significant rise observed in the secondary direction. This is because the Hall effect modifies the electromagnetic force by introducing a cross-field component, which alters the direction of the Lorentz force and reduces its retarding effect on the flow. Consequently, the fluid experiences less magnetic resistance, allowing for greater velocity development. In the secondary flow, the Hall-induced cross currents enhance the rotational motion, leading to stronger velocity profiles. Additionally, the improved momentum transfer between fluid and dust particles further contributes to the rise in their velocities. Thus, increasing Be supports enhanced flow in both directions by weakening magnetic damping and introducing favourable drift effects.

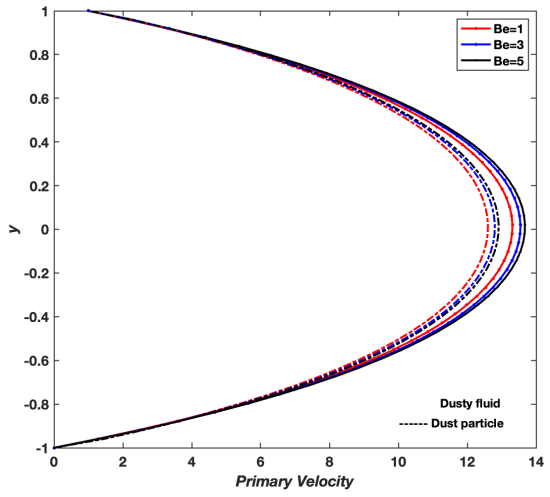

Fig. 2.37 Primary velocity profiles of fluid flow with Hall parameter Be, t= 1, Re= 2, Ge= 5, G= 0.01, R= 1, Ha^2 = 2, Bi= 2, C= $4 * \pi * 0.5$, Ek= 0.25, $\theta = (\pi/180) * 0.0025$

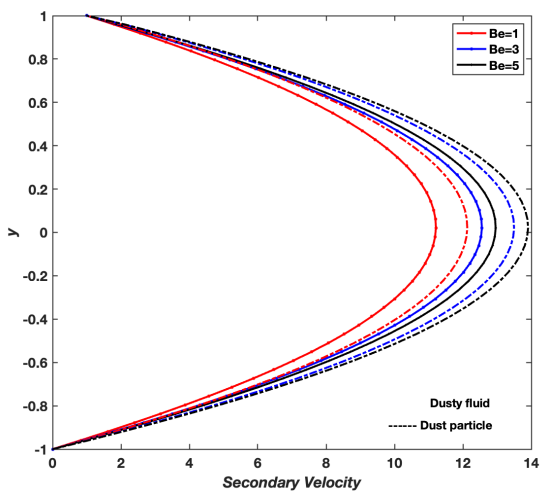

Fig. 2.38 Secondary velocity profiles of fluid flow with Hall parameter Be, t= 1, Re= 2, Ge= 5, G= 0.01, R= 1, Ha^2 = 2, Bi= 2, C= $4 * \pi * 0.5$, Ek= 0.25, $\theta = (\pi/180) * 0.0025$

In fluid dynamics, the Coriolis frequency parameter (C) plays a crucial role in determining the influence of rotational effects on fluid motion. It quantifies the strength of the Coriolis force, which depends on the system's rotation and is particularly significant in geophysical and astrophysical flows. Figure 2.39 and Figure 2.40 shows that, increasing the Coriolis frequency parameter (C) leads to a reduction in primary velocity and an enhancement in secondary velocity. This occurs due to the Coriolis force, which acts perpendicular to the direction of fluid motion and deflects the flow from the primary direction (x-axis) to the secondary direction (z-axis). As a result, the fluid experiences a loss of momentum in the primary direction and a corresponding increase in velocity in the secondary direction. The rotational influence grows stronger with increasing C, leading to an enhancement of the secondary circulation. Additionally, this cross-flow movement enhances the momentum exchange between the fluid and dust particles, contributing to increased velocities in the secondary profile. Hence, the Coriolis force significantly reshapes the flow dynamics in rotating systems.

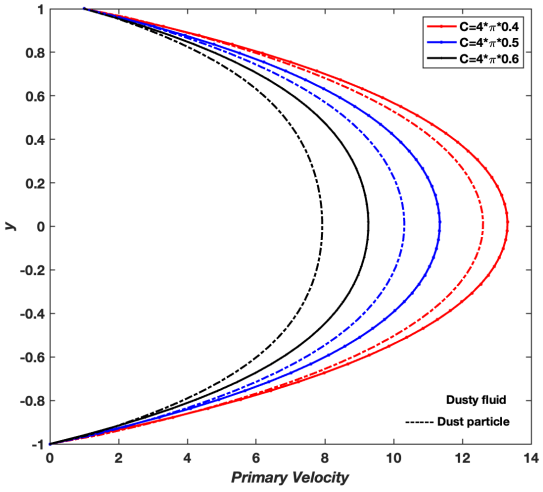

Fig. 2.39 Primary velocity profiles of fluid flow with Coriolis frequency parameter C, t= 1, Re= 2, Ge= 5, G= 0.01, R= 1, Ha^2 = 2, Bi= 2, Be= 2, Ek= 0.25, $\theta = (\pi/180) * 0.0025$

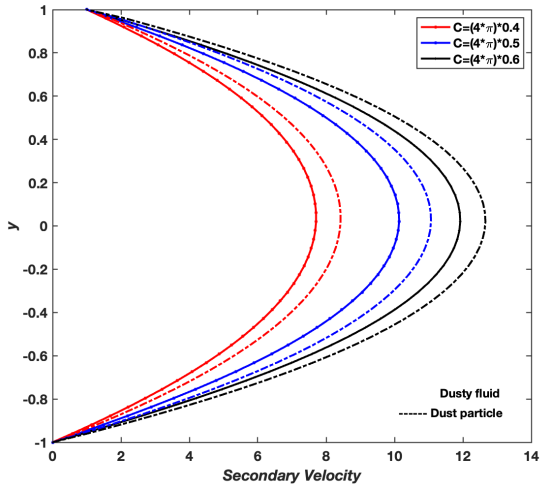

Fig. 2.40 Secondary velocity profiles of fluid flow with Coriolis frequency parameter C, t= 1, Re= 2, Ge= 5, G= 0.01, R= 1, Ha^2 = 2, Bi= 2, Be= 2, Ek= 0.25, $\theta = (\pi/180) * 0.0025$

Ekman number (Ek) is commonly used to describe flow characteristics influenced by planetary rotation, particularly in geophysical processes such as atmospheric and oceanic dynamics. Figures 2.41 and 2.42 illustrate the influence of the Ekman number Ek on the velocity profiles. As (Ek) increases, the primary velocity (Figure 2.41) decreases significantly due to the dominance of viscous forces, which resist fluid motion and dampen the primary flow. Conversely, the secondary velocity (Figure 2.42) increases with (Ek), indicating that reduced Coriolis effects allow greater lateral movement of the fluid. The higher viscosity associated with large Ekman numbers redistributes momentum, facilitating more uniform velocity gradients and promoting cross-flow motion. The dusty particles follow a similar trend due to stronger viscous coupling, reducing their axial velocity but increasing their secondary drift. Thus, the Ekman number plays a key role in modulating the balance between viscous damping and rotational dynamics.

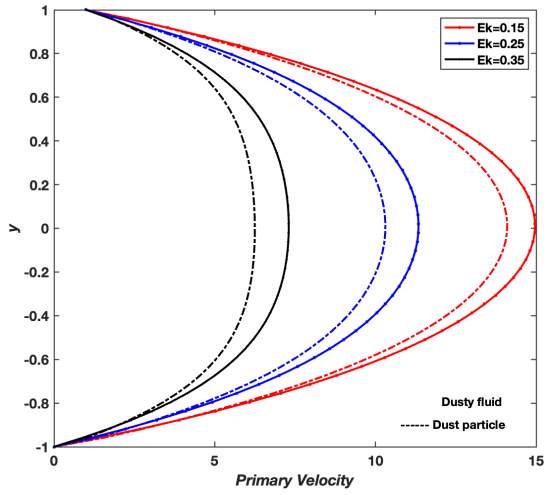

Fig. 2.41 Primary velocity profiles of fluid flow with Ekman number Ek, t= 1, Re= 2, Ge= 5, G= 0.01, R= 1, $Ha^2 = 2$, Bi= 2, Be= 2, C= $4 * \pi * 0.5$, $\theta = (\pi/180) * 0.0025$

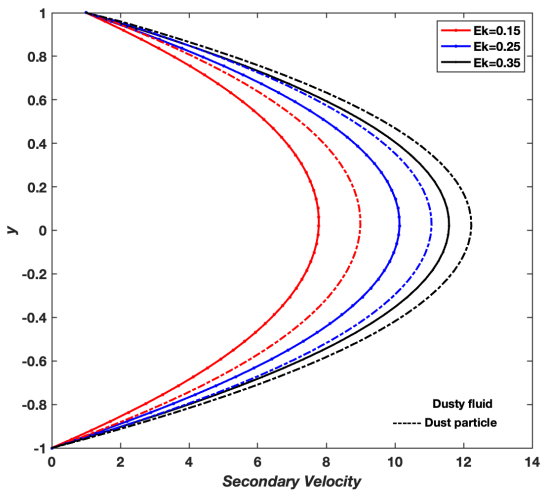

Fig. 2.42 Secondary velocity profiles of fluid flow with Ekman number Ek, t= 1, Re= 2, Ge= 5, G= 0.01, R= 1, $Ha^2 = 2$, Bi= 2, Be= 2, C= $4 * \pi * 0.5$, $\theta = (\pi/180) * 0.0025$

Figures 2.43 and 2.44 illustrate how the parameter (G) affects the flow velocities. As seen in Figure 2.43, the primary velocity decreases with increasing (G), primarily due to enhanced electromagnetic drag that opposes the axial motion. However, Figure 2.44 reveals a subtle increase in the secondary velocity profile with higher (G), clearly shown in the magnified region, where the velocity curves shift outward. This trend suggests that the ion slip effect associated with higher (G) promotes transverse rotational motion in the fluid. The dusty fluid and particles exhibit consistent behavior, with suppressed primary velocity and a mild boost in secondary flow, reflecting the interplay between magnetic field influence and particle-fluid coupling.

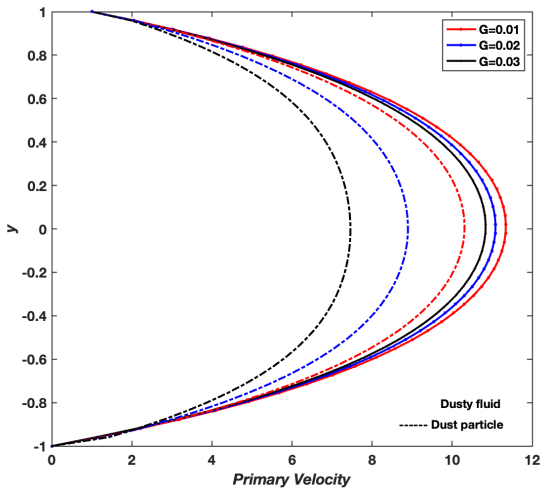

Fig. 2.43 Primary velocity profiles of fluid flow with varying G, t= 1, Re= 2, Ge= 5, R= 1, $Ha^2 = 2$, Bi= 2, Be= 2, C= $4 * \pi * 0.5$, Ek= 0.25, $\theta = (\pi/180) * 0.0025$

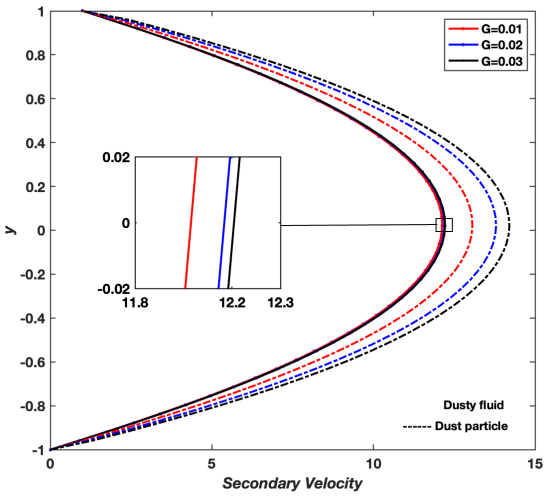

Fig. 2.44 Secondary velocity profiles of fluid flow with varying G, t= 1, Re= 2, Ge= 5, R= 1, $Ha^2 = 2$, Bi= 2, Be= 2, C= $4 * \pi * 0.5$, Ek= 0.25, $\theta = (\pi/180) * 0.0025$

Figures 2.45 and 2.46 show the variation of fluid and dust particle velocities along the channel in both the primary and secondary directions for different inclination angles (θ). The parabolic shape of the primary velocity profile indicates a balance between the driving force (pressure gradient) and viscous forces. The symmetry in the secondary velocity profile results from the Coriolis force, which acts equally on both sides of the channel. The influence of the inclination angle (θ) is evident in both profiles. In the primary velocity profile, the steeper gradient near the upper wall suggests increased shear stress due to greater velocity variation. Meanwhile, the increase in maximum secondary velocity with increasing inclination angle is attributed to the stronger Coriolis force at higher angles.

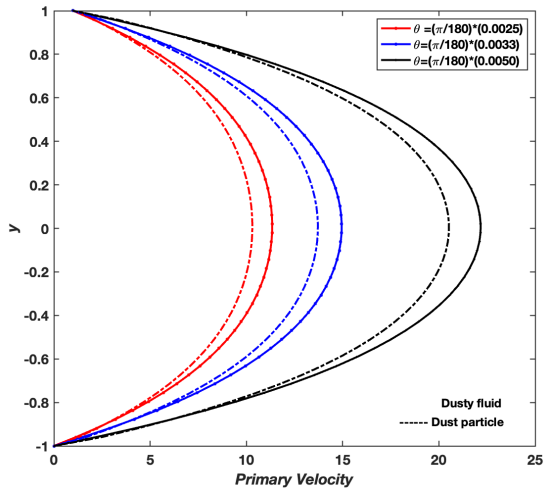

Fig. 2.45 Primary velocity profiles of fluid flow with angle θ, t= 1, Re= 2, Ge= 5, R= 1, $Ha^2 = 2$, Bi= 2, Be= 2, C= $4 * \pi * 0.5$, Ek=0.25

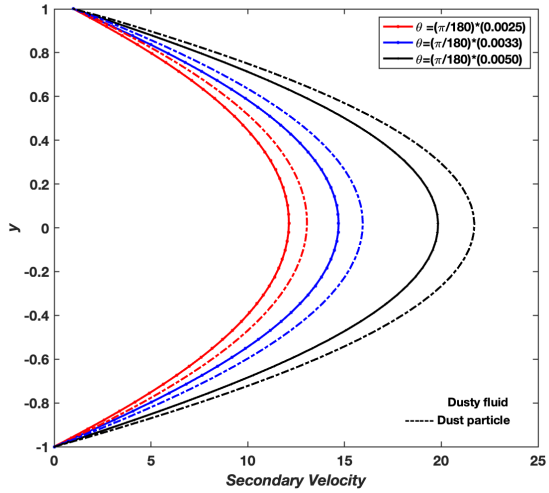

Fig. 2.46 Secondary velocity profiles of fluid flow with angle θ, t= 1, Re= 2, Ge= 5, G= 0.01, R= 1, $Ha^2 = 2$, Bi= 2, Be= 2, C= $4 * \pi * 0.5$, Ek= 0.25

2.4 Conclusion

In this chapter, the flow of dusty fluid in both horizontal and inclined channels has been analyzed under the influence of rotation and magnetic effects, with a focus on their impact on velocity profiles and energy requirements for fluid transport. A RBF-PSM was applied to solve the governing equations for dusty fluid flow in both channel configurations. The resulting velocity profiles were examined in the primary (x) and secondary (z) directions, highlighting the significant influence of rotation and magnetic

fields on the flow characteristics. Furthermore, the energy needed to drive the fluid was assessed, offering insight into the pumping requirements under both horizontal and inclined channel conditions. The significance of this study lies in its relevance to geophysical flows, industrial fluid transport systems, magnetohydrodynamic applications and understanding of dusty fluid flow in complex channel configurations, exploring the combined effects of rotation and magnetic influences on velocity profiles and energy requirements.

In the first part (*Section 2.2*), the horizontal channel configuration was analyzed. The governing equations for the coupled fluid–particle system were derived and non-dimensionalized to identify key controlling parameters. The entire fluid system has undergone a thorough analysis of the parameters that influence its behavior. The significant outcome of the study can be summarized as follows:

(a) The Coriolis frequency parameter (Ω) has a notable impact on both the primary and secondary velocity components. An increase in Ω reduces the magnitude of the primary velocity while causing a slight rise in the secondary velocity.

(b) The Ekman number (Ek) has a significant impact on the rotating dusty fluid flow. As the Ekman number increases, the primary velocities of both the particle and fluid phases reduce, while the secondary velocity exhibits an increasing trend.

(c) As the Reynolds number (Re) increases, the magnitude of the viscous forces decreases, resulting in a greater degree of correlation between the velocities of the fluid. Hence, the velocities along the x- and z-directions increase for both the fluid and the dusty particles.

(d) The Hartmann number (Ha) also affects the primary and secondary velocities of the fluid. Specifically, as the Hartmann number increases, the velocity of the fluid is reduced, and the flow becomes more laminar. This results in a reduction in both the primary and secondary velocities of the dusty fluid in a rotating frame.

(e) The primary and secondary velocity profiles of both fluid and particles increase with the ion slip parameter (B_i), Hall parameter (B_e), and with the increase in the

constant pressure gradient (G).

(f) The presence of dust particles in a fluid significantly affects the pumping power required for the fluid to flow. Dust particle drag increases the resistance to the flow, which requires more pumping power to maintain the flow rate.

In the second part (*Section 2.3*), similar modeling and analysis were extended to the inclined channel configuration. The channel was inclined at an angle θ with respect to the horizontal axis, introducing additional gravitational effects that modified the momentum balance. Here too, the focus was on examining the behavior and influence of various non-dimensional parameters on the velocity profiles, as well as evaluating the pumping power required for fluid transport. The key findings are as follows:

(a) The angle of inclination strongly affects both the velocity profiles and pumping power. As the angle increases, the velocity gradients become larger because of the stronger gravitational force acting against the flow. This increases the resistance to the fluid's movement, resulting in a sharp rise in pumping power. The secondary velocity profiles are also impacted, with more noticeable flow separation and shear stress as the angle increases.

(b) A clear inverse relationship between the Reynolds number (Re) and pumping power is observed. As Re increases, the pumping power decreases substantially. This indicates that higher inertia in the flow leads to reduced energy requirements, as the flow becomes more streamlined and encounters less resistance.

(c) As the Hartmann number (Ha) increases, the magnetic field suppresses the secondary flow, reducing velocity fluctuations and stabilizing the flow. The secondary velocity, driven by rotational effects, decreases in magnitude with increasing magnetic field intensity, reflecting a damping effect due to the Lorentz force.

(d) As time (t) progresses, the fluid becomes more resistant to flow, which leads to a slight reduction in primary velocity and an increase in pumping power. The study shows that the resistance builds over time due to the combined effects of viscosity and magnetic damping, demanding more energy to maintain the flow.

(e) The ion slip parameter (B_i) and Hall parameter (B_e) show minimal effects on both the velocity profiles and pumping power. The magnetic field–generated Lorentz force remains relatively stable, leading to only minor changes in flow resistance and velocity. Consequently, the overall effect of these parameters on the system is minimal.

A comparative analysis between the horizontal and inclined channel configurations reveals that while several dimensionless parameters (t, Ha^2, Re, Ek, and R) influence the flow behavior in both cases, the introduction of inclination (θ) leads to notable differences in flow structure and energy requirements. In particular, the gravitational component introduced in the inclined channel significantly amplifies the effects of the pressure gradient and alters both primary and secondary velocity profiles. The pumping power is observed to increase more sharply in the inclined configuration, due to the added resistance from the gravitational force.

Despite these differences, parameters like Re, Ha, and rotation-related quantities such as Ω and Ek show consistent trends in both settings, confirming their dominant roles in dictating flow characteristics. However, their quantitative impact varies due to the geometric influence of inclination.

Overall, the study in this chapter provides valuable insights into the interplay of rotational, magnetic, and gravitational effects on dusty fluid transport. These findings contribute to the optimization of channel design and energy-efficient transport in MHD-based engineering systems.

In the next chapter, we extend this analysis to Micropolar Dusty fluid models to explore how microstructural effects further influence flow dynamics under similar rotational and magnetic conditions.

Chapter 3

Numerical Analysis of Micropolar Dusty Fluid Flow in Horizontal/Inclined Channel under Rotating Frame of Reference

3.1 Introduction

As discussed in *Chapter 1, Section 1.6.1*, micropolar fluids constitute a class of non-Newtonian fluids characterized by suspended microstructures exhibiting independent rotational motion alongside translational velocity. This extension of classical fluid mechanics incorporates micro-rotational effects and couple stresses into the governing equations of fluid flow. Building on this foundation, the present chapter focuses on *micropolar dusty fluids*, which combine the micropolar fluid model with suspended dust particles dispersed in the fluid medium. This two-phase system involves solid particles interacting with a micropolar fluid, where both micro-rotation of the fluid elements and particle-fluid interactions fundamentally alter flow behavior.

Micropolar dusty fluid concept arises naturally from the integration of micropolar fluid theory [4] and dusty fluid dynamics originally introduced by Saffman [23]. The

presence of dust particles introduces new complexities such as increased effective viscosity and altered momentum transfer, which cannot be captured by either micropolar or dusty fluid models alone. Such fluids are prevalent in diverse engineering applications including enhanced oil recovery, chemical processing, and materials engineering, where particulate suspensions coexist with microstructural fluid behavior. Subsequent work by Ahmadi [125] advanced the understanding of boundary layer flows and velocity profile modifications under micropolar effects. Devakar et al. [126] emphasize the critical importance of incorporating micropolar fluid properties for accurate modeling of multiphase flows in horizontal channel configurations, highlighting its relevance to industrial processes involving layered immiscible fluids. Recent investigations by Vidyanidhi et al. [120] and Lou et al. [42] analyzed micropolar dusty fluids under magnetic and rotational fields, demonstrating significant impacts on velocity, temperature, and micro-rotation profiles.

Channel geometries are fundamental to the study and application of micropolar dusty fluids. Two canonical configurations, horizontal and inclined channels serves as key models in industrial and environmental engineering contexts. A *horizontal channel* features two parallel plates with gravity acting perpendicular to the flow, influencing flow stability and pressure, whereas an *inclined channel* is angled relative to the horizontal, introducing a gravity-driven component along the flow direction that affects pressure and flow rates. Research by Chakraborty and Medhi [115] and Roja et al. [116] highlights the critical influence of channel inclination on entropy generation, heat transfer, and momentum transport in micropolar dusty fluids.

Rotational and electrically conductive micropolar dusty fluid flows are characterized by the interplay of rotation, microrotation, magnetic fields, and complex interactions between micropolar fluid microstructures and suspended dust particles, all of which significantly influence the flow dynamics. Rotational effects impart Coriolis and centrifugal forces that modify angular momentum and stress distributions, while magnetic fields introduce Lorentz forces affecting flow resistance and stability. Nadeem et al. [71] showed that rotation enhances velocity and microrotation profiles in MHD mi-

cropolar nanofluid flow between horizontal plates, improving stability and heat transfer. Beg et al. [117] demonstrated that Coriolis and centrifugal forces from rotation significantly affect flow stability and velocity in oscillatory MHD Couette flow. Zaidi and Ahmad [127] examined MHD convection in an electrically conducting fluid within an inclined microchannel, showing that magnetic fields generate Lorentz forces which reduce velocity and alter temperature profiles, thereby impacting thermal boundary layer thickness and heat transfer rates. Kocic et al. [128] demonstrated that magnetic fields in MHD micropolar fluid flow through porous media significantly affect velocity and microrotation by imposing Lorentz forces that modify momentum and thermal transport.

Micropolar dusty fluid with thermal effects are characterized by added complexity due to thermal gradients that influence both fluid motion and micro rotations. Heat transfer mechanisms including conduction, convection, and radiation interact with suspended dust particles, thereby affecting the overall energy distribution within the fluid. Studies by Kaneez et al. [129] and Narayana et al. [130] reveal that thermal radiation and Hall currents significantly alter velocity, temperature, and micro-rotation profiles. Understanding these thermal effects is vital for optimizing energy transfer and minimizing entropy generation in engineering systems. Javed and Siddiqi [73] investigated heat transfer in viscosity-variable micropolar fluid flow under MHD effects, while Yadav and Yadav [74] analyzed the effects of radiative heat transfer and magnetic forces on entropy production in conducting micropolar and Newtonian fluid flows through a horizontally oriented porous channel.These studies collectively highlight the importance of thermal interactions in regulating flow behavior and improving thermal efficiency in micropolar dusty fluid systems.

Although prior work has extensively investigated micropolar and dusty fluids separately, and to some extent their combination, important gaps remain. In particular, the combined effects of rotation, magnetic fields, and channel inclination on micropolar dusty fluids have not been comprehensively explored, especially concerning pumping power, velocity, temperature, and microrotation profiles under realistic conditions. Numerical techniques such as the radial basis function pseudospectral method have shown promise

for solving these complex problems but require further application to capture multi-parameter interactions in practical geometries. This study aims to fill these gaps by systematically analyzing micropolar dusty fluid flow in horizontal and inclined channels, incorporating rotational, magnetic, and thermal effects. It further evaluates pumping power requirements and detailed flow characteristics.

To achieve these objectives, the chapter is organized into two main sections. First section concentrates on the formulation and computational analysis of micropolar dusty fluid flow in a horizontal channel, covering velocity, temperature, microrotation profiles, and pumping power. The second section applies a similar approach to the inclined channel, presenting the mathematical formulation and corresponding results. In conclusion, the chapter highlights the core results and emphasizes their importance in applied contexts as well as in guiding subsequent studies.

3.2 Mathematical Modeling of Micropolar Dusty Fluid Flow in an Horizontal Channel

This section develops the mathematical formulation for the unsteady flow of an incompressible, electrically conducting micropolar dusty fluid flowing through a horizontal channel bounded by two infinite parallel plates at $y = -1$ and $y = 1$. The flow is driven by the motion of the upper plate along with a constant pressure gradient in the x-direction. The system undergoes uniform rotation at angular velocity Ω around the y-axis and is affected by an externally imposed transverse magnetic field B_0 aligned in the same direction. The modelling setup under consideration is presented in Figure 3.1.

The flow exhibits velocities along the x and z directions due to the combined effects of the plate movement, rotational Coriolis forces, and electromagnetic Lorentz forces. In addition to the fluid velocity and micropolar micro-rotation dynamics, the model incorporates the dust particle phase velocity and temperature fields for both fluid and particles, thus fully describing the coupled multiphase thermal-hydrodynamic system.

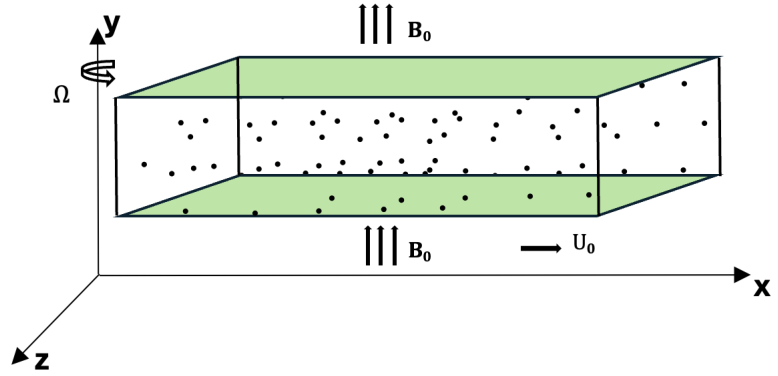

Fig. 3.1 Schematic of a Horizontal Channel with Micropolar Dusty Fluid Flow

3.2.1 Key Features of the Model

The model incorporates the following key aspects:

(a) **Geometry and Flow:** The fluid and particles flow in a horizontal channel bounded by parallel plates at $y = \pm 1$. The upper plate moves with constant velocity, and a steady pressure gradient acts along the x-axis.

(b) **Micropolar Fluid Phase:** The fluid exhibits micropolar behavior characterized by the micro-rotation vector $\mathbf{M}$, vortex viscosity κ, and spin viscosity γ, enabling the description of microstructural rotational effects alongside classical velocity fields.

(c) **Dust Particle Phase:** Suspended spherical dust particles with volume fraction ϕ interact dynamically with the fluid through drag forces proportional to the relative velocity between phases.

(d) **Thermal Fields:** Separate temperature fields T and T_p describe the fluid and dust particle phases respectively, coupled through thermal relaxation characterized by the parameter τ_T.

(e) **Electromagnetic Influence:** A uniform magnetic field B_0 generates Lorentz forces opposing fluid motion. The electromagnetic effects depend on electrical conductivity σ, ion slip B_i, and Hall parameter B_e.

(f) **Rotation Effects:** The system's rotation at a fixed angular velocity Ω around the y-axis generates Coriolis effects, which are explicitly considered, while centrifugal effects are absorbed into the pressure term through an appropriate modification.

3.2.2 Governing Equations of Micropolar Dusty Fluid

To develop the governing equations for the micropolar dusty fluid system, it is essential to incorporate the fundamental equations governing micropolar fluids and dusty fluids, both of which have been studied in detail in *Chapter 1*, *Sections 1.6.1 and 1.6.2*, respectively. The equations describing each phase are given below.

(a) **Governing Equations of Micropolar Fluid and Dusty Fluid:** From *Section 1.6.1*, we adopt the continuity, linear momentum, angular momentum, and energy equations describing the micropolar fluid phase [4]. From *Section 1.6.2*, we adopt the dusty fluid governing equations with volume fraction effects [36] for both phases.

(i) **Micropolar Fluid:**

$$\nabla \cdot \mathbf{u} = 0 \tag{3.1}$$

$$\rho_f \left(\frac{\partial \mathbf{u}}{\partial t} + (\mathbf{u} \cdot \nabla)\mathbf{u} \right) = -\nabla P + (\mu + \kappa)\nabla^2 \mathbf{u} + \kappa \nabla \times \mathbf{M} + \rho_f \mathbf{g} \tag{3.2}$$

$$\rho_f j \frac{D\mathbf{M}}{Dt} = \gamma \nabla^2 \mathbf{M} - \kappa \left(2\mathbf{M} - \nabla \times \mathbf{u}\right) + \mathbf{c} \tag{3.3}$$

$$\rho_f c_p \left(\frac{\partial T}{\partial t} + \mathbf{u} \cdot \nabla T \right) = \nabla \cdot (k \nabla T) + \Phi \tag{3.4}$$

(ii) **Dusty Fluid:**

$$\frac{\partial}{\partial t}\left[(1-\phi_p)\rho_f\right] + \nabla\cdot\left[(1-\phi_p)\rho_f\mathbf{u}\right] = 0 \tag{3.5}$$

$$\frac{\partial}{\partial t}\left(\phi_p\rho_p\right) + \nabla\cdot\left(\phi_p\rho_p\mathbf{u}_p\right) = 0 \tag{3.6}$$

$$(1-\phi_p)\rho_f\left(\frac{\partial\mathbf{u}}{\partial t} + (\mathbf{u}\cdot\nabla)\mathbf{u}\right) = -(1-\phi_p)\nabla P + \mu\nabla^2\mathbf{u} + \frac{\phi_p\rho_p}{\tau_p}(\mathbf{u}_p-\mathbf{u}) + (1-\phi_p)\rho_f\mathbf{g} \tag{3.7}$$

$$\phi_p\rho_p\left(\frac{\partial\mathbf{u}_p}{\partial t} + (\mathbf{u}_p\cdot\nabla)\mathbf{u}_p\right) = -\phi_p\nabla P - \frac{\phi_p\rho_p}{\tau_p}(\mathbf{u}_p-\mathbf{u}) + \phi_p\rho_p\mathbf{g} \tag{3.8}$$

$$(1-\phi_p)\rho_f c_p\left(\frac{\partial T}{\partial t} + \mathbf{u}\cdot\nabla T\right) = k\nabla^2 T - \frac{\phi_p\rho_p c_{pp}}{\tau_T}(T-T_p) + (1-\phi_p)Q \tag{3.9}$$

$$\phi_p\rho_p c_{pp}\left(\frac{\partial T_p}{\partial t} + \mathbf{u}_p\cdot\nabla T_p\right) = \frac{\phi_p\rho_p c_{pp}}{\tau_T}(T-T_p) \tag{3.10}$$

where: $\mathbf{u} = (u_1, u_2, u_3)$ and $\mathbf{u}_p$ denote the fluid and particle velocity vectors, respectively. The volume fractions of the particle and fluid phases are ϕ_p and $1-\phi_p$. The densities are ρ_f for the fluid and ρ_p for the particles. P represents pressure, μ is the fluid dynamic viscosity, κ the vortex (micro-rotation) viscosity, $\mathbf{M}$ the microrotation vector, j the microinertia per unit mass, γ the spin viscosity, and $\mathbf{c}$ the external body couple. The particle momentum relaxation time is τ_p, while $\mathbf{g}$ denotes body acceleration (e.g., gravity). The fluid and particle temperatures are T and T_p with specific heats c_p and c_{pp}, respectively. Thermal conductivity of the fluid is k, τ_T is the thermal relaxation time, Q is the volumetric heat source, and Φ is the viscous dissipation function including micropolar contributions.

(b) **Incorporation of Rotation and Magnetic Field:** The effects of rotation and magnetic field modify the above equations:

(i) **Rotation:** In a frame rotating at angular velocity Ω, the Coriolis force

$$2\rho_f(\Omega \times \mathbf{u}) \tag{3.11}$$

as shown in Equation 1.73 of *Section 1.7*, adds to the fluid momentum equations, accounting for apparent accelerations due to rotation.

(ii) **Magnetic Field:** A uniform magnetic field B_0 produces a Lorentz force opposing fluid motion:

$$\mathbf{F}_L = \sigma B_0^2 \frac{(1 + B_i B_e)}{(1 + B_i B_e)^2 + B_e^2}\mathbf{u} \tag{3.12}$$

where σ is electrical conductivity, B_i the ion slip parameter, and B_e the Hall parameter.

(c) **Derivation of the Modified Governing Equations:** The governing equations for micropolar dusty fluid flow under the effects of rotation and a magnetic field are formulated by integrating several fundamental components. The micropolar fluid phase is described by the continuity, linear momentum, angular momentum, and energy equations, presented in equations (3.1) to (3.4). The dusty fluid phase, including the influence of finite particle volume fraction, is governed by the conservation and interaction equations outlined in (3.5) to (3.10). The additional physical influences of system rotation and magnetic field are incorporated through the Coriolis and Lorentz force terms in equations (3.11) and (3.12), respectively. By combining these sets, the resulting modified governing equations comprehensively capture the coupled and time-dependent behavior of the micropolar dusty fluid system within the horizontal channel.

$$\rho_f \left(\frac{\partial \mathbf{u}}{\partial t} + 2(\Omega \times \mathbf{u}) + (\mathbf{u} \cdot \nabla)\mathbf{u} \right) = -\nabla P + (\mu + \kappa)\nabla^2 \mathbf{u} + \kappa \nabla \times \mathbf{M} - \mathbf{F}_L + \frac{\phi_p \rho_p}{1 - \phi_p}\chi(\mathbf{u}_p - \mathbf{u}) \tag{3.13}$$

$$\rho_p \frac{\partial \mathbf{u}_p}{\partial t} = \rho_p \chi(\mathbf{u} - \mathbf{u}_p) \tag{3.14}$$

$$\rho_f j \frac{\partial \mathbf{M}}{\partial t} = \gamma \nabla^2 \mathbf{M} - \kappa \left(2\mathbf{M} - \nabla \times \mathbf{u}\right) \tag{3.15}$$

$$\rho_f c_p \left(\frac{\partial T}{\partial t}\right) = k\nabla^2 T + \mu \left|\nabla \mathbf{u}\right|^2 + \kappa \left|2\mathbf{M} - \nabla \times \mathbf{u}\right|^2 + \beta \left|\nabla \mathbf{M}\right|^2 - \frac{\phi_p \rho_p c_{p,p}}{1-\phi_p} \frac{1}{\tau_T}(T - T_p) + Q + \frac{\phi_p \rho_p}{1-\phi_p} \chi \left|\mathbf{u}_p - \mathbf{u}\right|^2 + \mathbf{F}_L \cdot \mathbf{u} \tag{3.16}$$

$$\rho_p c_{p,p} \left(\frac{\partial T_p}{\partial t}\right) = \frac{\rho_p c_{p,p}}{\tau_T}(T - T_p) \tag{3.17}$$

Note: In modeling the dust particle phase, certain simplifying assumptions are often employed wherein convective acceleration, pressure gradient, gravitational body force, and rotational Coriolis effects may be neglected in some governing equations. These approximations are justified particularly for small, rigid particles suspended in dilute flows where interphase drag forces dominate the particle dynamics, and inertial and body forces are comparatively insignificant.

where:

- $\mathbf{u}, \mathbf{u}_p$ = Fluid and particle velocity vectors, respectively.
- ϕ_p = Particle volume fraction, with $1 - \phi_p$ representing the fluid fraction.
- Ω = Angular velocity vector, introducing Coriolis effects via $2\rho_f(\Omega \times \mathbf{u})$.
- $\mathbf{M}$ = Microrotation vector; κ = Vortex viscosity; γ = Spin viscosity.
- χ = Interphase momentum transfer coefficient (drag parameter).

$$\chi = \frac{1}{\tau_p(1-\phi_p)},$$

- τ_p, τ_T = Relaxation times for momentum and temperature exchange between fluid and particle phases.
- $c_p, c_{p,p}$ = Specific heat of fluid and particles, respectively.
- Φ, Q = Viscous dissipation and internal heat source in the fluid.
- β = Microrotational heat diffusion coefficient.

The modified governing equations (3.13) to (3.17), consistent with the assumptions of fully developed horizontal channel flow, take the following *component form*:

$$\rho_f \left(\frac{\partial u_1}{\partial t} - 2\Omega u_3 \right) = -\frac{\partial P}{\partial x} + (\mu + \kappa)\frac{\partial^2 u_1}{\partial y^2} + \kappa \frac{\partial \mathbf{M}}{\partial y} - \frac{\sigma B_0^2 (1 + B_i B_e)}{(1 + B_i B_e)^2 + B_e^2} u_1 + \frac{\phi_p \rho_p}{1 - \phi_p} \chi (u_{1p} - u_1) \tag{3.18}$$

$$\rho_f \left(\frac{\partial u_3}{\partial t} + 2\Omega u_1 \right) = -\frac{\partial P}{\partial z} + (\mu + \kappa)\frac{\partial^2 u_3}{\partial y^2} + \kappa \frac{\partial M}{\partial y} - \frac{\sigma B_0^2 (1 + B_i B_e)}{(1 + B_i B_e)^2 + B_e^2} u_3 + \frac{\phi_p \rho_p}{1 - \phi_p} \chi (u_{3p} - u_3) \tag{3.19}$$

$$\rho_p \frac{\partial u_{1p}}{\partial t} = \rho_p \chi (u_1 - u_{1p}) \tag{3.20}$$

$$\rho_p \frac{\partial u_{3p}}{\partial t} = \rho_p \chi (u_3 - u_{3p}) \tag{3.21}$$

$$\rho_f j \frac{\partial M}{\partial t} = \gamma \frac{\partial^2 M}{\partial y^2} - \kappa \left(2M + \frac{\partial u_1}{\partial y} \right) \tag{3.22}$$

$$\rho_f c_p \frac{\partial T}{\partial t} = k \frac{\partial^2 T}{\partial y^2} + \mu \left(\frac{\partial u_1}{\partial y} \right)^2 + \kappa \left(2M + \frac{\partial u_1}{\partial y} \right)^2 + \beta \left(\frac{\partial M}{\partial y} \right)^2 + \frac{\sigma B_0^2 (1 + B_i B_e)}{(1 + B_i B_e)^2 + B_e^2} u_1^2 + \frac{\phi_p \rho_p c_{p,p}}{1 - \phi_p} \frac{1}{\tau_T} (T_p - T) + Q + \frac{\phi_p \rho_p}{1 - \phi_p} \chi (u_1 - u_{1p})^2 \tag{3.23}$$

$$\frac{\partial T_p}{\partial t} = \frac{(T - T_p)}{\tau_T} \tag{3.24}$$

(d) **Dimensionless Variables and Scales:** To simplify the governing equations and facilitate numerical analysis, we introduce the following characteristic scales:

- Characteristic length: L (half-distance between plates)
- Characteristic velocity: U_0

- Characteristic time: $\dfrac{L}{U_0}$
- Characteristic pressure: $\rho_f U_0^2$
- Characteristic microrotation: $\dfrac{U_0}{L}$
- Characteristic temperature: $T_2 - T_1$

Using these, the dimensionless variables are defined as:

$$y^* = \frac{y}{L}, \quad t^* = \frac{tU_0}{L}, \quad u_i^* = \frac{u_i}{U_0}, \quad u_{ip}^* = \frac{u_{ip}}{U_0},$$
$$M^* = \frac{ML}{U_0}, \quad T^* = \frac{T - T_1}{T_2 - T_1}, \quad T_p^* = \frac{T_p - T_1}{T_2 - T_1}, \quad P^* = \frac{P}{\rho_f U_0^2}$$

where T_1 and T_2 denote the temperatures corresponding to the lower and upper plates, in that order. For simplicity, superscript asterisks are omitted in the subsequent equations.

(e) **Initial and Boundary Conditions:** The initial and boundary conditions are:

- At $t = 0$:

$$u_1(y,0) = u_3(y,0) = u_{1p}(y,0) = u_{3p}(y,0) = 0,$$
$$M(y,0) = 0, \quad T(y,0) = T_p(y,0) = 0$$

- At $y = -1$ (for all $t > 0$):

$$u_1 = u_3 = u_{1p} = u_{3p} = 0, \quad M = T = T_p = T_1$$

- At $y = 1$ (for all $t > 0$):

$$u_1 = u_3 = u_{1p} = u_{3p} = 1, \quad M = T = T_p = T_2$$

(f) **Dimensionless Parameters:** The dimensionless parameters used in the governing equations, defined as discussed in *Section 1.9* of *Chapter 1*, are given by:

Reynolds number:	$Re = \dfrac{\rho_f U_0 L}{\mu}$
Micropolar parameter:	$\eta = \dfrac{\kappa}{\mu}$
Hartmann number squared:	$Ha^2 = \dfrac{\sigma B_0^2 L^2}{\mu}$
Eckert number:	$Ec = \dfrac{U_0^2}{c_p(T_2 - T_1)}$
Prandtl number:	$Pr = \dfrac{\mu c_p}{k}$
Dimensionless dissipation parameter:	$\delta = \dfrac{\beta}{\mu L^2}$
Particle concentration parameter:	$R = \dfrac{\phi_p \rho_p L^2}{(1-\phi_p)\mu}$
Density ratio parameter:	$R_1 = \dfrac{\rho_f}{\rho_p}$
Coriolis frequency parameter:	$C = 4\pi\Omega$
Ekman number:	$Ek = \dfrac{Re}{4\pi}$

(g) **Dimensionless Governing Equations:** By introducing nondimensional variables and parameters, the governing relations (3.18) to (3.24) are transformed into the nondimensional form presented below:

$$\frac{\partial u_1}{\partial t} = Ge(t) + \frac{\eta}{Re}\frac{\partial M}{\partial y} + \frac{1+\eta}{Re}\frac{\partial^2 u_1}{\partial y^2} - \frac{Ha^2}{Re}\left(\frac{(1+BiBe)u_1 + Beu_3}{(1+BiBe)^2 + Be^2}\right) - \frac{R}{Re}(u_1 - u_{1p}) - \frac{2CEk}{Re}u_3 \tag{3.25}$$

$$\frac{\partial u_3}{\partial t} = Ge(t) + \frac{\eta}{Re}\frac{\partial M}{\partial y} + \frac{1+\eta}{Re}\frac{\partial^2 u_3}{\partial y^2} - \frac{Ha^2}{Re}\left(\frac{(1+BiBe)u_3 + Beu_1}{(1+BiBe)^2 + Be^2}\right) - \frac{R}{Re}(u_3 - u_{3p}) + \frac{2CEk}{Re}u_1 \tag{3.26}$$

$$\frac{\partial u_{1p}}{\partial t} = \frac{RR_1}{Re}(u_1 - u_{1p}) - \frac{C}{2\pi}u_{3p} \tag{3.27}$$

$$\frac{\partial u_{3p}}{\partial t} = \frac{RR_1}{Re}(u_3 - u_{3p}) + \frac{C}{2\pi}u_{1p} \tag{3.28}$$

$$\frac{\partial M}{\partial t} = \frac{1}{Re}\left(1 + \frac{\eta}{2}\right)\frac{\partial^2 M}{\partial y^2} - \frac{\eta}{Re}\left(2M + \frac{\partial u_1}{\partial y}\right) \tag{3.29}$$

$$\frac{\partial T}{\partial t} = \frac{1}{PrRe}\frac{\partial^2 T}{\partial y^2} + \frac{Ec}{Re}\left[\left(\frac{\partial u_1}{\partial y}\right)^2 + \eta\left(2M + \frac{\partial u_1}{\partial y}\right)^2 + \delta\left(\frac{\partial M}{\partial y}\right)^2\right] + \frac{EcHa^2}{Re}\left(\frac{(1+BiBe)}{(1+BiBe)^2+Be^2}\right)u_1^2 + \frac{2R}{3PrRe}(T_p - T) + \frac{REc}{Re}(u_1 - u_{1p})^2 \tag{3.30}$$

$$\frac{\partial T_p}{\partial t} = -\frac{2RR_1}{3PrRe}(T_p - T) \tag{3.31}$$

3.2.3 Numerical Solution using Radial Basis Function Pseudospectral Method

The numerical solution of the governing system of partial differential equations (3.25) to (3.31) for the micropolar dusty fluid flow is obtained using the RBF-PSM. This method provides a meshfree, highly accurate spectral approximation of spatial derivatives, which is particularly advantageous in handling the complex coupled nature of the micropolar and particulate phases.

Following the general framework established in *Chapter 1*, *Section 1.10.7*, the solution variables are approximated as linear combinations of radial basis functions centered at scattered nodes in the spatial domain. The approximate solution for a generic variable $z(y,t)$ is expressed as

$$z(y,t) \approx \sum_{j=1}^{N} \lambda_j(t)\,\phi(\|y - y_j\|) \tag{3.32}$$

where ϕ denotes the wendland RBF (as per Equation (2.13) of *Section 2.2.3*), $\lambda_j(t)$ are time-dependent coefficients, and $\{y_j\}_{j=1}^{N}$ are the spatial collocation points (see *Chapter 1*, Equation (1.96)).

The spatial derivatives required in the governing equations are computed by constructing differentiation matrices based on the derivatives of the RBFs. Specifically, the first and second derivative matrices, D_1 and D_2, are formed by

$$D_1 = D_x A^{-1}, \quad D_2 = D_{xx} A^{-1} \tag{3.33}$$

where A is the interpolation matrix with entries $A_{ij} = \phi(\|y_i - y_j\|)$, and D_x, D_{xx} contain the corresponding first and second derivatives of the RBFs evaluated at the nodes (refer to *Chapter 1*, Equations (1.105) - (1.109)).

By substituting these differentiation matrices into the equations (3.25) to (3.31), the partial differential equations are converted into a system of coupled ODEs in time. The resultant system, defined at the discrete nodal points, is given by:

$$\begin{aligned}\frac{du_1}{dt} &= G_e(t) + \frac{\eta}{Re} D_1\mathbf{M} + \frac{1+\eta}{Re} D_2 u_1 - \frac{Ha^2}{Re}\frac{(1+Bi\,Be)}{(1+Bi\,Be)^2+Be^2}u_1 \\ &\quad - \frac{Ha^2}{Re}\frac{Be}{(1+Bi\,Be)^2+Be^2}u_3 - \frac{R}{Re}(u_1 - u_{1p}) - \frac{2CEk}{Re}u_3 \end{aligned} \tag{3.34}$$

$$\begin{aligned}\frac{du_3}{dt} &= G_e(t) + \frac{\eta}{Re} D_1\mathbf{M} + \frac{1+\eta}{Re} D_2 u_3 - \frac{Ha^2}{Re}\frac{(1+Bi\,Be)}{(1+Bi\,Be)^2+Be^2}u_3 \\ &\quad - \frac{Ha^2}{Re}\frac{Be}{(1+Bi\,Be)^2+Be^2}u_1 - \frac{R}{Re}(u_3 - u_{3p}) + \frac{2CEk}{Re}u_1 \end{aligned} \tag{3.35}$$

$$\frac{du_{1p}}{dt} = \frac{RR_1}{Re}(u_1 - u_{1p}) - \frac{C}{2\pi}u_{3p} \tag{3.36}$$

$$\frac{du_{3p}}{dt} = \frac{RR_1}{Re}(u_3 - u_{3p}) + \frac{C}{2\pi}u_{1p} \tag{3.37}$$

$$\frac{d\mathbf{M}}{dt} = \frac{1}{Re}\left(1 + \frac{\eta}{2}\right) D_2\mathbf{M} - \frac{\eta}{Re}\left(2\mathbf{M} + D_1 u_1\right) \tag{3.38}$$

$$\begin{aligned}\frac{dT}{dt} &= \frac{1}{Pr\,Re} D_2 T + \frac{Ec}{Re}\left[(D_1 u_1)^2 + \eta\,(2M + D_1 u_1)^2 + \delta\,(D_1\mathbf{M})^2\right] \\ &\quad + \frac{Ec\,Ha^2}{Re}\frac{(1+Bi\,Be)}{(1+Bi\,Be)^2+Be^2}u_1^2 + \frac{2R}{3Pr\,Re}(T_p - T) + \frac{REc}{Re}(u_1 - u_{1p})^2 \end{aligned} \tag{3.39}$$

$$\frac{dT_p}{dt} = -\frac{2RR_1}{3Pr\,Re}(T_p - T) \tag{3.40}$$

SSP RK43 Scheme: The system of ordinary differential equations (3.34) to (3.40) is solved using SSP RK43, which maintains the stability properties of forward Euler schemes while offering higher-order temporal accuracy, making it suitable for stiff, coupled systems.

The SSP RK43 method's theoretical formulation and details are provided in *Chapter 2*, *Section 2.2.3*.

(a) The solution process begins with the initialization of the solution vector $\mathbf{U}^0$ at initial time $t = 0$, where all dependent variables are set to zero consistent with the initial conditions.

(b) A suitable time step Δt is selected based on stability and accuracy considerations.

(c) For each time step from t_n to $t_{n+1} = t_n + \Delta t$, intermediate stage solutions $\mathbf{U}^{(k)}$, with $k = 1, 2, 3$, are computed by evaluating the system's right-hand side functions $\mathbf{F}(t, \mathbf{U})$(as described in *Section 2.2.3*) corresponding to equations (3.34) to (3.40) using the SSP RK43 Butcher tableau coefficients.

(d) Boundary conditions are enforced at every intermediate stage $\mathbf{U}^{(k)}$ to ensure physical and mathematical consistency.

(e) The intermediate stages are combined to update the solution vector $\mathbf{U}^{n+1}$ at the new time level.

(f) This iterative procedure is repeated at each successive time level until the simulation reaches its predetermined final duration.

3.2.4 Pumping Power Analysis

Pumping power quantifies the energy required to move a fluid from one location to another and serves as a critical performance metric in fluid transport systems. It is fundamentally dependent on two key parameters: the volume flow rate and the pressure drop across the channel or conduit. These concepts form the basis for evaluating the energetic efficiency of fluid motion in practical applications, particularly in systems involving complex fluids such as micropolar dusty fluids under the influence of magnetic and rotational effects.

The foundational expressions and governing relationships for pumping power, volume flow rate, and pressure drop have already been introduced and discussed in detail in

Chapter 1, Section 1.8. Here, we use $\rho_f = 1050kg/m^3$, which is understood to represent the density of animal blood according to [131], to analyse the behaviour of this micropolar fluid in relation to pumping power.

Upon reviewing the Table 3.1, notable findings emerge. Specifically, an increase in the parameters $t, Ha, Be, \eta, Pr, R_1, Ec$ and Ec, leads to a significant rise in pumping power. Conversely, parameters such as R, Re, and Bi demonstrate a noteworthy decrease in pumping power, while parameters C and Ek exhibit fluctuating trends.

Table 3.1: Volume Flow Rate, Pressure Drop, and Pumping Power for Various Parameter Values

Parameter	**Volume Flow Rate**	**Pressure Drop**	**Pumping Power**
$t = 0.10$	0.178030814	47.94276338	8.535289171
$t = 0.30$	0.234403261	83.11128728	19.48155679
$t = 0.50$	0.277896554	116.8151129	32.46251734
$t = 0.70$	0.320874137	155.740705	49.97316429
$t = 0.90$	0.361584116	197.7658946	71.5090062
$Ha^2 = 1.00$	0.277939556	116.851268	32.47758957
$Ha^2 = 2.00$	0.278034236	116.9308918	32.51079116
$Ha^2 = 3.00$	0.279477169	118.1477295	33.01959297
$Ha^2 = 4.00$	0.28064361	119.1360031	33.43475798
$Ha^2 = 5.00$	0.281466138	119.8353692	33.72959857
$R = 50.00$	0.278496246	117.3198233	32.67313036
$R = 75.00$	0.262794223	104.4634435	27.45238946
$R = 100.00$	0.255959352	99.10024156	25.3656336
$R = 125.00$	0.252014299	96.06895705	24.21075089
$R = 150.00$	0.249327669	94.0315649	23.44467091
$Re = 1.00$	0.37451136	424.3192125	158.9123653
$Re = 2.00$	0.278957276	117.7085735	32.83566303

continued on next page

Table 3.1: Volume Flow Rate, Pressure Drop, and Pumping Power for various parameters

Parameter	**Volume Flow Rate**	**Pressure Drop**	**Pumping Power**
$Re = 3.00$	0.241670362	58.89633025	14.23349744
$Re = 4.00$	0.220996074	36.93786856	8.163123942
$Re = 5.00$	0.207040499	25.93601874	5.369806256
$Bi = 1.00$	0.278834338	117.6048469	32.79226966
$Bi = 2.00$	0.278034236	116.9308918	32.51079116
$Bi = 3.00$	0.278720685	117.508995	32.7521876
$Bi = 4.00$	0.279227271	117.9365373	32.93109744
$Bi = 5.00$	0.279447507	118.1226518	33.00908055
$Be = 1.00$	0.279313323	118.0092401	32.96155305
$Be = 2.00$	0.278034236	116.9308918	32.51079116
$Be = 3.00$	0.278638033	117.4393131	32.72305925
$Be = 4.00$	0.279130878	117.855125	32.89700451
$Be = 5.00$	0.279353433	118.0431352	32.9757551
$\eta = 0.30$	0.258487466	101.0675382	26.12469185
$\eta = 0.40$	0.26571617	106.7993666	28.37831863
$\eta = 0.50$	0.279387689	118.0720874	32.98788768
$\eta = 0.60$	0.29304667	129.8991441	38.06651157
$\eta = 0.70$	0.305499518	141.1736905	43.12849439
$Pr = 1.00$	0.268234932	108.8336966	29.19299923
$Pr = 2.00$	0.278034236	116.9308918	32.51079116
$Pr = 3.00$	0.299753612	135.9131759	40.74046546
$Pr = 4.00$	0.323105874	157.9146479	51.02315034
$Pr = 5.00$	0.345254356	180.3063588	62.25155579
$Ec = 0.30$	0.21545495	70.21754816	15.12871831
$Ec = 0.40$	0.24660599	91.98985859	22.68525013

continued on next page

Table 3.1: Volume Flow Rate, Pressure Drop, and Pumping Power for various parameters

Parameter	**Volume Flow Rate**	**Pressure Drop**	**Pumping Power**
$Ec = 0.50$	0.278957089	117.7084157	32.83559701
$Ec = 0.60$	0.311364981	146.6466819	45.66064125
$Ec = 0.70$	0.343570304	178.5516827	61.34505588
$C = 0.10$	0.278243322	117.1068255	32.58419213
$C = 0.20$	0.278034236	116.9308918	32.51079116
$C = 0.30$	0.279198308	117.9120727	32.92085117
$C = 0.40$	0.280112234	118.6852811	33.24519917
$C = 0.50$	0.280708347	119.1909723	33.45790079
$Ek = 0.15$	0.27850677	117.3286902	32.67683453
$Ek = 0.20$	0.278040704	116.9363325	32.51306022
$Ek = 0.25$	0.278957089	117.7084157	32.83559701
$Ek = 0.30$	0.279612532	118.2622055	33.0675947
$Ek = 0.35$	0.279933845	118.5341608	33.18172343

end of table

3.2.5 Stability Analysis

Numerical techniques stability analysis is important because stable methods provide accurate and dependable findings while unstable methods can produce inaccurate or divergent results. The matrix method for stability is a commonly used tool in scientific computing and numerical analysis because it provides a quick and easy way to evaluate the stability of a numerical solution. With this approach, the differential equation's approximate solution is created as a matrix from the linear form of the difference equation, and its eigenvalues are afterwards examined. These eigenvalues dictate the stability of the numerical approach; if the magnitudes of all the eigenvalues have negative real part,

the method is said to be stable. An examination of matrix stability was conducted for a range of values of N (node points). The related matrix's eigenvalues for ($N = 30$) and ($N = 50$) are shown in Figures 3.2 and 3.3 respectively. The approach stays steady even with the number of node points in Figure 3.3 increasing. Because none of the eigenvalues have an imaginary part and are all negative.

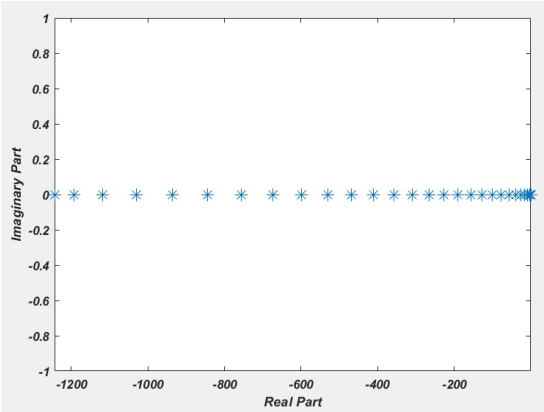

Fig. 3.2 Stability diagram derived through eigenvalue analysis of the associated matrix for $N = 30$

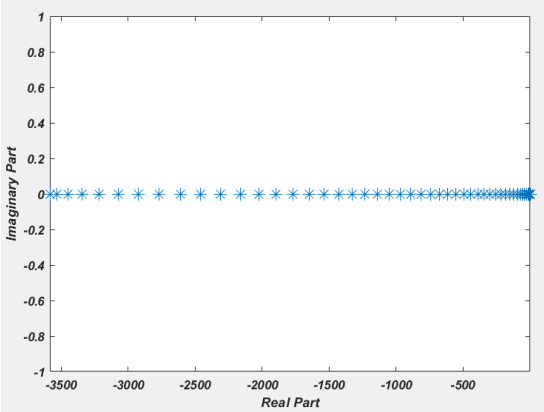

Fig. 3.3 Stability diagram derived through eigenvalue analysis of the associated matrix for $N = 50$

3.2.6 Analysis of Velocity, Temperature and Microrotation Profiles

In this subsection, the behavior of velocity, microrotation, and temperature fields in a micropolar dusty fluid is examined under the influence of various governing parameters. The analysis is carried out to understand how changes in these parameters alter the primary flow structure, the microrotational dynamics of the suspended particles, and the thermal distribution within the channel. Special emphasis is placed on interpreting the physical mechanisms—such as momentum transfer, particle–fluid interactions, rotational effects, and heat exchange—that are responsible for the observed profiles. Through this investigation, the graphical results are connected with the underlying fluid–particle physics, thereby providing deeper insights into the complex interplay of microstructural effects and thermal transport in micropolar dusty flows.

As time increases in a fluid flow, the primary and secondary velocities of the micropolar dusty fluid and dust particles tend to increase as well, assuming a constant pressure gradient. This is because the fluid particles experience an increasing amount of momentum transfer and acceleration as they move through the flow field. The relationship between the velocity and time can be seen in Figures 3.4 and 3.5, which typically takes the form of a parabolic curve. This means that the fluid particles near the center of the flow tend to move faster than those near the walls, creating a velocity gradient that is highest at the centerline.

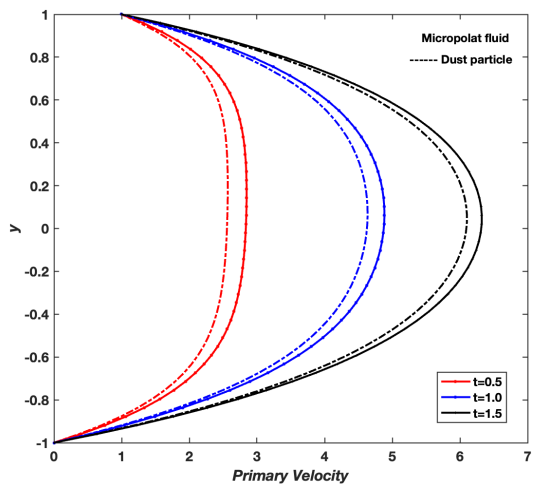

Fig. 3.4 Primary velocity profiles of fluid flow with varying time t, $Ge = 20$, $Re = 2$, $R = 100$, $Ha^2 = 2$, $Bi = 2$, $Be = 2$, $\eta = 0.5$, $Pr = 2$, $\delta = 2$, $R_1 = 0.4$, $Ec = 0.5$, $C = 0.2$, $Ek = 0.25$

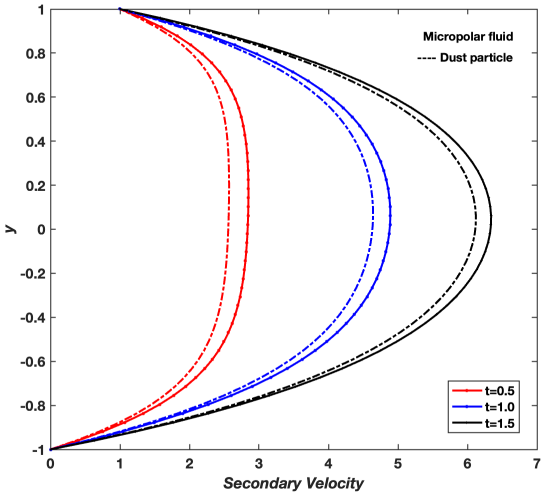

Fig. 3.5 Secondary velocity profiles of fluid flow with varying time t, $Ge = 20$, $Re = 2$, $R = 100$, $Ha^2 = 2$, $Bi = 2$, $Be = 2$, $\eta = 0.5$, $Pr = 2$, $\delta = 2$, $R_1 = 0.4$, $Ec = 0.5$, $C = 0.2$, $Ek = 0.25$

We can see how variations in constant pressure affect the primary and secondary velocities of both the micropolar dusty fluid and the dust particles by looking at Figures 3.6 and 3.7. The graphs showing this phenomenon have a parabolic shape, and it is obvious that the velocities rise as the pressure rises.

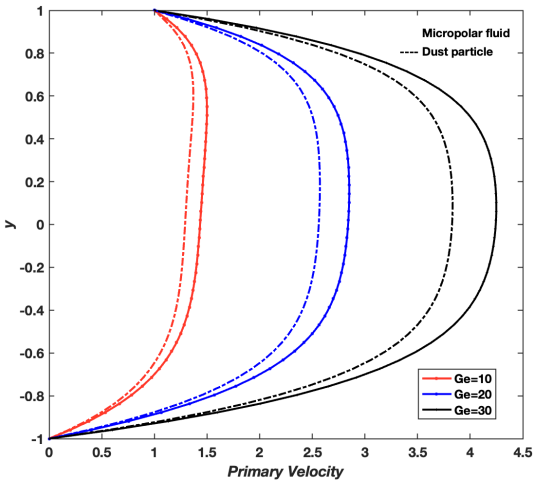

Fig. 3.6 Primary velocity profiles of fluid flow with varying pressure Ge, $t = 0.5$, $Re = 2$, $R = 100$, $Ha^2 = 2$, $Bi = 2$, $Be = 2$, $\eta = 0.5$, $Pr = 2$, $\delta = 2$, $R_1 = 0.4$, $Ec = 0.5$, $C = 0.2$, $Ek = 0.25$

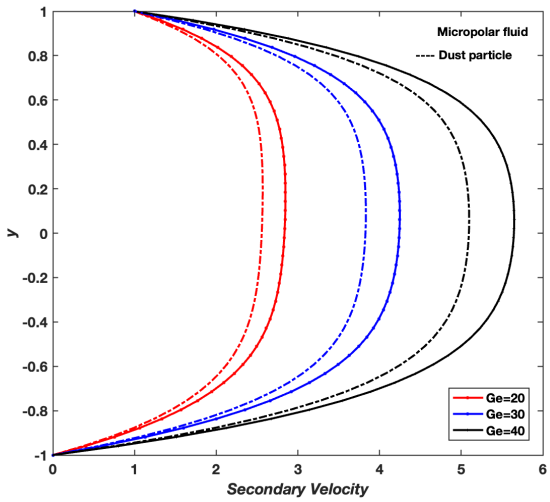

Fig. 3.7 Secondary velocity profiles of fluid flow with varying pressure Ge, $t = 0.5$, $Re = 2$, $R = 100$, $Ha^2 = 2$, $Bi = 2$, $Be = 2$, $\eta = 0.5$, $Pr = 2$, $\delta = 2$, $R_1 = 0.4$, $Ec = 0.5$, $C = 0.2$, $Ek = 0.25$

The Hartmann number also referred to as the micropolar fluid parameter that used to describe the behaviour of micropolar fluids. It represents the ratio between the characteristic length of the flow and that of the micropolar fluid. The velocities along the x and z directions for both the micropolar dusty fluid and particles decrease with increasing Ha. Moreover, the velocities of the fluid and particles remain fairly close to each other. Figures 3.8 and 3.9 showing these velocities also have a parabolic form.

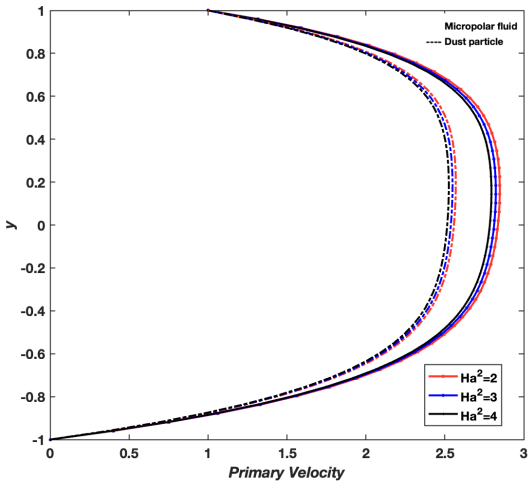

Fig. 3.8 Primary velocity profiles of fluid flow with Hartmann number Ha^2, $t = 0.5$, $Ge = 20$, $Re = 2$, $R = 100$, $Bi = 2$, $Be = 2$, $\eta = 0.5$, $Pr = 2$, $\delta = 2$, $R_1 = 0.4$, $Ec = 0.5$, $C = 0.2$, $Ek = 0.25$

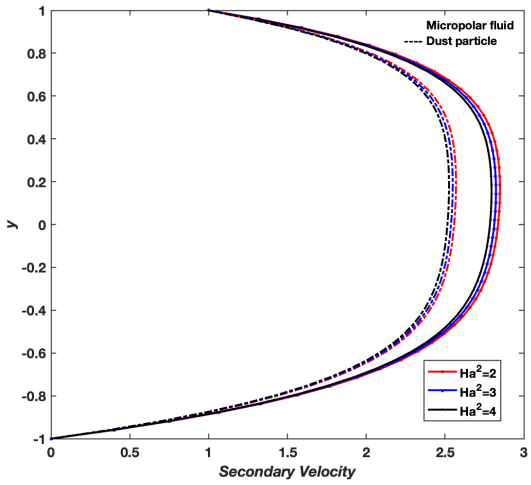

Fig. 3.9 Secondary velocity profiles of fluid flow with Hartmann number Ha^2, $t = 0.5$, $Ge = 20$, $Re = 2$, $R = 100$, $Bi = 2$, $Be = 2$, $\eta = 0.5$, $Pr = 2$, $\delta = 2$, $R_1 = 0.4$, $Ec = 0.5$, $C = 0.2$, $Ek = 0.25$

Particle concentration is the quantity of particles per unit volume of a medium, expressed either as the number of particles or the mass of particles. An increase in R leads to changes in both primary and secondary velocities of the micropolar dusty fluid and its particles. Particularly, the velocity of the micropolar dusty fluid drops as the velocity of the dusty particles increases. Figures 3.10 and 3.11's velocity graphs exhibit a parabolic curve.

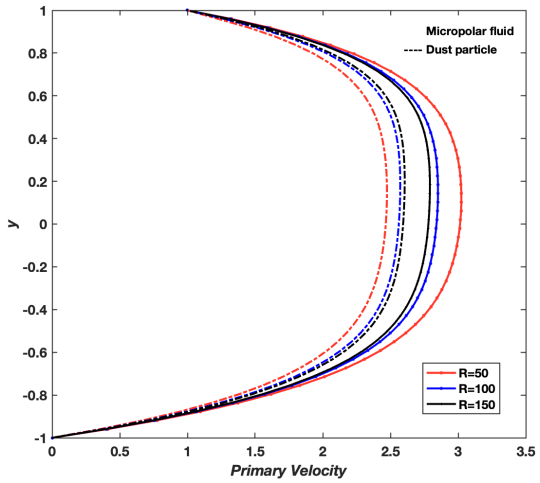

Fig. 3.10 Primary velocity profiles of fluid flow with varying particle concentration parameter R, $Ge = 20$, $Re = 2$, $Ha^2 = 2$, $Bi = 2$, $Be = 2$, $\eta = 0.5$, $Pr = 2$, $\delta = 2$, $R_1 = 0.4$, $Ec = 0.5$, $C = 0.2$, $Ek = 0.25$

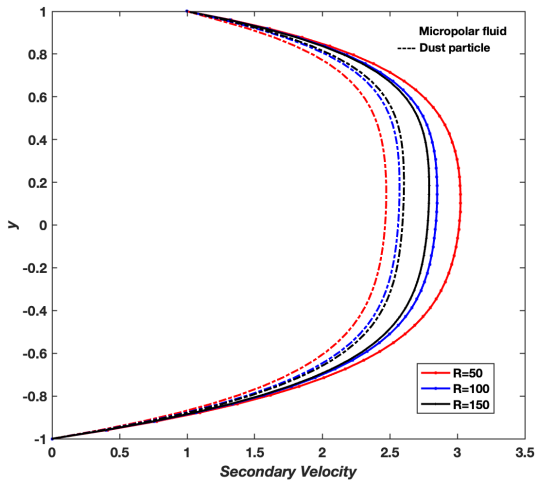

Fig. 3.11 Secondary velocity profiles of fluid flow with varying particle concentration parameter R, $Ge = 20$, $Re = 2$, $Ha^2 = 2$, $Bi = 2$, $Be = 2$, $\eta = 0.5$, $Pr = 2$, $\delta = 2$, $R_1 = 0.4$, $Ec = 0.5$, $C = 0.2$, $Ek = 0.25$

The behaviour of plasmas in fluid flows is known as the ion slip parameter. It shows the proportion of the mean free path of ions to a typical flow length scale. The ion slip parameter is a non-dimensional parameter that quantifies the mobility of ions in a fluid when exposed to an electric field. The primary and secondary velocities of both micropolar dusty fluid and dusty particles increase as the ion slip parameter is increased can be seen in Figures 3.12 and 3.13. However, the fluid and particle velocities continue to be near to one another, and the resulting graphs have a parabolic form.

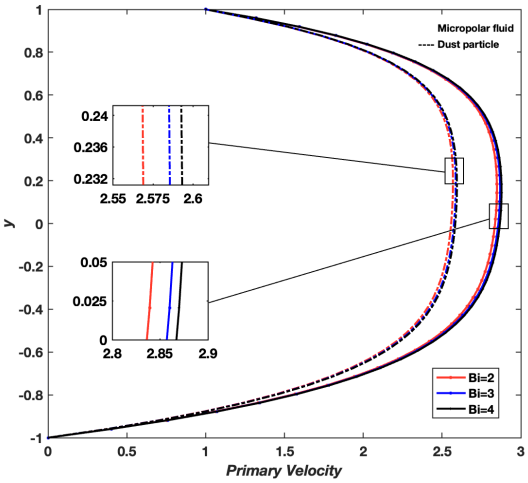

Fig. 3.12 Primary velocity profiles of fluid flow with varying Ion Slip parameter Bi, $t = 0.5$, $Ge = 20$, $Re = 2$, $R = 100$, $Ha^2 = 2$, $Be = 2$, $\eta = 0.5$, $Pr = 2$, $\delta = 2$, $R_1 = 0.4$, $Ec = 0.5$, $C = 0.2$, $Ek = 0.25$

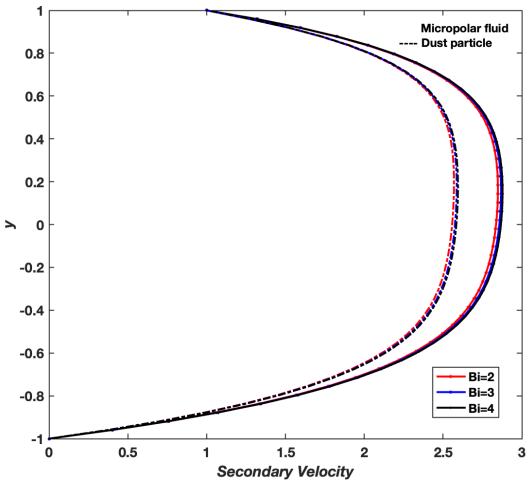

Fig. 3.13 Secondary velocity profiles of fluid flow with varying Ion Slip parameter Bi, $t = 0.5$, $Ge = 20$, $Re = 2$, $R = 100$, $Ha^2 = 2$, $Be = 2$, $\eta = 0.5$, $Pr = 2$, $\delta = 2$, $R_1 = 0.4$, $Ec = 0.5$, $C = 0.2$, $Ek = 0.25$

The Hall parameter significantly affects the fluid flow behaviour in a micropolar dusty fluid in a revolving frame. The magnitude of the Lorentz force acting on both fluid and particulate phases intensifies with higher values of the Hall parameter, leading to elevated velocities in the fluid and dust components, as illustrated in Figures 3.14 and 3.15.

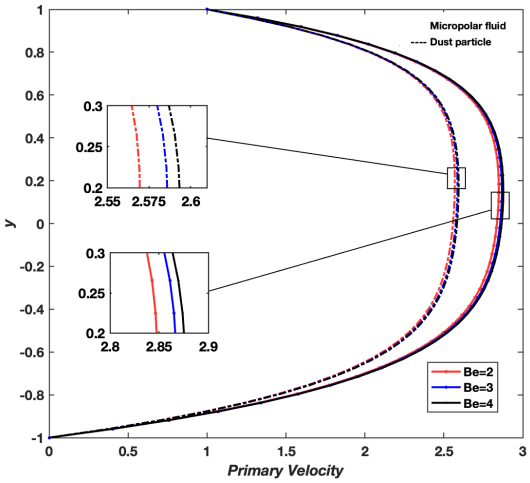

Fig. 3.14 Primary velocity profiles of fluid flow with varying Hall parameter Be, $t = 0.5$, $Ge = 20$, $Re = 2$, $R = 100$, $Ha^2 = 2$, $Bi = 2$, $\eta = 0.5$, $Pr = 2$, $\delta = 2$, $R_1 = 0.4$, $Ec = 0.5$, $C = 0.2$, $Ek = 0.25$

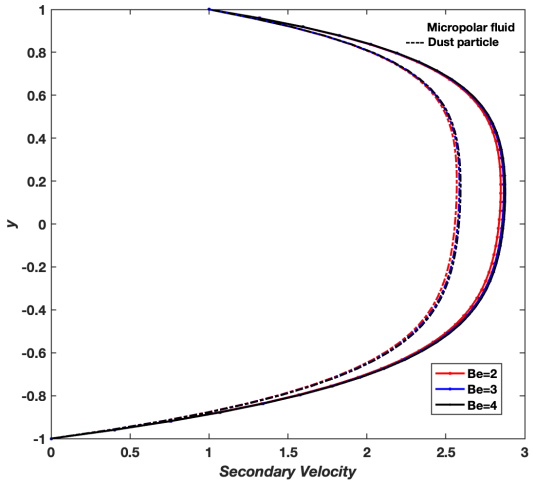

Fig. 3.15 Secondary velocity profiles of fluid flow with varying Hall parameter Be, $t = 0.5$, $Ge = 20$, $Re = 2$, $R = 100$, $Ha^2 = 2$, $Bi = 2$, $\eta = 0.5$, $Pr = 2$, $\delta = 2$, $R_1 = 0.4$, $Ec = 0.5$, $C = 0.2$, $Ek = 0.25$

The link between the fluid's velocity and its microstructure is quantified by the micropolar parameter. As observed in Figures 3.16 and 3.17, an increase in the micropolar parameter leads to a reduction in the velocities of both the micropolar fluid and suspended particles. Larger values of the micropolar parameter reflect enhanced microrotation effects, implying a stronger influence of internal spin and microstructural characteristics of the fluid particles. The internal spin creates additional resistance to the fluid motion resulting in the decrease of the primary velocity whereas with the increase in the micropolar parameter, the Coriolis-induced secondary velocities can be more pronounced because the microrotation adds to the complexity of the flow, enhancing the overall rotational effects. The fluid and particle velocities may appear to be tightly coordinated in some regions of the domain. Furthermore, the primary and secondary velocity profiles frequently have a parabolic shape.

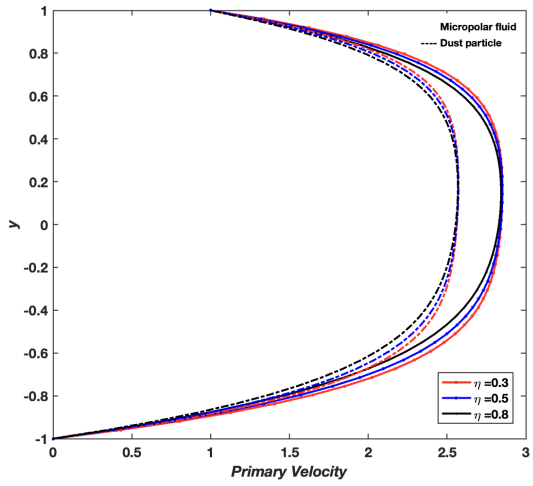

Fig. 3.16 Primary velocity profiles of fluid flow with varying micropolar parameter η, $t = 0.5$, $Ge = 20$, $Re = 2$, $R = 100$, $Ha^2 = 2$, $Bi = 2$, $Be = 2$, $Pr = 2$, $\delta = 2$, $R_1 = 0.4$, $Ec = 0.5$, $C = 0.2$, $Ek = 0.25$

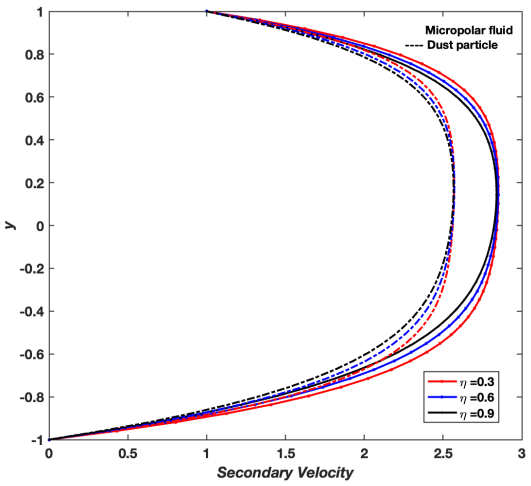

Fig. 3.17 Secondary velocity profiles of fluid flow with varying η, $t = 0.5$, $Ge = 20$, $Re = 2$, $R = 100$, $Ha^2 = 2$, $Bi = 2$, $Be = 2$, $Pr = 2$, $\delta = 2$, $R_1 = 0.4$, $Ec = 0.5$, $C = 0.2$, $Ek = 0.25$

The Prandtl number that describes the relative weights of momentum and heat transport inside the fluid. It can be observed from Figures 3.18 and 3.19 that as the Prandtl number increases, the fluid is less efficient at transferring thermal energy and more efficient at transferring momentum, this result in the velocity of the micropolar dusty fluid may be higher compared to a fluid with a lower Prandtl number.

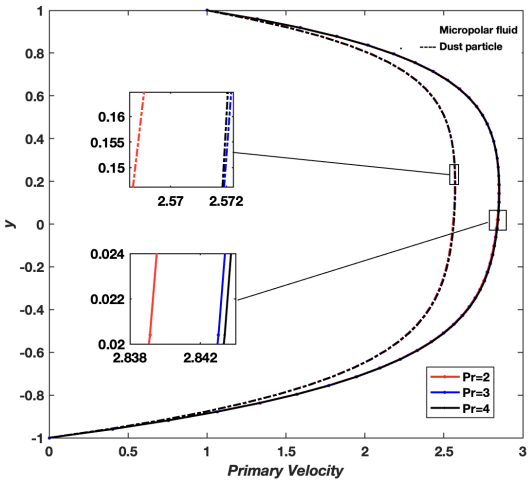

Fig. 3.18 Primary velocity profiles of fluid flow with varying Prandtl number Pr, $t = 0.5$, $Ge = 20$, $Re = 2$, $R = 100$, $Ha^2 = 2$, $Bi = 2$, $Be = 2$, $\eta = 0.5$, $\delta = 2$, $R_1 = 0.4$, $Ec = 0.5$, $C = 0.2$, $Ek = 0.25$

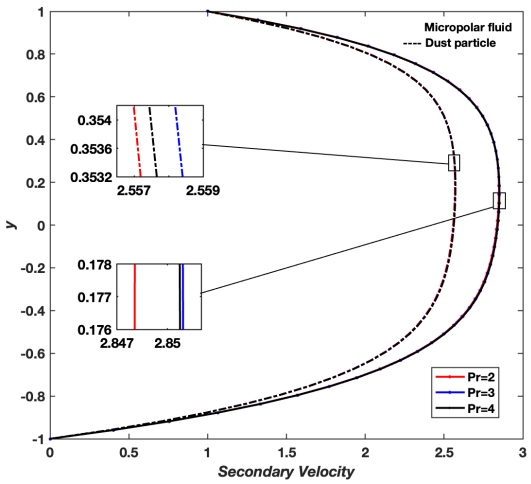

Fig. 3.19 Secondary velocity profiles of fluid flow with varying Prandtl number Pr, $t = 0.5$, $Ge = 20$, $Re = 2$, $R = 100$, $Ha^2 = 2$, $Bi = 2$, $Be = 2$, $\eta = 0.5$, $\delta = 2$, $R_1 = 0.4$, $Ec = 0.5$, $C = 0.2$, $Ek = 0.25$

The ratio of densities is calculated by dividing the density of one substance by the density of another substance. An increase in the density ratio between a micropolar dusty fluid and suspended particles results in an increase in both primary and secondary velocities for the micropolar dusty fluid and the dust particles can be seen in Figures 3.20 and 3.21. The velocity profiles are parabolic in shape.

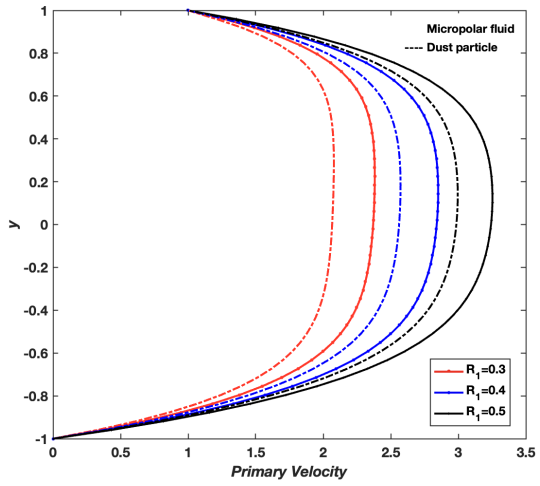

Fig. 3.20 Primary velocity profiles of fluid flow with varying ratio of densities R_1, $t = 0.5$, $Ge = 20$, $Re = 2$, $R = 100$, $Ha^2 = 2$, $Bi = 2$, $Be = 2$, $\eta = 0.5$, $Pr = 2$, $\delta = 2$, $Ec = 0.5$, $C = 0.2$, $Ek = 0.25$

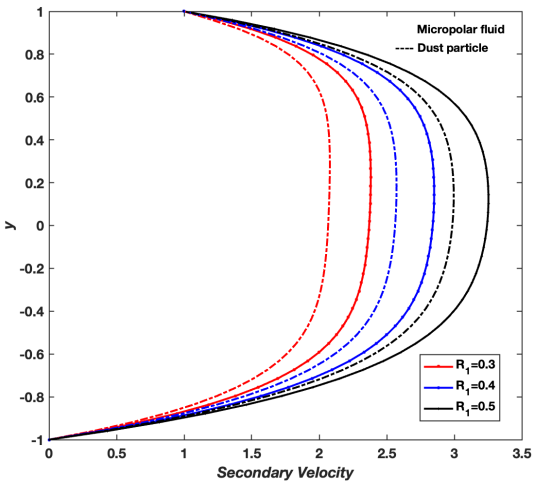

Fig. 3.21 Secondary velocity profiles of fluid flow with varying ratio of densities R_1, $t = 0.5$, $Ge = 20$, $Re = 2$, $R = 100$, $Ha^2 = 2$, $Bi = 2$, $Be = 2$, $\eta = 0.5$, $Pr = 2$, $\delta = 2$, $Ec = 0.5$, $C = 0.2$, $Ek = 0.25$

The Eckert number is used in fluid dynamics to characterize the ratio of kinetic energy of a fluid to its thermal energy. An increase in the Eckert number leads to a parabolic-shaped trend in the primary velocity of the micropolar dusty fluid and the suspended dust particles. However, the specific trend of the velocities can be different for each component, it can be observed from Figure 3.22. Figure 3.23 illustrates that the increase in the Eckert number is correlated with an increase in the secondary velocity of both the micropolar dusty fluid and for the dust particles.

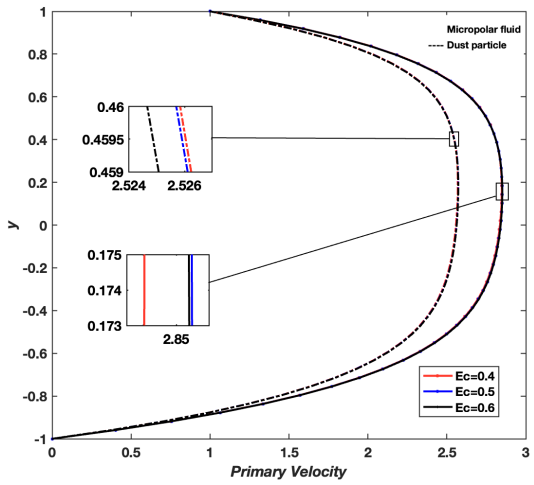

Fig. 3.22 Primary velocity profiles of fluid flow with varying Eckert number Ec, $t = 0.5$, $Ge = 20$, $Re = 2$, $R = 100$, $Ha^2 = 2$, $Bi = 2$, $Be = 2$, $\eta = 0.5$, $Pr = 2$, $\delta = 2$, $R_1 = 0.4$, $C = 0.2$, $Ek = 0.25$

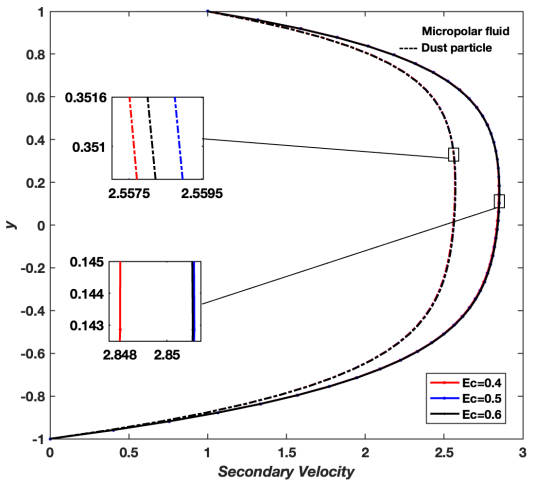

Fig. 3.23 Secondary velocity profiles of fluid flow with varying Eckert number Ec, $t = 0.5$, $Ge = 20$, $Re = 2$, $R = 100$, $Ha^2 = 2$, $Bi = 2$, $Be = 2$, $\eta = 0.5$, $Pr = 2$, $\delta = 2$, $R_1 = 0.4$, $C = 0.2$, $Ek = 0.25$

The primary and secondary velocity falls as the Coriolis frequency parameter rises as the Coriolis force has a greater impact on the flow. Because the magnetic field and the Coriolis force act in opposing directions and can partially cancel each other out, this effect is more pronounced in the presence of a magnetic field. Therefore, as shown in Figures 3.24 and 3.25, a greater Coriolis frequency parameter can produce a primary and secondary velocity profile in a rotating flow of dusty fluid that is more uniform and stable.

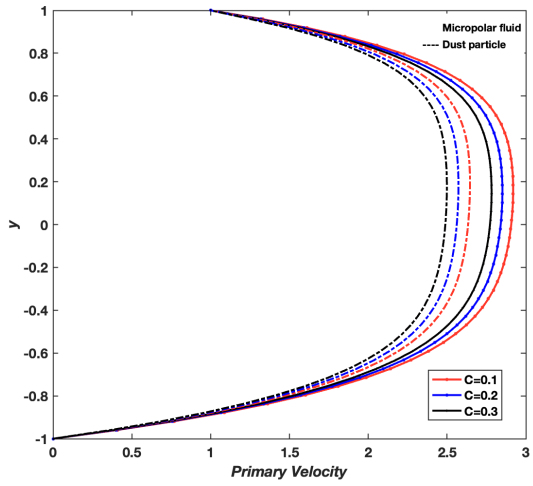

Fig. 3.24 Primary velocity profiles of fluid flow with varying Coriolis frequency parameter C, $t = 0.5$, $Ge = 20$, $Re = 2$, $R = 100$, $Ha^2 = 2$, $Bi = 2$, $Be = 2$, $\eta = 0.5$, $Pr = 2$, $\delta = 2$, $R_1 = 0.4$, $Ec = 0.5$, $Ek = 0.25$

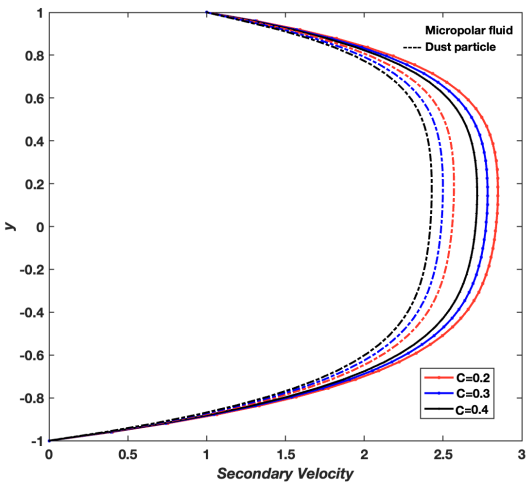

Fig. 3.25 Secondary velocity profiles of fluid flow with varying Coriolis frequency parameter C, $t = 0.5$, $Ge = 20$, $Re = 2$, $R = 100$, $Ha^2 = 2$, $Bi = 2$, $Be = 2$, $\eta = 0.5$, $Pr = 2$, $\delta = 2$, $R_1 = 0.4$, $Ec = 0.5$, $Ek = 0.25$

Figures 3.26 and 3.27 shows the impact of Ekman number on the primary and secondary velocites of the micropolar dusty fluid in a rotating flow. Figures 3.26 and 3.27 demonstrate that increasing the Ekman number reduces both primary and secondary velocities because of the combined influence of viscous forces and Lorentz forces generated by the magnetic field.

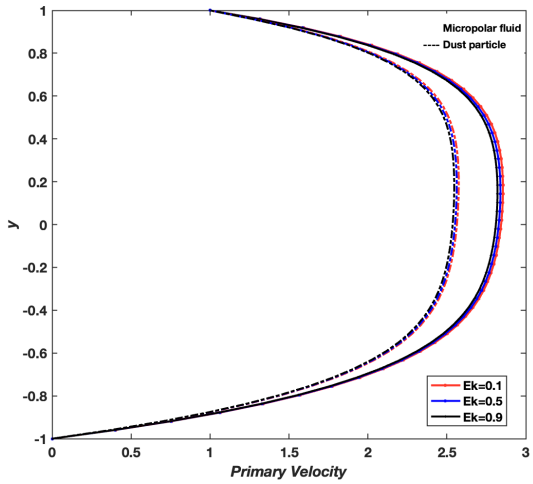

Fig. 3.26 Primary velocity profiles of fluid flow with varying Ekman number Ek, $t = 0.5$, $Ge = 20$, $Re = 2$, $R = 100$, $Ha^2 = 2$, $Bi = 2$, $Be = 2$, $\eta = 0.5$, $Pr = 2$, $\delta = 2$, $R_1 = 0.4$, $Ec = 0.5$, $C = 0.2$

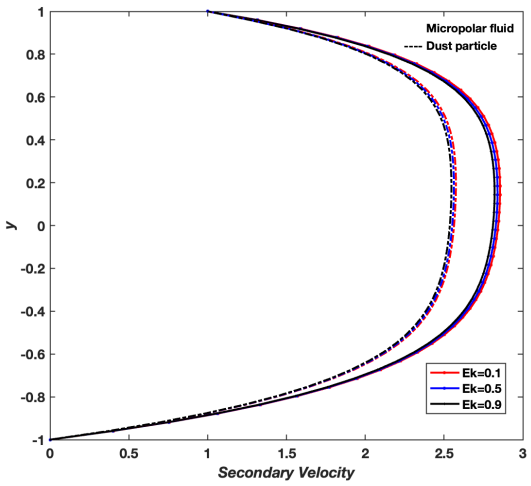

Fig. 3.27 Secondary velocity profiles of fluid flow with varying Ekman number Ek, $t = 0.5$, $Ge = 20$, $Re = 2$, $R = 100$, $Ha^2 = 2$, $Bi = 2$, $Be = 2$, $\eta = 0.5$, $Pr = 2$, $\delta = 2$, $R_1 = 0.4$, $Ec = 0.5$, $C = 0.2$

The ratio of inertial to viscous forces within a fluid medium is measured by the Reynolds number, a dimensionless metric. Lower viscous forces inside the fluid are indicated by higher Reynolds number values. The magnitude of the viscous forces reduces as the Reynolds number rises, leading to a higher degree of correlation between the fluid velocities. Figures 3.28 and 3.29 illustrates how this leads to an enhancement of the velocity profile of both fluids and dust particles.

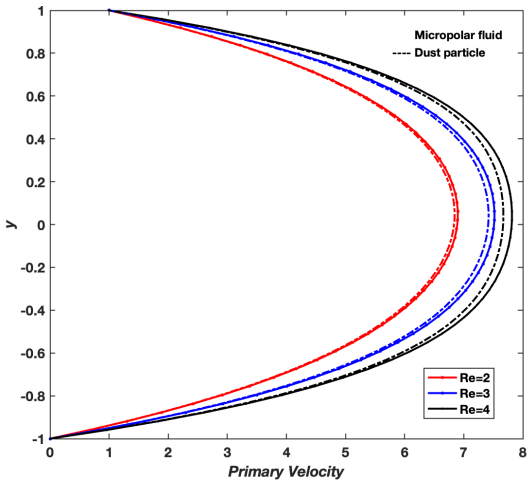

Fig. 3.28 Primary velocity profiles of fluid flow with varying Reynolds number Re, $t = 0.5$, $Ge = 20$, $R = 100$, $Ha^2 = 2$, $Bi = 2$, $Be = 2$, $\eta = 0.5$, $Pr = 2$, $\delta = 2$, $R_1 = 0.4$, $Ec = 0.5$, $C = 0.2$, $Ek = 0.25$

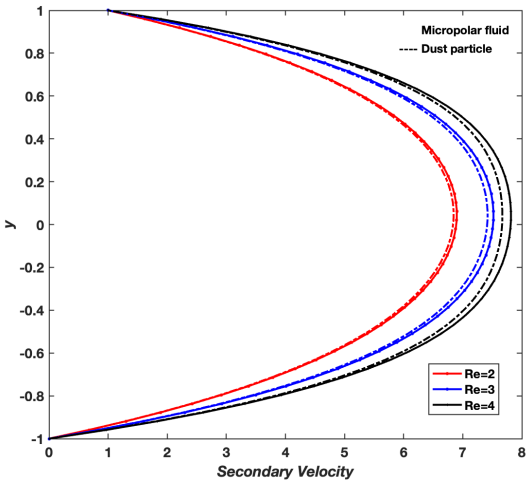

Fig. 3.29 Secondary velocity profiles of fluid flow with varying Reynolds number Re, $t = 0.5$, $Ge = 20$, $R = 100$, $Ha^2 = 2$, $Bi = 2$, $Be = 2$, $\eta = 0.5$, $Pr = 2$, $\delta = 2$, $R_1 = 0.4$, $Ec = 0.5$, $C = 0.2$, $Ek = 0.25$

Microrotation refers to the rotational motion of small particles suspended in a micropolar fluid. In micropolar fluids, fluid motion is characterized by translational velocity and microrotation, which represents the rotation of fluid elements at a microscopic level. When dust particles are present in micropolar fluids, the coupling between the fluid's microrotation and the suspended particles becomes important.

The effect of constant pressure (Ge) on angular velocities is demonstrated in Figure 3.30. It is observed that the increase in pressure increases the microrotation of the fluid noticeably. The graph depicted in Figure 3.31 shows the impact of time on microrotations. It is apparent that the microrotation increases over time, eventually reaching a stable state after a certain duration.

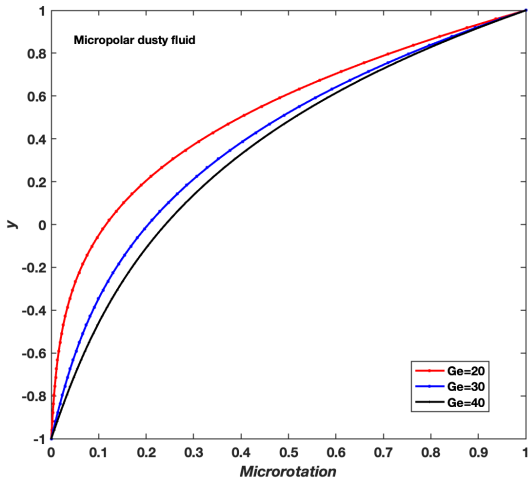

Fig. 3.30 Microrotation of fluid flow with varying constant pressure Ge, $t = 0.5$, $Re = 2$, $R = 200$, $Ha^2 = 2$, $Bi = 2$, $Be = 2$, $\eta = 0.5$, $Pr = 2$, $\delta = 2$, $R_1 = 0.4$, $Ec = 0.5$, $C = 0.2$, $Ek = 0.25$

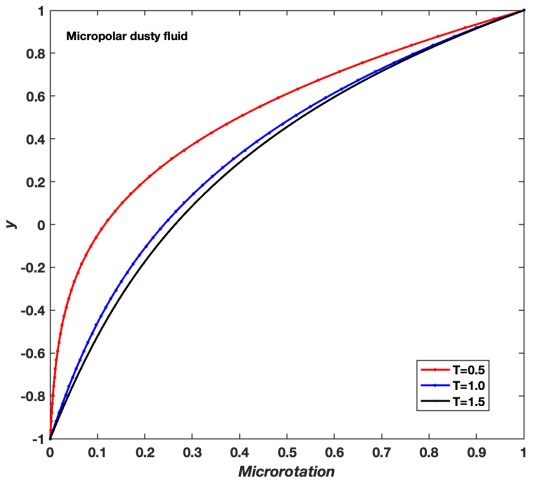

Fig. 3.31 Microrotation of fluid flow with varying time t, $Ge = 20$, $Re = 2$, $R = 100$, $Ha^2 = 2$, $Bi = 2$, $Be = 2$, $\eta = 0.5$, $Pr = 2$, $\delta = 2$, $R_1 = 0.4$, $Ec = 0.5$, $C = 0.2$, $Ek = 0.25$

Figure 3.32 shows that the microrotation profile increases with the increase in Reynold's number (Re). The influence of the micropolar parameter η on microrotation behavior is depicted in Figure 3.33. The microrotation initially increases with the micropolar parameter but eventually overlapped with the previous value. This is because the local angular velocity field induces rotations of fluid particles, and a stronger field will induce larger rotations.

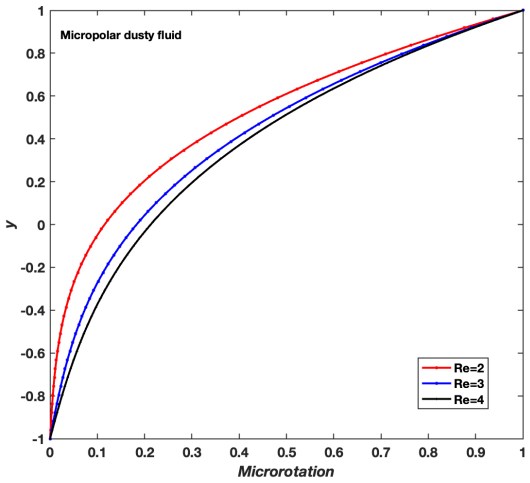

Fig. 3.32 Microrotation profiles of fluid flow with varying Reynolds number Re, $t = 0.5$, $R = 200$, $Ha^2 = 2$, $Bi = 2$, $Be = 2$, $\eta = 0.5$, $Pr = 2$, $\delta = 2$, $R_1 = 0.4$, $Ec = 0.5$, $C = 0.2$, $Ek = 0.25$

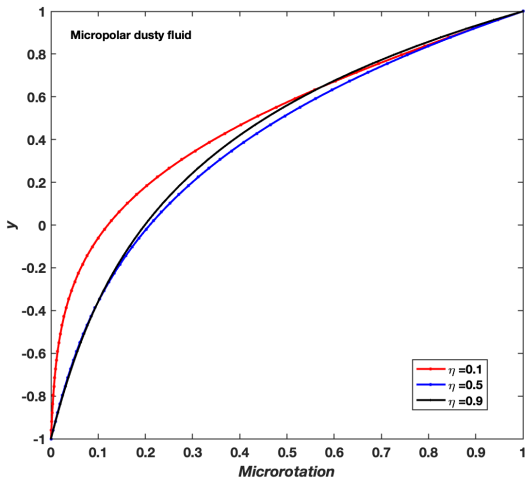

Fig. 3.33 Microrotation profiles of fluid flow with varying micropolar parameter η, $t = 0.5$, $Ge = 20$, $Re = 2$, $R = 100$, $Ha^2 = 2$, $Bi = 2$, $Be = 2$, $Pr = 2$, $\delta = 2$, $R_1 = 0.4$, $Ec = 0.5$, $C = 0.2$, $Ek = 0.25$

An increase in a constant pressure, causes the temperature of the micropolar dusty fluid and dusty particles to increase due to the increase in internal energy of the fluid particles. The temperature profile is parabolic as illustrated in Figure 3.34, with the temperature being highest at the centerline of the flow and decreasing towards the walls of the flow channel. Figure 3.35 shows the effect of time on the temperature profile of micropolar dusty fluid and dust particles. Increase in temperature can be observe due to the friction and collisions between the fluid particles and the dust particles, which transfer energy and cause heating.

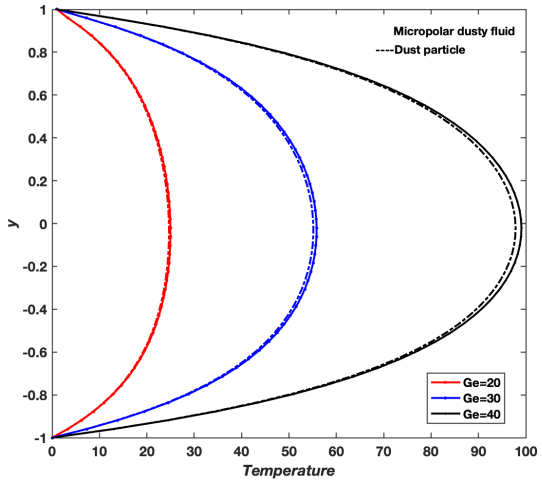

Fig. 3.34 Temperature profiles of fluid flow with varying constant pressure Ge, $t = 3$, $Re = 2$, $R = 50$, $Ha^2 = 1$, $Bi = 0.2$, $Be = 0.2$, $\eta = 0.2$, $Pr = 0.5$, $\delta = 1$, $R_1 = 0.8$, $Ec = 0.8$, $C = 0.2$, $Ek = 0.25$

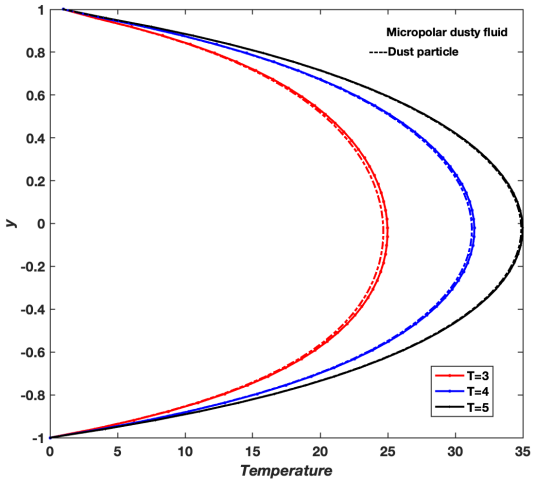

Fig. 3.35 Temperature profiles of fluid flow with varying time t, $Ge = 20$, $Re = 2$, $R = 50$, $Ha^2 = 1$, $Bi = 0.2$, $Be = 0.2$, $\eta = 0.2$, $Pr = 0.5$, $\delta = 1$, $R_1 = 0.8$, $Ec = 0.8$, $C = 0.2$, $Ek = 0.25$

Figure 3.36 shows that increasing the Reynolds number results in more friction and energy loss in the fluid, which raises the fluid's temperature and that of the dust particles. From Figure 3.37 we can observe an increase in the particle concentration parameter leads to a decrease in the temperature of the fluid and the dust particles, as the concentration of microscale particles in the fluid increases, the effective viscosity of the fluid also increases, this increased viscosity can lead to increased friction and energy dissipation in the fluid, resulting in the decrement of temperature.

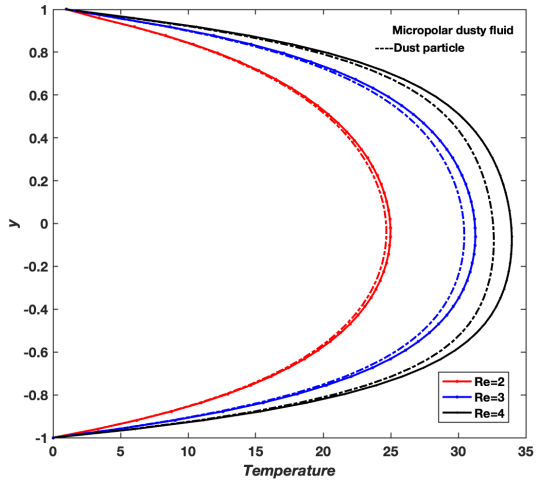

Fig. 3.36 Temperature profiles of fluid flow with varying Reynolds number Re, $t = 3$, $Ge = 20$, $R = 50$, $Ha^2 = 1$, $Bi = 0.2$, $Be = 0.2$, $\eta = 0.2$, $Pr = 0.5$, $\delta = 1$, $R_1 = 0.8$, $Ec = 0.8$, $C = 0.2$, $Ek = 0.25$

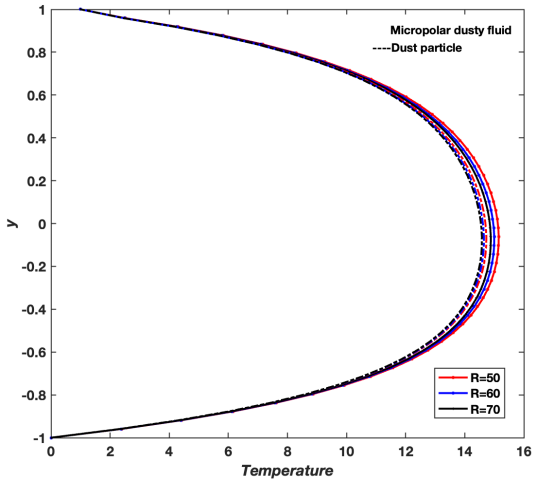

Fig. 3.37 Temperature profiles of fluid flow with varying particle concentration parameter R, $t = 3$, $Ge = 20$, $Re = 2$, $Ha^2 = 1$, $Bi = 0.2$, $Be = 0.2$, $\eta = 0.2$, $Pr = 0.5$, $\delta = 1$, $R_1 = 0.8$, $Ec = 0.8$, $C = 0.2$, $Ek = 0.25$

An increase in the Hartmann number results in a rise in the temperatures of both the fluid and dust particles, as displayed in Figure 3.38. From Figure 3.39 we can see that, increasing the ion slip parameter can lead to an increase in the effective viscosity of the fluid and results in increased friction and energy dissipation, this leads to an increase in the overall temperature of the fluid and the dust particles.

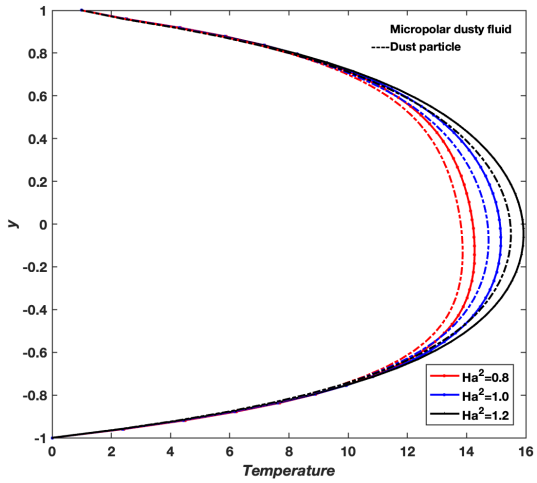

Fig. 3.38 Temperature profiles of fluid flow with varying Hartmann number Ha^2, $t = 3$, $Ge = 20$, $Re = 2$, $R = 50$, $Bi = 0.2$, $Be = 0.2$, $\eta = 0.2$, $Pr = 0.5$, $\delta = 1$, $R_1 = 0.8$, $Ec = 0.8$, $C = 0.2$, $Ek = 0.25$

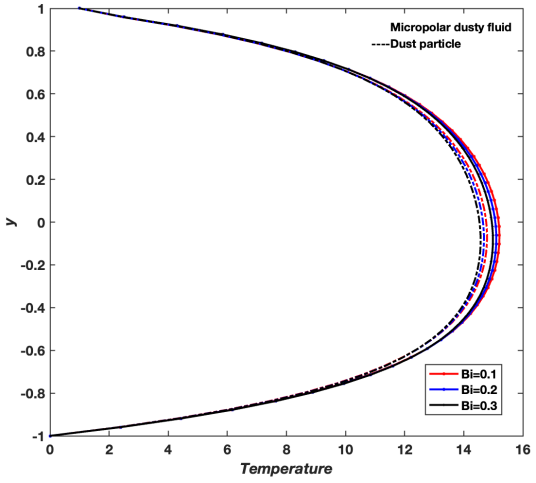

Fig. 3.39 Temperature profiles of fluid flow with varying Ion slip parameter Bi, $t = 3$, $Ge = 20$, $Re = 2$, $R = 50$, $Ha^2 = 1$, $Be = 0.2$, $\eta = 0.2$, $Pr = 0.5$, $\delta = 1$, $R_1 = 0.8$, $Ec = 0.8$, $C = 0.2$, $Ek = 0.25$

Effect of increasing the Hall parameter leads to a decrease in the temperature of a micropolar dusty fluid and the dust particles can be seen in Figure 3.40. This is due to the fact that a higher Hall parameter can lead to increased electromagnetic forces, which enhances the mixing and heat transfer between the fluid and the particles, this lead to a potentially lower overall temperatures. An increase in the micropolar parameter causes the fluid's effective viscosity to rise, which increases friction and energy loss. The fluid and the particles' overall temperature rises as a result of this as seen in Figure 3.41.

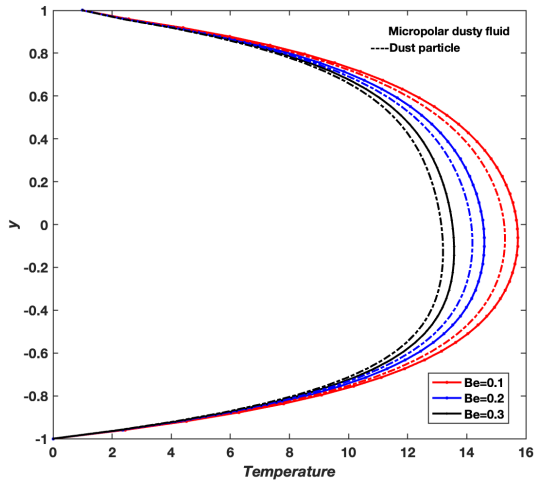

Fig. 3.40 Temperature profiles of fluid flow with varying Hall parameter Be, $t = 3$, $Ge = 20$, $Re = 2$, $R = 50$, $Ha^2 = 1$, $Bi = 0.2$, $\eta = 0.2$, $Pr = 0.5$, $\delta = 1$, $R_1 = 0.8$, $Ec = 0.8$, $C = 0.2$, $Ek = 0.25$

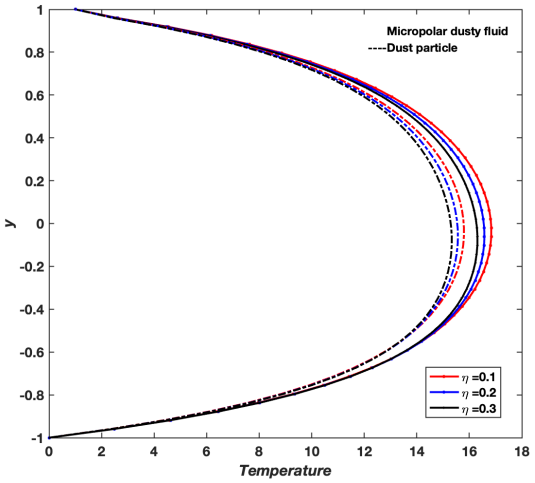

Fig. 3.41 Temperature profiles of fluid flow with varying micropolar parameter η, $t = 3$, $Ge = 20$, $Re = 2$, $R = 50$, $Ha^2 = 1$, $Bi = 0.2$, $Be = 0.2$, $Pr = 0.5$, $\delta = 1$, $R_1 = 0.8$, $Ec = 0.8$, $C = 0.2$, $Ek = 0.25$

When the prandtl number rises, the fluid is transferring heat more effectively than momentum. This leads to an increase in heat transfer and a decrease in the temperature gradient, which results in an increase in temperature as illustrated in 3.42. Figure 3.43 shows that as the ratio of densities increases, the temperature of dusty particles and micropolar dusty fluid rises. It can also be seen that the temperature difference between the micropolar dusty fluid and the dusty particles is larger.

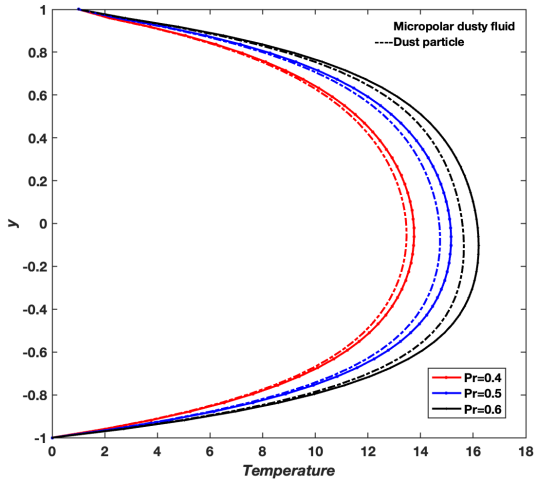

Fig. 3.42 Temperature profiles of fluid flow with varying Prandtl number Pr, $t = 3$, $Ge = 20$, $Re = 2$, $R = 50$, $Ha^2 = 1$, $Bi = 0.2$, $Be = 0.2$, $\eta = 0.2$, $\delta = 1$, $R_1 = 0.8$, $Ec = 0.8$, $C = 0.2$, $Ek = 0.25$

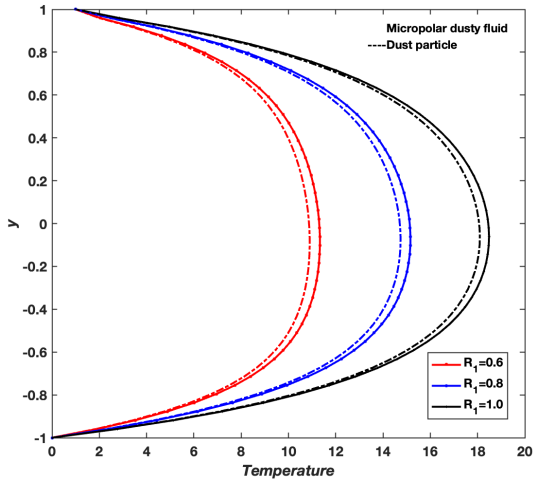

Fig. 3.43 Temperature profiles of fluid flow with varying ratio of densities R_1, $t = 3$, $Ge = 20$, $Re = 2$, $R = 50$, $Ha^2 = 1$, $Bi = 0.2$, $Be = 0.2$, $\eta = 0.2$, $Pr = 0.5$, $\delta = 1$, $Ec = 0.8$, $C = 0.2$, $Ek = 0.25$

As the Eckert number rises, the rotational motion of the fluid intensifies mixing and convection, which boosts heat transfer and elevates temperature, as observed in Figure 3.44.

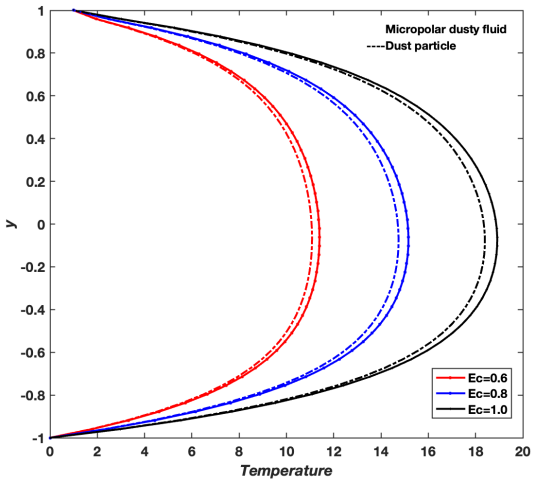

Fig. 3.44 Temperature profiles of fluid flow with varying Eckert number Ec, $t = 3$, $Ge = 20$, $Re = 2$, $R = 50$, $Ha^2 = 1$, $Bi = 0.2$, $Be = 0.2$, $\eta = 0.2$, $Pr = 0.5$, $\delta = 1$, $R_1 = 0.8$, $C = 0.2$, $Ek = 0.25$

3.3 Mathematical Modeling of Micropolar Dusty Fluid Flow in an Inclined Channel

The mathematical modeling of micropolar dusty fluid flow is extended here from the horizontal channel configuration (discussed in *Section 3.2*) to the inclined channel geometry. This extension is crucial for capturing the combined effects of gravitational forces along the channel inclination, rotation, magnetic field, and micropolar interactions, which are pertinent to many engineering and geophysical flow scenarios.

The inclined channel consists of two infinite parallel plates separated by a distance $2L$ and inclined at an angle θ with respect to the horizontal axis. The fluid flow is driven by the motion of the upper plate and a constant pressure gradient along the flow direction aligned with the channel incline. The system undergoes uniform rotation about the y-axis, and the fluid is subjected to a transverse magnetic field. The presence of dust particles suspended uniformly within the micropolar fluid introduces interphase

momentum and thermal coupling, thus complicating the flow dynamics.

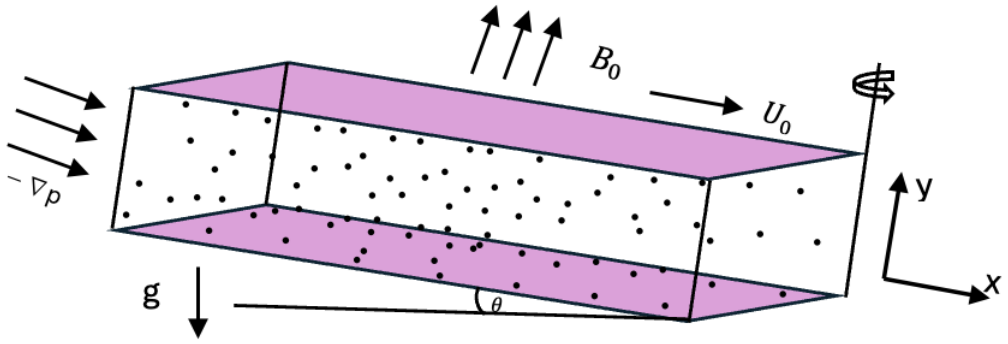

Fig. 3.45 Schematic of an Inclined Channel with Micropolar Dusty Fluid Flow

3.3.1 Key Features of the Model

The essential features of the inclined channel model are summarized as follows:

(a) **Inclined Channel Geometry:** The flow region is bounded by two infinitely long, parallel plates set at an angle θ relative to the horizontal. The x-axis is oriented along the incline, and the transverse coordinate y measures the perpendicular distance between the plates, scaled by half the channel width L.

(b) **Micropolar Dusty Fluid:** The fluid phase is characterized by micropolar behavior, capturing micro-rotational effects via the microrotation vector $\mathbf{M}$, vortex viscosity κ, and spin viscosity γ. Suspended spherical dust particles with volume fraction ϕ interact dynamically with the fluid phase through drag forces proportional to the relative velocity difference.

(c) **Rotation and Magnetic Field Effects:** Uniform rotation at angular velocity Ω induces Coriolis and centrifugal forces, affecting both primary and secondary velocity components. A uniform, static magnetic field B_0 applied transversely generates Lorentz forces opposing fluid motion, modulated by ion slip Bi and Hall Be parameters.

(d) **Gravitational Inclination Effects:** The channel inclination introduces a gravitational acceleration component $g \sin\theta$ along the flow direction, which acts as an

additional body force on both fluid and particle phases, influencing momentum transfer and flow stability.

(e) **Velocity Components:** The fluid velocity vector is $\mathbf{u} = (u_1, 0, u_3)$, representing primary flow along x and secondary flow along z arising from rotation-induced Coriolis effects. The dust particle velocity vector is $\mathbf{u}_p = (u_{1p}, 0, u_{3p})$.

3.3.2 Modified Governing Equations

Building upon the governing equations derived for micropolar dusty fluid flow in a horizontal channel (Equations (3.13) - (3.17)), the inclined channel formulation incorporates the gravitational force component along the channel inclination. The resulting dimensional momentum equations for the fluid and particle phases become:

$$\rho_f \left(\frac{\partial \mathbf{u}}{\partial t} + 2(\Omega \times \mathbf{u}) + (\mathbf{u} \cdot \nabla)\mathbf{u} \right) = -\nabla P + (\mu + \kappa)\nabla^2 \mathbf{u} + \kappa \nabla \times \mathbf{M} - \mathbf{F}_L + \frac{\phi_p \rho_p}{1 - \phi_p} \chi (\mathbf{u}_p - \mathbf{u}) + \rho_f \mathbf{g}_\theta \tag{3.41}$$

$$\rho_p \frac{\partial \mathbf{u}_p}{\partial t} = \rho_p \chi (\mathbf{u} - \mathbf{u}_p) + \rho_p \mathbf{g}_\theta \tag{3.42}$$

$$\rho_f j \frac{\partial \mathbf{M}}{\partial t} = \gamma \nabla^2 \mathbf{M} - \kappa \left(2\mathbf{M} - \nabla \times \mathbf{u} \right) \tag{3.43}$$

$$\rho_f c_p \left(\frac{\partial T}{\partial t} \right) = k \nabla^2 T + \mu \left| \nabla \mathbf{u} \right|^2 + \kappa \left| 2\mathbf{M} - \nabla \times \mathbf{u} \right|^2 + \beta \left| \nabla \mathbf{M} \right|^2 - \frac{\phi_p \rho_p c_{p,p}}{1 - \phi_p} \frac{1}{\tau_T} (T - T_p) + Q + \frac{\phi_p \rho_p}{1 - \phi_p} \chi \left| \mathbf{u}_p - \mathbf{u} \right|^2 + \mathbf{F}_L \cdot \mathbf{u} \tag{3.44}$$

$$\rho_p c_{p,p} \left(\frac{\partial T_p}{\partial t} \right) = \frac{\rho_p c_{p,p}}{\tau_T} (T - T_p) \tag{3.45}$$

Note: In modeling the dust particle phase, simplifications are commonly made by neglecting convective acceleration, pressure gradients, gravitational, and Coriolis forces. These assumptions are valid for small, rigid particles in dilute suspensions where drag forces dominate particle behavior and inertial or body forces have minimal impact.

where:

- $\mathbf{g}_\theta = g \sin\theta \, \mathbf{i}$ is the gravitational acceleration component along the channel incline
- $\mathbf{u}, \mathbf{u}_p$ = Fluid and particle velocity vectors, respectively.
- ϕ_p = Particle volume fraction, with $1 - \phi_p$ representing the fluid fraction.
- Ω = Angular velocity vector, introducing Coriolis effects via $2\rho_f(\Omega \times \mathbf{u})$.
- $\mathbf{F}_L$ = Lorentz force, given by

$$\mathbf{F}_L = \sigma B_0^2 \frac{(1 + B_i B_e)}{(1 + B_i B_e)^2 + B_e^2} \mathbf{u},$$

  where σ is the electrical conductivity, B_0 is the magnetic field strength, and B_i, B_e are the ion slip and Hall parameters.
- $\mathbf{M}$ = Microrotation vector; κ = Vortex viscosity; γ = Spin viscosity.
- χ = Interphase momentum transfer coefficient (drag parameter).

$$\chi = \frac{1}{\tau_p(1 - \phi_p)},$$

- τ_p, τ_T = Relaxation times for momentum and temperature exchange between fluid and particle phases.
- $c_p, c_{p,p}$ = Specific heat of fluid and particles, respectively.
- Φ, Q = Viscous dissipation and internal heat source in the fluid.
- β = Microrotational heat diffusion coefficient.

The modified governing equations (3.41) to (3.45) expressed in the following *compo-*

nent form:

$$\rho_f\left(\frac{\partial u_1}{\partial t}-2\Omega u_3\right)=-\frac{\partial P}{\partial x}+(\mu+\kappa)\frac{\partial^2 u_1}{\partial y^2}+\kappa\frac{\partial \mathbf{M}}{\partial y}-\frac{\sigma B_0^2(1+B_iB_e)}{(1+B_iB_e)^2+B_e^2}u_1 + \frac{\phi_p\rho_p}{1-\phi_p}\chi(u_{1p}-u_1)+\rho_f g\sin\theta \tag{3.46}$$

$$\rho_f\left(\frac{\partial u_3}{\partial t}+2\Omega u_1\right)=(\mu+\kappa)\frac{\partial^2 u_3}{\partial y^2}+\kappa\frac{\partial \mathbf{M}}{\partial y}-\frac{\sigma B_0^2(1+B_iB_e)}{(1+B_iB_e)^2+B_e^2}u_3 + \frac{\phi_p\rho_p}{1-\phi_p}\chi(u_{3p}-u_3) \tag{3.47}$$

$$\rho_p\frac{\partial u_{1p}}{\partial t}=\rho_p\chi(u_1-u_{1p})+\rho_p g\sin\theta \tag{3.48}$$

$$\rho_p\frac{\partial u_{3p}}{\partial t}=\rho_p\chi(u_3-u_{3p}) \tag{3.49}$$

$$\rho_f j\frac{\partial \mathbf{M}}{\partial t}=\gamma\frac{\partial^2 \mathbf{M}}{\partial y^2}-\kappa\left(2\mathbf{M}+\frac{\partial u_1}{\partial y}\right) \tag{3.50}$$

$$\rho_f c_p\frac{\partial T}{\partial t}=k\frac{\partial^2 T}{\partial y^2}+\mu\left(\frac{\partial u_1}{\partial y}\right)^2+\kappa\left(2M+\frac{\partial u_1}{\partial y}\right)^2+\beta\left(\frac{\partial \mathbf{M}}{\partial y}\right)^2+\frac{\sigma B_0^2(1+B_iB_e)}{(1+B_iB_e)^2+B_e^2}u_1^2 + \frac{\phi_p\rho_p c_{p,p}}{1-\phi_p}\frac{1}{\tau_T}(T_p-T)+Q+\frac{\phi_p\rho_p}{1-\phi_p}\chi(u_1-u_{1p})^2 \tag{3.51}$$

$$\frac{\partial T_p}{\partial t}=\frac{(T-T_p)}{\tau_T} \tag{3.52}$$

(a) **Dimensionless Variables:** To simplify the governing equations and facilitate numerical analysis, we introduce the following characteristic scales:

- Characteristic length: L (half-distance between plates)
- Characteristic velocity: U_0
- Characteristic time: $\dfrac{L}{U_0}$
- Characteristic pressure: $\rho_f U_0^2$
- Characteristic microrotation: $\dfrac{U_0}{L}$

- Characteristic temperature: $T_2 - T_1$

Using these, the dimensionless variables are defined as:

$$y^* = \frac{y}{L}, \quad t^* = \frac{tU_0}{L}, \quad u_i^* = \frac{u_i}{U_0}, \quad u_{ip}^* = \frac{u_{ip}}{U_0},$$
$$M^* = \frac{\mathbf{M}L}{U_0}, \quad T^* = \frac{T - T_1}{T_2 - T_1}, \quad T_p^* = \frac{T_p - T_1}{T_2 - T_1}, \quad P^* = \frac{P}{\rho_f U_0^2}$$

where T_1 and T_2 denote the temperatures corresponding to the lower and upper plates, in that order. For simplicity, superscript asterisks are omitted in the subsequent equations.

(b) **Initial and Boundary Conditions:** The initial and boundary conditions are:

- At $t = 0$:

$$u_1(y,0) = u_3(y,0) = u_{1p}(y,0) = u_{3p}(y,0) = 0,$$
$$M(y,0) = 0, \quad T(y,0) = T_p(y,0) = 0$$

- At $y = -1$ (for all $t > 0$):

$$u_1 = u_3 = u_{1p} = u_{3p} = 0, \quad M = T = T_p = T_1$$

- At $y = 1$:

$$u_1 = u_3 = u_{1p} = u_{3p} = 1, \quad M = T = T_p = T_2$$

(c) **Dimensionless Parameters:** The dimensionless parameters used in the governing equations, defined as discussed in *Section 1.9* of *Chapter 1*, are given by:

Reynolds number:	$Re = \dfrac{\rho_f U_0 L}{\mu}$
Micropolar Parameter:	$\eta = \dfrac{\kappa}{\mu}$
Hartmann number squared:	$Ha^2 = \dfrac{\sigma B_0^2 L^2}{\mu}$
Eckert number:	$Ec = \dfrac{U_0^2}{c_p(T_2 - T_1)}$
Prandtl number:	$Pr = \dfrac{\mu c_p}{k}$
Dissipation parameter:	$\delta = \dfrac{\beta}{\mu L^2}$
Particle concentration parameter:	$R = \dfrac{\phi_p \rho_p L^2}{(1-\phi_p)\mu}$
Density ratio parameter:	$R_1 = \dfrac{\rho_f}{\rho_p}$
Coriolis frequency parameter:	$C = 4\pi\Omega$
Ekman number:	$Ek = \dfrac{Re}{4\pi}$

(d) **Dimensionless Governing Equations:** By introducing nondimensional variables and parameters, the governing relations (3.46) to (3.52) are transformed into the nondimensional form presented below:

$$\frac{\partial u_1}{\partial t} = Ge(t) + \frac{\eta}{Re}\frac{\partial \mathbf{M}}{\partial y} + \frac{1+\eta}{Re}\frac{\partial^2 u_1}{\partial y^2} - \frac{Ha^2}{Re}\left(\frac{(1+BiBe)u_1 + Beu_3}{(1+BiBe)^2 + Be^2}\right) - \frac{R}{Re}(u_1 - u_{1p}) - \frac{2CEk}{Re}u_3 + \frac{\sin\theta}{F} \tag{3.53}$$

$$\frac{\partial u_3}{\partial t} = \frac{\eta}{Re}\frac{\partial \mathbf{M}}{\partial y} + \frac{1+\eta}{Re}\frac{\partial^2 u_3}{\partial y^2} - \frac{Ha^2}{Re}\left(\frac{(1+BiBe)u_3 + Beu_1}{(1+BiBe)^2 + Be^2}\right) - \frac{R}{Re}(u_3 - u_{3p}) + \frac{2CEk}{Re}u_1 \tag{3.54}$$

$$\frac{\partial u_{1p}}{\partial t} = \frac{RR_1}{Re}(u_1 - u_{1p}) - \frac{C}{2\pi}u_{3p} + \frac{\sin\theta}{F} \tag{3.55}$$

$$\frac{\partial u_{3p}}{\partial t} = \frac{RR_1}{Re}(u_3 - u_{3p}) + \frac{C}{2\pi}u_{1p} \tag{3.56}$$

$$\frac{\partial \mathbf{M}}{\partial t} = \frac{1}{Re}\left(1 + \frac{\eta}{2}\right)\frac{\partial^2 \mathbf{M}}{\partial y^2} - \frac{\eta}{Re}\left(2\mathbf{M} + \frac{\partial u_1}{\partial y}\right) \tag{3.57}$$

$$\frac{\partial T}{\partial t} = \frac{1}{PrRe}\frac{\partial^2 T}{\partial y^2} + \frac{Ec}{Re}\left[\left(\frac{\partial u_1}{\partial y}\right)^2 + \eta\left(2\mathbf{M} + \frac{\partial u_1}{\partial y}\right)^2 + \delta\left(\frac{\partial \mathbf{M}}{\partial y}\right)^2\right] + \frac{EcHa^2}{Re}\left(\frac{(1+BiBe)}{(1+BiBe)^2+Be^2}\right)u_1^2 + \frac{2R}{3PrRe}(T_p - T) + \frac{REc}{Re}(u_1 - u_{1p})^2 \tag{3.58}$$

$$\frac{\partial T_p}{\partial t} = -\frac{2RR_1}{3PrRe}(T_p - T) \tag{3.59}$$

3.3.3 Numerical Solution using Radial Basis Function Pseudospectral Method

The system of PDE's (3.53) to (3.59) governing micropolar dusty fluid flow in an inclined channel is now solved using the RBF-PSM. This method offers a meshfree approach with spectral accuracy, enabling precise approximation of spatial derivatives and effective handling of complex boundary conditions and domain geometries. A detailed exposition of the RBF-PSM methodology is provided in *Chapter 1*, *Section 1.10.7*, which lays the theoretical foundation for its application.

The key steps involved in employing RBF-PSM to solve the system of PDEs can be outlined as follows:

(a) **Domain Discretization:** The spatial domain $y \in [-1, 1]$ is discretized into N collocation nodes y_i where $i = 1, 2, \ldots, N$.

(b) **RBF Approximation:** Each dependent variable $z(y,t) \in \{u_1, u_3, u_{1p}, u_{3p}, M, T, T_p\}$ is approximated as a linear combination of radial basis functions centered at the nodes:

$$z(y,t) \approx \sum_{j=1}^{N} \lambda_j(t)\, \phi(\|y - y_j\|)$$

where ϕ is the wendland radial basis function (as per Equation (2.13) of *Section 2.2.3*) and $\lambda_j(t)$ are the time-dependent coefficients.

(c) **Interpolation Matrix Construction:** The interpolation matrix A with elements

$A_{ij} = \phi(\|y_i - y_j\|)$ is constructed, enabling the relation $\mathbf{z} = A\boldsymbol{\lambda}$ between function values and coefficients.

(d) **Formation of Differentiation Matrices:** Differentiation matrices D_1 and D_2, corresponding to the first and second derivatives with respect to y, are formed by differentiating the RBFs and applying the relation:

$$D_1 = D_x A^{-1}, \quad D_2 = D_{xx} A^{-1}$$

where D_x and D_{xx} contain derivatives of the basis functions evaluated at node points.

(e) **Transformation to System of ODEs:** Substituting these differentiation matrices into the original PDE system transforms the spatial derivatives into matrix multiplications, yielding the following system of ordinary differential equations (ODEs):

$$\begin{aligned}\frac{du_1}{dt} &= Ge(t) + \frac{\eta}{Re} D_1 \mathbf{M} + \frac{1+\eta}{Re} D_2 u_1 - \frac{Ha^2}{Re} \frac{(1 + BiBe)u_1 + Beu_3}{(1 + BiBe)^2 + Be^2} \\ &\quad - \frac{R}{Re}(u_1 - u_{1p}) - \frac{2CEk}{Re} u_3 + \frac{\sin\theta}{F}\end{aligned} \tag{3.60}$$

$$\begin{aligned}\frac{du_3}{dt} &= Ge(t) + \frac{\eta}{Re} D_1 \mathbf{M} + \frac{1+\eta}{Re} D_2 u_3 - \frac{Ha^2}{Re} \frac{(1 + BiBe)u_3 + Beu_1}{(1 + BiBe)^2 + Be^2} \\ &\quad - \frac{R}{Re}(u_3 - u_{3p}) + \frac{2CEk}{Re} u_1\end{aligned} \tag{3.61}$$

$$\frac{du_{1p}}{dt} = \frac{RR_1}{Re}(u_1 - u_{1p}) - \frac{C}{2\pi} u_{3p} + \frac{\sin\theta}{F} \tag{3.62}$$

$$\frac{du_{3p}}{dt} = \frac{RR_1}{Re}(u_3 - u_{3p}) + \frac{C}{2\pi} u_{1p} \tag{3.63}$$

$$\frac{dM}{dt} = \frac{1}{Re}\left(1 + \frac{\eta}{2}\right) D_2 \mathbf{M} - \frac{\eta}{Re}\left(2M + D_1 u_1\right) \tag{3.64}$$

$$\frac{dT}{dt} = \frac{1}{PrRe} D_2 T + \frac{Ec}{Re}\left[(D_1 u_1)^2 + \eta\left(2\mathbf{M} + D_1 u_1\right)^2 + \delta(D_1 \mathbf{M})^2\right] + \frac{EcHa^2}{Re}\frac{(1+BiBe)}{(1+BiBe)^2+Be^2}u_1^2 + \frac{2R}{3PrRe}(T_p - T) + \frac{REc}{Re}(u_1 - u_{1p})^2 \tag{3.65}$$

$$\frac{dT_p}{dt} = -\frac{2RR_1}{3PrRe}(T_p - T) \tag{3.66}$$

Here, each variable $u_1, u_3, u_{1p}, u_{3p}, \mathbf{M}, T, T_p$ is understood as a vector of nodal values.

(f) **Time Integration Using SSP RK43 Scheme:** The system of ODEs (3.60) to (3.66) is solved in time using the SSP RK43. This method preserves the stability properties of forward Euler schemes while achieving higher order temporal accuracy, rendering it well-suited for stiff, coupled systems such as the present one. The SSP RK43 method is detailed in *Chapter 2*, *Section 2.2.3*.

The implementation involves:

(i) **Initialization:** Setting the initial solution vector $\mathbf{U}^0$ at $t = 0$ as

$$\mathbf{U}^0 = \begin{bmatrix} u_1^0 \\ u_3^0 \\ u_{1p}^0 \\ u_{3p}^0 \\ M^0 \\ T^0 \\ T_p^0 \end{bmatrix} = \mathbf{0},$$

in accordance with the problem's initial conditions.

(ii) **Time Step Selection:** Choosing an appropriate time step Δt respecting stability and accuracy requirements.

(iii) **Stage Computations:** For each time step $t_n \to t_{n+1} = t_n + \Delta t$, compute intermediate stage solutions $\mathbf{U}^{(k)}$, $k = 1, 2, 3$, via weighted evaluations of

the right-hand side functions $\mathbf{F}(t, \mathbf{U})$(as described in *Section 2.2.3*) corresponding to system (3.60) to (3.66), according to the SSP RK43 Butcher tableau.

(iv) **Boundary Conditions:** Enforce boundary conditions on each intermediate stage solution $\mathbf{U}^{(k)}$ to maintain physical consistency.

(v) **Solution Update:** Aggregate the intermediate stages to obtain $\mathbf{U}^{n+1}$, the solution at the next time level.

(vi) **Iteration:** This iterative procedure is repeated at each successive time level until the simulation reaches its predetermined final duration.

3.3.4 Pumping Power Analysis

Pumping power represents the mechanical energy required to transport a fluid through a channel or conduit over a given time. It is an essential indicator of the efficiency of fluid transport, particularly in systems involving complex fluids like micropolar dusty fluids under magnetic and rotational influences. As discussed in *Chapter 1*, *Section 1.8*, the determination of pumping power relies fundamentally on two key parameters: the volume flow rate and the pressure drop across the channel. The governing expressions for each of these quantities were introduced and explained in detail in the aforementioned section.

In this chapter, we extend that foundational discussion by analyzing the variations in pumping power under different parametric conditions. The fluid considered here is assigned a density of $\rho = 1050\,\mathrm{kg/m^3}$, which is representative of animal blood, as noted in [131], to evaluate the micropolar fluid behavior with biomedical relevance.

Table 3.2 reveals the following notable findings with respect to the sensitivity of pumping power to changes in various parameters:

(a) Parameters t, η, and θ significantly increase the required pumping power.

(b) Parameters R and Re exhibit a notable decrease in pumping power.

(c) Other parameters result in only marginal changes—either slight increases or decreases—with less pronounced effects on pumping power.

Table 3.2: Volume Flow Rate, Pressure Drop, and Pumping Power for Various Parameter Values

Parameter	**Volume Flow Rate**	**Pressure Drop**	**Pumping Power**
$t = 0.01$	0.122513531	22.70391854	2.781537217
$t = 0.03$	0.199888511	60.43776192	12.08081421
$t = 0.05$	0.255034432	98.38532972	25.09164667
$t = 0.07$	0.302613748	138.5192138	41.91781844
$t = 0.09$	0.346653395	181.7705933	63.01139326
$Re = 1$	0.149318456	67.45120065	10.07170912
$Re = 2$	0.122957153	22.86863854	2.811862697
$Re = 3$	0.109581055	12.10911495	1.326929587
$Re = 4$	0.101231491	7.750576082	0.784602376
$Re = 5$	0.095424629	5.509518656	0.525743772
$R = 50$	0.122513531	22.70391854	2.781537217
$R = 75$	0.120151084	21.83675456	2.62370972
$R = 100$	0.117852749	21.00932733	2.476006991
$R = 125$	0.115746647	20.2651373	2.345621702
$R = 150$	0.113835262	19.60136563	2.231326586
$Ha^2 = 1$	0.12255017	22.71750036	2.784033524
$Ha^2 = 2$	0.122835926	22.82356697	2.803553987
$Ha^2 = 3$	0.122919867	22.85477084	2.809305387
$Ha^2 = 4$	0.122952133	22.86677098	2.811518261
$Ha^2 = 5$	0.122961402	22.87021878	2.812154155
$Bi = 1$	0.122473517	22.68909072	2.778812749
$Bi = 2$	0.122835926	22.82356697	2.803553987
$Bi = 3$	0.122977875	22.87634702	2.813284537
$Bi = 4$	0.123059358	22.90667208	2.818880358
$Bi = 5$	0.123113466	22.92682008	2.822600275

continued on next page

Table 3.2: Volume Flow Rate, Pressure Drop, and Pumping Power for various parameters

Parameter	**Volume Flow Rate**	**Pressure Drop**	**Pumping Power**
$Be = 1$	0.122464299	22.68567514	2.778185295
$Be = 2$	0.122835926	22.82356697	2.803553987
$Be = 3$	0.122978114	22.87643591	2.813300935
$Be = 4$	0.123059226	22.90662312	2.81887132
$Be = 5$	0.123113052	22.92666604	2.822571828
$\eta = 0.3$	0.11665237	20.58352933	2.401117479
$\eta = 0.4$	0.119884932	21.74011859	2.60631263
$\eta = 0.5$	0.122947824	22.86516827	2.811222679
$\eta = 0.6$	0.125909737	23.98011934	3.019330509
$\eta = 0.7$	0.128787392	25.08877208	3.231117523
$Pr = 1$	0.122513531	22.70391854	2.781537217
$Pr = 1.5$	0.122835926	22.82356697	2.803553987
$Pr = 2$	0.122956803	22.86850814	2.811838648
$Pr = 2.5$	0.123026075	22.89428297	2.816593773
$Pr = 3$	0.123072372	22.91151721	2.819774763
$\delta = 1$	0.122513531	22.70391854	2.781537217
$\delta = 1.5$	0.122835926	22.82356697	2.803553987
$\delta = 2$	0.122956803	22.86850814	2.811838648
$\delta = 2.5$	0.123026075	22.89428297	2.816593773
$\delta = 3$	0.123072372	22.91151721	2.819774763
$Ec = 0.3$	0.122513531	22.70391854	2.781537217
$Ec = 0.4$	0.122835926	22.82356697	2.803553987
$Ec = 0.5$	0.122956803	22.86850814	2.811838648
$Ec = 0.6$	0.123026075	22.89428297	2.816593773
$Ec = 0.7$	0.123072372	22.91151721	2.819774763

continued on next page

Table 3.2: Volume Flow Rate, Pressure Drop, and Pumping Power for various parameters

Parameter	**Volume Flow Rate**	**Pressure Drop**	**Pumping Power**
$C = 0.1$	0.122519825	22.7062514	2.781965938
$C = 0.15$	0.122839098	22.82474568	2.803771171
$C = 0.2$	0.122956803	22.86850814	2.811838648
$C = 0.25$	0.12302289	22.8930975	2.816375011
$C = 0.3$	0.123065995	22.90914313	2.819336498
$Ek = 0.1$	0.12252096	22.70667216	2.782043265
$Ek = 0.2$	0.122838422	22.8244945	2.80372489
$Ek = 0.25$	0.122956803	22.86850814	2.811838648
$Ek = 0.3$	0.123023568	22.89335001	2.816421607
$Ek = 0.35$	0.123067353	22.9096487	2.819429826
$\theta = (\pi/180) * 0.0001$	0.122513531	22.70391854	2.781537217
$\theta = (\pi/180) * 0.0002$	0.139981329	29.63964076	4.148996311
$\theta = (\pi/180) * 0.0003$	0.157247609	37.40251539	5.881456113
$\theta = (\pi/180) * 0.0004$	0.174462284	46.04005326	8.03225285
$\theta = (\pi/180) * 0.0005$	0.191653984	55.56078996	10.64844674

end of table

3.3.5 Analysis of Velocity, Temperature and Microrotation profiles

Figures 3.46 and 3.47 display the velocity profiles for both a micropolar dusty fluid and the suspended dust particles, illustrating primary and secondary velocities at time intervals $t = 1, 2$, and 3. The parabolic shape of both profiles, which is indicative of laminar flow, shows that velocities peak in the middle and decrease close to the walls. Both the fluid and particle velocities rise over time, and the gap between them decreases, indicating that the particles are accelerating toward the fluid's speed. Rotational forces and the magnetic field, which promote momentum exchange and result in a more synchronized flow over time, are responsible for this gradual alignment.

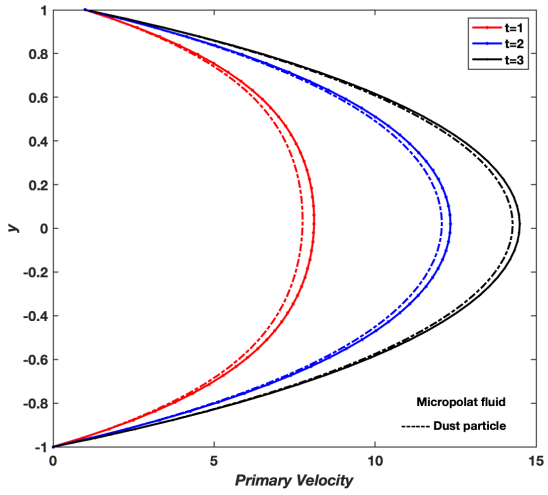

Fig. 3.46 Primary velocity profiles of fluid flow with varying time t, $Ge = 30$, $Re = 2$, $R = 100$, $Ha^2 = 2$, $Bi = 2$, $Be = 2$, $\eta = 0.5$, $C = 0.2$, $Ek = 0.25$, $Pr = 2$, $\delta = 2$, $R_1 = 0.4$, $Ec = 0.5$, $\theta = (\pi/180) * 0.0001$

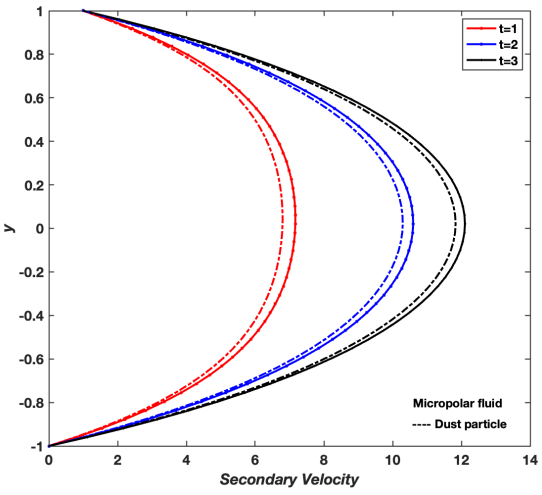

Fig. 3.47 Secondary velocity profiles of fluid flow with varying time t, $Ge = 30$, $Re = 2$, $R = 100$, $Ha^2 = 2$, $Bi = 2$, $Be = 2$, $\eta = 0.5$, $C = 0.2$, $Ek = 0.25$, $Pr = 2$, $\delta = 2$, $R_1 = 0.4$, $Ec = 0.5$, $\theta = (\pi/180) * 0.0001$

The Reynolds number (Re) is a dimensionless measure used to predict flow behavior across various scenarios, helping to distinguish between laminar (smooth and stable) and turbulent (chaotic) flow patterns. Figures 3.48 and 3.49 illustrate the velocity profiles at varying Reynolds numbers ($Re = 1, 2,$ and 3). Both profiles show a steeper parabolic shape as the Reynolds number (Re) rises, particularly in the vicinity of the channel walls, suggesting higher momentum transfer and shear stress. Higher Reynolds number (Re) values in the primary velocity profile (Figure 3.48) result in sharper gradients close to the walls, indicating greater flow energy and possible instability. As Reynolds number (Re) increases, the fluid-particle velocity differential in the secondary velocity profile (Figure 3.49) diminishes, suggesting better coupling and a more synchronized flow. These profiles show how increased Reynolds number (Re) increases the fluid's velocity and energy, which leads to better fluid-dust particle interaction.

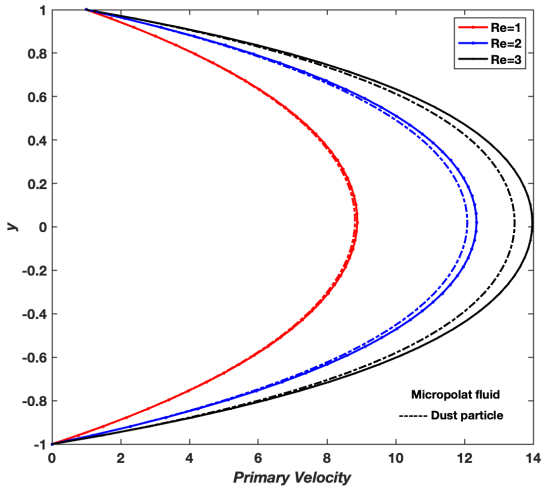

Fig. 3.48 Primary velocity profiles of fluid flow with varying Reynolds number Re, $Ge = 30$, $t = 2$, $R = 100$, $Ha^2 = 2$, $Bi = 2$, $Be = 2$, $\eta = 0.5$, $C = 0.2$, $Ek = 0.25$, $Pr = 2$, $\delta = 2$, $R_1 = 0.4$, $Ec = 0.5$, $\theta = (\pi/180) * 0.0001$

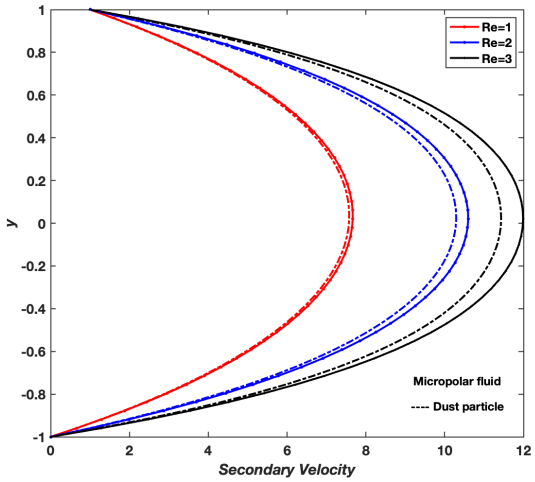

Fig. 3.49 Secondary velocity profiles of fluid flow with varying Reynolds number Re, $Ge = 30$, $t = 2$, $R = 100$, $Ha^2 = 2$, $Bi = 2$, $Be = 2$, $\eta = 0.5$, $C = 0.2$, $Ek = 0.25$, $Pr = 2$, $\delta = 2$, $R_1 = 0.4$, $Ec = 0.5$, $\theta = (\pi/180) * 0.0001$

The particle concentration parameter, denoted by (R), is a dimensionless quantity used in dusty fluid flow analysis to assess the proportion of solid particles within the fluid. Higher values of (R) indicate a greater particle load in the fluid, while lower values reflect a smaller concentration. Figures 3.50 and 3.51 illustrate the primary and secondary velocity profiles for a micropolar dusty fluid (solid lines) and dust particles (dashed lines) at different values of (R). As (R) increases, both primary and secondary velocities for the fluid are decreasing but velocities for the dust particles are increasing. Due to increase in particle concentration the particles and fluid interact more strongly. This causes the particles to take more momentum from the fluid, making the particles move faster while the fluid slows down. In simple terms, the particles draw energy from the fluid, leading to lower fluid velocities and higher particle velocities. This shift in energy between the fluid and particles explains the change in their speeds.

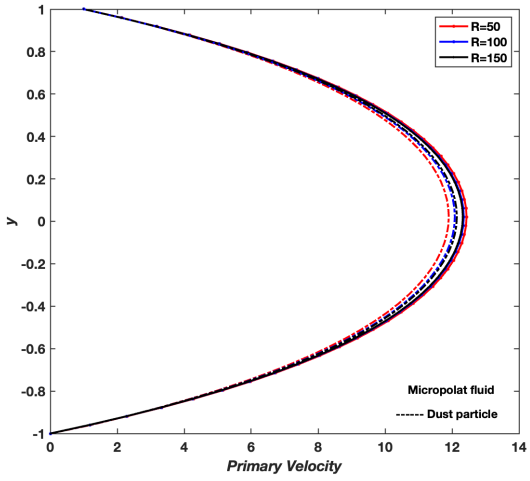

Fig. 3.50 Primary velocity profiles of fluid flow with varying particle concentration parameter R, $Ge = 30$, $t = 2$, $Re = 2$, $Ha^2 = 2$, $Bi = 2$, $Be = 2$, $\eta = 0.5$, $C = 0.2$, $Ek = 0.25$, $Pr = 2$, $\delta = 2$, $R_1 = 0.4$, $Ec = 0.5$, $\theta = (\pi/180) * 0.0001$

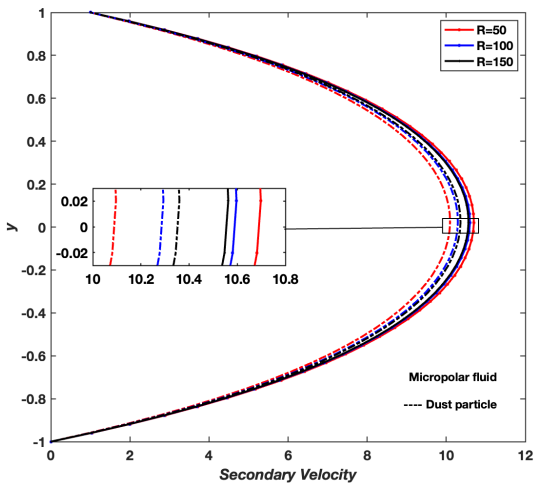

Fig. 3.51 Secondary velocity profiles of fluid flow with varying particle concentration parameter R, $Ge = 30$, $t = 2$, $Re = 2$, $Ha^2 = 2$, $Bi = 2$, $Be = 2$, $\eta = 0.5$, $C = 0.2$, $Ek = 0.25$, $Pr = 2$, $\delta = 2$, $R_1 = 0.4$, $Ec = 0.5$, $\theta = (\pi/180) * 0.0001$

In magnetohydrodynamics, the Hartmann number is a dimensionless quantity that represents the relative strength of the magnetic forces to viscous forces in the flow. Figures 3.52 and 3.53 show that increasing Ha^2 leads to a decrease in both primary and secondary velocities. Stronger magnetic field impact is indicated by a higher Hartmann number (Ha^2). When exposed to a magnetic field, a conducting fluid experiences Lorentz forces. In both primary and secondary directions, the Lorentz forces generated with increasing Hartmann number (Ha) act to resist the fluid motion. As a result of this resistance, the flow is suppressed and velocities drop.

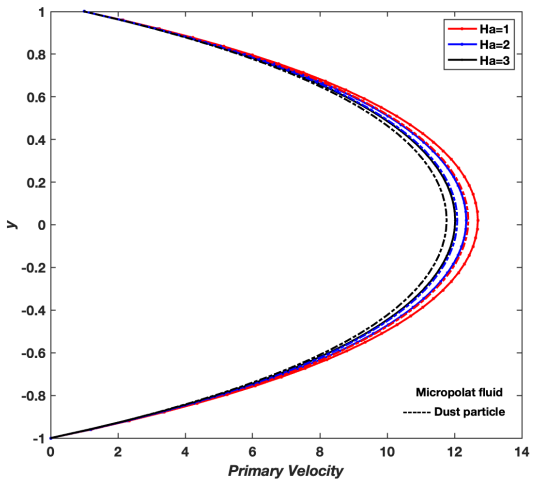

Fig. 3.52 Primary velocity profiles of fluid flow with varying Hartmann number Ha^2, $Ge = 30$, $t = 2$, $R = 100$, $Re = 2$, $Bi = 2$, $Be = 2$, $\eta = 0.5$, $C = 0.2$, $Ek = 0.25$, $Pr = 2$, $\delta = 2$, $R_1 = 0.4$, $Ec = 0.5$, $\theta = (\pi/180) * 0.0001$

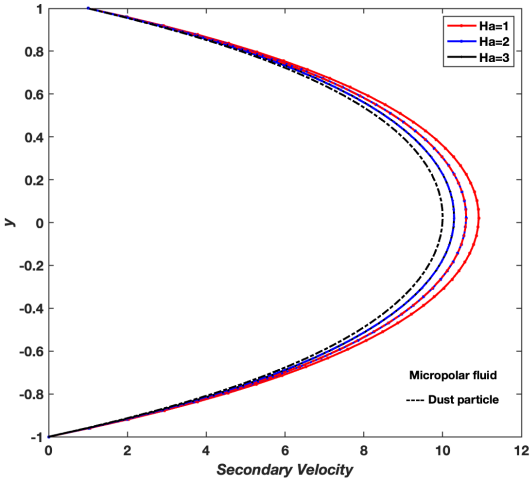

Fig. 3.53 Secondary velocity profiles of fluid flow with varying Hartmann number Ha^2, $Ge = 30$, $t = 2$, $R = 100$, $Re = 2$, $Bi = 2$, $Be = 2$, $\eta = 0.5$, $C = 0.2$, $Ek = 0.25$, $Pr = 2$, $\delta = 2$, $R_1 = 0.4$, $Ec = 0.5$, $\theta = (\pi/180) * 0.0001$

The ion slip parameter, (Bi), indicates the relative importance of ion-neutral collisions compared to ion-electron collisions. In Figure 3.54, increases in $(Bi = 1, 2)$, and 3 suggest a higher frequency of ion-neutral collisions, reducing the fluid's effective electrical conductivity. This reduced conductivity weakens the magnetic field's damping effect on the flow, allowing velocity to increase. Figures 3.54 and 3.55 show that, for both primary and secondary velocities, the dusty fluid and dust particle velocities display a parabolic profile. As (Bi) rises, both primary and secondary velocities of the fluid and particles increase, reflecting the decreased influence of the magnetic field with higher ion slip values.

In our study the ion slip acts like a shield, reducing the impact of the wind (magnetic field) and allowing the fluid and particles to move more freely.

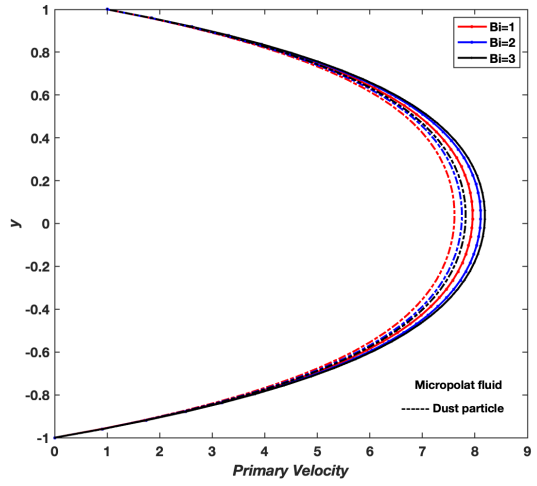

Fig. 3.54 Primary velocity profiles of fluid flow with varying Ion Slip parameter Bi, $Ge = 30$, $t = 2$, $R = 100$, $Ha^2 = 2$, $Re = 2$, $Be = 2$, $\eta = 0.5$, $C = 0.2$, $Ek = 0.25$, $Pr = 2$, $\delta = 2$, $R_1 = 0.4$, $Ec = 0.5$, $\theta = (\pi/180) * 0.0001$

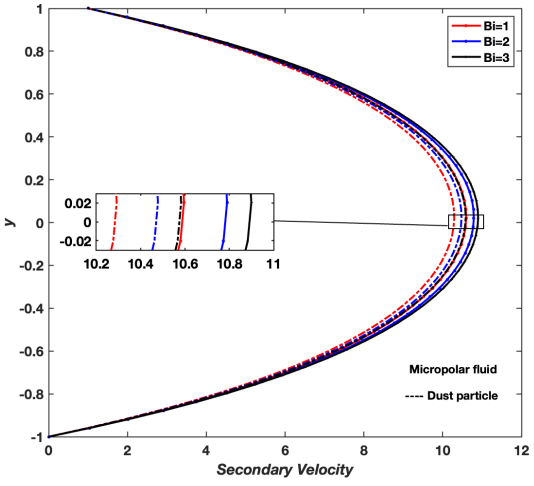

Fig. 3.55 Secondary velocity profiles of fluid flow with varying Ion Slip parameter Bi, $Ge = 30$, $t = 2$, $R = 100$, $Ha^2 = 2$, $Re = 2$, $Be = 2$, $\eta = 0.5$, $C = 0.2$, $Ek = 0.25$, $Pr = 2$, $\delta = 2$, $R_1 = 0.4$, $Ec = 0.5$, $\theta = (\pi/180) * 0.0001$

In magnetohydrodynamics, which examines the interaction between magnetic fields and electrically conducting fluids—the Hall parameter is a key factor. As (Be) increases, the primary velocity profiles (Figure 3.56) show a slight increase near the channel walls, but a slightly flatter profile in the central region. With increasing (Be), the secondary velocity profiles (Figure 3.57) show a clear increase in magnitude; thus, a higher Hall parameter enhances the secondary flow, leading to stronger vortices and circulation patterns within the channel.

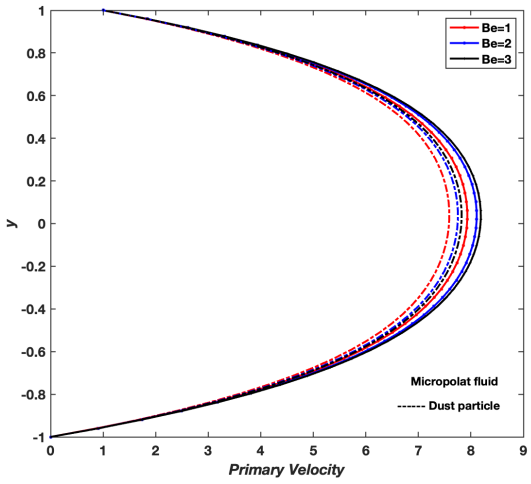

Fig. 3.56 Primary velocity profiles of fluid flow with varying Hall parameter Be, $Ge = 30$, $t = 2$, $R = 100$, $Ha^2 = 2$, $Bi = 2$, $Re = 2$, $\eta = 0.5$, $C = 0.2$, $Ek = 0.25$, $Pr = 2$, $\delta = 2$, $R_1 = 0.4$, $Ec = 0.5$, $\theta = (\pi/180) * 0.0001$

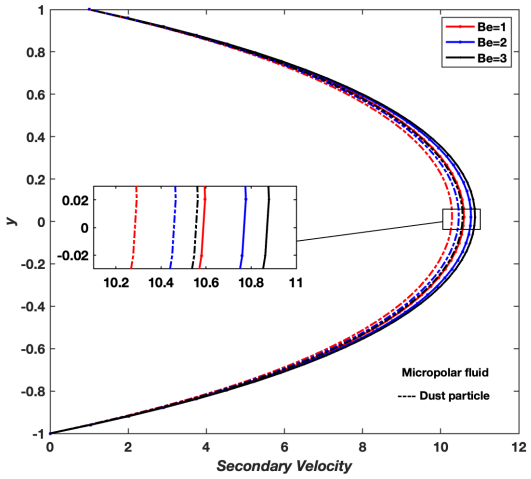

Fig. 3.57 Secondary velocity profiles of fluid flow with varying Hall parameter Be, $Ge = 30$, $t = 2$, $R = 100$, $Ha^2 = 2$, $Bi = 2$, $Re = 2$, $\eta = 0.5$, $C = 0.2$, $Ek = 0.25$, $Pr = 2$, $\delta = 2$, $R_1 = 0.4$, $Ec = 0.5$, $\theta = (\pi/180) * 0.0001$

The micropolar parameter characterizes how the fluid's velocity interacts with its internal microstructure. As illustrated in Figures 3.58 and 3.59, increasing the micropolar parameter (η) results in a reduction of both the primary and secondary velocities for the micropolar fluid and suspended particles. Higher micropolar values indicate stronger microrotation effects, meaning the internal spin and microstructure of fluid particles exert greater influence. This internal spin introduces additional resistance, lowering primary velocity, while the increase in (η) can enhance Coriolis-induced secondary velocities, as microrotation adds rotational complexity to the flow. Fluid and particle velocities may appear closely aligned in certain areas, and both primary and secondary velocity profiles often exhibit a parabolic shape.

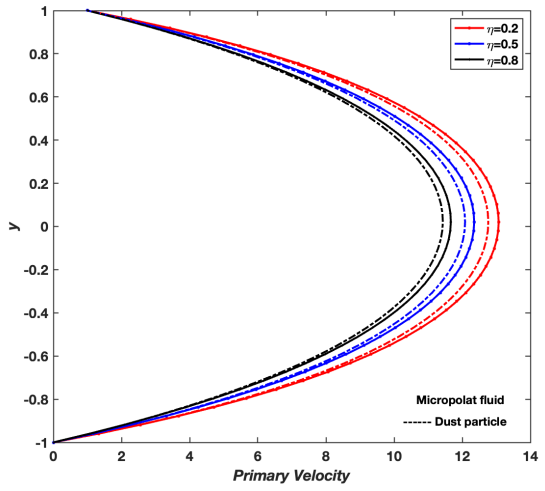

Fig. 3.58 Primary velocity profiles of fluid flow with varying micropolar parameter η, $Ge = 30$, $t = 2$, $R = 100$, $Ha^2 = 2$, $Bi = 2$, $Be = 2$, $Re = 2$, $C = 0.2$, $Ek = 0.25$, $Pr = 2$, $\delta = 2$, $R_1 = 0.4$, $Ec = 0.5$, $\theta = (\pi/180) * 0.0001$

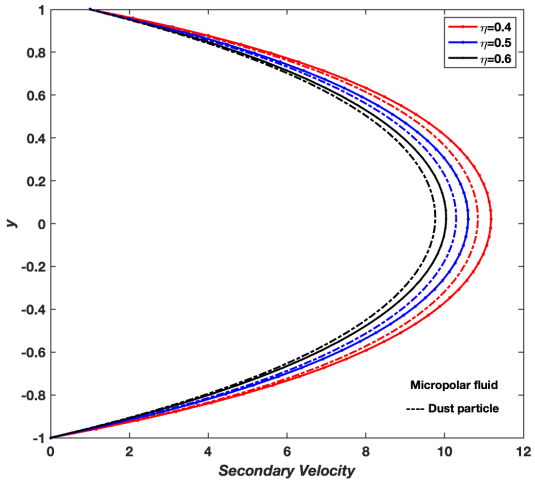

Fig. 3.59 Secondary velocity profiles of fluid flow with varying micropolar parameter η, $Ge = 30$, $t = 2$, $R = 100$, $Ha^2 = 2$, $Bi = 2$, $Be = 2$, $Re = 2$, $C = 0.2$, $Ek = 0.25$, $Pr = 2$, $\delta = 2$, $R_1 = 0.4$, $Ec = 0.5$, $\theta = (\pi/180) * 0.0001$

In fluid dynamics, the Ekman number (Ek) represents the ratio of viscous forces to Coriolis forces, often used to evaluate the balance between these forces resulting from planetary rotation, particularly in geophysical scenarios involving the atmosphere and oceans. Figure 3.60 illustrates the effect of the Ekman number on the primary velocity profile in a micropolar dusty fluid flow and dust particles. As the Ekman number (Ek) increases, the primary velocity profile flattens due to the thickening of the Ekman layer, leading to greater drag forces on the particles, which results in observable differences in velocities between the fluid and particles, as seen in the zoomed-in image. Similarly, Figure 3.61 displays the secondary velocity profiles for the dusty fluid flow across a range of Ekman numbers (from 0.15 to 0.35), also highlighting subtle variations in the zoomed-in view. Both profiles exhibit parabolic shapes, with the secondary velocity profile being inverted relative to the primary velocity profile.

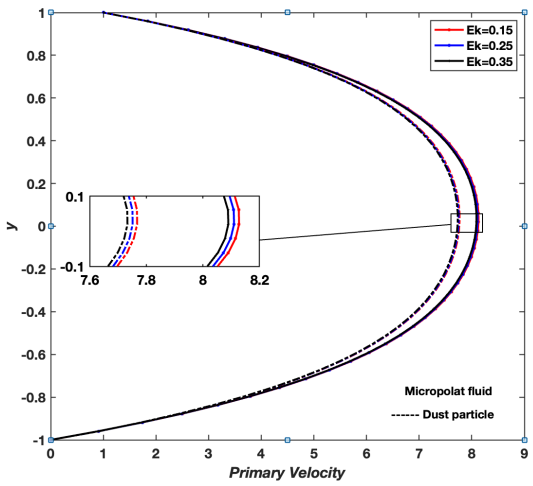

Fig. 3.60 Primary velocity profiles of fluid flow with varying Ekman number Ek, $Ge = 30$, $t = 2$, $R = 100$, $Ha^2 = 2$, $Bi = 2$, $Be = 2$, $\eta = 0.5$, $C = 0.2$, $Re = 2$, $\delta = 2$, $R_1 = 0.4$, $Ec = 0.5$, $\theta = (\pi/180) * 0.0001$

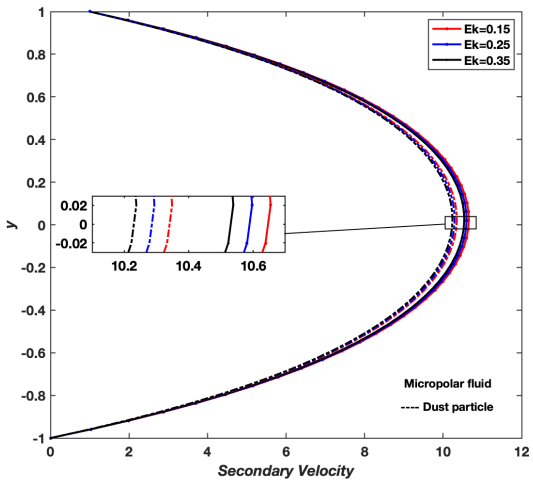

Fig. 3.61 Secondary velocity profiles of fluid flow with varying Ekman number Ek, $Ge = 30$, $t = 2$, $R = 100$, $Ha^2 = 2$, $Bi = 2$, $Be = 2$, $\eta = 0.5$, $C = 0.2$, $Re = 2$, $\delta = 2$, $R_1 = 0.4$, $Ec = 0.5$, $\theta = (\pi/180) * 0.0001$

Figures 3.62 and 3.63 depict the primary and secondary velocity profiles with variations in the inclination angle (θ) while other parameters remain constant. The micropolar fluid and dust particles show a rise in primary velocity as (θ) increases, especially in the vicinity of the channel center. Greater (θ) lowers flow resistance in the principal velocity profile, enabling maximum velocities close to the channel's core. The reason for this increase is that the flow along the major direction is enhanced by the angled gravitational component. The combined effects of rotation and inclination cause more noticeable secondary currents in the secondary velocity profile as (θ) increases. As (θ) increases, the magnetic force exerts a greater damping effect on the secondary flow components. This occurs because the Lorentz force, induced by the magnetic field, acts in a direction that opposes the secondary motion, thereby reducing its magnitude.

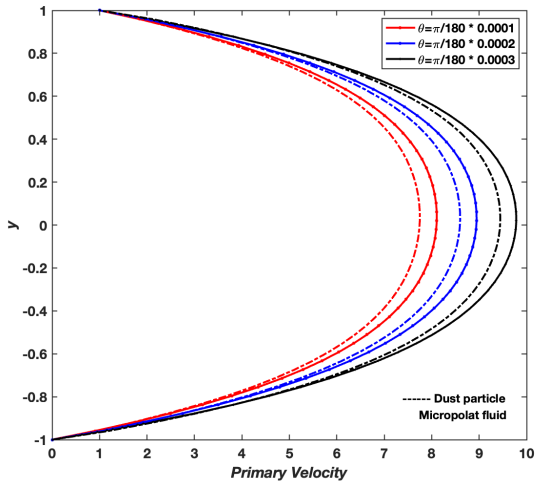

Fig. 3.62 Primary velocity profiles of Micropolar dusty fluid flow with varying angle θ, $Ge = 30$, $t = 2$, $R = 100$, $Ha^2 = 2$, $Bi = 2$, $Be = 2$, $\eta = 0.5$, $C = 0.2$, $Ek = 0.25$, $Pr = 2$, $\delta = 2$, $R_1 = 0.4$, $Ec = 0.5$, $Re = 2$

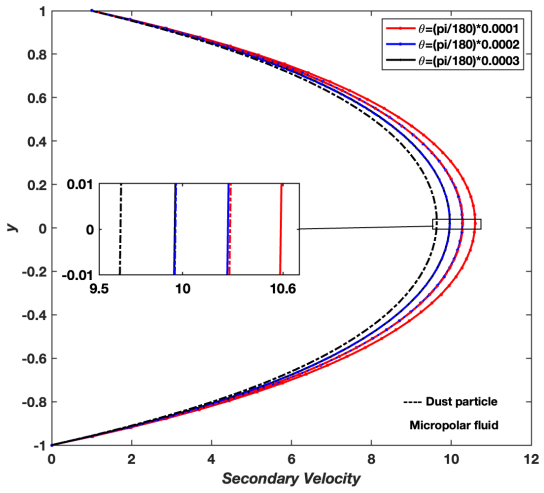

Fig. 3.63 Secondary velocity profiles of Micropolar dusty fluid flow with varying angle θ, $Ge = 30$, $t = 2$, $R = 100$, $Ha^2 = 2$, $Bi = 2$, $Be = 2$, $\eta = 0.5$, $C = 0.2$, $Ek = 0.25$, $Pr = 2$, $\delta = 2$, $R_1 = 0.4$, $Ec = 0.5$, $Re = 2$

Microrotation describes the rotational movement of tiny particles within a micropolar fluid, where fluid behavior is defined not only by its translational velocity but also by the rotational motion of its micro-elements. This additional rotational aspect, unique to micropolar fluids, reflects the microscopic spinning of fluid particles and contributes to a more complex flow pattern. When dust particles are present in such fluids, the interaction between the fluid's microrotation and the particles becomes crucial, affecting both the overall fluid dynamics and particle behavior.

Figure 3.64 illustrates the influence of constant pressure (Ge) on angular velocities. As pressure increases ($Ge = 20, 30,$ and 40), there is a noticeable decline in fluid microrotation, suggesting a dampening effect on rotational motion at higher pressures. Additionally, Figure 3.65 demonstrates the effect of time ($t = 0.3$ to 0.7) on microrotation. Here, microrotation gradually decreases over time, eventually stabilizing, which implies that the rotational dynamics reach equilibrium after a certain period. These observations highlight the combined effects of pressure and time on fluid behavior, particularly in systems where microrotation plays a key role.

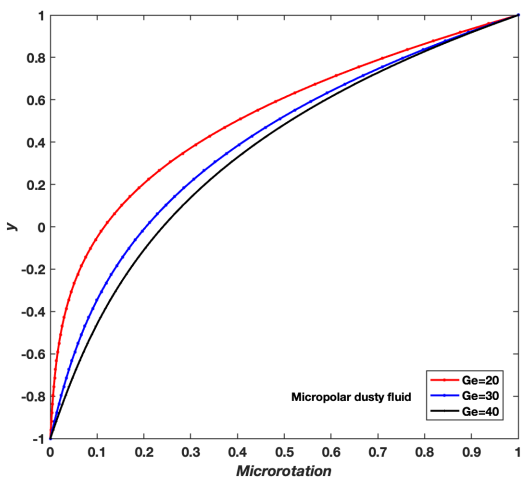

Fig. 3.64 Microrotation profiles of fluid flow with varying constant pressure Ge, $t = 0.5$, $Re = 2$, $R = 100$, $Ha^2 = 2$, $Bi = 2$, $Be = 2$, $\eta = 0.5$, $Pr = 2$, $\delta = 2$, $R_1 = 0.4$, $Ec = 0.5$, $C = 0.2$, $Ek = 0.25$, $\theta = (\pi/180) * 0.0001$

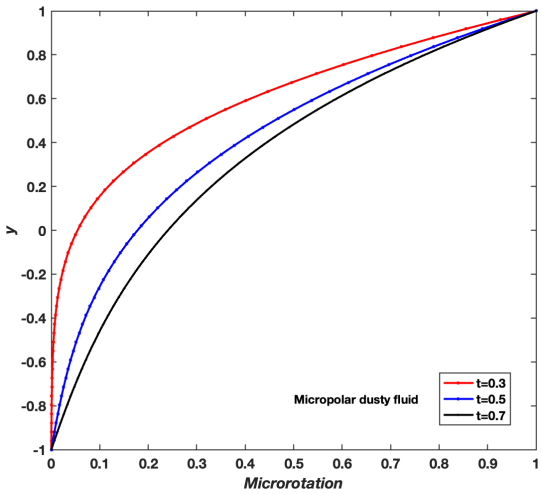

Fig. 3.65 Microrotation profiles of fluid flow with varying time t, $Ge = 30$, $Re = 2$, $R = 100$, $Ha^2 = 2$, $Bi = 2$, $Be = 2$, $\eta = 0.5$, $Pr = 2$, $\delta = 2$, $R_1 = 0.4$, $Ec = 0.5$, $C = 0.2$, $Ek = 0.25$, $\theta = (\pi/180) * 0.0001$

Figure 3.66 demonstrates that the microrotation profile grows as the Reynolds number ($Re = 2, 3,$ and 4) increases, indicating an enhancement in rotational effects with higher flow rates. In Figure 3.67, the impact of the micropolar parameter ($\eta = 0.4, 0.5,$ and 0.6) on microrotation is depicted. Initially, an increase in (η) leads to a rise in microrotation, but the profile eventually aligns with the previous values. This behavior occurs because the local angular velocity field induces rotations in fluid particles, with a stronger field initially enhancing these rotations before reaching a saturation point. This suggests a threshold effect where further increases in (η) produce minimal impact on microrotation.

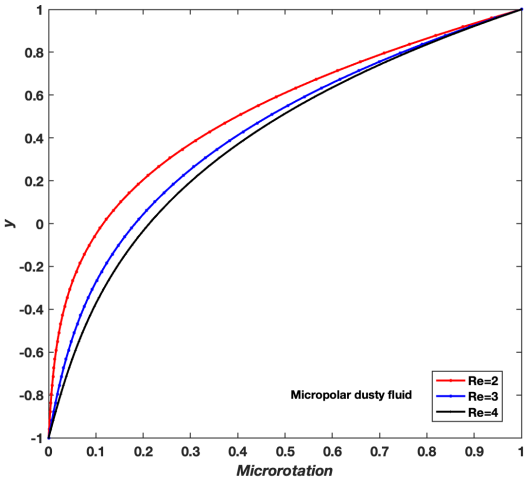

Fig. 3.66 Microrotation profiles of fluid flow with varying Reynolds number Re, $Ge = 30$, $t = 0.5$, $R = 100$, $Ha^2 = 2$, $Bi = 2$, $Be = 2$, $\eta = 0.5$, $Pr = 2$, $\delta = 2$, $R_1 = 0.4$, $Ec = 0.5$, $C = 0.2$, $Ek = 0.25$, $\theta = (\pi/180) * 0.0001$

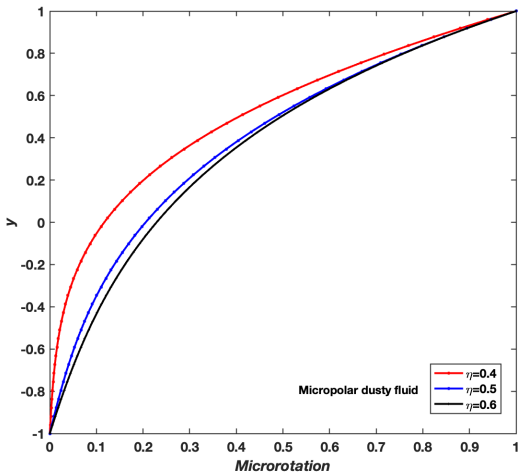

Fig. 3.67 Microrotation profiles of fluid flow with varying micropolar parameter η, $Ge = 30$, $Re = 2$, $R = 100$, $Ha^2 = 2$, $Bi = 2$, $Be = 2$, $t = 0.5$, $Pr = 2$, $\delta = 2$, $R_1 = 0.4$, $Ec = 0.5$, $C = 0.2$, $Ek = 0.25$, $\theta = (\pi/180) * 0.0001$

Figure 3.68 illustrates that as constant pressure (Ge) increases, the temperature of the fluid flow rises. This is because higher pressure enhances fluid motion, increasing frictional forces and energy dissipation as heat, which elevates the temperature profile. In Figure 3.69, the effect of time (t) on temperature shows a gradual stabilization. Initially, temperature fluctuations occur, but as time progresses, the temperature distribution becomes more uniform. This indicates that the system is approaching thermal equilibrium, with energy dissipation reaching a steady state over time.

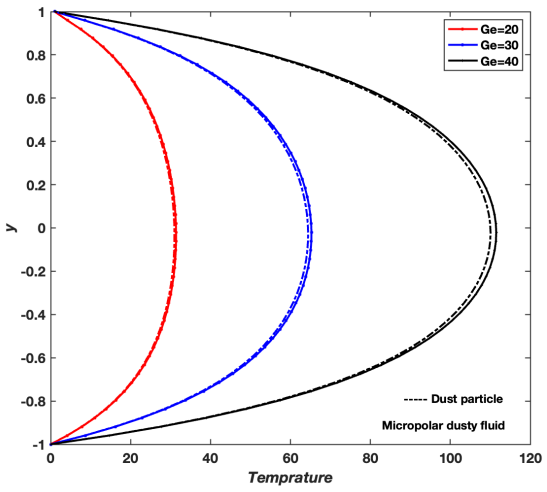

Fig. 3.68 Temperature profiles of fluid flow with varying constant pressure Ge, $t = 3$, $Re = 2$, $R = 50$, $Ha^2 = 1$, $Bi = 0.2$, $Be = 0.2$, $\eta = 0.2$, $Pr = 0.5$, $\delta = 1$, $R_1 = 0.8$, $Ec = 0.8$, $C = 0.2$, $Ek = 0.25$, $\theta = (\pi/180) * 0.0001$

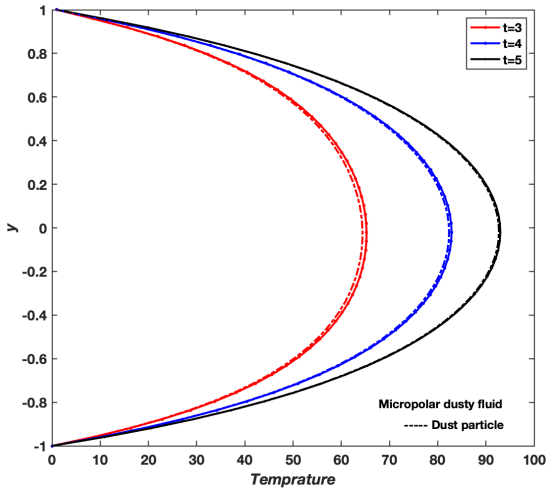

Fig. 3.69 Temperature profiles of fluid flow with varying time t, $Ge = 30$, $Re = 2$, $R = 50$, $Ha^2 = 1$, $Bi = 0.2$, $Be = 0.2$, $\eta = 0.2$, $Pr = 0.5$, $\delta = 1$, $R_1 = 0.8$, $Ec = 0.8$, $C = 0.2$, $Ek = 0.25$, $\theta = (\pi/180) * 0.0001$

Figure 3.70 illustrates that as (Re) Reynolds number increases, the temperature of both fluid and dust particles rises. Higher (Re) values correspond to increased inertial forces, which amplify frictional effects within the fluid. This friction generates additional heat, leading to a rise in temperature. An increase in particle concentration (R) leads to a reduction in the temperatures of the fluid and dust particles, as seen in Figure 3.71. Higher particle concentration raises the effective viscosity, thereby increasing resistance to flow. Although this could theoretically add to friction, the increased viscosity also stabilizes the flow and reduces excessive velocity, leading to a net reduction in temperature. This behavior indicates that particle-laden fluids can exhibit reduced heat generation under higher concentration.

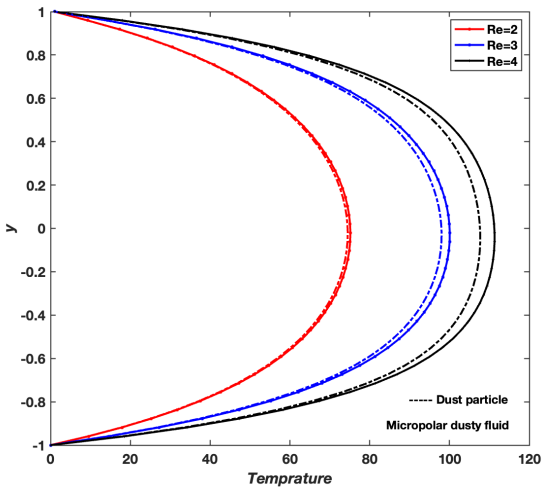

Fig. 3.70 Temperature profiles of fluid flow with varying Reynolds number Re, $t = 3$, $Ge = 30$, $R = 50$, $Ha^2 = 1$, $Bi = 0.2$, $Be = 0.2$, $\eta = 0.2$, $Pr = 0.5$, $\delta = 1$, $R_1 = 0.8$, $Ec = 0.8$, $C = 0.2$, $Ek = 0.25$, $\theta = (\pi/180) * 0.0001$

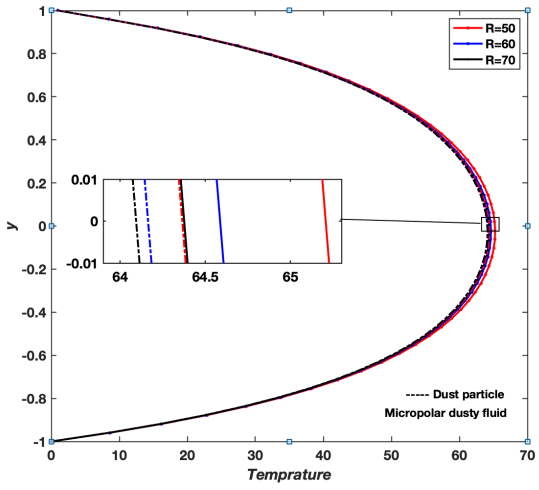

Fig. 3.71 Temperature profiles of fluid flow with varying particle concentration parameter R, $t = 3$, $Re = 2$, $Ge = 30$, $Ha^2 = 1$, $Bi = 0.2$, $Be = 0.2$, $\eta = 0.2$, $Pr = 0.5$, $\delta = 1$, $R_1 = 0.8$, $Ec = 0.8$, $C = 0.2$, $Ek = 0.25$, $\theta = (\pi/180) * 0.0001$

The Hartmann number reflects the magnetic field's influence. As (Ha) increases, the temperature profile of the fluid and dust particles declines, as can be observed in Figure 3.72. A stronger magnetic field exerts a damping effect, which reduces fluid motion and thereby decreases frictional heating. Physically, this signifies that the magnetic field provides a stabilizing effect, limiting energy dissipation through heat. Figure 3.73 shows that increasing (Bi) reduces temperature, indicating more ion-neutral collisions that decrease the fluid's effective conductivity. This reduction in conductivity weakens the magnetic field's capacity to generate Lorentz forces, leading to lower energy dissipation and subsequently, a drop in temperature.

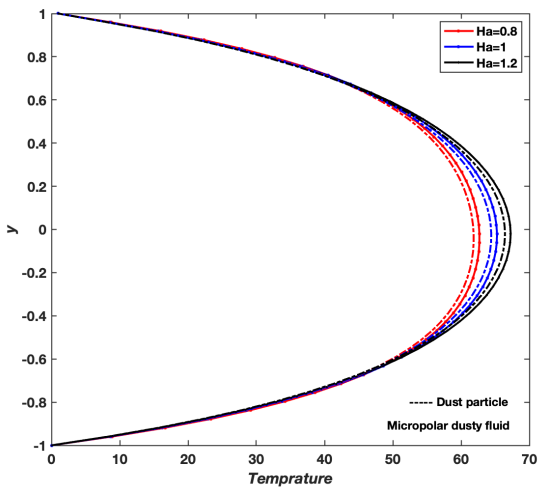

Fig. 3.72 Temperature profiles of fluid flow with varying Hartmann number Ha^2, $t = 3$, $Re = 2$, $R = 50$, $Ge = 30$, $Bi = 0.2$, $Be = 0.2$, $\eta = 0.2$, $Pr = 0.5$, $\delta = 1$, $R_1 = 0.8$, $Ec = 0.8$, $C = 0.2$, $Ek = 0.25$, $\theta = (\pi/180) * 0.0001$

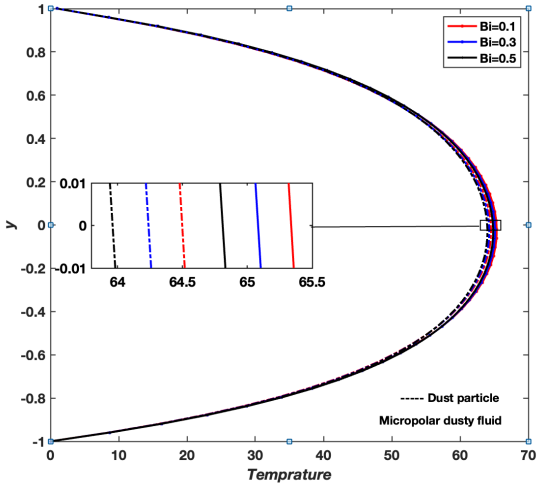

Fig. 3.73 Temperature profiles of fluid flow with varying Ion slip parameter Bi, $Ge = 30$, $Re = 2$, $R = 50$, $Ha^2 = 1$, $t = 3$, $Be = 0.2$, $\eta = 0.2$, $Pr = 0.5$, $\delta = 1$, $R_1 = 0.8$, $Ec = 0.8$, $C = 0.2$, $Ek = 0.25$, $\theta = (\pi/180) * 0.0001$

Higher values of the Hall parameter (Be) lower the temperature profile, as the Hall effect redistributes Lorentz forces within the fluid. This redistribution modifies the current path and reduces the energy dissipation associated with magnetic interactions, resulting in a cooler temperature profile, as can be seen in Figure 3.74. As per Figure 3.75, an increase in (η) results in a gradual decrease in temperature. The micropolar parameter is associated with microrotation effects; as it increases, the fluid exhibits enhanced internal rotation, which stabilizes the overall flow and reduces shear. This leads to less frictional heating and thus a lower temperature.

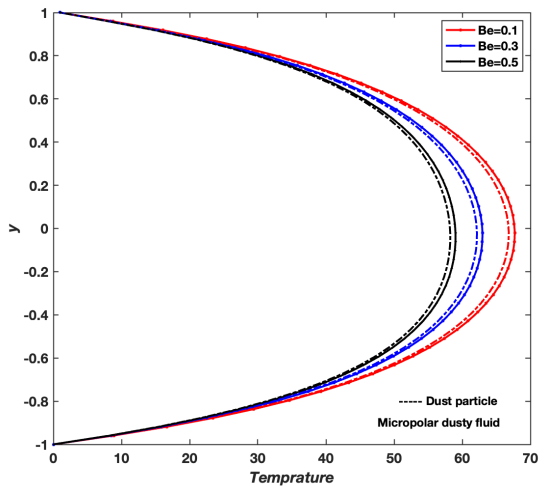

Fig. 3.74 Temperature profiles of fluid flow with varying Hall parameter Be, $Ge = 30$, $Re = 2$, $R = 50$, $Ha^2 = 1$, $Bi = 0.2$, $t = 3$, $\eta = 0.2$, $Pr = 0.5$, $\delta = 1$, $R_1 = 0.8$, $Ec = 0.8$, $C = 0.2$, $Ek = 0.25$, $\theta = (\pi/180) * 0.0001$

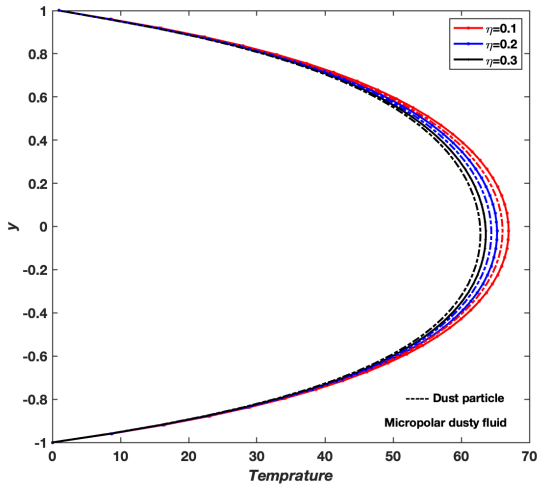

Fig. 3.75 Temperature profiles of fluid flow with varying micropolar parameter η, $Ge = 30$, $Re = 2$, $R = 50$, $Ha^2 = 1$, $Bi = 0.2$, $Be = 0.2$, $t = 3$, $Pr = 0.5$, $\delta = 1$, $R_1 = 0.8$, $Ec = 0.8$, $C = 0.2$, $Ek = 0.25$, $\theta = (\pi/180) * 0.0001$

The Prandtl number reflects the ratio of momentum diffusivity to thermal diffusivity. Figures 3.76 and 3.77 illustrate that higher (Pr) values lead to increased temperature in the fluid, suggesting that heat conduction is less effective relative to momentum transfer. This causes heat to accumulate in the fluid rather than dissipating quickly, raising the temperature. With higher (Ec), there is a rise in temperature, indicating that kinetic energy from fluid motion is more efficiently converted into thermal energy. This implies that faster-moving particles in the flow contribute significantly to temperature elevation. The parabolic temperature distribution in the results shows thermal energy is spread evenly across the inclined channel, balancing the impact of boundary conditions and other physical factors.

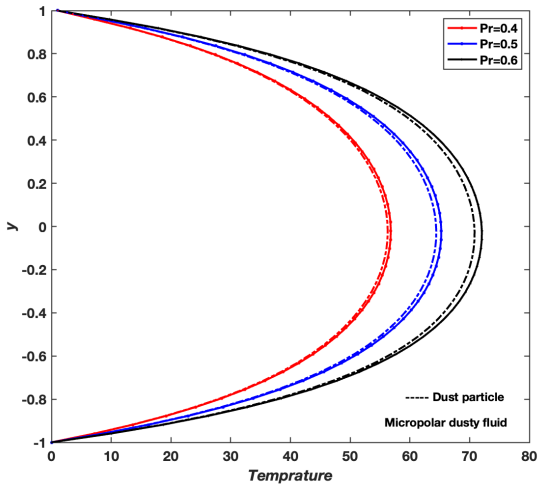

Fig. 3.76 Temperature profiles of fluid flow with varying Prandtl number Pr, $Ge = 30$, $Re = 2$, $R = 50$, $Ha^2 = 1$, $Bi = 0.2$, $Be = 0.2$, $\eta = 0.2$, $t = 3$, $\delta = 1$, $R_1 = 0.8$, $Ec = 0.8$, $C = 0.2$, $Ek = 0.25$, $\theta = (\pi/180) * 0.0001$

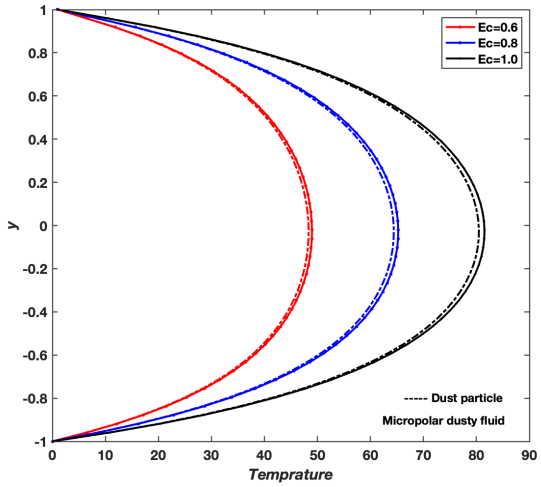

Fig. 3.77 Temperature profiles of fluid flow with varying Eckert number Ec, $t = 3$, $Ge = 30$, $Re = 2$, $R = 50$, $Ha^2 = 1$, $Bi = 0.2$, $Be = 0.2$, $\eta = 0.2$, $Pr = 0.5$, $\delta = 1$, $R_1 = 0.8$, $C = 0.2$, $Ek = 0.25$, $\theta = (\pi/180) * 0.0001$

3.4 Conclusion

This chapter presented a comprehensive investigation of micropolar dusty fluid flow in both horizontal and inclined channel configurations under the influence of rotation, magnetic field, and heat transfer phenomena. The study aimed to understand how the microstructural behavior of the fluid, coupled with the dynamics of suspended dust par-

ticles, combined with rotational and electromagnetic forces, affects momentum and heat transport in such geometries. To achieve this, the governing equations accounting for velocity, particle interaction, microrotation, and temperature were first derived through physical modeling and then transformed into their non-dimensional forms. A meshless RBF-PSM was employed to solve these coupled equations for both channel orientations. The solution process yielded primary (x-direction) and secondary (z-direction) velocity profiles, which were analyzed across a range of key dimensionless parameters such as the Coriolis frequency, Hartmann number, micropolar parameters, and Reynolds number. Similarly, temperature profiles were studied for various dimensionless parameters governing heat transfer behavior . Additionally, the pumping power required to sustain the flow in the absence of an imposed pressure gradient was computed for each configuration.

In the first part (*Section 3.2*), micropolar dusty fluid flow was examined in a horizontal channel, where the system was subjected to rotation about the y-axis with angular velocity Ω, and influenced by a magnetic field B_0. The fluid system was comprehensively analyzed to understand the influence of various governing parameters. The key findings of this investigation are summarized as follows:

(a) An increase in the Coriolis frequency parameter (Ω) amplifies the inertial forces within the fluid, leading to an enhancement of both primary and secondary velocities of the micropolar dusty fluid.

(b) The velocities of both the micropolar fluid and suspended particles decrease with an increase in the micropolar parameter (η), whereas the temperatures of the fluid and particles rise due to an increase in effective viscosity, which enhances friction and energy dissipation.

(c) The Hartmann number (Ha^2) significantly influences fluid motion. As η increases, both the primary and secondary velocities of the fluid decrease. Additionally, a higher Hartmann number results in an increase in the temperature of the fluid and dust particles due to enhanced Joule heating.

(d) With an increase in the Reynolds number (Re), the influence of viscous forces

diminishes, leading to stronger coupling between fluid and particle velocities. Consequently, the primary and secondary velocities, along with the thermal states of the fluid and particulate phases, increase.

(e) A higher micropolar parameter (η) results in a reduction in the velocities of both the micropolar fluid and suspended particles. Moreover, the presence of dust particles increases flow resistance, thereby requiring greater pumping power to sustain the desired flow rate.

In the second part (*Section 3.3*), the analysis was extended to an inclined channel oriented at an angle θ with the horizontal axis. The channel's inclination adds gravitational components along its direction, affecting both the fluid motion and the associated heat transfer. The same numerical approach was employed to obtain velocity and temperature distributions, as well as the corresponding pumping power, for various non-dimensional parameters. The key findings are as follows:

(a) We observed the predicted behavior from the primary velocity profile as θ increases, but the secondary velocity profiles indicate a drop in amplitude as the Hall effect that generates the secondary flow is overshadowed by the stronger primary flow. Gravity accelerates the fluid as θ increases, which increases shear stresses at the walls. This, in turn, raises frictional resistance and requires more energy to pump the fluid at higher flow rates, thereby increasing the pumping power.

(b) Typically, as particle concentration (R) rises, dust particle velocity decreases—much like movement is restricted in a crowded room. However, in this case, an increase in dust particle velocity was observed. This effect is likely due to intensified interactions such as collisions and momentum transfer between particles, creating a "collective motion" or "drafting" effect. This allows particles to move more efficiently together, resulting in a "slip" effect, where particles move more freely with reduced drag, potentially lowering the pumping power requirements.

(c) In relation to the Hartmann number (Ha^2), the magnetic field acts as a kind of "brake" on fluid mobility. This braking effect intensifies as Ha^2 increases, reduc-

ing both primary and secondary velocities. One contributing factor is the magnetic field's orientation with respect to the flow direction. The Lorentz force introduced by the magnetic field imposes additional resistance, resulting in a modest increase in pumping power as more energy is required to overcome it.

(d) Variation in the micropolar parameter (η) reduces the velocity profile for both the dust phase and the micropolar dusty fluid. A higher η increases resistance to microrotation, which inhibits momentum transfer and raises the effective viscosity of the fluid. Consequently, the higher resistance demands more pumping power to maintain the desired flow rate.

(e) The Reynolds number (Re) and pumping power exhibit an inverse relationship: as Re increases, the required pumping power decreases. Higher Re diminishes the significance of viscous forces, leading to lower internal friction and reduced energy loss through viscous dissipation. This efficiency lowers the energy needed to sustain the desired flow.

(f) Both the primary and secondary velocity profiles of the micropolar dusty fluid flow tend toward stability as time (t) progresses, indicating the system is approaching a steady state. The pumping power steadily increases with t because dust particles in the fluid elevate its effective viscosity and introduce drag, opposing the flow. As the flow rate increases over time, so does this drag, requiring the pump to exert more energy to maintain the flow.

(g) Velocity profiles and pumping power remain almost unchanged under variations of Be, Bi, Ec, and Ek. These parameters cause only minor variations in flow resistance and velocity, largely due to the relatively constant Lorentz force from the magnetic field. As such, their overall influence on the system remains minimal.

The results presented in Tables 3.1 and 3.2 highlight the impact of channel orientation on the behavior of micropolar dusty fluid flow. While trends across key parameters remain qualitatively similar, the inclined channel exhibits stronger gravitational effects, which enhance flow acceleration and wall shear, thereby increasing pumping power.

Velocity and temperature distributions in the inclined configuration respond more sensitively to parameter changes, especially at higher inclination angles. Furthermore, particle interaction effects become more prominent in inclined flow. These observations highlight the significant role of inclination in altering fluid dynamics and energy requirements, underlining the necessity of accounting for geometry in flow system design.

Chapter 4

Flow and thermal analysis of Jeffrey fluid in a rotating horizontal channel under the effect of magnetic field

4.1 Introduction

Jeffrey fluids, a class of viscoelastic non-Newtonian fluids characterized by stress relaxation and retardation effects, were introduced in *Section 1.6.3* of *Chapter 1*, where their historical development, rheological properties, and industrial applications (e.g., polymer processing, biomedical systems, and lubrication) were discussed in detail. This chapter focuses on Jeffrey fluid dynamics in horizontal channel configurations, where the interplay of rotational forces, MHD, and thermal effects introduces unique transport phenomena critical for applications such as microfluidic devices, energy systems, and industrial fluid transport.

Horizontal channels defined by two parallel plates aligned perpendicular to gravitational acceleration, provide a foundational geometry for studying pressure-driven and boundary-driven flows of Jeffrey fluids. The viscoelastic nature of Jeffrey fluids enables precise control over velocity profiles and stress distributions in such configurations, making them ideal for optimizing processes like pharmaceutical mixing and thermal management systems. Recent studies, such as Fiza et al. [76] and Rani [77], have

demonstrated that Jeffrey fluids in horizontal channels exhibit distinct flow characteristics under magnetic fields, including modified velocity profiles and enhanced heat transfer rates due to Lorentz force interactions. For instance, Rani's analysis of oscillatory Couette flow revealed that radiative heat transfer and magnetic fields significantly alter temperature gradients and flow stability.

Rotation and electrical conductivity further enriches the fluid dynamics of Jeffrey fluids in horizontal channels. System rotation generates Coriolis forces that modify momentum transport, while MHD effects induce Lorentz forces that oppose fluid motion, creating complex flow structures. Studies by Hayat et al. [66] and Kumar and Sharma [132] have shown that increasing the Hartmann number dampens velocity profiles, whereas rotation parameters enhance secondary flows, leading to asymmetric velocity distributions. These coupled effects are particularly relevant in aerospace engineering and nuclear reactor cooling systems, where precise flow control under electromagnetic constraints is essential. Shehzad et al. [133] explore how magnetic fields, along with internal heat generation and thermal radiation, influence the flow dynamics and heat transfer characteristics, highlighting their combined effect on the system's performance. Similarly, Akbar et al. [134] and Das et al. [135] show that the magnetic field affects the velocity and temperature profiles by dampening fluid motion.

Heat transfer in Jeffrey fluid flows is profoundly influenced by viscoelasticity, MHD, and rotational forces. Gerdroodbary et al. [75] demonstrated that thermal radiation amplifies temperature profiles in Jeffrey-Hamel flows, while Vijay and Sharma [136] highlighted the role of temperature-dependent viscosity in modifying heat transfer rates under rotating MHD conditions. Dogonchi et al. [137] further observed that viscous dissipation and Joule heating in horizontal channels elevate local Nusselt numbers, emphasizing the need to account for energy losses in high-velocity applications.

Despite the extensive body of literature, several research gaps remain in the comprehensive understanding of Jeffrey fluid behavior in horizontal channels, especially when considering the simultaneous effects of rotation, magnetohydrodynamics, and heat transfer. Existing studies often focus on isolated effects or simplified configura-

tions, leaving the integrated impact of these parameters underexplored. Furthermore, numerical methods employed in prior analyses require validation and stability assessment to ensure the accuracy and reliability of the solutions. There is also a need to evaluate key engineering metrics such as pumping power and to characterize the influence of various dimensionless parameters on velocity and temperature distributions comprehensively.

To address these gaps, this work focuses on formulating a detailed model of Jeffrey fluid flow in a horizontal channel by incorporating the combined effects of rotation, MHD, and thermal transport. The equations governing the system are addressed using RBF-PSM, a highly accurate, mesh-free numerical method. The methodology includes validating the numerical approach by comparing results with existing analytical or numerical solutions, followed by a stability analysis to ensure the robustness of the scheme. Further analysis will focus on velocity and temperature profiles for various controlling parameters, concluding with an evaluation of pumping power requirements. Accordingly, this chapter presents the mathematical modeling and boundary conditions, details the numerical solution technique, discusses validation and stability results, analyzes the flow and thermal characteristics, and concludes with the pumping power assessment.

4.2 Mathematical Modeling

This section develops the mathematical model for the flow of an incompressible Jeffrey fluid through a horizontal channel formed by two infinite parallel plates, as described in Figure 4.1. The fluid motion is generated by the movement of the upper plate combined with a uniformly applied pressure gradient along the channel length. The fluid is electrically conducting and subjected to an external uniform magnetic field applied perpendicular to the flow direction. Additionally, the system rotates uniformly about an axis normal to the plates, necessitating the inclusion of rotational effects. The combined influences of viscoelasticity, magnetohydrodynamics, and rotation on the fluid flow and thermal fields are analyzed in this framework.

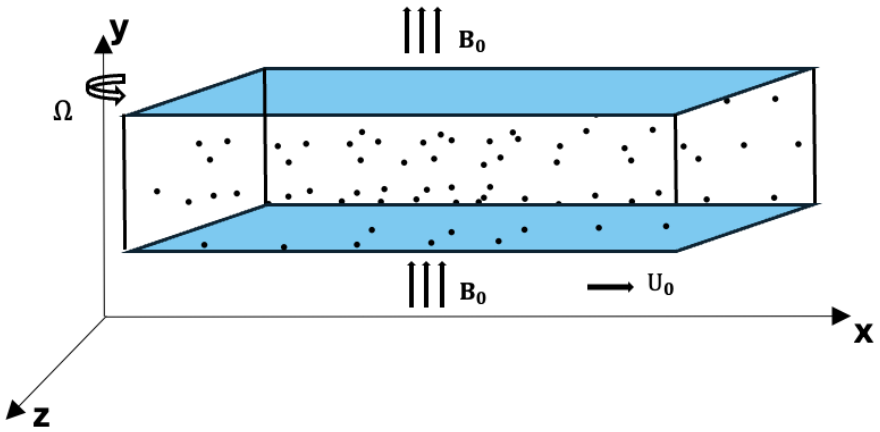

Fig. 4.1 Schematic of a Horizontal Channel with Jeffrey Fluid Flow

4.2.1 Key Features of the Model

(a) **Horizontal Channel Geometry:**

(i) The fluid moves within a horizontal channel formed by two parallel plates of infinite length, spaced a finite distance apart.

(ii) A steady pressure gradient along the x-axis drives the flow, while the upper plate moves at a constant velocity.

(iii) The flow domain is assumed sufficiently wide and long to neglect end and side effects, justifying a one-dimensional variation predominantly in the transverse y-direction.

(b) **Jeffrey Fluid Characteristics:**

(i) The fluid is incompressible and electrically conductive, allowing interaction with the imposed magnetic field.

(ii) It exhibits viscoelastic behavior modeled by the Jeffrey constitutive equation, characterized by relaxation time λ_1.

(iii) The model captures nonlinear elastic effects through the extra stress tensor related to the velocity gradients and their material derivatives.

(c) **External Magnetic Field:**

(i) A constant magnetic field $\mathbf{B}_0$ acts along the y-direction, perpendicular to the primary flow.

(ii) The magnetic field induces Lorentz forces $\mathbf{F}_L$ within the electrically conducting fluid, which act as resistive body forces opposing the flow.

(iii) The model incorporates the influence of Hall current and ion-slip, introducing additional parameters—Hall parameter B_e and ion-slip parameter B_i—that modify the effective electromagnetic resistance.

(d) **Rotating Reference Frame:**

(i) A uniform angular velocity Ω is applied to the system, establishing a rotating reference frame.

(ii) Rotation introduces Coriolis and centrifugal forces affecting the fluid momentum.

(iii) The Coriolis force, $2\rho_f(\Omega \times \mathbf{u})$, is explicitly included as an acceleration term in the momentum equation.

(iv) The centrifugal force is absorbed into the modified pressure gradient due to incompressibility and channel geometry assumptions.

(e) **Flow Dynamics:**

(i) The velocity field exhibits both primary flow in the x-direction driven by the plate motion and pressure gradient, and secondary flow in the z-direction induced by rotational effects.

(ii) The velocity vector is represented as

$$\mathbf{u} = u_1\mathbf{i} + u_2\mathbf{j} + u_3\mathbf{k}$$

where u_1, u_2, u_3 correspond to velocity components in x, y, and z directions respectively.

(iii) The flow is assumed laminar, incompressible, and fully developed along the channel length.

4.2.2 Governing Equations of Jeffrey Fluid

(a) **Standard Governing Equattions:** The classical governing equations for an incompressible Jeffrey fluid flow [55] are as follows (for details refer to *Chapter 1*, Equations (1.63) - (1.65)):

(i) **Continuity Equation:** The incompressibility condition mandates

$$\nabla \cdot \mathbf{u} = 0 \tag{4.1}$$

(ii) **Momentum Equation:** The momentum balance is governed by

$$\rho_f \left(\frac{\partial \mathbf{u}}{\partial t} + \mathbf{u} \cdot \nabla \mathbf{u} \right) = -\nabla P + \nabla \cdot \mathbf{S} \tag{4.2}$$

where ρ_f is the fluid density, P is the pressure, and $\mathbf{S}$ is the extra stress tensor characterizing the viscoelastic Jeffrey fluid behavior.

The constitutive relation for $\mathbf{S}$ is given by:

$$\mathbf{S} + \lambda_1 \frac{D\mathbf{S}}{Dt} = \mu \left(\mathbf{R}_1 + \lambda_2 \frac{D\mathbf{R}_1}{Dt} \right) \tag{4.3}$$

with

$$\mathbf{R}_1 = \nabla \mathbf{u} + (\nabla \mathbf{u})^T$$

and where μ is the dynamic viscosity, λ_1 the relaxation time, λ_2 the retardation time, and $\frac{D}{Dt}$ denotes the material derivative.

For steady or simplified flow, $\mathbf{S}$ reduces to

$$\mathbf{S} = \frac{\mu}{1 + \lambda_1} \left(\mathbf{R}_1 + \lambda_2 \frac{D\mathbf{R}_1}{Dt} \right) \tag{4.4}$$

(iii) **Energy Equation:** The energy conservation is expressed by

$$\rho_f c_p \left(\frac{\partial T}{\partial t} + \mathbf{u} \cdot \nabla T \right) = \nabla \cdot (k \nabla T) + \Phi \tag{4.5}$$

where c_p is the specific heat at constant pressure, T is temperature, k is thermal conductivity, and Φ represents the viscous dissipation function.

(b) **Incorporation of Rotation and Magnetic Field:**

(i) **Effects of Rotation:** The flow is considered in a frame rotating uniformly with angular velocity Ω about the y-axis. This frame induces additional inertial forces:

1. *Coriolis force:* Acts as an apparent force modifying fluid acceleration, expressed as (as described in Equation (1.73) of *Section 1.7*)

$$2\rho_f(\mathbf{\Omega} \times \mathbf{u})$$

2. *Centrifugal force:* Typically absorbed into the pressure gradient term due to incompressibility and channel geometry assumptions and is not explicitly included in the momentum equations.

Thus, the momentum equation is augmented by the Coriolis term as

$$\rho_f \left(\frac{\partial \mathbf{u}}{\partial t} + 2(\Omega \times \mathbf{u}) + \mathbf{u} \cdot \nabla \mathbf{u} \right) = -\nabla P + \nabla \cdot \mathbf{S} \tag{4.6}$$

(ii) **Effects of Magnetic Field:** The fluid is subjected to a uniform magnetic field B_0 in the y-direction. The electromagnetic force per unit volume, known as the Lorentz force $\mathbf{F}_L$, acts as a resistive body force opposing fluid motion. Accounting for Hall and ion-slip phenomena, $\mathbf{F}_L$ is modeled as

$$\mathbf{F}_L = -\sigma B_0^2 \frac{1 + B_i B_e}{(1 + B_i B_e)^2 + B_e^2} \mathbf{u} \tag{4.7}$$

where σ is the electrical conductivity, B_i the ion-slip parameter, and B_e the Hall parameter.

(c) **Modified Governing Equations of Jeffrey Fluid:** Combining the classical Jeffrey fluid equations from (4.1) to (4.5) with the rotation (Equation (4.6)) and magnetic field effects (Equation (4.7)) detailed above, and considering that viscous effects predominantly occur in the y-direction, following are the continuity, momentum, and energy equations governing the flow of the incompressible Jeffrey fluid under these combined effects:

$$\nabla \cdot \mathbf{u} = 0 \tag{4.8}$$

$$\rho_f \left(\frac{\partial \mathbf{u}}{\partial t} + 2(\Omega \times \mathbf{u}) + \mathbf{u} \cdot \nabla \mathbf{u} \right) = -\nabla P + \frac{\mu}{1+\lambda_1} \frac{\partial^2 \mathbf{u}}{\partial y^2} - \sigma B_0^2 \frac{1 + B_i B_e}{(1 + B_i B_e)^2 + B_e^2} \mathbf{u} \tag{4.9}$$

$$\rho_f c_p \frac{\partial T}{\partial t} = k \frac{\partial^2 T}{\partial y^2} + \frac{\mu}{1+\lambda_1} \left(\frac{\partial \mathbf{u}}{\partial y} \right)^2 + \sigma B_0^2 \frac{1 + B_i B_e}{(1 + B_i B_e)^2 + B_e^2} \mathbf{u}^2 \tag{4.10}$$

Where:

- $\mathbf{u}$ = Velocity vector
- ρ_f = Fluid density
- P = Pressure
- μ = Dynamic viscosity
- λ_1 = Relaxation time
- Ω = Angular velocity vector (rotation)
- σ = Electrical conductivity
- B_0 = Applied magnetic field strength
- B_i = Ion-slip parameter
- B_e = Hall parameter
- c_p = Specific heat at constant pressure

- T = Temperature
- k = Thermal conductivity

Note: In the present analysis, the retardation time λ_2 is neglected by assuming $\lambda_2 = 0$, which simplifies the constitutive model while retaining the dominant viscoelastic effects captured by the relaxation time λ_1. This assumption is commonly adopted in literature under steady or simplified flow conditions where the retardation effects are minimal.

(d) **Dimensionless Scales and Variables:** To facilitate mathematical analysis and numerical computation, the governing equations are transformed into dimensionless form using characteristic scales. Let L denote the half-distance between the channel plates, and U_0 represent the characteristic velocity scale associated with the upper plate velocity. The characteristic time scale is defined as $\frac{L}{U_0}$, while pressure is scaled by $\rho_f U_0^2$.

The following dimensionless variables are introduced:

$$y^* = \frac{y}{L}, \quad t^* = \frac{tU_0}{L}, \quad u_i^* = \frac{u_i}{U_0} \quad (i = 1, 3), \quad T^* = \frac{T - T_1}{T_2 - T_1}, \quad P^* = \frac{P}{\rho_f U_0^2}$$

where T_1 and T_2 are the temperatures at the lower and upper plates respectively. For brevity, the asterisks will be omitted henceforth, with all variables understood to be dimensionless unless otherwise stated.

(e) **Initial and Boundary Conditions:** The dimensionless initial and boundary conditions for the velocity and temperature fields are prescribed as follows:

Initial conditions (at $t = 0$):

$$u_1(y, 0) = u_3(y, 0) = 0, \quad T(y, 0) = 0$$

Boundary conditions (for all $t > 0$) at the channel walls $y = \pm 1$:

$$u_1(-1, t) = 0, \quad u_1(1, t) = 1, \quad u_3(-1, t) = 0, \quad u_3(1, t) = 1,$$

$$T(-1,t) = 0, \quad T(1,t) = 1$$

These conditions correspond to no-slip velocity at the stationary lower plate and unit velocity at the moving upper plate, along with prescribed dimensionless temperatures at the boundaries.

(f) **Dimensionless Parameters:** Several dimensionless parameters arise naturally in the non-dimensionalization process, capturing the relative effects of inertia, magnetic field, rotation, and thermal properties (for details refer to *Section 1.9*):

Reynolds number:	$Re = \dfrac{\rho_f U_0 L}{\mu}$
Hartmann number:	$Ha^2 = \dfrac{\sigma B_0^2 L^2}{\mu}$
Coriolis frequency parameter:	$C = 4\pi\Omega$
Ekman number:	$Ek = \dfrac{Re}{4\pi}$
Prandtl number:	$Pr = \dfrac{\mu c_p}{k}$
Eckert number:	$Ec = \dfrac{U_0^2}{c_p(T_2 - T_1)}$
Jeffrey fluid relaxation parameter:	$\lambda = \lambda_1 \dfrac{U_0}{L}$

The parameters Be and Bi remain dimensionless and are retained as introduced as specified in the fundamental equations.

(g) **Dimensionless Governing Equations:** Using the above scales and parameters, the governing equations of the Jeffrey fluid flow, incorporating rotation and magnetic field effects, reduce to the following dimensionless partial differential equations:

$$\frac{\partial u_1}{\partial t} = Ge(t) + \frac{1}{Re(1+\lambda)}\frac{\partial^2 u_1}{\partial y^2} - \frac{Ha^2}{Re}\left(\frac{(1+Bi\,Be)u_1 + Be\,u_3}{(1+Bi\,Be)^2 + Be^2}\right) - \frac{2CEk}{Re}u_3 \quad (4.11)$$

$$\frac{\partial u_3}{\partial t} = \frac{1}{Re(1+\lambda)}\frac{\partial^2 u_3}{\partial y^2} - \frac{Ha^2}{Re}\left(\frac{(1+Bi\,Be)u_3 - Be\,u_1}{(1+Bi\,Be)^2 + Be^2}\right) + \frac{2CEk}{Re}u_1 \quad (4.12)$$

$$\frac{\partial T}{\partial t} = \frac{1}{Pr\,Re}\frac{\partial^2 T}{\partial y^2} + \frac{Ec}{Re(1+\lambda)}\left(\frac{\partial u_1}{\partial y}\right)^2 + \frac{Ec\,Ha^2}{Re}\left(\frac{1+Bi\,Be}{(1+Bi\,Be)^2 + Be^2}\right)u_1^2 \quad (4.13)$$

Here, $Ge(t) = -\frac{\partial P}{\partial x}$ represents the dimensionless applied pressure gradient, which may be time-dependent. The terms correspond to viscous diffusion, Lorentz force due to magnetic field, Coriolis force induced by rotation, thermal conduction, viscous dissipation, and Joule heating respectively.

4.3 Numerical Solution and Results

4.3.1 Radial Basis Function Pseudospectral Method

To numerically solve the dimensionless governing equations (4.11) to (4.13) describing the Jeffrey fluid flow and thermal behavior in the horizontal channel, the RBF-PSM is employed. This meshless spectral technique, detailed in *Chapter 1 (Section 1.10)* and particularly in *Section 1.10.7*, offers high spatial accuracy by leveraging the global approximation properties of radial basis functions combined with spectral convergence. The principal steps of this method are summarized as follows:

(a) **Spatial Discretization and Node Selection:** The physical domain along the transverse coordinate $y \in [-1, 1]$ is discretized into N collocation points $\{y_i\}_{i=1}^{N}$. These nodes serve as centers for the RBF's and need not be uniformly distributed.

(b) **Choice of Radial Basis Function:** For the present problem, the Wendland radial basis function ϕ is selected due to its compact support and favorable smoothness properties (see Equation (2.13), *Section 2.2.3*, *Chapter 2*). This choice ensures numerical stability and sparsity in the resulting matrices. The shape parameter ϵ controls the flatness of ϕ, impacting the accuracy and conditioning of the approximation.

(c) **Approximation of Solution:** The unknown velocity components $u_1(y, t)$, $u_3(y, t)$, and temperature $T(y, t)$ are approximated as linear combinations of the chosen radial basis functions centered at the collocation points, following the representation:

$$z(y, t) \approx \sum_{j=1}^{N} \lambda_j(t)\, \phi(\|y - y_j\|),$$

where z represents a generic dependent variable and $\lambda_j(t)$ are the time-dependent coefficients to be determined (refer to Equation (1.92), *Section 1.10.3, Chapter 1*).

(d) **Formation of Differentiation Matrices:** Spatial derivatives are discretized by constructing differentiation matrices corresponding to the first and second derivatives, denoted by D_1 and D_2, respectively. These matrices are assembled as

$$D_1 = D_x A^{-1}, \quad D_2 = D_{xx} A^{-1},$$

where A is the interpolation matrix with entries $A_{ij} = \phi(\|y_i - y_j\|)$, and D_x, D_{xx} contain evaluations of the first and second derivatives of ϕ at the collocation points (see Equations (1.106) to (1.109), *Chapter 1*).

(e) **Transformation to a System of Ordinary Differential Equations:** Substituting the RBF approximations and replacing spatial derivatives by the differentiation matrices, the governing PDEs (4.11) - (4.13) reduce to the following system of ODEs with respect to time:

$$\frac{du_1}{dt} = \mathrm{Ge}(t) + \frac{1}{\mathrm{Re}(1+\lambda)} D_2 u_1 - \frac{\mathrm{Ha}^2}{\mathrm{Re}} \left[\frac{(1 + \mathrm{Bi}\,\mathrm{Be})u_1 + \mathrm{Be}\,u_3}{(1 + \mathrm{Bi}\,\mathrm{Be})^2 + \mathrm{Be}^2} \right] - \frac{2C\mathrm{Ek}}{\mathrm{Re}} u_3, \tag{4.14}$$

$$\frac{du_3}{dt} = \frac{1}{\mathrm{Re}(1+\lambda)} D_2 u_3 - \frac{\mathrm{Ha}^2}{\mathrm{Re}} \left[\frac{(1 + \mathrm{Bi}\,\mathrm{Be})u_3 - \mathrm{Be}\,u_1}{(1 + \mathrm{Bi}\,\mathrm{Be})^2 + \mathrm{Be}^2} \right] + \frac{2C\mathrm{Ek}}{\mathrm{Re}} u_1, \tag{4.15}$$

$$\frac{dT}{dt} = \frac{1}{\mathrm{Pr}\,\mathrm{Re}} D_2 T + \frac{\mathrm{Ec}}{\mathrm{Re}(1+\lambda)} (D_1 u_1)^2 + \frac{\mathrm{Ec}\,\mathrm{Ha}^2}{\mathrm{Re}} \frac{1 + \mathrm{Bi}\,\mathrm{Be}}{(1 + \mathrm{Bi}\,\mathrm{Be})^2 + \mathrm{Be}^2} u_1^2. \tag{4.16}$$

Here, the vectors u_1, u_3, T contain the nodal values of the primary velocity, secondary velocity, and temperature fields, respectively. The differentiation matrices D_1 and D_2 approximate the first and second spatial derivatives. The parameters $\mathrm{Ge}(t)$, Re, Ha, Be, Bi, C, Ek, Pr, Ec, and λ denote the dimensionless pressure gradient, Reynolds number, Hartmann number, Hall parameter, ion-slip parameter, rotation and Ekman numbers, Prandtl number, Eckert number, and Jeffrey fluid relaxation parameter, respectively.

(f) **Time Integration Using SSP RK43 Scheme:** The system of ordinary differential equations (4.14)–(4.16), obtained via the RBF-PSM, can be expressed in vector

form as:

$$\frac{d\mathbf{U}}{dt} = \mathbf{F}(t, \mathbf{U}), \tag{4.17}$$

where

$$\mathbf{U} = \begin{bmatrix} \mathbf{u}_1 \\ \mathbf{u}_3 \\ \mathbf{T} \end{bmatrix}, \quad \mathbf{F}(t, \mathbf{U}) = \begin{bmatrix} F_1(t, \mathbf{U}) \\ F_2(t, \mathbf{U}) \\ F_3(t, \mathbf{U}) \end{bmatrix}$$

represents the functions corresponding to the velocity and temperature fields, involving the spatial differentiation matrices and physical parameters.

The detailed methodology for solving the ODE system are outlined in Section 2.2.3. The present time integration follows the same procedure, employing the SSP RK43 to advance the solution in time.

The following are the principal steps to solve the system of ODEs using the SSP RK43 scheme:

(i) **Initialization:** The initial condition $\mathbf{U}^0$ is prescribed based on the physical problem at $t = 0$. The time step Δt is selected to ensure numerical stability and accuracy.

(ii) **Stage Computations:** The SSP RK43 scheme advances the solution from time t_n to $t_{n+1} = t_n + \Delta t$ through the following intermediate stages:

$$\mathbf{U}^{(1)} = \mathbf{U}^n + \frac{\Delta t}{2}\mathbf{F}\left(t_n, \mathbf{U}^n\right), \tag{4.18}$$

$$\mathbf{U}^{(2)} = \mathbf{U}^{(1)} + \frac{\Delta t}{2}\mathbf{F}\left(t_n + \frac{\Delta t}{2}, \mathbf{U}^{(1)}\right), \tag{4.19}$$

$$\mathbf{U}^{(3)} = \frac{2}{3}\mathbf{U}^n + \frac{1}{3}\mathbf{U}^{(2)} + \frac{\Delta t}{6}\mathbf{F}\left(t_n + \Delta t, \mathbf{U}^{(2)}\right). \tag{4.20}$$

At each stage, suitable boundary conditions are applied to the intermediate solution vectors $\mathbf{U}^{(1)}$, $\mathbf{U}^{(2)}$, and $\mathbf{U}^{(3)}$ to maintain the physical consistency of the flow and thermal fields.

(iii) **Final Update:** The solution at the next time level is obtained by

$$\mathbf{U}^{n+1} = \mathbf{U}^{(3)} + \frac{\Delta t}{2}\mathbf{F}\left(t_n + \frac{\Delta t}{2}, \mathbf{U}^{(3)}\right), \tag{4.21}$$

followed by the enforcement of boundary conditions on $\mathbf{U}^{n+1}$.

These steps summarize the procedure to solve the system of ODEs using the SSP RK43 scheme.

4.3.2 Radial Basis Function Pseudospectral Method Validation

The comparative analysis presented in the graphs illustrates the performance of two numerical methods, RBF-PSM and the Modified Cubic B-Spline Differential Quadrature Method (MCBS DQM)—in evaluating the velocity profiles of a Jeffrey fluid at time $t = 3$. The primary and secondary velocity profiles, each plotted against the spatial coordinate, demonstrate the fluid's behavior under the specified conditions. The RBF-PSM, which served as the primary method for the broader analysis, shows consistent results across the velocity profiles, as evidenced by the smooth curves in both graphs. To validate the reliability of RBF-PSM, a comparison with MCBS DQM was conducted at $t = 3$, revealing close alignment between the two approaches. The zoomed-in sections of the graphs highlight the minor variations, such as the slight differences in velocity values (e.g., 0.281 vs. 0.279 for secondary velocity and 0.395 vs. 0.393 for primary velocity), underscoring the robustness and accuracy of RBF-PSM while confirming that MCBS DQM produces comparable outcomes, thus reinforcing confidence in the chosen method for modeling Jeffrey fluid dynamics.

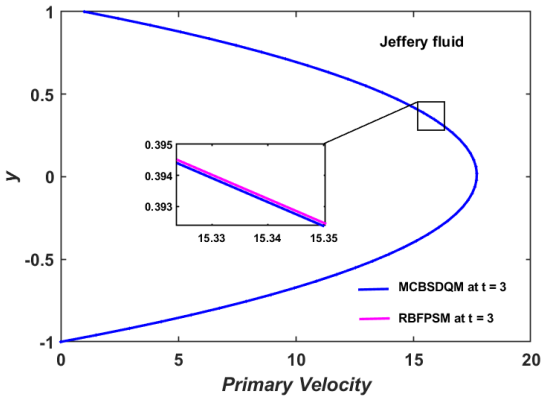

Fig. 4.2 Comparison of Primary Velocity Profiles at $t = 3$ for Jeffrey Fluid Using MCBS-DQM and RBF-PSM

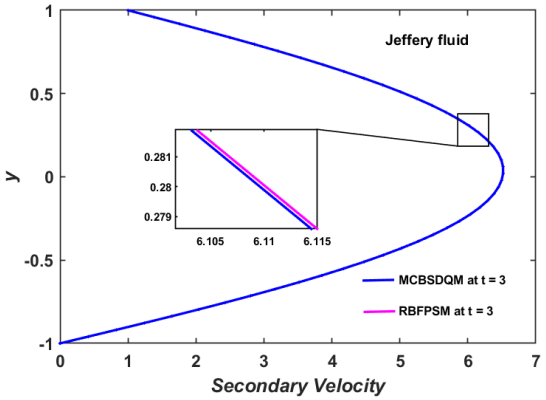

Fig. 4.3 Comparison of Secondary Velocity Profiles at $t = 3$ for Jeffrey Fluid Using MCBS-DQM and RBF-PSM

As highlighted in section (3.3), the choice of an effective shape parameter plays a critical role in the RBF-PSM. The selection of this parameter significantly influences both the accuracy of the RBF approximation and the computational stability of the solution. In this study, the shape parameter, optimized using the Leave-One-Out Cross-Validation (LOOCV) algorithm, is determined to be $\epsilon = 0.100039$.

4.3.3 Stability Analysis

Evaluating the stability of numerical methods is essential, as it ensures the reliability and precision of computational results, while unstable approaches can yield erroneous or divergent outcomes. This study uses matrix-based stability analysis, a standard and efficient method in scientific computing and numerical analysis, to evaluate the reliability of the proposed numerical approach. The approach involves constructing an approximate representation of the differential equation in matrix form, derived from its linear difference equation formulation, followed by a detailed analysis of the matrix's eigenvalues. These eigenvalues serve as indicators of stability: the method is deemed stable if the real parts of all eigenvalues are negative.

Stability evaluations were conducted across various values of N (node points). The eigenvalues of the corresponding matrix for $N = 30$ and $N = 50$ are depicted in Figures 4.4 and 4.5, respectively. For $N = 30$, the eigenvalues, represented in the complex plane, show a distribution of uniformly negative real parts and minimal imaginary components, signifying strong stability. Likewise, for $N = 50$, the eigenvalues maintain negative real parts without any imaginary components, and the stability persists even with an increased number of node points. The consistent negativity of the real parts and absence of positive values in both cases affirm the stability of the numerical method across the evaluated range of node points.

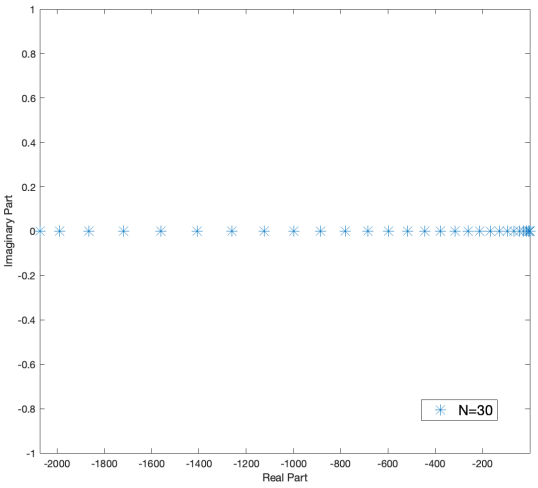

Fig. 4.4 Stability diagram derived through eigenvalue analysis of the associated matrix for $N = 30$

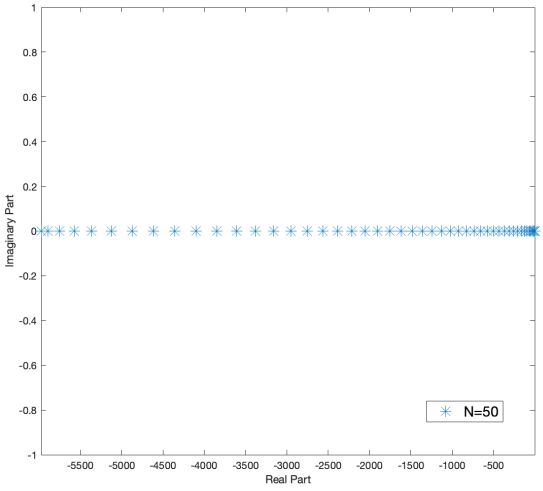

Fig. 4.5 Stability diagram derived through eigenvalue analysis of the associated matrix for $N = 50$

4.3.4 Analysis of Velocity Profiles

In this subsection, the velocity profiles are analyzed, which governs the viscoelastic response of the fluid. The discussion highlights how variations in this parameter influence the flow structure by modifying the rate of momentum transfer and altering the temporal relaxation behavior of the fluid elements. The interpretation of the graphical results emphasizes the physical mechanisms through which the relaxation parameter regulates the velocity field, offering a clearer understanding of its role in shaping the overall flow dynamics.

Figures 4.6 and 4.7 illustrate how the primary and secondary velocities change over time, with each curve corresponding to a specific time ($t = 1$, $t = 2$, and $t = 3$). The primary velocity graph shows a sinusoidal pattern with oscillations that decay over time. The secondary velocity graph also exhibits oscillatory behavior, but the oscillations are less pronounced compared to the primary velocity. The amplitude of the oscillations decreases as time progresses for both primary and secondary velocities, indicating a damping effect. The Jeffrey fluid's viscosity dissipates kinetic energy, contributing to the damping of the oscillations. For both velocity profiles, the initial oscillations represent the transient response of the fluid to the applied forces. Both graphs are influenced by the Coriolis force, which arises due to the rotation of the system. The increasing velocities indicate that the system is still in the transient phase, where the driving forces are causing the flow to accelerate.

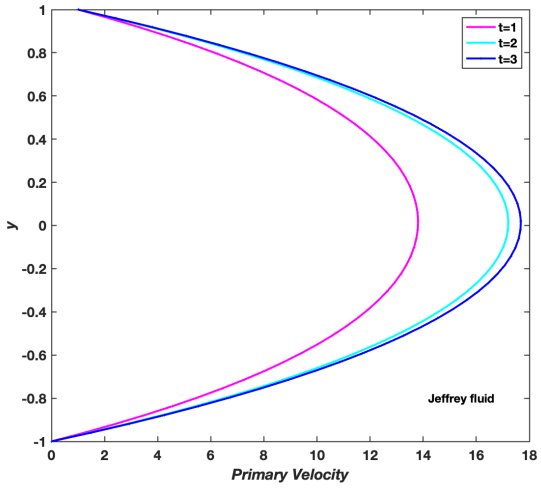

Fig. 4.6 Primary velocity profiles of fluid flow with varying time t, $Ge = 20$, $Re = 1$, $Ha^2 = 1$, $Bi = 2$, $Be = 2$, $C = 1$, $Ek = 0.25$, $Ec = 0.5$, $\lambda = 1$, $Pr = 3$

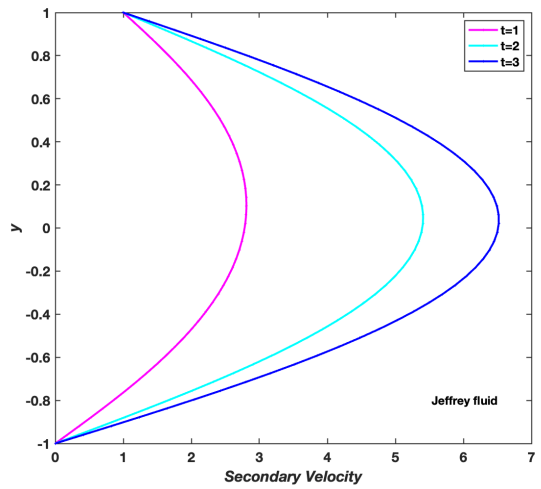

Fig. 4.7 Secondary velocity profiles of fluid flow with varying time t, $Ge = 20$, $Re = 1$, $Ha^2 = 1$, $Bi = 2$, $Be = 2$, $C = 1$, $Ek = 0.25$, $Ec = 0.5$, $\lambda = 1$, $Pr = 3$

The primary and secondary velocity profiles in Figures 4.8 and 4.9 show the variation of u_1, and u_3, respectively with respect to different values of Ge $(15, 20$ and $25)$. The primary velocity profile exhibits a parabolic shape, which is typical for pressure-driven flows between parallel plates. Whereas the secondary velocity profile exhibits a more complex shape compared to the primary velocity profile. As Ge increases, the primary velocity increases as expected. Nevertheless, the growth is not linear, as the magnetic field and rotational forces exert opposing effects. On the other hand, with an increase in Ge, the secondary velocity also increases, but the effect is less pronounced compared to the primary velocity. This is because the secondary flow is primarily driven by the Coriolis force, which is indirectly influenced by the pressure gradient. Both velocity profiles start at zero, then reach a maximum in the middle, and later decrease back to zero due to the no-slip condition. However, the primary velocity u_1 is generally higher in magnitude compared to the secondary velocity u_3. The results are consistent with the expected behavior when the pressure gradient Ge increases.

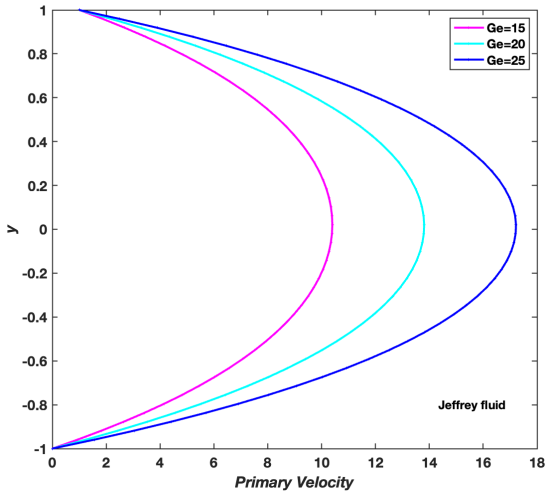

Fig. 4.8 Primary velocity profiles of fluid flow with varying pressure Ge, $t = 1$, $Re = 1$, $Ha^2 = 1$, $Bi = 2$, $Be = 2$, $C = 1$, $Ek = 0.25$, $Ec = 0.5$, $\lambda = 1$, $Pr = 3$

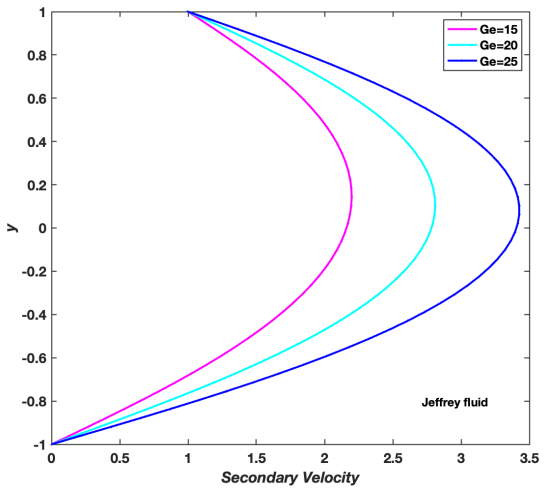

Fig. 4.9 Secondary velocity profiles of fluid flow with varying pressure Ge, $t = 1$, $Re = 1$, $Ha^2 = 1$, $Bi = 2$, $Be = 2$, $C = 1$, $Ek = 0.25$, $Ec = 0.5$, $\lambda = 1$, $Pr = 3$

The graphs in Figures 4.10 and 4.11 show how the primary and secondary velocities change along the coordinate y for various values of ($Re = 1, 1.5$, and 2). Both velocity profiles reach a maximum at the center of the channel ($y = 0$) and gradually decrease towards the walls ($y = \pm 1$). As Reynolds number Re increases, the maximum primary velocity also increases, due to reduction in viscous effects. Also, higher Re values correspond to a more flattened profile near the center, indicative of a more developed flow. Unlike the primary velocity, the secondary velocities decrease because, at higher Re, inertial forces dominate, reducing the impact of Coriolis-induced secondary motion. The flow becomes more stable, and secondary circulation is suppressed. The primary velocity profile exhibits a parabolic shape, while the secondary velocity profile is more asymmetric due to rotational and MHD effects. The primary velocity is significantly higher than the secondary velocity but is later more sensitive to changes in Re, showing a sharper variation with increasing Reynolds number.

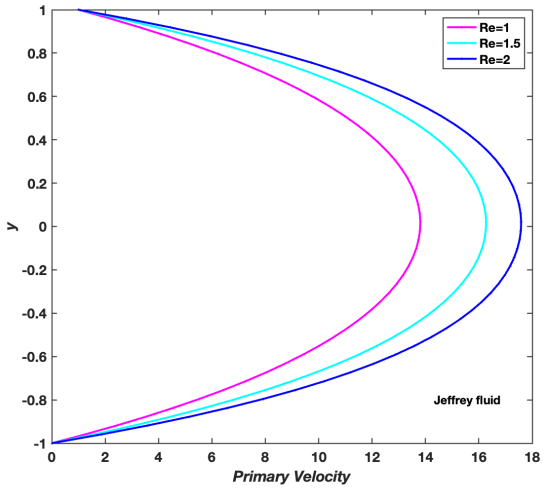

Fig. 4.10 Primary velocity profiles of fluid flow with varying Reynolds number Re, $t = 1$, $Ge = 20$, $Ha^2 = 1$, $Bi = 2$, $Be = 2$, $C = 1$, $Ek = 0.25$, $Ec = 0.5$, $\lambda = 1$, $Pr = 3$

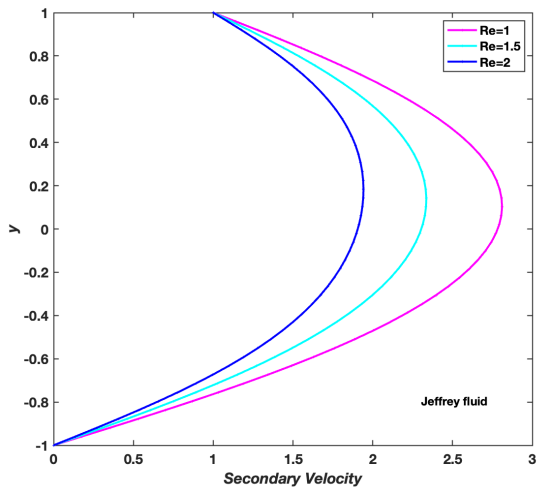

Fig. 4.11 Secondary velocity profiles of fluid flow with varying Reynolds number Re, $t = 1$, $Ge = 20$, $Ha^2 = 1$, $Bi = 2$, $Be = 2$, $C = 1$, $Ek = 0.25$, $Ec = 0.5$, $\lambda = 1$, $Pr = 3$

In Figures 4.12 and 4.13, the primary velocity u_1 and secondary velocity u_3 profiles are analyzed by varying the Hartmann number while keeping other parameters constant. The Hartmann number is a dimensionless quantity that represents the ratio of electromagnetic forces to viscous forces. The primary velocity profile is more symmetric and parabolic, while the secondary velocity profile shows slight asymmetry due to rotational effects. An increase in the Hartmann number corresponds to a stronger magnetic field, which amplifies the Lorentz force and suppresses fluid motion. Consequently, with rising Hartmann number, both primary and secondary velocities diminish, although the reduction in secondary velocity is comparatively weaker than in the primary velocity.

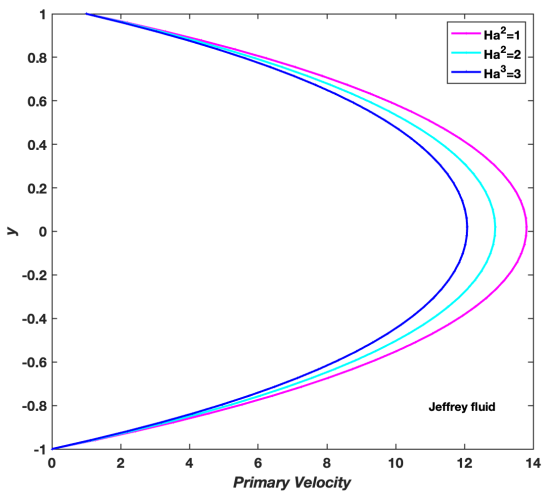

Fig. 4.12 Primary velocity profiles of fluid flow with varying Hartmann number Ha^2, $Ge = 20$, $t = 1$, $Re = 1$, $Bi = 2$, $Be = 2$, $C = 1$, $Ek = 0.25$, $Ec = 0.5$, $\lambda = 1$, $Pr = 3$

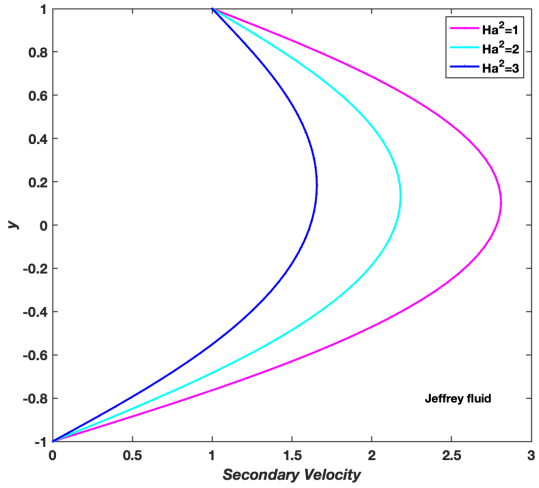

Fig. 4.13 Secondary velocity profiles of fluid flow with varying Hartmann number Ha^2, $Ge = 20$, $t = 1$, $Re = 1$, $Bi = 2$, $Be = 2$, $C = 1$, $Ek = 0.25$, $Ec = 0.5$, $\lambda = 1$, $Pr = 3$

Figures 4.14 and 4.15 explore the impact of the ion slip parameter B_i on the primary u_1 and secondary u_3 velocity profiles. The ion slip parameter B_i accounts for ion slip when a magnetic field is applied, altering the Lorentz force and affecting the fluid motion. As the ion slip parameter increases ($B_i = 1, 2,$ and 3), both primary and secondary velocities increase. In the case of primary velocity, a higher B_i means that the ion slip effect becomes more significant, which reduces the resistance to fluid motion caused by the magnetic field. As a result, the primary velocity increases because the damping effect of the magnetic field is weakened. The secondary flow is driven by the Coriolis force, which is influenced by the primary flow. Since the primary velocity increases with B_i, the Coriolis force also becomes stronger, leading to an increase in the secondary velocity. The primary velocity u_1 is less sensitive to changes in B_i compared to the secondary velocity u_3. The diminished effect of magnetic forces on the secondary flow, resulting from ion slip, allows the secondary velocity to respond more noticeably to B_i, producing wider spacing between the curves.

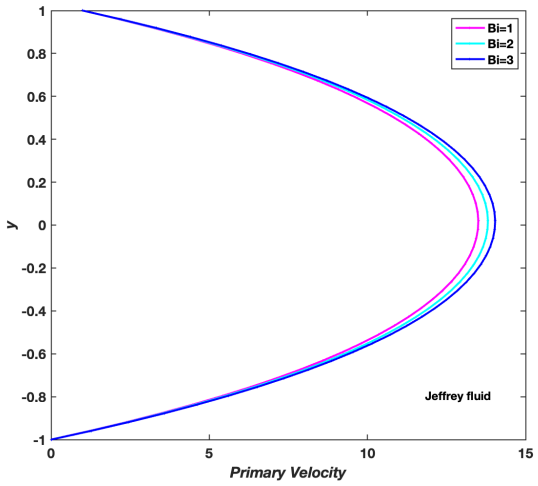

Fig. 4.14 Primary velocity profiles of fluid flow with varying Ion Slip parameter Bi, $Ge = 20$, $t = 1$, $Re = 1$, $Ha^2 = 1$, $Be = 2$, $C = 1$, $Ek = 0.25$, $Ec = 0.5$, $\lambda = 1$, $Pr = 3$

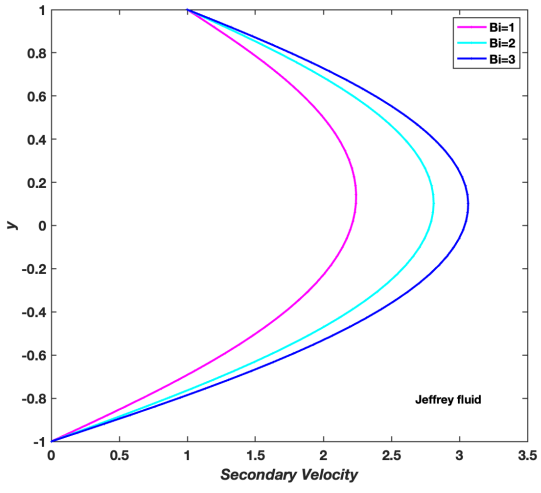

Fig. 4.15 Secondary velocity profiles of fluid flow with varying Ion Slip parameter Bi, $Ge = 20$, $t = 1$, $Re = 1$, $Ha^2 = 1$, $Be = 2$, $C = 1$, $Ek = 0.25$, $Ec = 0.5$, $\lambda = 1$, $Pr = 3$

Primary and secondary velocity graphs show a parabolic profile in Figures 4.16 and 4.17 with variations in the Hall parameter ($Be = 1, 2,$ and 3), the velocity is highest near the center of the channel and decreasing toward the walls due to the no-slip boundary condition. The increase in both primary and secondary velocities with increasing Be is attributed to the Hall effect, which reduces the effective resistance to the primary flow while simultaneously enhancing the transverse flow. By generating a transverse current, the Hall effect weakens the opposition from the Lorentz force, allowing the primary flow to accelerate. Simultaneously, this transverse current induces a stronger secondary flow in that direction, further amplified by the Coriolis and centrifugal forces.

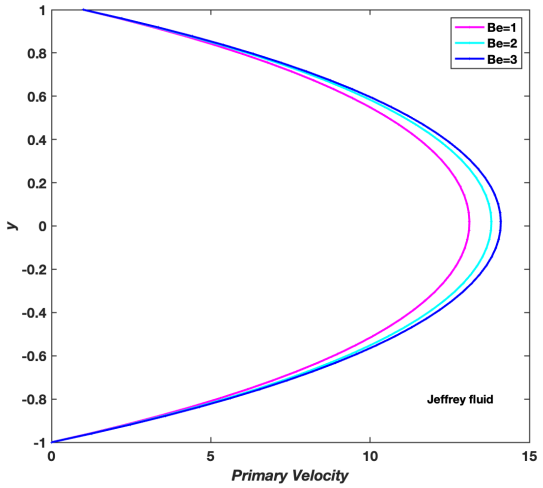

Fig. 4.16 Primary velocity profiles of fluid flow with varying Hall parameter Be, $Ge = 20$, $t = 1$, $Re = 1$, $Ha^2 = 1$, $Bi = 2$, $C = 1$, $Ek = 0.25$, $Ec = 0.5$, $\lambda = 1$, $Pr = 3$

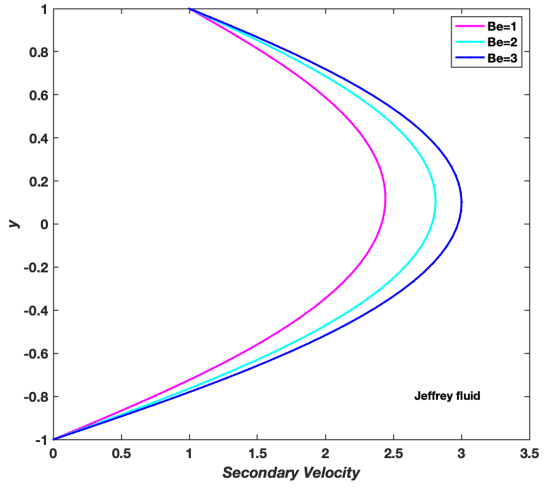

Fig. 4.17 Secondary velocity profiles of fluid flow with varying Hall parameter Be, $Ge = 20$, $t = 1$, $Re = 1$, $Ha^2 = 1$, $Bi = 2$, $C = 1$, $Ek = 0.25$, $Ec = 0.5$, $\lambda = 1$, $Pr = 3$

The following graphs show the primary and secondary velocity profiles, where the parameter varied is the Ekman number ($Ek = 0.15, 0.25,$ and 0.35). As the Ekman number Ek increases, the primary velocity decreases. This is because the Ekman number represents the ratio of viscous forces to rotational forces. A higher Ekman number means that viscous forces dominate over rotational forces, leading to greater resistance to the primary flow and a reduction in velocity. However, the increase in secondary velocity with increasing Ek is due to the viscous forces altering the balance of forces to enhance the secondary flow. With increasing Ek, weakened rotational forces allow viscous effects to alter the flow, enhancing the secondary velocity.

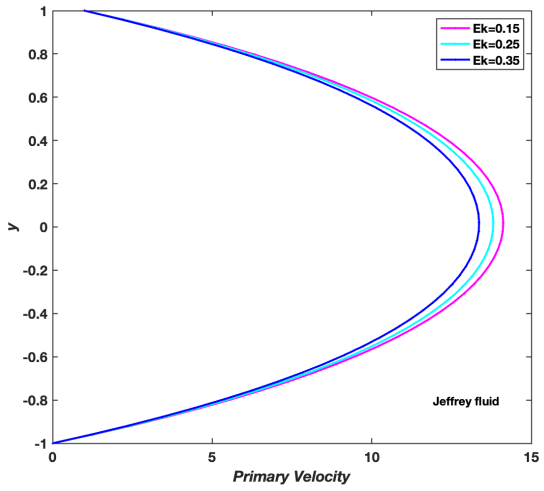

Fig. 4.18 Primary velocity profiles of fluid flow with varying Ekman number Ek, $Ge = 20$, $t = 1$, $Re = 1$, $Ha^2 = 1$, $Bi = 2$, $C = 1$, $Be = 2$, $Ec = 0.5$, $\lambda = 1$, $Pr = 3$

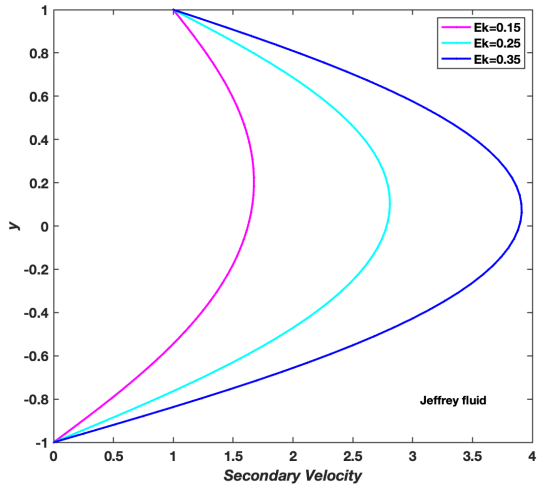

Fig. 4.19 Secondary velocity profiles of fluid flow with varying Ekman number Ek, $Ge = 20$, $t = 1$, $Re = 1$, $Ha^2 = 1$, $Bi = 2$, $C = 1$, $Be = 2$, $Ec = 0.5$, $\lambda = 1$, $Pr = 3$

The parameter C in these graphs (Figures 4.20 and 4.21) is defined as $C = 4\pi\Omega$, where Ω is the angular velocity of the rotating system. This parameter represents the Coriolis frequency parameter, which quantifies the strength of the Coriolis force in the rotating reference frame. As the Coriolis parameter C increases, it starts influencing the flow more noticeably. The primary velocity slows down because the Coriolis force pushes against it, resisting the motion. At the same time, this force enhances the secondary velocity, strengthening the transverse flow in the rotating system. Since the primary velocity is mainly controlled by the pressure gradient, changes in C have a relatively mild effect, which is why the curves remain close together. In contrast, the secondary velocity is directly driven by the Coriolis force, making it much more sensitive to C, which explains why its curves are more widely spaced.

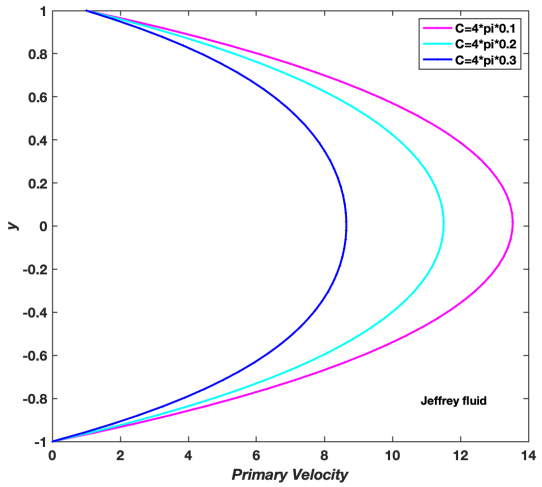

Fig. 4.20 Primary velocity profiles of fluid flow with varying C, $Ge = 20$, $t = 1$, $Re = 1$, $Ha^2 = 1$, $Bi = 2$, $Ek = 0.25$, $Be = 2$, $Ec = 0.5$, $\lambda = 1$, $Pr = 3$

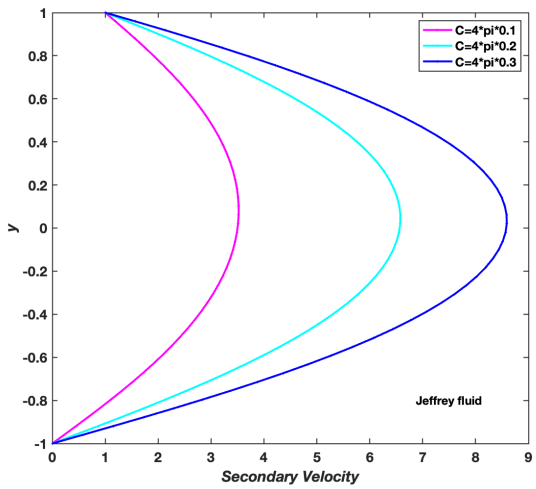

Fig. 4.21 Secondary velocity profiles of fluid flow with varying C, $Ge = 20$, $t = 1$, $Re = 1$, $Ha^2 = 1$, $Bi = 2$, $Ek = 0.25$, $Be = 2$, $Ec = 0.5$, $\lambda = 1$, $Pr = 3$

Figures 4.22 and 4.23 depict the primary and secondary velocity profiles with the Jeffrey fluid parameter λ varied at values of $0.5, 1.5$, and 2.5. The primary velocity profile typically exhibits a parabolic or near-parabolic shape due to the dominance of the pressure gradient and viscous forces. The secondary velocity profile, however, tends to display a complicated structure because of transverse influences like the Coriolis effect and fluid elasticity. The Jeffrey fluid parameter λ introduces elastic effects, which modify these profiles by altering the fluid's ability to store and release elastic energy. As λ increases, the fluid exhibits more elastic effects, which generally enhance the primary velocity. This happens because elasticity helps the fluid store and release energy, reducing resistance to the primary flow. Increasing λ amplifies the secondary velocity. This occurs because the enhanced elasticity of the fluid allows for greater energy transfer to the transverse flow, which is driven by the Coriolis force.

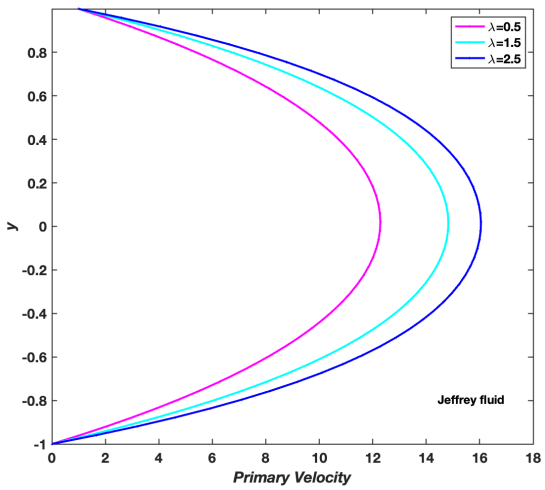

Fig. 4.22 Primary velocity profiles of fluid flow with varying Jeffrey fluid parameter λ, $Ge = 20$, $t = 1$, $Re = 1$, $Ha^2 = 1$, $Bi = 2$, $Ek = 0.25$, $Be = 2$, $Ec = 0.5$, $C = 1$, $Pr = 3$

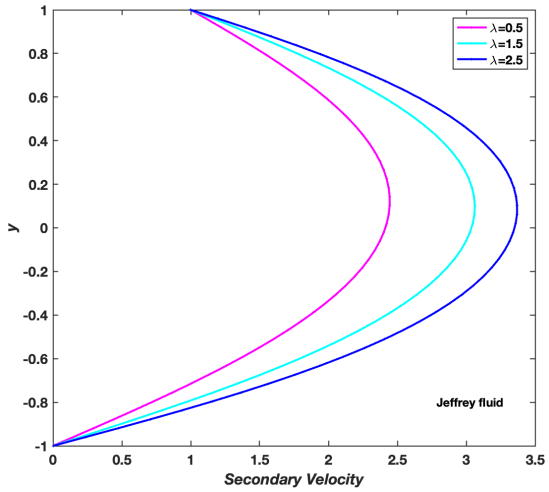

Fig. 4.23 Secondary velocity profiles of fluid flow with varying Jeffrey fluid parameter λ, $Ge = 20$, $t = 1$, $Re = 1$, $Ha^2 = 1$, $Bi = 2$, $Ek = 0.25$, $Be = 2$, $Ec = 0.5$, $C = 1$, $Pr = 3$

4.3.5 Analysis of Temperature Profiles

Effect of Time and Pressure on Temperature Profiles:

As time progresses, the temperature distribution in the Jeffrey fluid changes noticeably. Initially, at $t = 1$, the profile appears relatively uniform, but as time moves to $t = 2$ and $t = 3$, a steeper gradient develops. This indicates that the fluid is gradually heating up due to two main factors: viscous dissipation, where internal friction generates heat, and Joule heating, which arises from the coupling of the fluid with the magnetic field. Over time, these effects build up, leading to a more pronounced temperature variation, especially near the boundaries, suggesting an increase in heat transfer efficiency as the system evolves. This pattern is consistent with the expected behavior of such fluid flows.

As the pressure gradient Ge increases (with values of 15, 20, and 25), the temperature profile becomes steeper, indicating a more rapid rise in temperature. This happens because a stronger pressure gradient enhances fluid flow, leading to greater viscous dissipation—the heat generated due to internal friction within the fluid. As a result, the overall temperature of the fluid rises more sharply, creating a pronounced temperature gradient across the channel.

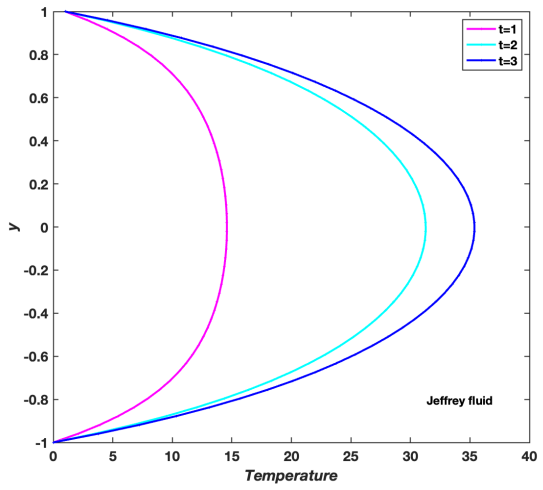

Fig. 4.24 Temperature profiles of fluid flow with varying time t, $Ge = 20$, $Re = 1$, $Ha^2 = 1$, $Bi = 2$, $Be = 0.5$, $C = 4 * \pi * 0.1$, $Ek = 0.25$, $Ec = 0.5$, $\lambda = 1$, $Pr = 1$. Temperature profiles of fluid flow with varying time (t)

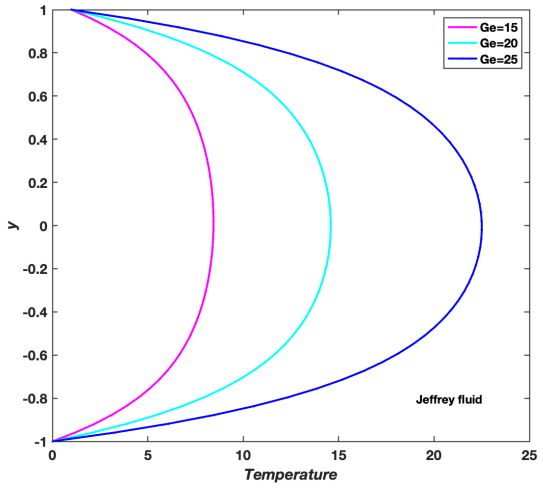

Fig. 4.25 Temperature profiles of fluid flow with varying pressure Ge, $t = 1$, $Re = 1$, $Ha^2 = 1$, $Bi = 2$, $Be = 0.5$, $C = 4 * \pi * 0.1$, $Ek = 0.25$, $Ec = 0.5$, $\lambda = 1$, $Pr = 1$. Temperature profiles of fluid flow with varying pressure (Ge)

The temperature profile behaves differently with changes in the Reynolds number and the Hartmann number. As the Reynolds number increases, the temperature profile becomes less steep, indicating slower heating of the fluid. This occurs because higher Reynolds numbers correspond to more turbulent flow, which enhances mixing and results in a more uniform temperature distribution, reducing the temperature gradient. In contrast, as the Hartmann number increases, the temperature profile becomes steeper, signifying a more rapid rise in temperature. This is due to the stronger magnetic field associated with a higher Hartmann number, which amplifies the Lorentz force and increases Joule heating, leading to a greater temperature gradient across the channel. Thus, while increasing Re smooths out the temperature variation, increasing Ha^2 intensifies it.

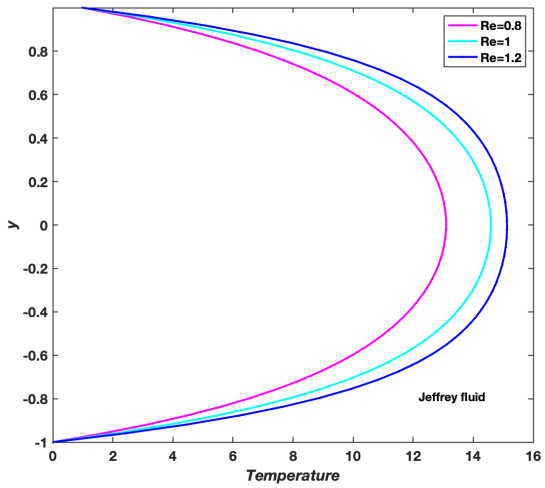

Fig. 4.26 Temperature profiles of fluid flow with varying Reynolds number Re, $t = 1$, $Ge = 20$, $Ha^2 = 1$, $Bi = 2$, $Be = 0.5$, $C = 4 * \pi * 0.1$, $Ek = 0.25$, $Ec = 0.5$, $\lambda = 1$, $Pr = 3$. Temperature profiles of fluid flow with varying Reynolds number (Re)

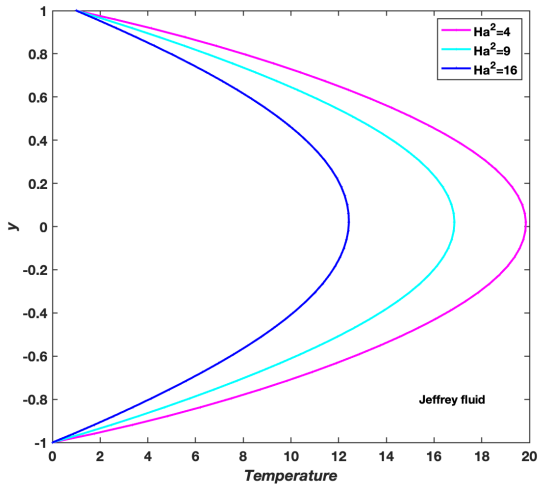

Fig. 4.27 Temperature profiles of fluid flow with varying Hartmann number Ha^2, $Ge = 20$, $Re = 1$, $Bi = 2$, $Be = 2$, $C = 4 * \pi * 0.1$, $Ek = 0.25$, $Ec = 0.5$, $\lambda = 1$, $Pr = 3$. Temperature profiles of fluid flow with varying Hartmann number (Ha^2)

As the ion slip parameter ($Bi = 1, 2,$ and 3) and the Hall parameter ($Be = 0.3, 0.5,$ and 0.7) increase, the temperature profile becomes less steep, indicating a slower temperature rise in temperature. This occurs because both parameters influence the Lorentz force, which affects Joule heating. A higher ion slip parameter reduces the coupling between ions and the fluid, weakening the effective Lorentz force and subsequently decreasing Joule heating. Similarly, an increase in Be adds extra resistance to the fluid motion as a result of the Hall effect, which reduces the Lorentz force and restricts Joule heating. Consequently, the temperature gradient decreases, leading to a more uniform temperature distribution.

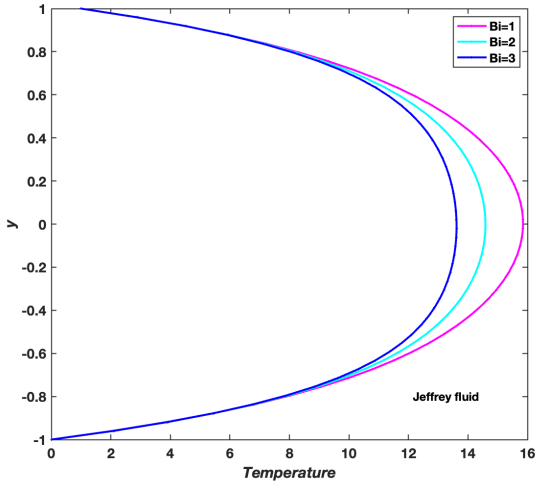

Fig. 4.28 Temperature profiles of fluid flow with varying Ion Slip parameter Bi, $Ge = 20$, $t = 1$, $Re = 1$, $Ha^2 = 1$, $Be = 2$, $C = 4 * \pi * 0.1$, $Ek = 0.25$, $Ec = 0.5$, $\lambda = 1$, $Pr = 3$. Temperature profiles of fluid flow with varying Ion Slip parameter (Bi)

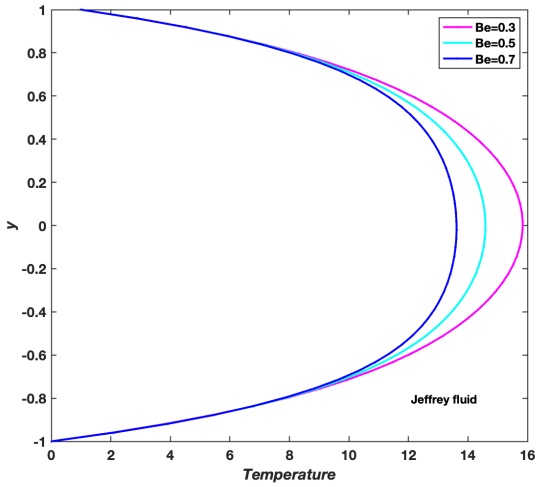

Fig. 4.29 Temperature profiles of fluid flow with varying Hall parameter Be, $Ge = 20$, $t = 1$, $Re = 1$, $Ha^2 = 1$, $Bi = 2$, $C = 4 * \pi * 0.1$, $Ek = 0.25$, $Ec = 0.5$, $\lambda = 1$, $Pr = 3$. Temperature profiles of fluid flow with varying Hall parameter (Be)

As the Eckert number ($Ec = 0.3, 0.5$, and 0.7) increases, the temperature profile becomes steeper, indicating a more rapid temperature rise due to greater viscous dissipation. Since the Eckert number represents the ratio of kinetic energy to enthalpy, a higher value implies that more heat is generated from fluid friction, resulting in a steeper temperature gradient. In contrast, as the Coriolis frequency parameter ($C = 4 * \pi * 0.1$, $C = 4 * \pi * 0.2$, and $C = 4 * \pi * 0.3$) increases, the temperature profile becomes less steep, suggesting a slower rate of heating. This occurs because stronger rotational effects enhance fluid mixing, promoting a more uniform temperature distribution and reducing the temperature gradient. Thus, while an increase in Ec intensifies heating through viscous dissipation, an increase in C promotes better mixing and stabilizes the temperature distribution.

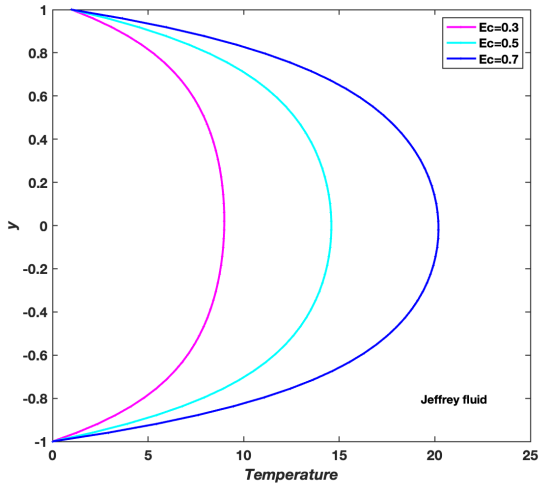

Fig. 4.30 Temperature profiles of fluid flow with varying Eckert number Ec, $Ge = 20$, $t = 1$, $Re = 1$, $Ha^2 = 1$, $Bi = 2$, $C = 4 * \pi * 0.1$, $Ek = 0.25$, $Be = 0.5$, $\lambda = 1$, $Pr = 3$. Temperature profiles of fluid flow with varying Eckert number (Ec)

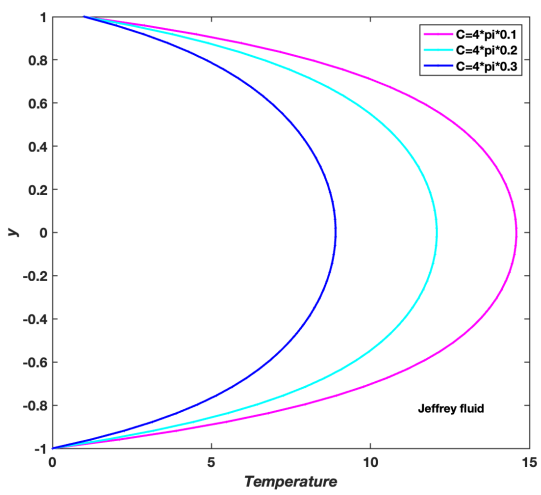

Fig. 4.31 Temperature profiles of fluid flow with varying C, $Ge = 20$, $t = 1$, $Re = 1$, $Ha^2 = 1$, $Bi = 2$, $Ek = 0.25$, $Be = 2$, $Ec = 0.5$, $\lambda = 1$, $Pr = 3$. Temperature profiles of fluid flow with varying C

As the Ekman number ($Ek = 0.15, 0.25,$ and 0.35) and the Jeffrey fluid parameter ($\lambda = 0.5, 0.75,$ and 1) increase, the temperature profile becomes less steep, indicating a slower temperature rise. A higher Ekman number strengthens the influence of rotational forces relative to viscous forces, enhancing fluid mixing and resulting in a more uniform temperature distribution with a reduced temperature gradient. Similarly, an increase in the λ enhances the elasticity of the fluid, thereby reducing viscous dissipation and subsequently lowering the heat generated. As a result, both parameters contribute to a smoother temperature distribution by reducing the steepness of the temperature profile.

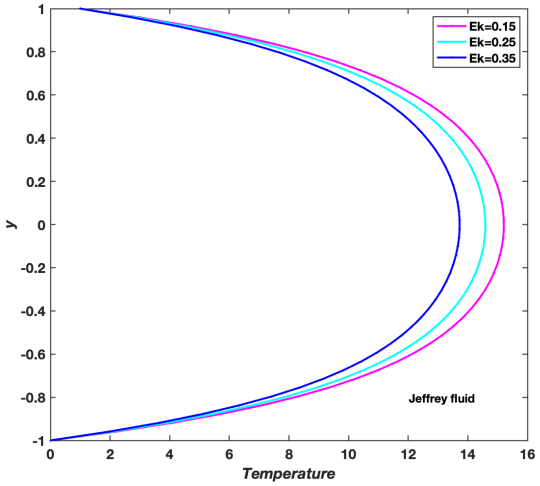

Fig. 4.32 Temperature profiles of fluid flow with varying Ekman number Ek, $Ge = 20$, $t = 1$, $Re = 1$, $Ha^2 = 1$, $Bi = 2$, $C = 4 * \pi * 0.1$, $Be = 2$, $Ec = 0.5$, $\lambda = 1$, $Pr = 3$. Temperature profiles of fluid flow with varying Ekman number (Ek)

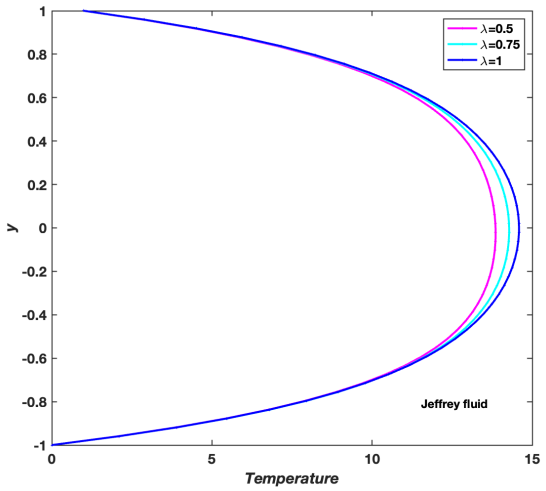

Fig. 4.33 Temperature profiles of fluid flow with varying Jeffrey fluid parameter λ, $Ge = 20$, $t = 1$, $Re = 1$, $Ha^2 = 1$, $Bi = 2$, $Ek = 0.25$, $Be = 2$, $Ec = 0.5$, $C = 4 * \pi * 0.1$, $Pr = 3$. Temperature profiles of fluid flow with varying Jeffrey fluid parameter (λ)

4.3.6 Pumping Power Analysis

(a) Pumping power measures the energy required to transport a fluid from one location to another.

(b) In this analysis, a density $\rho = 1000\, kg/m^3$ as described in [138], here fluid behavior similar to water.

(c) Table 4.1 reveals notable findings:

(i) Parameters t, significantly increase pumping power.

(ii) Parameters Re, Ha, C, and λ show a notable decrease in pumping power.

(iii) Other parameters show a slight increase or decrease in pumping power, with less pronounced effects.

Table 4.1: Volume Flow Rate, Pressure Drop, and Pumping Power for Various Parameter Values

Parameter	**Volume Flow Rate**	**Pressure Drop**	**Pumping Power**
$t = 0.1$	0.244519	172.265509	42.122176
$t = 0.2$	0.327495	309.016542	101.201253
$t = 0.3$	0.384639	426.265554	163.958394
$t = 0.4$	0.427237	525.909154	224.687749
$t = 0.5$	0.459706	608.883554	279.907582
$Re = 1$	0.244519	172.265509	42.122176
$Re = 2$	0.181548	47.481667	8.620198
$Re = 3$	0.152869	22.443511	3.430916
$Re = 4$	0.135619	13.248172	1.796707
$Re = 5$	0.123805	8.832386	1.093491
$Ha = 1$	0.244519	172.265509	42.122176
$Ha = 4$	0.239338	165.042616	39.500941
$Ha = 9$	0.231184	153.989334	35.599939
$Ha = 16$	0.220699	140.337497	30.972331
$Ha = 25$	0.208633	125.412135	26.165114
$Bi = 1$	0.243463	170.781571	41.579073
$Bi = 2$	0.244519	172.265509	42.122176
$Bi = 3$	0.245046	173.009611	42.39539
$Bi = 4$	0.245344	173.430376	42.550145

continued on next page

Table 4.1: Volume Flow Rate, Pressure Drop, and Pumping Power for various parameters

Parameter	**Volume Flow Rate**	**Pressure Drop**	**Pumping Power**
$Bi = 5$	0.245532	173.695251	42.647661
$Be = 1$	0.243369	170.648765	41.530583
$Be = 2$	0.244519	172.265509	42.122176
$Be = 3$	0.245023	172.977197	42.383477
$Be = 4$	0.245306	173.37568	42.530018
$Be = 5$	0.245485	173.630107	42.62367
$C = 4\pi \times 0.1$	0.244519	172.265509	42.122176
$C = 4\pi \times 0.2$	0.239516	165.287966	39.589056
$C = 4\pi \times 0.3$	0.23435	158.235875	37.082647
$C = 4\pi \times 0.4$	0.229032	151.135507	34.614898
$C = 4\pi \times 0.5$	0.22357	144.012878	32.196992
$Ek = 0.15$	0.246473	175.029747	43.140095
$Ek = 0.25$	0.244519	172.265509	42.122176
$Ek = 0.35$	0.242538	169.485125	41.106517
$Ek = 0.45$	0.24053	166.690282	40.093938
$Ek = 0.55$	0.238495	163.882668	39.085245
$\lambda = 0.6$	0.27087	211.395176	57.260601
$\lambda = 0.8$	0.256594	189.699079	48.675579
$\lambda = 1.0$	0.244519	172.265509	42.122176
$\lambda = 1.2$	0.234133	157.942258	36.979481
$\lambda = 1.4$	0.225076	145.959077	32.85186

end of table

4.4 Conclusion

This work examines the flow characteristics of an electrically conducting Jeffrey fluid in a horizontal channel, subject to a rotating frame, pressure-driven flow, and the effect of an applied magnetic field. The complex interplay of these forces was modeled mathematically, and the governing equations were solved using dimensionless parameters and the RBF-PSM. The analysis focused on understanding velocity and temperature profiles under varying conditions, as well as the impact of different parameters on the pumping power required to maintain flow. This study extends the existing theoretical framework by integrating multiple variables and techniques for the first time, including rotating frame, magnetic fields, horizontal channel geometry, Jeffrey fluid dynamics and the Radial Basis Function method, to analyze and determine velocity, temperature profiles, and pumping power. By combining these elements, the research provides a novel approach to understanding the complex interactions among rotational forces, magnetic effects, and the viscoelastic behavior of Jeffrey fluids in horizontal channels. This work offers new insights into optimizing fluid transport systems under multifaceted conditions, particularly where rotational and magnetic influences are significant.

(a) The pumping power analysis revealed that parameters such as time (t) significantly increase pumping power, whereas the Reynolds number (Re), Hartmann number (Ha^2), Coriolis frequency parameter (C), and Jeffrey fluid parameter (λ) notably decrease pumping power. This indicates that rotational forces, magnetic fields, and fluid elasticity play crucial roles in reducing the energy required to transport the fluid, making these parameters critical for optimizing fluid transport systems.

(b) As the Reynolds number increases, the primary velocity rises due to the dominance of inertial forces over viscous forces, allowing the fluid to flow more freely. In contrast, the secondary velocity decreases because higher inertia suppresses transverse motion, reducing rotational effects. This is similar to blood flow: at low speeds, wall shear induces secondary circulation, but at high speeds, flow remains more streamlined, minimizing crosswise movement.

(c) An increase in the Hartmann number causes both primary and secondary velocities to decrease due to a stronger magnetic field enhancing the Lorentz force, which acts as a resistive force, damping fluid motion and reducing velocity. This is analogous to magnetohydrodynamic brakes in high-speed trains, where a strong magnetic field applied to a conducting fluid generates Lorentz forces that oppose motion and slow the train. Similarly, in this scenario, as magnetic field strength increases, it restricts fluid movement, leading to decreased velocity.

(d) As the Hall parameter (Be) increases, both primary and secondary velocities rise due to the Hall effect, which reduces resistance to the primary flow while enhancing transverse flow. The Hall effect generates a transverse current that weakens the Lorentz force's opposition, allowing the primary flow to accelerate. This behavior resembles how an electric field in plasma physics alters the motion of charged particles, reducing resistance and increasing flow speed.

(e) As the Coriolis frequency parameter (C) increases, the Coriolis force becomes more pronounced. The primary velocity, primarily driven by the pressure gradient along the x-axis, decreases because the Coriolis force opposes the direction of motion, effectively resisting the flow—much like a car moving on a rotating platform. As the platform spins faster (increasing C), the car (representing primary velocity) struggles to move forward due to an increasing sideways push (Coriolis force). Conversely, the secondary velocity, directly driven by the Coriolis force, increases as C grows, similar to how a sideways push causes the car to drift more significantly sideways (representing secondary velocity).

The findings from this study offer useful insights for the design and improvement of systems involving non-Newtonian fluids influenced by rotating frame and magnetic fields, such as MHD pumps, cooling mechanisms in rotating equipment, and microfluidic technologies. By employing a validated numerical approach and examining the role of key parameters on flow behavior, heat transfer, and energy input, the work contributes to a better understanding of how such systems might be optimized for improved performance and efficiency in practical settings.

Chapter 5

Conclusions and Recommendations

5.1 Summary and Conclusions

This thesis presents a comprehensive study on the flow behavior of various complex fluids, including dusty fluid, micropolar dusty fluid, and Jeffrey fluid, under the combined influences of rotating frame, magnetic field, external pressure gradient, and, in some cases, heat transfer. The investigation is carried out in horizontal and inclined channel configurations, and the numerical analysis is conducted using the RBF-PSM, a meshless technique well-suited for solving coupled partial differential equations.

Chapter 1 lays the theoretical foundation of the thesis by presenting the essential background related to fluid dynamics. It begins with the classification and properties of fluids and descriptions of various flow regimes. The governing equations for dusty fluid, micropolar fluid, and Jeffrey fluid are introduced based on continuum mechanics principles, including the conservation of mass, momentum, and energy. MHD is briefly reviewed, with a focus on how magnetic fields interact with conducting fluids. The chapter also discusses the rotating frame of reference in fluid systems. An important part of this chapter is the introduction of dimensionless parameters such as the Reynolds number, Hartmann number, Prandtl number, and Eckert number, which facilitate the scaling and interpretation of results. Finally, the Radial Basis Function Pseudospectral Method is introduced as a meshless, high-order numerical tool used for solving the governing equations in subsequent chapters.

Chapter 2 investigates the behavior of dusty fluid flow in both horizontal and inclined channels under the influence of rotating frame, an externally applied magnetic field, and a constant pressure gradient. The fluid and particle interactions are modeled through a two phase approach, capturing the momentum exchange between the fluid and the suspended dust particles. The governing equations are derived, transformed into dimensionless form, and solved numerically using the RBF-PSM. To confirm the reliability and convergence of the computed results, a stability study of the numerical method is performed. In the horizontal configuration, both velocity components are analyzed with respect to several key dimensionless parameters, revealing the effects of magnetic damping, rotational forces, and pressure driven flow on the velocity structure. In the inclined configuration, the introduction of gravitational effects along the direction of inclination further alters the flow dynamics, resulting in enhanced wall shear and an increase in pumping power. For both cases, the energy required to sustain fluid motion, referred to as pumping power, is computed and compared. The analysis highlights how channel orientation, pressure gradients, and external forces collectively influence velocity profiles, flow stability, and transport efficiency.

Chapter 3 extends the scope of the analysis to micropolar dusty fluids, which account for fluid microstructure and the rotational behavior of fluid elements. This chapter considers both horizontal and inclined channel configurations and incorporates the effects of heat transfer, magnetic field, rotating frame, and a constant external pressure gradient. The governing equations are more complex due to the inclusion of microrotation and thermal diffusion terms. These equations are transformed into dimensionless form and solved using the RBF-PSM. A detailed stability analysis is also conducted to examine the reliability and convergence behavior of the numerical method used. The study presents an in depth analysis of the primary and secondary velocity components, temperature distributions, and microrotation behavior for various physical and thermal parameters. The presence of micropolar effects leads to notable changes in flow resistance and thermal gradients, which in turn influence the pumping power required to sustain fluid motion. In inclined channels, the addition of gravitational effects further complicates the flow behavior, intensifying the interactions among momentum trans-

port, microrotation, and heat conduction. The results demonstrate that microstructural characteristics, thermal properties, and external driving forces together play a critical role in determining both fluid behavior and energy consumption.

Chapter 4 focuses on the analysis of Jeffrey fluid flow in a horizontal channel under the combined influence of rotating frame, magnetic field, heat transfer, and a constant external pressure gradient. Jeffrey fluid, being a viscoelastic non Newtonian fluid, accounts for both relaxation and retardation effects, adding complexity to the flow dynamics. The governing equations, incorporating momentum and energy balances, are derived, converted into dimensionless form, and solved numerically using the RBF-PSM. A stability analysis is carried out to ensure the reliability and convergence of the numerical approach. Furthermore, to validate the accuracy of the RBF-PSM, a comparative study is performed with results obtained using the MCBS DQM, demonstrating close agreement. The study presents detailed analyses of the primary and secondary velocity profiles and temperature distributions for various dimensionless parameters, such as the Hartmann number, Prandtl number, and jeffrey fluid parameter. The results illustrate how viscoelastic effects, in combination with external physical forces, influence fluid flow behavior and energy consumption. Pumping power calculations further quantify the energy required to maintain flow, offering valuable insight for the design of efficient fluid transport systems involving non Newtonian fluids.

The four chapters presented in this thesis collectively provide a unified and in depth investigation of complex fluid flows influenced by rotating frame, magnetic field, heat transfer, and pressure gradients, across different fluid models and geometrical settings. Through the application of the RBF-PSM along with supporting stability and validation analyses, the study offers valuable theoretical and computational insights into the behavior of dusty, micropolar dusty, and Jeffrey fluids.

5.2 Recommendations for Future Work

One promising direction for future research involves the study of *immiscible fluid systems* in a *rotating frame of reference*, influenced by *magnetic fields* and a *constant pres-*

sure gradient. These systems are found in many industrial and geophysical applications, where two fluids that do not mix, such as oil and water—flow together while remaining separated. A major difficulty in modeling such flows lies in accurately identifying and tracking the moving boundary between the two fluids. This boundary is not fixed; it changes shape and position based on fluid motion, surface tension, and external forces like rotation and magnetic fields. In rotating environments, the added effects of Coriolis and centrifugal forces make predicting the shape and motion of this boundary especially difficult.

Furthermore, future research may extend the analysis to multidirectional or three-dimensional flow regimes, thereby providing a more realistic representation of practical fluid behaviour. In addition, varying (rather than assuming constant) pressure gradients could contribute to a more general and adaptable formulation of rotating multiphase fluid systems.

Traditional numerical methods, such as the *Volume of Fluid* and *Level Set* approaches, often struggle with capturing this boundary sharply and may introduce errors that reduce physical accuracy. These methods may fail to clearly distinguish the boundary between the two fluids, leading to inaccurate predictions of their positions and movement over time. To address these challenges, future studies may focus on creating *hybrid numerical techniques* that integrate the advantages of multiple methods. In addition, *adaptive mesh refinement*, which increases resolution near the fluid boundary and the use of *data driven and artificial intelligence based approaches* could help track the movement and shape of the two phase boundary more precisely. Advancing these techniques would lead to better simulations of multiphase flows in rotating and magnetically active systems, including those used in chemical processing, fluid separation, and energy systems.

Bibliography

[1] Y. Cengel and J. Cimbala, "Fluid mechanics–fundamentals and applications, 3rd-edn," *McGrawHill Education*, 2014.

[2] J. D. Anderson, "Governing equations of fluid dynamics," in *Computational Fluid Dynamics: An Introduction*. Berlin, Heidelberg: Springer, 1992, pp. 15–51.

[3] ——, *Computational Fluid Dynamics: The Basics with Applications*, ser. Mechanical Engineering Series. New York: McGraw Hill Education, 1995.

[4] A. C. Eringen, "Theory of micropolar fluids," *Journal of Mathematics and Mechanics*, vol. 16, no. 1, pp. 1–18, 1966.

[5] J. Chen, C. C. Liang, and J. Lee, "Theory and simulation of micropolar fluid dynamics," *Proceedings of the Institution of Mechanical Engineers, Part N: Journal of Nanoengineering and Nanosystems*, vol. 224, no. 1, pp. 31–39, 2011.

[6] A. C. Eringen, *Micropolar Fluids: Theory and Applications*, 1st ed. Springer, 1999.

[7] K. Guedri, N. Ameer Ahammad, S. Nadeem, E. M. Tag-ElDin, A. U. Awan, and M. F. Yassen, "Insight into the heat transfer of third grade micropolar fluid over an exponentially stretched surface," *Scientific Reports*, vol. 12, no. 1, p. 15577, Sep 2022.

[8] J. Sui, P. Zhao, Z. Cheng, L. Zheng, and X. Zhang, "A novel investigation of a micropolar fluid characterized by nonlinear constitutive diffusion model in bound-

ary layer flow and heat transfer," *Physics of Fluids*, vol. 29, no. 3, p. 032001, 2017.

[9] B. Vasu, A. Dubey, O. A. Bég, and R. S. R. Gorla, "Micropolar pulsatile blood flow conveying nanoparticles in a stenotic tapered artery: Non-Newtonian pharmacodynamic simulation," *Computers in Biology and Medicine*, vol. 127, p. 104065, 2020.

[10] S. Tanuja, R. Kumar, and A. Chamkha, "Flow and heat transfer analysis on micropolar fluid through a porous medium between a clear and hybrid nanofluid," *Frontiers in Materials*, vol. 10, p. 1216757, 2023.

[11] T. Sowmya and N. Muralidhara, "Numerical simulation of journal bearings lubricated with couple stress and micropolar fluids," *Tribology International*, vol. 94, pp. 1–10, 2016.

[12] M. Devakar and A. Raje, "A magnetohydrodynamic time dependent model of immiscible Newtonian and micropolar fluids through a porous channel: A numerical approach," *Journal of Applied Fluid Mechanics*, vol. 12, no. 2, pp. 603–615, 2019.

[13] M. A. Abbas, N. Faraz, Y. Q. Bai, and Y. Khan, "Analytical study of the non orthogonal stagnation point flow of a micro polar fluid," *Journal of King Saud University - Science*, vol. 29, no. 1, pp. 126–132, 2017.

[14] K. Bhattacharyya and G. Layek, "Effects of thermal radiation on micropolar fluid flow and heat transfer over a porous shrinking sheet," *International Journal of Heat and Mass Transfer*, vol. 55, no. 11-12, pp. 2945–2952, 2012.

[15] C. K. Chen, Y. T. Yang, and K. H. Chang, "The effect of thermal radiation on entropy generation due to micro-polar fluid flow along a wavy surface," *Entropy*, vol. 13, no. 9, pp. 1595–1610, 2011.

[16] K. Mekheimer and M. Kot, "The micropolar fluid model for blood flow through a tapered artery with a stenosis," *Acta Mechanica Sinica*, vol. 24, no. 6, pp. 637–644, 2008.

[17] M. Aurangzaib, M. S. Uddin, K. Bhattacharyya, and S. Shafie, "Micropolar fluid flow and heat transfer over an exponentially permeable shrinking sheet," *Propulsion and Power Research*, vol. 5, no. 4, pp. 310–317, 2016.

[18] F. S. Aski, S. J. Nasirkhani, E. Mohammadian, and A. Asgari, "Application of adomian decomposition method for micropolar flow in a porous channel," *Propulsion and Power Research*, vol. 3, no. 1, pp. 15–21, 2014.

[19] S. Jangili and O. A. Bég, "Homotopy study of entropy generation in magnetized micropolar flow in a vertical parallel plate channel with buoyancy effect," *Heat Transfer Research*, vol. 49, no. 6, pp. 529–553, 2018.

[20] S. A. M. Mehryan, M. Izadi, and M. A. Sheremet, "Analysis of conjugate natural convection within a porous square enclosure occupied with micropolar nanofluid using local thermal non-equilibrium model," *Journal of Molecular Liquids*, vol. 250, pp. 353–368, 2018.

[21] O. A. Bég, J. Zueco, and T. B. Chang, "Numerical analysis of hydromagnetic gravity-driven thin film micropolar flow along an inclined plane," *Chemical Engineering Communications*, vol. 198, no. 3, pp. 312–331, 2010.

[22] P. Aparna, N. Pothanna, J. V. R. Murthy, and K. Sreelatha, "Flow generated by slow steady rotation of a permeable sphere in a micro-polar fluid," *Alexandria Engineering Journal*, vol. 56, no. 4, pp. 679–685, 2017.

[23] P. G. Saffman, "On the stability of laminar flow of a dusty gas," *Journal of Fluid Mechanics*, vol. 13, no. 1, pp. 120–128, 1962.

[24] ——, "The stability of laminar flow of a dusty fluid," *Journal of Fluid Mechanics*, vol. 27, no. 3, pp. 581–593, 1968.

[25] F. E. Marble, "Dynamics of dusty gases," *Annual Review of Fluid Mechanics*, vol. 2, pp. 397–446, 1970.

[26] R. C. Drew, "Mathematical modeling of two-phase flow," *Annual Review of Fluid Mechanics*, vol. 15, pp. 261–291, 1983.

[27] O. A. Bég, M. J. Uddin, T. A. Bég, M. J. Ahamed, and A. I. M. Ismail, "Numerical investigation of von karman swirling bioconvective nanofluid transport from a rotating disk in a porous medium," *Proceedings of the Institution of Mechanical Engineers, Part E: Journal of Process Mechanical Engineering*, vol. 235, no. 3, pp. 678–692, 2021.

[28] X. Liu, J. E. Penner, and M. Herzog, "Global modeling of aerosol dynamics: Model description, evaluation, and interactions between sulfate and nonsulfate aerosols," *Journal of Geophysical Research: Atmospheres*, vol. 110, no. D18, p. D18206, 2005.

[29] L. Wang, F. Wang, H. Liu, and Y. Li, "Cfd modeling of ventilation and dust flow behavior in polishing workshops," *PMC Public Health*, vol. 12, pp. 1234–1245, 2020.

[30] R. Kumar, S. Banerjee, A. Banik, T. K. Bandyopadhyay, and T. K. Naiya, "Simulation of single phase Non-Newtonian flow characteristics of heavy crude oil through horizontal pipelines," *Petroleum Science and Technology*, vol. 35, no. 6, pp. 615–624, 2017.

[31] N. Lavanya and S. Bhattacharyya, "Computational fluid dynamics—the futuristic innovation in pharmaceutical industry," *Indian Journal of Pharmaceutical Education and Research*, vol. 55, no. 4, pp. 930–942, 2021.

[32] B. J. Gireesha, G. K. Ramesh, and C. S. Bagewadi, "Heat transfer in MHD flow of a dusty fluid over a stretching sheet with viscous dissipation," *Advances in Applied Science Research*, vol. 3, no. 4, pp. 2392–2401, 2012.

[33] B. Armstrong, "The study of pharmaceutical powder mixing through improved flow characterisation and hopper design," PhD thesis, University of Birmingham, 2011.

[34] L. Debnath and A. K. Ghosh, "On unsteady hydromagnetic flows of a dusty fluid between two oscillating plates," *Applied Science Research*, vol. 45, no. 4, pp. 353–365, 1988.

[35] N. Datta, D. C. Dalal, and S. K. Mishra, "Unsteady heat transfer to pulsatile flow of a dusty viscous incompressible fluid in a channel," *International Journal of Heat and Mass Transfer*, vol. 36, no. 7, pp. 1783–1788, 1993.

[36] D. Dey, "Dusty hydromagnetic oldryod fluid flow in a horizontal channel with volume fraction and energy dissipation," *International Journal of Heat Technology*, vol. 34, no. 3, pp. 415–422, 2016.

[37] M. Jalil, S. Asghar, and S. Yasmeen, "An exact solution of MHD boundary layer flow of dusty fluid over a stretching surface," *Mathematical Problems in Engineering*, vol. 2017, pp. 1–5, 2017.

[38] N. Reddimalla, J. R. Murthy, V. R. K. Murthy, and S. Jangili, "Effect of magnetic field on unsteady flow of dusty fluid due to constant pressure gradient through a circular cylinder: An analytical treatment," in *Recent Advances in Applied Mathematics and Applications to the Dynamics of Fluid Flows*. Springer, 2023, pp. 195–202.

[39] H. A. Attia, "Transient circular pipe MHD flow of a dusty fluid considering hall effect," *Kragujevac Journal of Science*, vol. 23, no. 1, pp. 15–23, 2011.

[40] O. D. Makinde and T. Chinyoka, "Mhd transient flows and heat transfer of dusty fluid in a channel with variable physical properties and navier slip condition," *Computers & Mathematics with Applications*, vol. 60, no. 2, pp. 660–669, 2010.

[41] M. Bilal, S. Khan, F. Ali, M. Arif, I. Khan, and K. S. Nisar, "Couette flow of viscoelastic dusty fluid in a rotating frame along with the heat transfer," *Scientific Reports*, vol. 11, no. 1, p. 506, Jan 2021.

[42] Q. Lou, "Micropolar dusty fluid: Coriolis force effects on dynamics of MHD rotating fluid when Lorentz force is significant," *Mathematics*, vol. 10, no. 15, p. 2630, 2022.

[43] G. B. Jeffery, "The motion of ellipsoidal particles immersed in a viscous fluid," *Proceedings of the Royal Society of London. Series A*, vol. 102, no. 715, pp. 161–179, 1922.

[44] C. Truesdell and W. Noll, *The Non-Linear Field Theories of Mechanics*, 3rd ed., ser. Springer Tracts in Natural Philosophy. Springer, 2004, vol. 3.

[45] M. Kahshan, D. Lu, and A. M. Siddiqui, "A Jeffrey fluid model for a porous-walled channel: Application to flat plate dialyzer," *Scientific Reports*, vol. 9, no. 1, p. 15879, 2019.

[46] S. Ahmad, H. Muhammad, M. M. Hamza, G. Ojemeri, and U. Usman, "Magnetized oscillatory Jeffrey fluid flow in a porous channel with unequal wall temperature," *Dutse Journal of Pure and Applied Sciences*, vol. 10, no. 2C, pp. 261–272, 2024.

[47] S. Nallapu and G. Radhakrishnamacharya, "Jeffrey fluid flow through porous medium in the presence of magnetic field in narrow tubes," *Journal of Applied Mathematics*, vol. 2014, p. 713831, 2014.

[48] M. A. Rao, *Rheology of Fluid and Semisolid Foods: Principles and Applications*, 3rd ed. Springer, 2014.

[49] S. Siddiqa and R. Ellahi, "Analysis of MHD Jeffrey fluid in a vertical channel with porous media and chemical reaction," *Alexandria Engineering Journal*, vol. 56, no. 4, pp. 535–541, 2017.

[50] A. B. Raje, A. A. Kulkarni, and Anirudh, "Entropy analysis of the MHD Jeffrey fluid flow in an inclined porous pipe with convective boundaries," *Case Studies in Thermal Engineering*, vol. 34, p. 102038, 2023.

[51] D. Dey, "Dusty Jeffrey fluid flow in a rotating system with volume fraction and hall effect: An analytical approach," *Advances in Modelling and Analysis A*, vol. 55, no. 2, pp. 70–75, 2018.

[52] S. S. Motsa, P. Sibanda, G. T. Marewo, and S. Shateyi, "A note on improved homotopy analysis method for solving the Jeffery-Hamel flow," *Journal of Applied Mathematics*, vol. 2010, p. 359297, 2010.

[53] M. Ashraf, U. Qasim, M. Wakif, A. Afridi, M. Idrees, and I. L. Animasaun, "A generalized differential quadrature algorithm for simulating magnetohydrodynamic peristaltic flow of blood-based nanofluid," *Numerical Methods for Partial Differential Equations*, 2020.

[54] M. Asgir, M. B. Riaz, and A. Islam, "Exact analysis of fractionalised Jeffrey fluid in a channel with caputo and caputo fabrizio time derivative: A comparative study," *Acta Mechanica et Automatica*, vol. 17, no. 4, pp. 581–592, 2023.

[55] J. Ahmed, A. Shahzad, M. Khan, and R. Ali, "A note on convective heat transfer of an MHD Jeffrey fluid over a stretching sheet," *AIP Advances*, vol. 5, no. 11, p. 117118, 2015.

[56] I. Khan, "A note on exact solutions for the unsteady free convection flow of a Jeffrey fluid," *Zeitschrift für Naturforschung A*, vol. 70, no. 6, pp. 397–401, 2015.

[57] H. Alfvén, "Existence of electromagnetic-hydrodynamic waves," *Nature*, vol. 150, no. 3805, pp. 405–406, Oct 1942.

[58] G. K. Batchelor, *An Introduction to Fluid Dynamics*, 1st ed. Cambridge University Press, 1967.

[59] F. F. Chen, *Introduction to Plasma Physics and Controlled Fusion*. Springer, 1984.

[60] S. Molokov, R. Moreau, and H. Moffatt, *Magnetohydrodynamics: Historical Evolution and Trends*. Springer, 2007.

[61] V. M. Foliforov, "MHD machines in the industrial production and handling of mercury," *Magnetohydrodynamics*, vol. 21, no. 2, pp. 2–7, Oct. 1985.

[62] S. Kitanov and A. Podol'skii, "Analysis of Eddy-Current and Magnetic rail brakes for High-Speed trains," *The Open Transportation Journal*, vol. 2, pp. 19–24, 2008.

[63] M. Haghparast and M. R. A. Pahlavani, "A comparative study on the performance of marine magnetohydrodynamic motors with helical and linear channels," *IEEE Transactions on Magnetics*, vol. 55, no. 11, p. 8205008, 2019.

[64] W. T. Sproull, "Viscosity of dusty gases," *Nature*, vol. 190, pp. 976–978, 1961.

[65] S. Manjunatha and B. Gireesha, "Effects of variable viscosity and thermal conductivity on MHD flow and heat transfer of a dusty fluid," *Ain Shams Engineering Journal*, vol. 7, no. 1, pp. 505–515, 2016.

[66] T. Hayat, A. M. Siddiqui, and S. Asghar, "Magnetohydrodynamic flow of Oldroyd-B fluids," *Journal of Non-Newtonian Fluid Mechanics*, vol. 121, no. 3, pp. 237–251, 2004.

[67] A. M. Abd-Alla, S. M. Abo-Dahab, and M. M. Albalawi, "Magnetic field and gravity effects on peristaltic transport of a Jeffrey fluid in an asymmetric channel," *Abstract and Applied Analysis*, vol. 2014, p. 896121, 2014.

[68] S. Akram and S. Nadeem, "Influence of induced magnetic field and heat transfer on the peristaltic motion of a Jeffrey fluid in an asymmetric channel: closed form solutions," *Journal of Magnetism and Magnetic Materials*, vol. 328, pp. 11–20, 2013.

[69] A. Ahmad Dar and K. Elangovan, "Inclined magnetic field and rotation effects on micropolar fluid flow in an inclined channel," *New Journal of Science*, vol. 2016, no. 1, p. 5717542, 2016.

[70] P. K. Yadav and M. Roshan, "Mathematical modeling of blood flow in an annulus porous region between two coaxial deformable tubes: An advancement to peristaltic endoscope," *Chinese Journal of Physics*, vol. 88, 04 2024.

[71] S. Nadeem, S. Masood, R. Mehmood, and M. Sadiq, "Optimal and Numerical Solutions for an MHD Micropolar Nanofluid between Rotating Horizontal Parallel Plates," *PLOS ONE*, vol. 10, p. e0124016, 06 2015.

[72] S. Ghadikolaei, K. Hosseinzadeh, M. Yassari, H. Sadeghi, and D. Ganji, "MHD Boundary Layer Flow of Micropolar Dusty Nanofluid over a Stretching Sheet," *Journal of Molecular Liquids*, vol. 244, pp. 374–389, 2017.

[73] T. Javed and M. A. Siddiqui, "Energy transfer through mixed convection within square enclosure containing micropolar fluid with non-uniformly heated bottom wall under the MHD impact," *Journal of Molecular Liquids*, vol. 249, pp. 831–842, 2018.

[74] P. K. Yadav, A. Kumar, S. El-Sapa, A. Chamkha, and P. Kumar, "Impact of thermal radiation and oriented magnetic field on the flow of two immiscible fluids through porous media with different porosity," *Waves in Random and Complex Media*, pp. 1–33, 09 2022.

[75] M. B. Gerdroodbary, M. R. Takami, and D. Ganji, "Investigation of thermal radiation on traditional Jeffrey–Hamel flow to stretchable convergent/divergent channels," *Case Studies in Thermal Engineering*, vol. 6, pp. 28–39, 2015.

[76] M. Fiza, A. Alsubie, H. U. Jan, N. Hamadneh, S. Islam, and I. Khan, "Three-dimensional rotating flow of MHD Jeffrey fluid flow between two parallel plates with impact of hall current," *Mathematical Problems in Engineering*, vol. 2021, pp. 1–9, 2021.

[77] D. Rani, "Jeffrey fluid behaviour on oscillatory couette flow past two horizontal parallel plates in presence of MHD and radiative heat transfer," *International Journal of Innovative Technology and Exploring Engineering*, vol. 8, pp. 3252–3257, 2019.

[78] M. Bhatti, A. Zeeshan, N. Ijaz, A. Beg, and A. Kadir, "Mathematical modelling of nonlinear thermal radiation effects of EMHD peristaltic pumping of viscoelastic dusty fluid through a porous medium duct," *Engineering Science and Technology, an International Journal*, vol. 20, no. 4, pp. 1129–1139, 2017.

[79] W. Abbas, O. Khaled, S. Beshir, M. Abdeen, and M. Elshabrawy, "Analysis of chemical, ion slip, and thermal radiation effects on an unsteady magnetohydro-

dynamic dusty fluid flow with heat and mass transfer through a porous media between parallel plates," *Bulletin of the National Research Centre*, vol. 48, pp. 1–17, 2024.

[80] D. Dey, "Non-Newtonian effects on hydromagnetic dusty stratified fluid flow through a porous medium with volume fraction," *Proceedings of the National Academy of Sciences, India, Section A: Physical Sciences*, vol. 86, no. 1, pp. 47–56, 2016.

[81] C. Truesdell, *Introduction to Leonhard Euler's Opera Omnia: The Rational Mechanics of Flexible or Elastic Bodies, 1638–1788*, ser. Opera Omnia, Series II. Zürich: Orell Füssli, 1960, vol. X–XI.

[82] A. Persson, "How do we understand the Coriolis force?" *Bulletin of the American Meteorological Society*, vol. 79, no. 7, pp. 1373–1386, 1998.

[83] G. K. Vallis, *Atmospheric and Oceanic Fluid Dynamics: Fundamentals and Large-Scale Circulation*. Cambridge University Press, 2006.

[84] J. P. Johnston, "Effects of system rotation on turbulence structure: a review relevant to turbomachinery flows," *International Journal of Rotating Machinery*, vol. 4, no. 2, pp. 97–112, 1998.

[85] R. K. Smith, C. W. Schmidt, and M. T. Montgomery, "An investigation of rotational influences on tropical-cyclone size and intensity," *Quarterly Journal of the Royal Meteorological Society*, vol. 137, no. 660, pp. 1841–1855, 2011.

[86] S. Leblanc and C. Cambon, "Effects of the Coriolis force on the stability of Stuart vortices," *Journal of Fluid Mechanics*, vol. 356, pp. 353–379, 1998.

[87] K. Ward and Z. H. Fan, "Mixing in Microfluidic Devices and Enhancement Methods," *Journal of Micromechanics and Microengineering*, vol. 25, no. 9, p. 094001, 2015.

[88] K. A. M. Alharbi, N. Ijaz, A. Riaz, F. Altaf, and A. Zeeshan, "On multiphase wavy movements of Non-Newtonian Jeffery fluid in a rotating channel with mhd

and compliant walls: exact solutions," *Waves in Random and Complex Media*, pp. 1–23, 2022.

[89] J. R. Taylor, *Classical Mechanics*. University Science Books, 2005.

[90] F. M. White, *Fluid Mechanics*, 7th ed. McGraw-Hill Education, 2011.

[91] B. R. Munson, D. F. Young, T. H. Okiishi, and W. W. Huebsch, *Fundamentals of Fluid Mechanics*, 7th ed. Wiley, 2013.

[92] N. Kosulina, S. Kosulin, K. Korshunov, T. Nosova, and Y. Nosova, "Determination of hydrodynamic parameters of the sealed pressure extractor," *Informatyka, Automatyka, Pomiary w Gospodarce i Ochronie Środowiska*, vol. 11, no. 2, pp. 44–47, Jun. 2021.

[93] O. A. Akbari, H. Haghjoo, A. M. Abed, M. Karimi, A. Maghzian, G. A. S. Shabani, A. Anvari, N. Akkurt, and D. Toghraie, "Numerical investigation the hydrodynamic parameters of the flow in a wavy corrugated channel using different turbulence models," *Heliyon*, vol. 8, no. 12, p. e11901, 2022.

[94] M. D. Buhmann, *Radial Basis Functions: Theory and Implementations*, 1st ed. Cambridge University Press, 2003.

[95] E. J. Kansa, "Multiquadrics—a scattered data approximation scheme with applications to computational fluid-dynamics—i surface approximations and partial derivative estimates," *Computers & Mathematics with Applications*, vol. 19, no. 8-9, pp. 127–145, 1990.

[96] R. L. Hardy, "Multiquadric equations of topography and other irregular surfaces," *Journal of Geophysical Research*, vol. 76, no. 8, pp. 1905–1915, 1971.

[97] J. Duchon, "Splines minimizing rotation-invariant semi-norms in sobolev spaces," in *Constructive Theory of Functions of Several Variables*, ser. Lecture Notes in Mathematics, G. Meinguet, Ed. Berlin, Heidelberg: Springer, 1977, vol. 571, pp. 85–100.

[98] C. A. Micchelli, "Interpolation of scattered data: Distance matrices and conditionally positive definite functions," *Constructive Approximation*, vol. 2, pp. 11–22, 1986.

[99] G. E. Fasshauer, *Meshfree approximation methods with MATLAB*. World Scientific, 2007.

[100] G. S. Bhatia and G. Arora, "Radial basis function methods for solving partial differential equations-a review," *Indian Journal of Science and Technology*, vol. 9, no. 45, pp. 1–18, 2016.

[101] G. E. Fasshauer and M. J. McCourt, *Kernel-based Approximation Methods using MATLAB*, 1st ed. World Scientific, 2015.

[102] H. Wendland, *Scattered Data Approximation*, 1st ed. Cambridge University Press, 2005.

[103] B. Fornberg and N. Flyer, *A Primer on Radial Basis Functions with Applications to the Geosciences*, 1st ed. SIAM, 2015.

[104] G. B. Wright and B. Fornberg, "Scattered node compact finite difference-type formulas generated from radial basis functions," *Journal of Computational Physics*, vol. 212, no. 1, pp. 99–123, 2006.

[105] B. Fornberg and G. B. Wright, "Stable computation of multiquadric interpolants for all values of the shape parameter," *Computers & Mathematics with Applications*, vol. 47, no. 1, pp. 497–523, 2004.

[106] L. Ling and E. J. Kansa, "A least-squares preconditioner for radial basis functions collocation methods," *Advances in Computational Mathematics*, vol. 20, no. 1-3, pp. 299–316, 2004.

[107] V. Bayona, N. Flyer, and B. Fornberg, "Stable computations with gaussian radial basis function interpolation," *SIAM Journal on Scientific Computing*, vol. 39, no. 6, pp. A2562–A2583, 2017.

[108] N. Flyer and B. Fornberg, "Radial basis functions: Developments and applications to planetary scale flows," *Computers & Fluids*, vol. 46, no. 1, pp. 23–32, 2011.

[109] G. Arora and G. S. Bhatia, "A meshfree numerical technique based on radial basis function pseudospectral method for fisher's equation," *International Journal of Nonlinear Sciences and Numerical Simulation*, vol. 21, no. 1, pp. 37–49, 2020.

[110] ——, "Radial basis function pseudospectral method for solving standard fitzhugh-nagumo equation," *International Journal of Mathematical, Engineering and Management Sciences*, vol. 5, pp. 1488–1497, 12 2020.

[111] L. C. Evans, *Partial differential equations*. American Mathematical Society, 2022, vol. 19.

[112] S. Rippa, "An algorithm for selecting a good value for the parameter c in radial basis function interpolation," *Advances in Computational Mathematics*, vol. 11, no. 2, pp. 193–210, Nov 1999.

[113] A. J. M. Ferreira and G. E. Fasshauer, "An rbf-pseudospectral approach for the static and vibration analysis of composite plates using a higher-order theory," *International Journal for Computational Methods in Engineering Science and Mechanics*, vol. 8, no. 5, pp. 323–339, 2007.

[114] R. K. Chandrawat, V. Joshi, and O. A. Bég, "Numerical study of time dependent flow of immiscible Saffman dusty (fluid-particle suspension) and Eringen micropolar fluids in a duct with a modified cubic B-spline Differential Quadrature method," *International Communications in Heat and Mass Transfer*, vol. 130, p. 105758, 2022.

[115] S. Chakraborty and N. Medhi, "Mhd flow and heat transfer of a dusty viscoelastic liquid down an inclined channel in porous medium under variable viscosity and pressure," *Indian Journal of Theoretical Physics*, vol. 43, pp. 293–302, 1995.

[116] A. Roja, B. J. Gireesha, and B. Nagaraja, "Irreversibility investigation of Casson fluid flow in an inclined channel subject to a Darcy–Forchheimer porous medium: A numerical study," *Applied Mathematics and Mechanics*, vol. 42, no. 1, pp. 95–108, 2021.

[117] O. A. Bég, S. K. Ghosh, and M. Narahari, "Mathematical modeling of oscillatory MHD couette flow in a rotating highly permeable medium permeated by an oblique magnetic field," *Chemical Engineering Communications*, 2011.

[118] G. Kalpana and S. Saleem, "Heat transfer of magnetohydrodynamic stratified dusty fluid flow through an inclined irregular porous channel," *Nanomaterials*, vol. 12, no. 19, p. 3309, 2022.

[119] S. Chandrasekhar, *Hydrodynamic and Hydromagnetic Stability*. Oxford University Press, 1961.

[120] V. Vidyanidhi, G. K. Raju, and V. V. R. Rao, "Magnetohydrodynamic couette flow and heat transfer in a rotating system," *Defence Science Journal*, vol. 30, no. 4, pp. 369–380, 1980.

[121] M. D. Buhmann, "Radial basis functions," *Acta Numerica*, vol. 9, pp. 1–38, 2000.

[122] H. Wendland, "Piecewise polynomial, positive definite and compactly supported radial functions of minimal degree," *Advances in Computational Mathematics*, vol. 4, no. 1, pp. 389–396, 1995.

[123] E. Hairer and C. Lubich, "Numerical solution of ordinary differential equations," in *The Princeton Companion to Applied Mathematics*. Princeton University Press, 2012, pp. 293–305.

[124] Y. Norasia, M. Tafrikan, and B. Kamaluddin, "Analysis of the magnetohydrodynamics nanoviscous fluid based on volume fraction and thermophysical properties," *BAREKENG: Jurnal Ilmu Matematika dan Terapan*, vol. 17, pp. 0331–0340, 04 2023.

[125] G. Ahmadi, "Self-similar solution of incompressible micropolar boundary layer flow over a semi-infinite plate," *International Journal of Engineering Science*, vol. 14, no. 7, pp. 639–646, 1976.

[126] M. Devakar, A. Raje, and S. Kumar, "Numerical study on an unsteady flow of an immiscible micropolar fluid sandwiched between Newtonian fluids through a channel," *Journal of Applied Mechanics and Technical Physics*, vol. 59, pp. 980–991, 2018.

[127] H. N. Zaidi and N. Ahmad, "Mhd convection fluid flow and heat transfer in an inclined microchannel with heat generation," *American Journal of Applied Mathematics*, vol. 5, no. 5, pp. 124–131, 2017.

[128] M. Kocić, Ž. Stamenković, J. Petrović, and J. Bogdanović-Jovanović, "Mhd micropolar fluid flow in porous media," *Advances in Mechanical Engineering*, vol. 15, no. 6, 2023.

[129] H. Kaneez, "Numerical investigation on transport of momenta and energy in micropolar fluid suspended with dusty, mono and hybrid nano-structures," *Mathematics*, vol. 10, no. 15, p. 2630, 2022.

[130] P. V. S. Narayana, "Effects of hall current and radiation absorption on MHD micropolar fluid in a rotating system," *Journal of Applied Fluid Mechanics*, vol. 10, no. 5, pp. 1234–1245, 2017.

[131] L. Wang, X. Chu, J. Wan, and C. Xiu, "Implementation of micropolar fluids model and hydrodynamic behavior analysis using user-defined function in fluent," *Advances in Mechanical Engineering*, vol. 12, no. 7, 2020.

[132] S. Kumar and K. Sharma, "Entropy optimization analysis of marangoni convective flow over a rotating disk moving vertically with an inclined magnetic field and nonuniform heat source," *Heat Transfer*, vol. 52, pp. 1778–1805, 11 2022.

[133] S. A. Shehzad, Z. Abdullah, A. Alsaedi, F. M. Abbasi, and T. Hayat, "Thermally radiative three-dimensional flow of Jeffrey nanofluid with internal heat gener-

ation and magnetic field," *Journal of Magnetism and Magnetic Materials*, vol. 397, pp. 108–114, 2016.

[134] N. Akbar, D. Tripathi, O. Bég, and Z. Khan, "Mhd dissipative flow and heat transfer of casson fluids due to metachronal wave propulsion of beating cilia with thermal and velocity slip effects under an oblique magnetic field," *Acta Astronautica*, vol. 128, 07 2016.

[135] K. Das, N. Acharya, and P. K. Kundu, "Radiative flow of MHD Jeffrey fluid past a stretching sheet with surface slip and melting heat transfer," *Alexandria Engineering Journal*, vol. 54, no. 4, pp. 815–821, 2015.

[136] N. Vijay and K. Sharma, "Heat and mass transfer study of ferrofluid flow between co-rotating stretchable disks with geothermal viscosity: Ham Analysis," *Chinese Journal of Physics*, vol. 78, pp. 165–182, 2022.

[137] A. Dogonchi, K. Divsalar, and D. Ganji, "Flow and heat transfer of MHD nanofluid between parallel plates in the presence of thermal radiation," *Computer Methods in Applied Mechanics and Engineering*, vol. 310, pp. 58–76, 2016.

[138] A. Kucaba-Piętal, Z. Walenta, and Z. Peradzyński, "Molecular dynamics computer simulation of water flows in nanochannels," *Bulletin of the Polish Academy of Sciences Technical Sciences*, pp. 55–61, 2009.

List of Publications

1. **Himanshu**, G. S. Bhatia, and R. K. Chandrawat, "Investigation of micropolar dusty fluid flow in a rotational frame with magnetic field: A meshless radial basis function pseudospectral approach" *ZAMM - Journal of Applied Mathematics and Mechanics / Zeitschrift für Angewandte Mathematik und Mechanik*, vol. 104, no. 10, p. e202300868, 2024. (**SCI IF-3.2, SCOPUS SJR-0.388 Q2**)

2. **Himanshu**, G. S. Bhatia, and R. K. Chandrawat, "Computational study of pumping power for MHD dusty fluid in a rotating horizontal channel" *Journal of Nonlinear, Complex and Data Science, vol. 26, no. 5, 2025, pp. 239-263.* (**SCI IF-1.5, SCOPUS SJR-0.337**).

3. **Himanshu**, G. S. Bhatia, and R. K. Chandrawat, "Inclined Channel Flow of Magnetohydrodynamic Micropolar Dusty Fluids Under Rotation: An RBF-Pseudo-Spectral Approach and Pumping Power Computation" *ZAMM - Journal of Applied Mathematics and Mechanics / Zeitschrift für Angewandte Mathematik und Mechanik*, vol. 105, no. 10, p. e70239, 2025 (**SCI IF-3.2, SCOPUS SJR-0.388 Q2**).

4. **Himanshu**, G. S. Bhatia, and R. K. Chandrawat, “Flow and thermal analysis of jeffrey fluid in a rotating horizontal channel under magnetic field influence: a radial basis function pseudo-spectral approach,” Multiscale and Multidisciplinary Modeling, Experiments and Design, vol. 8, no. 7, p. 304, May 2025.
(**SCOPUS SJR-0.420 Q2**)

5. **Himanshu**, G. S. Bhatia, and R. K. Chandrawat, "Impact of Magnetic Field and Rotation on Dusty Fluid Flow in Inclined Channel: A Numerical Study Using the Radial Basis Function Pseudospectral Method," (Communicated)

Paper presented in Conferences

1. Himanshu, Gurpreet Singh Bhatia, and Rajesh Kumar Chandrawat, "Investigation of Micropolar Dusty Fluid Flow in a Rotational Frame with Magnetic Field: A Meshless Radial Basis Function Pseudospectral Approach" in the International Conference on Recent Advances in Fluid Mechanics and Nanoelectronics (ICRAFMN-2023) organized by Manipal Institute of Technology Bengaluru in association with National Institute of Technology Uttarakhand, during July 12–14, 2023.

2. Himanshu, Gurpreet Singh Bhatia, and Rajesh Kumar Chandrawat, "Impact of magnetic field and rotation on dusty fluid flow in inclined channel" in the One Day International Multidisciplinary Conference on “Multidisciplinarity & Sustainable Development: Global Trends, Challenges and Opportunities” organized by the Centre for Professional Development (CPD) & Internal Quality Assurance Cell (IQAC), NIILM University, Kaithal, Haryana, India on December 21, 2024.

List of Workshops

1. Attended the 12-days Online Refresher Course on "Heat and Mass Transfer: Basic and Advanced" organized by the Malaviya Mission Teacher Training Center at the Indian Institute of Information Technology, Design and Manufacturing, Kancheepuram, Chennai during March $10 - 22, 2025$.

2. Attended the 12-days Online Refresher Course on"Mathematical Sciences" organized by Teaching Learning Centre, Ramanujan College University of Delhi under the aegis of Ministry Of Education, Pandit Madan Mohan Malaviya National Mission on Teachers and Teaching during September 26^{th} - October $10^{th}, 2022$.